UNIVERSITY OF OXFORD

Liquid Crystals for Reconfigurable Intelligent Surfaces and Antennas

Bradley C. Mee
St. Edmund Hall

A thesis submitted for the degree of

Doctor of Philosophy

in the

Department of Engineering Science

Michaelmas 2025

Abstract

The wireless communications channel is subject to many deleterious effects: reconfigurable intelligent surfaces (RISs) and reconfigurable antennas (RAs) have emerged in recent years as technologies with the potential to address these effects, with the aim of improving the performance of the wireless link.

There currently exists contention in the reported literature on RIS technologies for radio frequencies between theoretical studies that assume the RIS can apply a continuous phase-shift to impinging electromagnetic (EM) waves, and practical demonstrations that can only achieve a discrete two-level (1-bit) phase adjustment by employing common electronic circuit elements such as p-i-n diodes. With the ever-increasing number of wirelessly connected devices in home and industrial environments, the need for antennas that can dynamically respond to worsening (frequency-dependent) channel conditions has become of paramount interest. Common iterations of RAs also utilise circuit elements that only allow discrete frequency changes, dramatically reducing the possible frequency points to which the antenna could be tuned.

Therefore, in this Thesis, the design, simulation, and experimental validation of RISs and RAs that incorporate nematic liquid crystal (LC) materials are considered as potential solutions to the limitations of conventional discrete phase and/or frequency modulation elements. In particular, nematic LCs are investigated for their utility in effecting a continuous and reversible alteration in either the operational frequency of RAs, or a phase-shift in the range of $0 - 360°$ of signals incident at the RIS, through an externally applied electric field. Employing these devices to adjust the phase, or frequency, of EM waves can lead to improvements in the wireless communications link, such as reducing bit error rates or increasing signal-to-noise ratio, without requiring large, power-consuming infrastructure such as communications relays or antenna arrays.

For this study, a range of experimental techniques are developed in-house for the fabrication of nematic LC devices used at radio frequencies (RF), including the development of a bespoke anechoic chamber utilised for conducting RF measurements. Following this, a frequency-reconfigurable bowtie antenna, featuring a thermally stimulated nematic LC, is demonstrated to produce a frequency shift of 21 MHz from the antenna, operating at 2

GHz. Then, the design and demonstration of a novel reconfigurable optically-transparent microstrip antenna, operating at 11 GHz is presented. External electric fields are applied across the nematic LC layer, which is precisely deposited onto the radiating area of the antenna via drop-on-demand inkjet printing, to cause a 90 MHz frequency shift, while the reduction in optical transmittance due to the addition of the LC and alignment layers is no more than 14%.

Next, a stringent set of technical criteria is delineated to produce an LC-based RIS unit cell that is suitable for fifth-generation new radio (5G NR) frequency bands, while allowing a fair comparison with the leading alternative for 5G NR. Full-wave EM simulations establish that this novel unit cell is adept at meeting each of the criteria and achieves a continuous phase-shift that is superior to the alternative technology. Further measurements of the unit cell support these simulations, indicating potential utility in developing a full LC-based RIS. Finally, a novel concept of a dual-mode RIS unit cell for visible light communications (VLC) is proposed. This unit cell extends the capability of a VLC system by operating in both reflection and transmission modes, controlled via an external voltage applied to a chiral nematic LC layer, while also effecting a continuous phase-shift on reflected light signals via a separate nematic LC layer.

Publications

Thesis

B. C. Mee, Q. Zheng, P. S. Grant, C. J. Stevens, S. J. Elston, S. M. Morris and J. P. Coon, "Reconfigurable Bowtie Antenna Using a Nematic Liquid Crystal," *2023 IEEE Conference on Antenna Measurements and Applications (CAMA)*, Genoa, Italy, 2023, pp. 507-512.

B. C. Mee, S. J. Elston, S. M. Morris and J. P. Coon, "Characterization of Dielectric Properties of Nematic Liquid Crystals Using an Optically-Transparent Microstrip Resonator at 5 GHz," *2025 IEEE 20th International Symposium on Antenna Technology and Applied Electromagnetics (ANTEM)*, St. John's, NL, Canada, 2025, pp. 93-96.

B. C. Mee, W. Kamal, A. Castrejon-Pita, W. Whittow, S. J. Elston, S. M. Morris and J. P. Coon, "Reconfigurable Optically-Transparent Antenna Using Drop-on-Demand Printed Nematic Liquid Crystals", 2025 (*under review*).

B. C. Mee, S. J. Elston, S. M. Morris and J. P. Coon, "Reconfigurable Intelligent Surface for 5G Millimetre-Wave Applications using Liquid Crystal-based Unit Cells", 2026 (*under review*).

B. C. Mee, S. J. Elston, S. M. Morris and J. P. Coon, "Dual-Mode Reconfigurable Intelligent Surface Unit Cell for Visible Light Communications", (in-preparation).

Not in this thesis

J. Ma, **B. C. Mee**, et al., "Advanced Image-Integrated Smart Windows using Printed Electrochromic Polymer-Dispersed Liquid Crystal Droplets", *Adv. Optical Mater.* 2025, e01586.

Presentations

"Characterization of Dielectric Properties of Nematic Liquid Crystals Using an Optically-Transparent Microstrip Resonator at 5 GHz", *2025 IEEE 20th International Symposium on Antenna Technology and Applied Electromagnetics (ANTEM)*, 2025. (Oral presentation).

"Reconfigurable Optically-Transparent Antenna Using a Nematic Liquid Crystal", *British Liquid Crystal Society Conference*, 2024. (Poster Presentation).

"Reconfigurable Bowtie Antenna Using a Nematic Liquid Crystal", *IEEE Conference on Antenna Measurements and Applications* 2023. (Oral Presentation).

Stimuli-Responsive Materials for Reconfigurable Intelligent Surfaces, *Oxford Photonics Day*, 2022. (Poster Presentation).

Patent Filings

B. C. Mee, S. J. Elston, S. M. Morris and J. P. Coon, 'Transparent Antenna', 159813 GB, 2025.

Acknowledgements

Firstly, I would like to acknowledge the unconditional and unwavering love and companionship of my faithful four-legged friend Hendrix.

After coming into academia following a ten-year career in the Royal Corps of Signals, I owe a lot of gratitude to many academics who have supported me from my undergraduate studies to now. Firstly, to Sian Williams, who accepted me onto an engineering foundation programme at Loughborough University, and Stephanie Thomas, who spent many hours helping me with maths; without this help I would not have been able to attend university.

During my undergraduate degree, James Flynn, Will Whittow, Chinthana Panagamuwa, Bucur Novac, and Rob Edwards were each fantastic lecturers who motivated me to follow a path into academia. Bucur, in particular, supported me in applying to some of the best engineering universities in the world.

After Loughborough, I completed a master's degree at Imperial College London, where Athanassios Manikas was my supervisor and who pushed me to work at a level I would not have otherwise achieved.

Whilst at Oxford, Justin Coon, Steve Morris and Steve Elston (aka the Steves) have all supervised me. They have always provided support, whether through teaching, allowing me to research the areas that I was interested in, or spending huge amounts of money on equipment.

I also owe thanks to many others within the research group at Oxford, in particular, Grahame Waqas, Zimo, Linpei, and Qianfang have all assisted me with teaching or conducting experiments. My fellow D. Phil. students Camron, Yihan, Mengmeng, Nathan, Alva, Zhi, and Ioannis have all been great friends and have made my time at Oxford far more enjoyable.

Contents

Chapter 1

Introduction

The ability to communicate information is a common feature of all aspects of life; from bird calls to trees exploiting complex networks of fungi to communicate beneath the forest floor, these signals are vital for the individual and the species to survive. The ability to communicate complex ideas has distinguished humans and enabled us to leverage an evolutionary advantage over competing species, and even our hominid cousins. Communication was key in enabling sophisticated cultures and advanced technological societies to develop: over a billion billion bits of information are transferred around the globe each day - the majority of which amounts to little more than gossip - yet without the ability to transmit ideas, *Homo Sapiens* would be doomed to forever re-invent the wheel.

There has always existed a drive for faster and more reliable methods to send information across large distances, from smoke signals to networks of satellites spanning the entire globe. In the 12th century, the Mongolians created a vast network of horse stables along trading routes to pass information across the empire at great speeds: Genghis Khan knew well that the transfer of information was vital for maintaining his empire.

The discovery of electromagnetism has allowed modern data rates to immensely exceed any earlier method of transmitting information and has interlinked the entire globe with near-instant communication. In the future, data rates will be increased further through high-frequency, high-power lasers using line of sight links, but beyond this is uncertain. Conjecture suggests that the discovery of the graviton could allow the manipulation of gravitational waves to communicate across the universe, or the development of brain-computer interfaces could directly link human cognition with digital systems.

1.1 Motivation and Context

Traditional wireless communications systems consist of a transmitter, receiver, and a channel through which information is sent. While it is possible to design and tailor the transmitter and receiver to meet specific application requirements, the wireless channel has erstwhile not been subject to substantial modification or control by engineers. Typically, a wireless signal travelling between two points will undergo path loss and shadowing, with multiple delayed copies of the transmitted signal arriving at the receiver, causing degradation of the received signal through destructive interference between the direct and delayed paths [1].

To address the limitations of the wireless channel, it has been proposed that two-dimensional (2D) surfaces comprising of a large number of sub-wavelength reflecting elements can be employed to affect a phase-shift onto the impinging waves such that they arrive in-phase with the strongest path and combine constructively. These reconfigurable intelligent surfaces (RISs) offer the opportunity to improve the performance of the wireless channel without incurring substantial increases in the total power consumption of the link, for example, compared with a relay [2].

Current research on the theoretical performance of RIS technologies relies on the assumption of achieving a continuous phase-shift from the unit elements. However, in practice this has yet to be realised, with a 1-bit phase change i.e., 0° or 180°, employed in practical systems [3], [4]. In fact, for all of the research carried out to date on RIS technology there are scant few published works that realise and characterise a physical implementation of a RIS device. **Figure 1.1** illustrates the benefit in employing RIS with continuous phase-shifts over a 1-bit or 2-bit phase-shift demonstrated through simulations carried out in MATLAB for a RIS-assisted wireless channel, based on the 3GPP Urban Micro channel model at 2 GHz [5], assuming a RIS located 20 meters from a stationary receiver. Here, the single-input single-output (SISO) case represents a typical wireless channel, where the probability of an outage, that is the probability that the capacity of the channel falls below a threshold value, decreases as the SNR increases. When including a RIS between the transmitter and receiver, the results indicate that a RIS with a continuous phase-shift outperforms a RIS with a 1-bit or 2-bit phase-shift (i.e.,

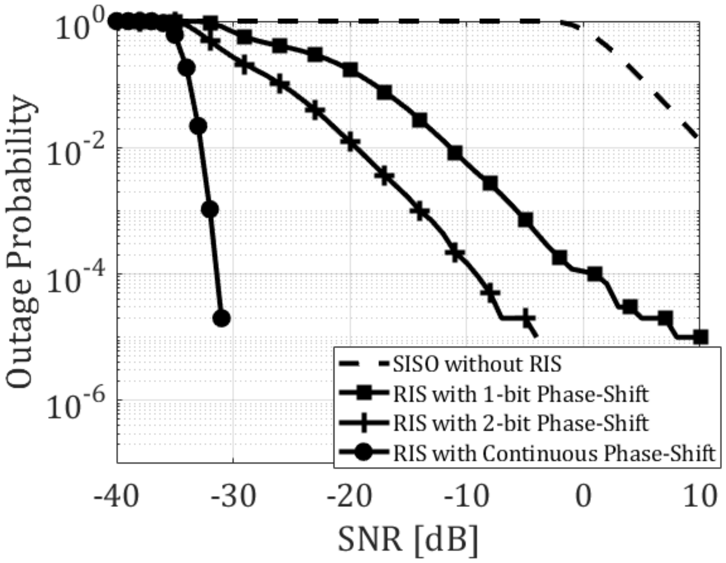

Figure 1.1: Performance comparison of a Reconfigurable Intelligent Surface (RIS). Results for the outage probability as a function of the signal-to-noise ratio (SNR) for a Single-input single-output (SISO) without RIS, RIS technology included with a 1-bit phase shift, RIS technology included with a 2-bit phase shift, and RIS technology included with a continuous phase shift capability. Simulations generated using a program written in MATLAB based on the 3GPP Urban Micro channel model at 2 GHz.

the RIS applies 2 or 4 discrete phase-values to the impinging signal) by up to 24 dB or 38 dB, respectively. Hence, the more precisely the phase-shift applied at the RIS matches the desired phase-shift, the better the system performs.

Fundamental to the operation of the RIS is the material from which it is formed. The material is not only required to be low cost and easily manufactured but also to possess properties that suit specific performance criteria such as efficiency or cost. As the RIS is intended to be passive, there is no increase in gain between incident and reflected waves, instead, only the phase of the impinging wave is affected by the RIS. Those RIS structures that have previously been reported utilised electric circuit components, such as diodes to achieve phase modulation. However, such devices can only facilitate a 1-bit phase-shift and to increase this would necessitate an increase in components and cost. Hence, a candidate material to elicit a continuous phase response from the RIS unit element will be investigated here, *videlicet*, nematic Liquid Crystals (LCs).

Nematic LCs are characterised by long-range orientational order but with no positional order, the nematic phase typically exists between more highly ordered LC, or crystalline, and isotropic liquid phases. Importantly, a nematic LC can be manipulated through external electric and magnetic fields due to their inherent anisotropic properties, a feature that has long been leveraged at optical wavelengths i.e., 400 nm - 700 nm[1]. Specific to this Thesis, the aim will be to exploit the anisotropy to produce a continuous phase-shift for signals impinging on a RIS at radio frequencies (RF). Numerous properties of LCs can be measured but there are particular parameters of importance for RIS technologies that must be optimised at RF. For example, the dielectric anisotropy and switching time of the LC will define the ability of the RIS to achieve a full phase-shift and the rate at which this happens. These characteristics will differ between LC materials, with bespoke mixtures available that optimise these parameters at RF. Thus, the work presented in this thesis will also investigate the means by which to identify, measure, and optimise for desirable LC properties.

Reconfigurable antennas (RAs) offer the capability to dynamically alter the otherwise static properties of an antenna, such as the frequency response, radiation pattern, or impedance, and are typically achieved by modifying of the physical structure to affect the distribution of the antennas' electric fields, or surface currents, in a controllable fashion. This can be utilised to improve the signal-to-noise-ratio at the receiver by monitoring the wireless channel and responding to interference from RF congestion, or other environmental changes, and switch to nearby frequencies that provide an improved quality of service. Hence, RAs are particularly expedient with the ever-increasing number of wirelessly connected devices. Nematic LCs will also be utilised in this Thesis to investigate the performance of LC-based RAs that can achieve a continuous frequency response by tuning the LC element. Furthermore, the methods in design, fabrication, and testing of these antennas closely match that of a RIS, and provide an experimental and simulation platform from which future LC-based RIS elements can be refined.

RIS and RA technology features prominently in academic and industrial research, however, there also exists a strong, and growing, market demand for these products. This industry is fuelled by fifth-generation (5G) and sixth-generation (6G) telecommunications advancements, specifically for urban infrastructure and millimetre wave (mm-

---

[1] In optics it is common to refer to electromagnetic waves in terms of wavelength, while for most other applications frequency is used.

wave) communications, and in the aerospace and defence sectors for unmanned aerial vehicles (UAVs), secure communications and satellite communications. The global market for RIS hardware technology has risen from £3.2 billion in 2023 to £4.2 billion in 2024 and is expected to reach £34 billion by 2033 [6]. RAs accounted for 7% of the overall antenna market in 2024, worth £1.4 billion, which is expected to rise to 9% by 2033 with an expected global market of £5.56 billion [7], [8]. The two biggest markets for RIS and RAs are the aforementioned telecommunications and defence sectors; however, the automotive and healthcare industries are also potential markets for vehicle-to-vehicle communications and health monitoring, respectively.

1.2 State-of-the-Art

1.2.1 Dielectric Characterisation Methods

The measurement of a material's dielectric properties in the RF spectrum can generally be split into two separate methods: resonance-based and transmission/reflection based. Resonance-based techniques for measuring dielectric properties of a nematic LC provide a higher accuracy than non-resonant methods [9]. The main disadvantage, however, is that resonant techniques can only measure low loss material due to a broadening resonance curve as the material loss increases. The complex permittivity is found by comparing the spectral shift of the two cases when the dielectric sample is not present and when it is present. Resonance techniques can be split into two further sub-categories.

Firstly, the dielectric resonance technique involves placing a sample into a resonant cavity with the resonance provided by the sample itself. For example, the split post dielectric resonator method was utilised in [10]. The second sub-category for resonant methods is the cavity perturbation technique where the sample dielectric provides a perturbation in the applied field within the resonant cavity. In [11], [12], a review of the characterisation of several different LC types, such as E7, BL111, and GT3-23001, was presented, all of which use the rectangular cavity perturbation method (RCPM) described in [13].

The primary benefit of employing transmission/reflection measurement techniques is the ability to perform measurements across a broad range of frequencies. However, these techniques suffer from poorer accuracy, an inability to measure low material losses, and the requirement of extensive calibration or curve fitting algorithms. Transmission/reflection techniques rely on an incident electromagnetic (EM) wave passing through the LC material and recording the scattering parameters (S-parameters), and can be conducted in free-space, or in a medium such as a coaxial line or microstrip line. The permittivity is then extracted via computer models fitting the simulated results to the measurements. Experiments conducted in [14] and [15] on devices that were fabricated based on the inverted microstrip line (IMSL) design, with a broadband measurement capability over 15 GHz - 65 GHz and 30 GHz - 60 GHz, respectively. However, the reported values for the material losses using IMSL were significantly higher than for the two independently measured RCPM techniques in [12], [16].

Recently, novel techniques to provide rapid and accurate measurements of the complex dielectric properties have been developed based on simple printed circuit boards (PCBs) with resonant microstrip lines, and do not require laborious calibration processes. In [17], the measurement of uniaxial anisotropic dielectric permittivity was achieved through a resonant strip sensor on a PCB, with the solid sample placed on top of two parallel resonant strips. This technique was adapted in [18], where the substrate was 3D printed with a cleft running between the two resonant strips into which the dielectric sample was placed. However, to adapt this method for LCs would require very high voltages to ensure the director is fully aligned, and complicated analytical calculations to determine the proportionality constants.

Another resonance based PCB method was reported in [19], where a nematic LC was characterised using an IMSL, and with a circular patch antenna in [20]. These devices were quick and low-cost to fabricate; however, they were subject to variations in the PCB manufacturing process. One recurring issue with the PCB-based design, e.g., [19], [20], [21], was that the thickness of the LC layer was $\gg 100\ \mu$m, where the surface anchoring can no longer reliably maintain a uniform alignment through the bulk material. Additionally, the voltage required to fully align the LC director parallel to the field would be $V > 100$ V, while each of the authors in [19], [20], [21] apply at most 30 V. Hence, the values reported for $\varepsilon_\perp$ and $\varepsilon_\parallel$ are average permittivities at best, due to the large LC layer thickness.

From considering the recent literature pertaining to the characterisation of dielectric permittivity, with particular emphasis on LCs, the following points are necessary in designing a device:

- the resonant technique is preferable to measure the complex permittivity and avoid laborious calibration processes. A resonant device will require;
    - the device to be simple and quick to fabricate,
    - enable measurements at multiple resonant modes,
    - a high Q-factor for reliable measurements of the material losses, and
    - a suitable microstrip line width to LC thickness ratio to reduce fringing.
- The dielectric permittivity should be extracted from a single measurement.
- Either a bias-tee is required, or the cavity should be decoupled from the RF input to protect the vector network analyser (VNA).
- Consideration of the LC layer thickness should be made regarding the LC alignment and applied voltage.

1.2.2 Reconfigurable and Transparent Antennas

Microstrip antennas have become commonplace for wireless communications systems, such as cellular phones [22], implanted medical devices [23] and satellites [24], due to their low weight, size, and cost of production. Such microstrip antennas are typically fabricated by removing copper cladding from a PCB substrate into the desired geometry, allowing a co-planar connection between the coaxial input and antenna feed. Antenna properties such as radiation pattern and operational frequency are dependent on the particular geometry of the conductor and substrate material [25].

The development of RAs that are small, inexpensive and reliable, has been driven over recent years by a number of factors including: alleviating the increasingly congested radio environment [26], as an aid to cellular [27] or vehicular networks [28], future technologies such as the 6G-IoT [29], and systems that require frequency-hopping and anti-jamming techniques [30].

The modification of the antenna functionality can be realised by the use of; tunable materials, for example in [31] where a frequency tunable patch antenna was achieved through mechanically altering an origami-inspired dielectric material; switching circuits [32], or physically altering the architecture of the antenna [33]. For any method employed in eliciting modifications, three main considerations must be addressed: the parameter to be changed, the method of doing so, whether alterations are continuous or discretised.

One of the specific challenges in designing an RA is in reliably tailoring one antenna property while maintaining the performance of other properties; for example, maintaining the bandwidth while altering the operating frequency. Many RA designs lack the ability to provide a continuous range in which the antenna can be tuned [32]. The dielectric anisotropy of nematic LCs has previously been investigated for use in RAs for wireless and space applications [34]. LCs have also been employed in a beam-steering lens antenna to implement a reconfigurable aperture in the 50 GHz - 75 GHz band in [35] and a pair of reflecting elements incorporated a nematic LC to produce a reconfigurable reflectarray at 78 GHz in [36].

Recently, a new class of patch antennas has been developed that are optically-transparent, while maintaining electrically conductivity to radio frequencies, i.e., 1 GHz – 100 GHz [37]. Such devices are realised by replacing the copper conductor with transparent conducting films (TCFs), or by substituting the solid copper with a fine mesh of a conductive alloy a few micrometers across. The substrate material most commonly employed is glass. The authors of [38] investigated the physical properties of TCFs in the visible EM spectrum from the Drude model of electrical conduction, deriving relationships between the quantum properties of a TCF and measurable parameters such as electrical resistance and transmittance. The work in [39], [40] was also directly related to the use of TCFs in optically-transparent antennas, where the effects of electron mobility, frequency, transparency, and film thickness were examined through a series of simulations to show that the efficiency of the antenna could be improved with higher electron mobility or frequency, while increasing film thickness was found to degrade transparency.

The practical benefits of optically-transparent antennas are particularly expedient with the advent of display technology, and the increasing number of wirelessly connected devices causing RF congestion. Studies in [41] and [42], implemented transparent antennas into the lenses of smart glasses, exhibiting the flexible nature of the thin films. Further applications include the development of transparent antennas into laptop displays [43], and cellular phones [44]. In [45], a transparent patch antenna was developed and integrated into solar cells for satellite applications, whereas a transparent antenna array was integrated into a solar cell in [46]. Results from these studies show that transparent antennas can be successfully integrated into solar cells, saving space and weight, while having a minimal effect on the current draw of the cell.

Throughout the literature on optically-transparent antennas there exists contention between the two materials typically employed as electrical conductors, namely:

- **Transparent Conducting Films**

  TCFs are oxide doped semiconductors that are deposited into a thin film between 100 nm - 500 nm thick and exhibit excellent transparency in the optical domain but limited electrical conductivity. Typically, the TCF employed is indium-tin oxide (ITO) [47], whereas a multi-layer film using indium-zinc-tin oxide (IZTO) and silver (Ag) has been tested in [41] and [48], and fluorine doped tin oxide (FTO) was investigated in [49].

- **Metal Meshes**

  Metal meshes (MM) consist of typical metals used in electronics, such as copper, silver or gold, that are deposited in fine meshes a few tens of micrometers across, in various patterns and filling factors that affect the antenna efficiency or transparency. This trade-off was elucidated in [50], where honeycomb, square, diamond and circle meshes with varying filling factors were scrutinised. In [51], a copper grid 100 μm thick was etched using a photolithography process, and a square lattice 200 μm thick was contrasted with a micro-MM 20 μm thick in [52]. A diamond lattice using Ag alloy was studied in [44].

The optical transmittance of a MM, T_{mesh}, is calculated from the mesh geometry by

$$T_{mesh} = (1 - \Psi)^2 \tag{1.1}$$

where Ψ is the filling factor, that is, the ratio of the conductive grid to empty space

$$\Psi = \frac{w}{w+g} \tag{1.2}$$

with w relating to the line width of the metal conductor and g the gap between conductive tracks. As such, the transparency is greatly affected by alterations to the mesh geometry. In comparison, TCFs are not subject to such changes. The primary difference between the two classes of materials is that TCFs produce improved optical transparency, whereas MMs exhibit enhanced electrical conductivity.

To date, there have been only two studies that consider the application of LCs in an optically transparent antenna. In [42], an LC layer forms part of the lens in virtual reality smart glasses, although the LC does not play any role in the operation of the antenna. In Aghabeyki et al. [53], the authors integrated the LC mixture GT7-29001 into a beam-steering reflectarray at 29 GHz, with the GT7-29001 LC effecting a phase-shift on signals incident at the array, which employed a MM grid with $g = 300$ μm. For electrode gaps of this size, it is unlikely that the LC in these areas can effectively control the phase-shift of incident RF signals as the electric field strength in these gaps was not sufficient to reorientate the LC director, although simulations in [53] suggest that this is not the case. However, those simulations neglect important physical relationships between the LC director and anchoring effects through the bulk material at large distances, that is, $>$ 100 μm, and do not portray the entire picture. This is further illustrated by comparing this phased-array with the results from another LC-based phased array in [54][2] which reports a phase-shift of 16.5°/V, whereas Aghabeyki et al. achieved 6.5°/V. Furthermore, due to the large thickness of the LC layer, the transparency achieved by the final device is $<$ 45% at wavelengths $<$ 500 nm and is no better than 70% in any portion of the visible spectrum.

RAs are an active research area but there remain several areas that are worthy of investigation:

- methods to reconfigure a single antenna property without impinging on another,

---

[2] The reflectarray in this study was not optically transparent; however, that does not effect the achievable phase-shift from the LC.

- materials to elicit a continuous reconfiguration, e.g., in frequency response, rather than a discretised response, and
- studies that model the performance of a RA configuration compared with a single-input single-output (SISO), or multiple-input multiple-output (MIMO) system.

Several general challenges remain to be addressed in regard to optical transparency:

- the trade-off between optical transparency and electrical conductivity,
- improving antenna efficiency and gain,
- selecting the conductive material to form the antenna structure, and
- combining optically-transparent conductors with traditional electronics that are opaque.
- Specifically to transparent RAs, an optically-transparent material to produce the reconfiguration.

1.2.3 Reconfigurable Intelligent Surfaces

With the demand for mobile data traffic expected to rise from 100 exabytes to 368 exabytes between 2022-2027 [55], the requirements for 5G and 6G technologies has led to the development of metasurfaces as a means to exert a degree of control over the erstwhile uncontrollable wireless environment. Initial papers, with well-cited examples including: [2], [56], [57], identified metasurfaces as a potential solution: developing them into the RIS concept and providing overviews of RIS operation and theoretical models, characterising performance bounds and outlining the possibilities and limitations.

However, these were facile mathematical models and are not sufficient to characterise the RIS environment in a tractable and reliable manner. Hence, later studies were focused on the communications performance of RIS-assisted wireless channels. In [58], free-space path loss models for RIS-assisted channels, including formulae for the RIS radiation pattern, near and far-field beamforming, and free-space path loss of RIS channels were detailed, alongside experimental results. The achievable RIS-assisted channel gain was shown in [59] to be $\mathcal{O}(N^2)$, where N is the number of independent phase-shifting elements, when employing a RIS in the far-field but is upper bounded by 1/9 in the near-field. The N^2 increase in channel gain in the far field was shown via numerical results to hold for RISs with 10^6 elements, however, from a theoretical perspective this behaviour cannot hold indefinitely and will eventually saturate for very large N.

It is common for RIS performance studies to benchmark the RIS against existing performance improvement techniques, e.g., relays. In [2], it was shown that under idealised conditions, a RIS can outperform a simple decode-and-forward (DF) relay. **Figure 1.2** demonstrates a key result from this study: for a RIS with N elements, and with the receiver situated close enough to the RIS, the RIS requires lower transmit power to achieve the same rate as a DF relay, while both outperform a SISO system.

Recent performance-related RIS studies have considered deviating from the established model of a passive RIS (p-RIS) to an active-RIS (a-RIS). In [60], an a-RIS was compared to a p-RIS for the same total link budget, and in [61] an a-RIS signal model was derived and the simulated performance based on that signal model was presented. These works suggested that optimal power splitting between the transmitter and RIS can lead to superior performance, compared with equal power splitting, or a p-RIS for a small number of elements, N. However, as N increases, the power required to manage the a-RIS components will increase. As the performance of the p-RIS will also improve with N^2, it is likely that the p-RIS could eventually win out.

Implementations of a practical RIS have been carried out to test the theoretical models posited for RIS channel gain performance and path loss model. For example, Tang et al., built three RISs with $N = 10200$, 1700 and 256, at an operating frequency, F, of $F = 10.5$ GHz for the two larger RIS, and $F = 4.25$ GHz for the smaller, to test their own path loss model in [62]. The experimental results were congruent with the theoretical model and simulations, however, this experiment only sought to measure the receiver power and did not transmit data or apply individual phase-shifts at the RIS elements. A prototype RIS was reported in [3], where an $N = 1100$ element RIS at $F = 5.8$ GHz with a 1-bit phase-shift was tested. Indoor and outdoor trials produced a ≥ 26 dB power gain, compared to a copper plate, by employing a novel beamforming algorithm with the RIS. Long-range trials (500 m), on the other hand, achieved a rate of 32 Mbps with 20 MHz bandwidth, using 16-QAM (quadrature amplitude modulation)

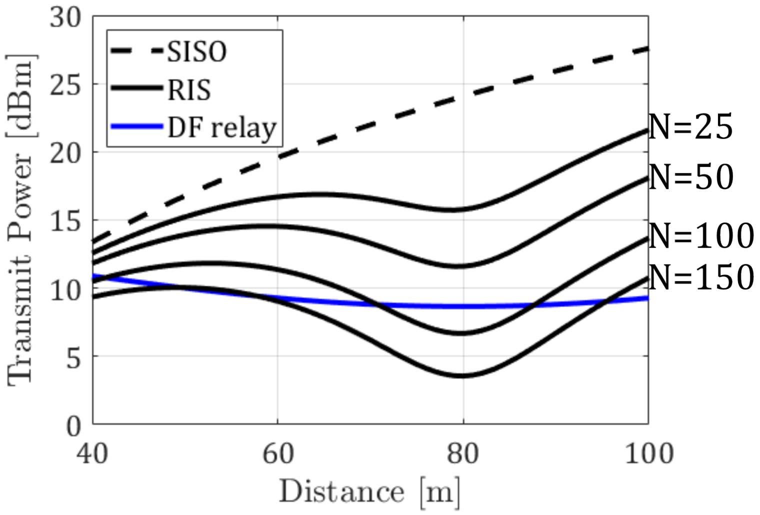

Figure 1.2: Comparison of the minimum required transmitted power, against distance between the transmitter and receiver, for SISO, RIS, and a DF relay. The results are for a rate of $\bar{R} = 6$ bits/s/Hz, with the RIS and relay located 80 m from the transmitter, for varying number of RIS elements, N [2].

to transmit a HD video.

The design, fabrication, and measurement of a RIS for 5G mm-wave frequencies, specifically the n257 (26.5 GHz - 29.5 GHz) and n258 (24.25 GHz - 27.5 GHz) bands, was reported [4]. The unit cell design was updated by removing circular cut-outs from the typical reflecting patch to increase the bandwidth, producing a wideband response. In this case, a 1-bit p-i-n diode was used to elicit a 0° or 180° phase-shift from the unit cell, which was designed to produce a relatively flat phase response (±20°) across the entire bandwidth. The unit cells were embedded into a 20×20 array to form the RIS, which yielded a received signal enhancement of 24.7 dB in the near-field and 18.9 dB in the far-field. However, the authors did not dynamically address the RIS elements, but instead calculated the phase pattern based on a fixed Tx, RIS and Rx distance. Moreover, the authors also did not run any trials transmitting data or modulated waveforms, as has been shown in other works.

One important factor in delivering RIS technology is how to supply the RIS with accurate channel state information (CSI) without requiring large overhead (pilot signals) or power-consuming electronics at the RIS. To reduce the dimensionality of the pilot signal, the authors in [63] exploit spatial correlation in the RIS elements to reduce pilot length, and improve estimation performance using a novel reduced-subspace least-squares channel estimator, outperforming the basic least-squares estimator.

In [64] a novel parametric maximum likelihood estimation technique for line of sight channel estimation was presented. By adaptively selecting RIS configurations from a reduced sized codebook, they maintained accuracy at low SNRs with simulations suggesting a significant reduction in pilot overhead from 1025 (non-parametric) to as few as 6–8 pilots. An alternative method for reducing pilot overhead was the deep learning-based joint channel estimation scheme reported in [65]. The technique included all RIS unit cells in the channel estimation matrix which was transmitted to the BS. Grouping the RIS elements together and then correcting the errors incurred from this using the deep-learning approach led to an improvement in channel estimation accuracy and reduced model time, over the benchmark algorithm.

To date, there has been little research that has investigated a RIS structure incorporating LCs, although many works have alluded to the potential of an LC-based RIS. As an example, an LC-based RIS was simulated and fabricated with measurements in the near and far-fields in [66]. There were few details on the unit element construction in this case, e.g., the patch diameter or LC material. The authors used a Rotman lens to find the direction of arrival of the transmitter antenna to acquire CSI; however, the most important CSI is the phase information at the receiver, so at best it was a minor reduction in CSI overhead (the authors do not quantify the CSI reduction of the rotman lens). The RIS element construction was copper on a glass substrate, without any details on why or how it was made. Nonetheless, measurements of the RIS showed it to be useful in indoor and outdoor scenarios, near and far-field trials, although the authors only use a 1-bit shift. Separately, in [67], a unit cell of a LC-based RIS element, was presented. Rather than a resonant structure, the unit cell utilised a defected delay line with LC employed to apply a phase-shift along the line. The LC was 4.6 μm thick, producing switching times in the millisecond range. The work was predominantly simulation based, with measurements of the radiation performance only. The authors claimed to achieve a 360° phase-shift from the LC-based defected delay line, however, no simulations or measurements to support this claim were included in the work.

Work directed at improving, or characterising, the performance of LC materials in RIS technology has been considered in recent years. Towards this end, the LC relaxation time was addressed in [68], where an LC was doped with a reactive mesogen and the cavity polymerised to form domains for anchoring the LC. The polymer network LC realised a fifty-fold decrease in the LC relaxation time, however, this reduced the LC tuning range by a third. A model of the Fréedericksz transition used to design a bias signal that reduced the LC switch-on time by a factor of 100 was demonstrated in [69], with a technique known as overdrive that is commonly used in the optical domain, with the novelty here in implementing the scheme at RF. The reported method does not improve the relaxation time. Work in [68] was primarily a characterisation of four different dual-frequency LCs (DFLCs) using a reflectarray operating at 75 GHz -110 GHz. Initial measurements estimated the dielectric permittivity of each DFLC, then, the rise and decay times of the DFLC were measured, with the use of overdrive to reduce the switching times. Previous use of overdrive could not affect the relaxation time, however, here the LC was dual-frequency and overdrive was effective. The work demonstrated that using DFLCs alone reduced the relaxation time by a factor of five, although using DFLCs with overdrive reduced the switch on/off time by two orders of magnitude, such that they were both on the order of milliseconds for an LC thickness of 0.05 mm.

Open Research Questions for RIS

Several current open research questions, relating to RIS technology in general are:

- **Achievable Phase-Shift**

  Theoretical work on RIS performance assumes implementation of a RIS with a continuous phase-shift; however, only a discrete phase-shift RIS has been demonstrated experimentally. While the discrete case still provides a benefit over a SISO link, the gains are modest: a RIS with a continuous phase-shift could realise significant uptake of the technology. However, the two limiting factors are: CSI overhead for transmitting precise phase values to each element in the RIS, and the cost of the unit cells increasing, for example, practical demonstrations utilise a single p-i-n diode for 1-bit but would require two diodes for 2-bit.

- **Channel Estimation**

  Several methods have been proposed to reduce overhead from pilot signals used to transmit CSI. The most common workaround is to reduce the RIS elements to a 1-bit on/off state. Algorithms have been developed to improve channel estimation or reduce the overhead of pilot signals but there is currently no agreed-upon solution.

- **Multiple-User RIS**

  Considerations of RIS deployment are typically based on a single user. However, most, if not all, telecommunications standards incorporate multiple users. This could be achieved by allocating RIS usage based on time, power allocation, user performance, or physically sectioning the RIS into several sub-RISs. However, proper analysis into which of these provides the best overall performance is required.

Questions related to LC-based RIS include:

- **Materials to Produce a Phase-Shift**

  Commercially available LC materials are predominantly suited to optical/display applications and offer undesirable performance in the RF domain. However, the rise of reconfigurable RF technologies, in particular RIS and RA, have led to the development of LCs with superior tuning range performance at RF and lower losses. For example, the tuning range of E7 was measured to be 0.45 at 19 GHz, whereas the nematic LC GT3-23001, designed for RF applications, achieved a range of 0.8 at 19 GHz [70]. However, the achievable phase-range and switching times of these materials must be investigated for RIS technologies.

- **Switching Time**

  LC switching times are fundamental to the application of the RIS, with times in the millisecond range required for wireless communications, and likely in the microsecond range for future mm-wave standards. However, switching time is often a trade-off with tuning range due to the physical properties of the LC. Recent developments have mitigated this by using dual-frequency LCs with large applied voltages to reduce switching times but the LC-based RIS use-case may deviate from telecommunications to a system where constraints on switching time are not so strict, e.g., health monitoring.

- **Unit Cell Design**

  A resonance structure is typical, but other designs have been demonstrated. In either case, a design that allows for a large tuning range, short switching time and does not consume large quantities of LC is required. Although in practice, any design is likely to be a trade-off between these requirements.

1.3 Scope and Layout of Thesis

This Thesis will predominantly focus on the 1 GHz to 40 GHz frequency range, which will be assumed forthwith when referring to 'RF', unless otherwise stated. This frequency range was selected to cover current and future wireless communications bands, set limits on the scope of this work, and due to the cost of measurement hardware with increasing frequency, in particular towards terahertz frequencies. The aim of this Thesis is to investigate the feasibility of incorporating nematic LCs into RF devices to produce controllable reconfiguration in the characteristics of those devices through new designs and, in some cases, the use of additive manufacturing techniques. Specifically, the LC will be employed to elicit a controllable frequency response in RAs, and modulate the phase of EM waves reflected by a RIS. For RIS technology, a unit element (or unit cell) will be investigated. To support this aim, the dielectric properties of nematic LCs will also be characterised at RF. An exception to the RF frequency range focus is made for Chapter 8, where a RIS unit element design for a visible light communications (VLC) system is proposed. This deviation was made due to the increasing interest in RIS technologies for VLC and the long-standing use of nematic LCs for optical devices making them ideal candidates for effecting a phase-shift from the RIS unit cell. The remainder of this Thesis is structured in the following manner:

- in Chapter 2, the background theory pertaining to dielectrics, LCs, microwave circuit theory and wireless communication theory, including the RIS-assisted channel and RIS structure is detailed. The work in this Thesis covers a broad range of topics and as such, a brief introduction to each topic will be presented, with references to more detailed discussions or derivations of equations used where necessary.

- In Chapter 3, experimental methods and techniques employed in the fabrication, measurement and simulation for work in the research chapters will be discussed. This includes common LC device preparation methods, and RF measurement techniques, that have been developed for this Thesis, and will focus on the work that was required to bridge the two domains. In particular, the construction of a bespoke anechoic chamber to facilitate a range of RF measurements of new LC-based devices is described in detail and is a major contribution of the Thesis.

- In Chapter 4, a reconfigurable bowtie antenna featuring a nematic LC and operating at 2 GHz is designed, simulated, fabricated, and characterised. Starting with a traditional bowtie design, it is then altered such that the antenna can accommodate a nematic LC in a way that affects a tunable frequency response. Thermal tuning of the LC is employed to produce a reconfigurable antenna that is not dependent on the application of an external electric or magnetic field. This work was published in the 2023 IEEE Conference on Antenna Measurements and Applications, and an oral presentation was given at the conference.

- Chapter 5 reports a method to characterise the dielectric permittivity and material losses of a nematic LC at a frequency of 5 GHz. This technique utilises a transparent microstrip line resonator design to estimate the LC properties and includes EM simulations to assess the effect of the glass substrates on the microwave behaviour. The research contained in this chapter aids in the design of transparent LC-based RF devices used elsewhere in this Thesis. Further to this, LC director profile simulations that include a thermal noise term are developed and results are presented to show the effect of large LC layers on the resulting LC director profile. The experimental work on characterising a nematic LC was published in the 2025 IEEE 20th International Symposium on Antenna Technology and Applied Electromagnetic, with an oral presentation given at the conference.

- Chapter 6 then details the fabrication and measurement of a new reconfigurable optically-transparent microstrip patch antenna operating at a frequency of 11 GHz. Here, the nematic LC is incorporated into the antenna through drop-on-demand inkjet printing to precisely deposit the LC onto the desired area to impart a response, thereby reducing material wastage. A manuscript detailing this work was submitted to the journal of Advanced Engineering Materials and is currently under review. A patent has been filed on the techniques related manufacturing the reconfigurable transparent antenna.

- In Chapter 7, several candidates for a RIS unit cell operating at a frequency of 28 GHz are investigated. Specific constraints on the unit cell performance are delineated. Simulations of the unit cell are used to discern the geometry and achievable phase-shift, with the most promising designs then fabricated and measured using the bespoke anechoic chamber developed in this thesis. The results are tested against the constraints to evaluate their feasibility in a practical RIS. This work was submitted to the 2026 IEEE Conference on Communications.
- Chapter 8 considers a RIS unit cell tailored for use in a visible light communications system. The proposed dual-mode unit cell is a novel design, utilising a chiral nematic LC with a reflection band tuned to visible wavelengths to achieve a phase-shift in both a transmission and reflection mode of the RIS, from a single unit element. The element is tested using interferometry and the experiment results are accompanied by MATLAB director profile simulations. A manuscript for this work is in-preparation.
- The final chapter, Chapter 9, concludes this Thesis by discussing the aims outlined in this Chapter and how they were met, or not met. Comments on how to move forward with particular aspects of this work to either improve the performance, or develop the technical readiness, will also be covered.

Chapter 2

Background

In this Chapter, the background topics that underpin this Thesis will be introduced. The scope of this Thesis covers a broad range of topics including: dielectrics, liquid crystals (LCs), microwave engineering and wireless communications; as such, only the most essential background theory will be discussed, with supplementary concepts, equations, or derivations referenced where necessary. Further background theory will be introduced where it is relevant only to that specific chapter.

It should be mentioned here that due to the broad range of topics covered in this Thesis, there are several instances where notation for certain values is re-used. For example, when discussing LCs, the LC director is always denoted by $\mathbf{n}$; however, in wireless communications it is standard to represent the channel noise with n. Care has been taken to mitigate this, but some crossover exists. To avoid confusion, definitions will be made clear in each section. It should also be clear within the context of the topic; for example, when discussing statistical noise in the communications channel, the LC director is not relevant.

The remainder of this Chapter is structured as follows: Firstly, the response of dielectric media to an external field will be discussed in Section 2.1, followed by the physical properties of LCs in Section 2.2. The behaviour of microstrip devices, such as antennas, at microwave frequencies is established in Section 2.3. Thence, the background relating to transparent conductive films (TCFs) will be detailed in Section 2.4, before wireless communications theory is presented in Section 2.5, followed by an introduction to reconfigurable intelligent surface (RIS) operation, hardware, and equivalent models are outlined in Section 2.6.

2.1 Dielectrics

Dielectrics are insulating materials that do not conduct electricity, yet when placed in an electric field the electrons and nucleus are pulled in opposing directions, inducing a small dipole moment in the atoms and molecules that constitute the material, proportional to the electric field. In the most simple case, the vacuum electric field strength, $\mathbf{E}$, is related by the density of electric flux through a surface, $\mathbf{D}$, and the vacuum permittivity constant ε_0. However, the electric field displacement through matter is more complex.

Consider a facile example of a water molecule floating in otherwise free space: the two hydrogen atoms have a net positive charge while the oxygen atom has a larger, net negative charge. Hence, a dipole is moment created due to the centres of gravity of the positive and negative charges not coinciding. Now, the application of an external electric field to such a material aligns the positive charges with the field and negative charges opposing the field, leading to an additional polarisation that augments the electric flux density, by the polarisation vector $\mathbf{P}$, that is,

$$\begin{aligned}\mathbf{D} &= \varepsilon_0\mathbf{E} + \mathbf{P} \\ &= \varepsilon_0\mathbf{E} + \varepsilon_0\chi_e\mathbf{E}\end{aligned} \tag{2.1}$$

where $\mathbf{P} = \varepsilon_0\chi_e\mathbf{E}$ and χ_e is the electric susceptibility. With some simple rearranging, the electric flux density through a medium can be described by

$$\mathbf{D} = \varepsilon_0\mathbf{E}(1 + \chi_e) = \varepsilon_0\varepsilon_r\mathbf{E} \tag{2.2}$$

where $\varepsilon_r = (1 + \chi_e)$ is the relative dielectric permittivity of the medium.

Permittivity can also be described as a complex term by $\varepsilon = \varepsilon' - j\varepsilon''$, where the imaginary term accounts for the thermal losses in the medium. However this term cannot be distinguished from conductor losses. Hence, the overall loss from the dielectric medium is defined as the loss tangent, given by

$$\tan\delta = \frac{\omega\varepsilon'' + \sigma}{\omega\varepsilon'} \tag{2.3}$$

with σ and ω referring to the material conductivity and angular frequency of the applied field, respectively. Materials in the microwave region are generally characterised by the relative dielectric constant and, accordingly, the loss tangent simplifies to the ratio of the imaginary and real parts of ε_r; that is, $\tan\delta = \varepsilon_r''/\varepsilon_r'$.

For an anisotropic material, it is not simply the case that the polarisation vector and electric field vector are in the same direction. The application of a one-dimensional (1D) electric field, along the x-axis, for example, to a single anisotropic molecule in three-dimensional (3D) space, may cause a dipole moment about the x-axis and z-axis. Hence, the electric field and electric displacement vectors are related by a rank-two tensor of the form

$$\begin{bmatrix} P_x \\ P_y \\ P_z \end{bmatrix} = \begin{bmatrix} \varepsilon_{xx} & \varepsilon_{xy} & \varepsilon_{xz} \\ \varepsilon_{yx} & \varepsilon_{yy} & \varepsilon_{yz} \\ \varepsilon_{zx} & \varepsilon_{zy} & \varepsilon_{zz} \end{bmatrix} \begin{bmatrix} E_x \\ E_y \\ E_z \end{bmatrix} = \boldsymbol{\varepsilon} \begin{bmatrix} E_x \\ E_y \\ E_z \end{bmatrix} \cdot \varepsilon_0 \tag{2.4}$$

so it can be seen that while the electric field may only have a component along x, the electric polarisation may have components along x, y, and z.

2.2 Liquid Crystals

Calamitic nematic LCs consist of long, rod-like molecules that have no long-range positional order but do exhibit an average orientational order, which is the preferred direction of the long molecular axis, known as the LC director and denoted by the unit vector $\mathbf{n}$, with the orientation of any single molecule, with respect to the LC director, θ, depicted in **Figure 2.1**. Due to the rotational symmetry of calamitic nematic LCs around the director, the vector $\mathbf{n} = -\mathbf{n}$.

For an uniaxial, orientationally ordered rod-like LC molecule, as in a calamitic nematic LC, and assuming an electric field along the molecular axis, the symmetry exhibited reduces the second-rank tensor from Equation 2.4 to

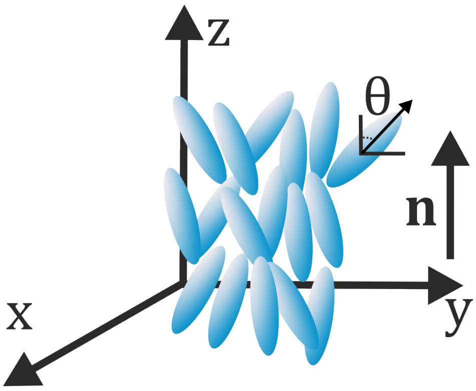

Figure 2.1: Each uniaxial LC molecule may be in a random orientation, θ, whereas the LC director $\mathbf{n}$ is the average pointing direction of all molecules.

$$\boldsymbol{\varepsilon} = \begin{bmatrix} \varepsilon_{r,\perp} & 0 & 0 \\ 0 & \varepsilon_{r,\perp} & 0 \\ 0 & 0 & \varepsilon_{r,\parallel} \end{bmatrix} \tag{2.5}$$

where $\varepsilon_{r,\perp}$ and $\varepsilon_{r,\parallel}$ refer to the relative dielectric permittivity measured perpendicular and parallel to the director, respectively. Hence, an electric field applied along the positive z-direction would experience a different permittivity if the LC director was aligned along the x or y-directions, given by $\varepsilon_{r,\perp}$, compared with if it was aligned along the z-direction i.e., $\varepsilon_{r,\parallel}$. The difference in the relative dielectric permittivity is defined as the dielectric anisotropy, given by

$$\Delta\varepsilon_r = \varepsilon_{r,\parallel} - \varepsilon_{r,\perp} \tag{2.6}$$

The permittivity can take a continuum of values between the two principal dielectric permittivities, such as through the application of an external electric or magnetic field. The difference in permittivity may be positive or negative depending on the LC compound/mixture, however, only LCs exhibiting positive dielectric anisotropy will be considered in this Thesis.

2.2.1 Elastic Deformations

In an unperturbed nematic LC, the global minimum of its free energy is related to a uniform director orientation: a degree of elastic free energy is then required to distort the uniform director field [71]. This elastic energy is known as the Frank-Oseen free energy. If the average orientation of two consecutive molecules is parallel, the energy between them is at a minimum. Conversely, if the average orientation becomes some arbitrary angle, the interaction energy increases.

Deformations to the LC medium can be described in terms of three fundamental distortions: splay, bend and twist, with each of these distortions portrayed in **Figure 2.2**. Each of these require elastic energy to impose distortions upon the director, with the constant of elasticity given by K_{11}, K_{22}, and K_{33} for splay, twist, and bend, respectively. Assuming a Cartesian coordinate system with the z-axis parallel to the director, where the uniaxial property of the LC allows the x and y-axes to be chosen arbitrarily, the energy for each curvature away from the director is given by the following components

$$\begin{aligned} \text{Splay:} \quad & \nabla \cdot \mathbf{n} \\ \text{Twist:} \quad & \mathbf{n} \cdot (\nabla \times \mathbf{n}) \\ \text{Bend:} \quad & \mathbf{n} \times (\nabla \times \mathbf{n}) \end{aligned} \tag{2.7}$$

The Frank-Oseen elastic free energy density, u_F, can then be described by

$$u_F = \frac{K_{11}}{2}(\nabla \cdot \mathbf{n})^2 + \frac{K_{22}}{2}(\mathbf{n} \cdot (\nabla \times \mathbf{n}))^2 + \frac{K_{33}}{2}|\mathbf{n} \times (\nabla \times \mathbf{n})|^2 \tag{2.8}$$

Assuming that the perturbation of the director field is limited to the xz-plane, that is, $\mathbf{n} = [\cos\theta, 0, \sin\theta]^T$ and $|\mathbf{n}| = 1$ and by also assuming that $K_{11} = K_{22} = K_{33} = K$, the Frank-Oseen free energy density can be simplified to

$$u_F = \frac{K}{2}\left[(\nabla \cdot \mathbf{n})^2 + |\nabla \times \mathbf{n}|^2\right] \tag{2.9}$$

The general relationship between the tilt angle and the dielectric permittivity tensor can be described by

$$\boldsymbol{\varepsilon}(\theta) = \varepsilon_{r,\perp}\mathbf{I} + \Delta\varepsilon_r \mathbf{n} \otimes \mathbf{n} \tag{2.10}$$

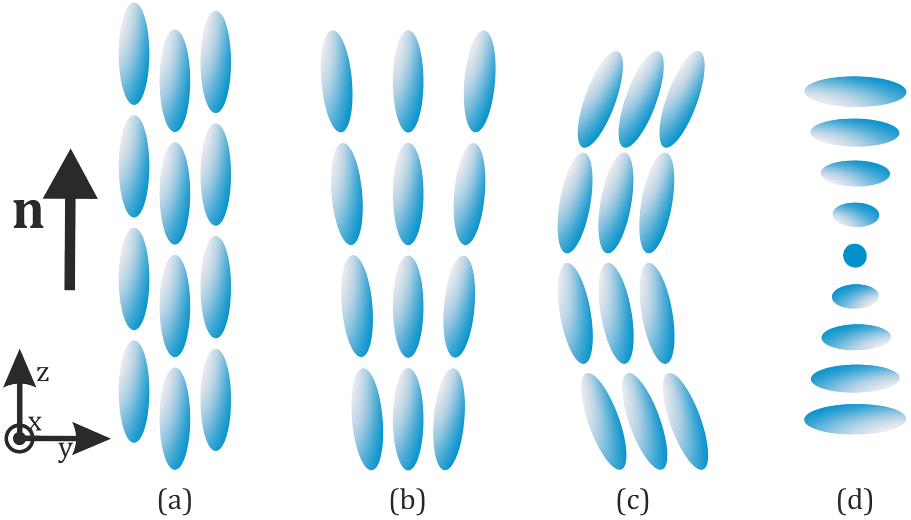

Figure 2.2: (a) orientationally ordered LC director, (b) with induced deformations in splay, (c) bend, and (d) twist.

where **I** is the identity matrix. For the case of a simple tilted layer, Equation 2.10 becomes

$$\boldsymbol{\varepsilon}(\theta) = \varepsilon_{r,\perp}\mathbf{I} + \Delta\varepsilon_r[\cos\theta, 0, \sin\theta]^T \otimes [\cos\theta, 0, \sin\theta]^T \tag{2.11}$$

2.2.2 Deformations in an Electric Field

The LC director field is susceptible to deformations via external physical influences, including but not limited to; electric fields, magnetic fields, surface anchoring and thermal fluctuations. These distortions of the director field can lead to changes in the optical and dielectric properties of the LC: in this Thesis, the primary mechanism to affect these changes will be an external electric field. The general term that describes dielectric energy density, u_e, is

$$u_e = -\frac{1}{2}\mathbf{D} \cdot \mathbf{E} \tag{2.12}$$

hence, with an absence of charge, that is, $\nabla \cdot \mathbf{D} = 0$, D_z is constant and by symmetry, **E** will only have a component in the z-direction and its magnitude will be a function of z. Under this assumption, for the case of an anisotropic material, Equation 2.11 reduces to $\varepsilon_r = \varepsilon_{zz}$, where ε_{zz} is defined as

$$\varepsilon_{zz} = \varepsilon_{\perp} + \Delta\varepsilon_r \sin^2\theta \tag{2.13}$$

and by expanding **D** according to Equation 2.2, the dielectric energy density becomes

$$u_e = -\frac{1}{2}\varepsilon_0(\varepsilon_{\perp}E^2 + \Delta\varepsilon \sin^2\theta E^2) \tag{2.14}$$

With no field applied to the LC material, elastic torques will balance to minimise the free energy of the director distribution. The presence of an electric field will induce a torque according to

$$t = -\Delta\varepsilon_r E^2 \cos\theta \sin\theta \tag{2.15}$$

For a nematic LC with positive dielectric anisotropy, the torque is in stable equilibrium when the field is parallel to the director, but in unstable equilibrium when the applied field is perpendicular to $\mathbf{n}$. To reorientate the LC director, this equilibrium must be destabilised through the application of an external electric or magnetic field that exceeds the elastic energy; for example, an electric field needs to be applied that satisfies the condition $\Delta\varepsilon_r\varepsilon_0E^2 > K/H_{LC}^2$, or in terms of the electric field,

$$E > \sqrt{\frac{K}{\Delta\varepsilon_r\varepsilon_0H_{LC}^2}} \tag{2.16}$$

where H_{LC} is the distance over which the director is deformed i.e., the LC thickness. Reorientation occurs above a critical voltage threshold. By integrating the elastic energy and dielectric energy per unit area, the Euler-Lagrange free energy minimisation can be applied, assuming; the maximum distortion, θ_m, is small, and $\sin\theta\cos\theta \approx \theta$. Applying the boundary condition $H_{LC} = \xi_e\pi$, where the electrical coherence length, ξ_e, increases proportionally with H_{LC} and is described by [72]

$$\xi_e = \frac{H_{LC}}{V}\sqrt{\frac{K}{\Delta\varepsilon_r\varepsilon_0}} \tag{2.17}$$

which is the transition from the LC layer/substrate boundary and the point at which the LC is aligned to an applied electric field, depicted schematically in **Figure 2.3**.

Now, the threshold voltage, V_{Th}, above which reorientation occurs is [73]

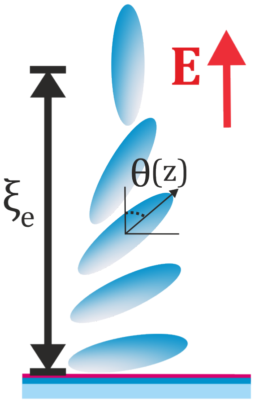

Figure 2.3: Electrical coherence length, ξ_e, is the distance to transition from the interface of the substrate and LC layer (governed by the alignment layer) to the point at which the LC molecules/director align with an applied electric field.

$$V_{Th} = \pi\sqrt{\frac{K}{\Delta\varepsilon_r\varepsilon_0}} \tag{2.18}$$

which is known as the Fréedericksz transition. A voltage above this threshold will induce the LC director to begin to align parallel with the associated electric field: increasing the voltage to $V \gg V_{Th}$ aligns the LC director to be parallel to the electric field and removing the voltage allows the LC director to return to the low energy state. Thus, controlling the LC director alters the relative dielectric permittivity of the LC and produces a continuously tunable material, described in **Figure 2.4**. For most nematic LCs $V_{Th} \approx 1$ V, whereas the voltage required to align the director parallel to the electric field depends on the thickness of the LC layer and thus should be considered in terms of a minimum electric field strength of ≈ 100 kV/m - any further increase will result in minimal changes to the director alignment. The 10%-90% response time for a nematic LC to respond to an electric field, τ_{on}, is approximated by

$$\tau_{on} = \frac{\gamma_1 H_{LC}^2 V_{Th}^2}{K_{11}\pi^2(V_a^2 - V_{Th}^2)} \tag{2.19}$$

where V_a is the applied voltage, and the approximate time taken to return to the low-energy state once the electric field is removed, τ_{off}, is

$$\tau_{off} = \frac{\gamma_1 H_{LC}^2}{K_{11}\pi^2} \tag{2.20}$$

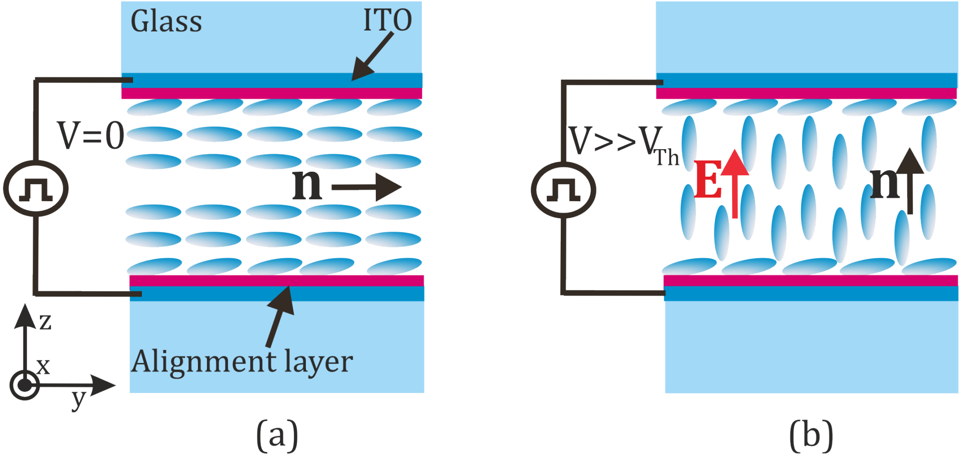

Figure 2.4: (a) When employing homogeneous (planar) alignment layers, and no applied voltage, the LC director will align horizontally through the bulk of the LC, defined by the rubbing direction of the alignment layers. Applying a voltage $V > V_{Th}$ will force the director to begin to align with the applied electric field. (b) Increasing the voltage to $V \gg V_{Th}$ will align the director almost parallel to the field (**E**), with a small discrepancy due to the alignment layer.

where γ_1 is the rotational viscosity and H_{LC} is the thickness of the LC layer.

2.2.3 Frequency Dependence

The application of static fields (d.c.) to a nematic LC has been shown to induce unwanted electrochemical effects [72]. This is often avoided through the use of low frequency a.c. fields to control deformations to the LC director; however, this then introduces a frequency dependence property of the dielectric material, which follows the Debye relaxation response. The frequency dependence of nematic LCs is non-trivial and requires the consideration of macroscopic effects and molecular motion.

Nevertheless, a simplified model of the frequency dependence can be considered by removing the effects of induced dipole moments. Under this assumption, the real part of the frequency dependent permittivity can be written as

$$\varepsilon_{\perp}(\omega) = \varepsilon_{\infty} + K_T\left[\frac{\mu_1^2(1+2S)}{1+j\omega\tau_1} + \frac{\mu_2^2(1-S)}{1+j\omega\tau_2}\right] \tag{2.21}$$

$$\varepsilon_{\parallel}(\omega) = \varepsilon_{\infty} + K_T\left[\frac{\mu_1^2(1-S)}{1+j\omega\tau_1} + \frac{\mu_2^2(1+S/2)}{1+j\omega\tau_2}\right] \tag{2.22}$$

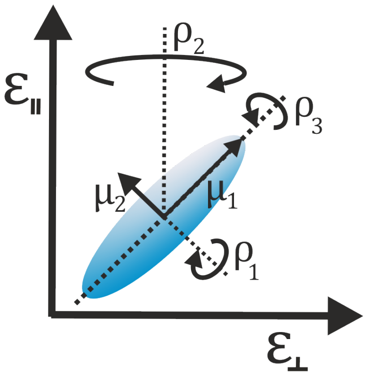

Figure 2.5: Rotation for an uniaxial nematic molecule with two dipole moments. Typically, the relaxation frequency for each rotation mode follows $\rho_1 \ll \rho_2 \ll \rho_3$.

where ε_∞ is the high-frequency permittivity limit (as $w \to \infty$), K_T is a constant that includes thermal and molecular effects, S is the scalar order parameter and μ_1 and μ_2 refer to the permanent dipole moments respectively, and τ_1 and τ_2 related to the characteristic relaxation time of each dipole moment μ_1 and μ_2, respectively. As a result, each permittivity undergoes dielectric relaxation at two separate stages due to the dipole moments.

The relaxation frequencies correspond to molecular rotation and, for a uniaxial LC with two moments of inertia, these are; rotation about the short molecular axis (ρ_1), precessional motion (ρ_2), and rotation around the long molecular axis (ρ_3), shown in **Figure 2.5**. The dielectric permittivity is a function of these three types of motion and cannot occur above certain frequencies: for a calamitic LC, the rotation about the short axis will only occur at lower frequencies; the precessional motion continues up to high frequencies while rotations about the nematic axis continue up to very high frequencies. This effect is illustrated in **Figure 2.6**.

It is clear that the relative value of the permittivity will be higher at low frequencies and reduce after each rotation mode. It is also the case that when applying an alternating electric field at high frequencies, the director has less time to align with the field before the polarity is switched. The upshot of these effects is that at higher frequencies, such as the RF range, the relative values of the permittivity, and the variation between the principal values (i.e., parallel and perpendicular to the director), is significantly reduced.

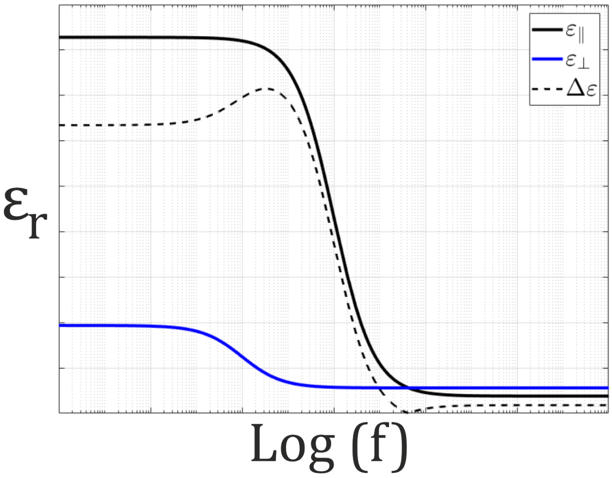

Figure 2.6: Relative dielectric permittivity as a function of the frequency of the applied field demonstrating dielectric relaxation. The precise values for $\varepsilon_{||}$ and $\varepsilon_{\perp}$, and the relaxation frequency, are material dependent. Typical relaxation frequencies for the LC mixture E7 are on the order of 1 kHz and 10 MHz for the low and high frequency relaxation, respectively.

2.3 Microwave Theory

2.3.1 Patch Antenna Using the Cavity Model

Microstrip patch antennas can be accurately modelled by treating the radiating patch, substrate, and groundplane as a dielectric-loaded cavity bounded by upper and lower electrical conductors, and magnetic walls at the sides, with the geometry illustrated in **Figure** 2.7. This model produces an open circuit at each end of the patch, corresponding to a voltage peak, whereas the current is at a minimum, hence this antenna is known as a voltage radiator, rather than a current radiator (as most antennas are).

Assuming the ratio between the patch width, W_p, and substrate height, H_{sub}, is $W_p/H_{sub} \gg 1$, fringing fields appear at each end of the patch, corresponding to the peak electric field strength: it is these fringing fields that induce radiation from the antenna, as well as increase the effective length of the patch, as depicted in **Figure** 2.8. A high value of relative dielectric permittivity, ε_r, will reduce fringing, hence, utilising a low ε_r will increase fringing and improve the radiation efficiency, although patch antennas typically suffer from poor efficiency due to reflections generated at the short edges.

When the height of the patch is small compared to the operating wavelength, λ, that

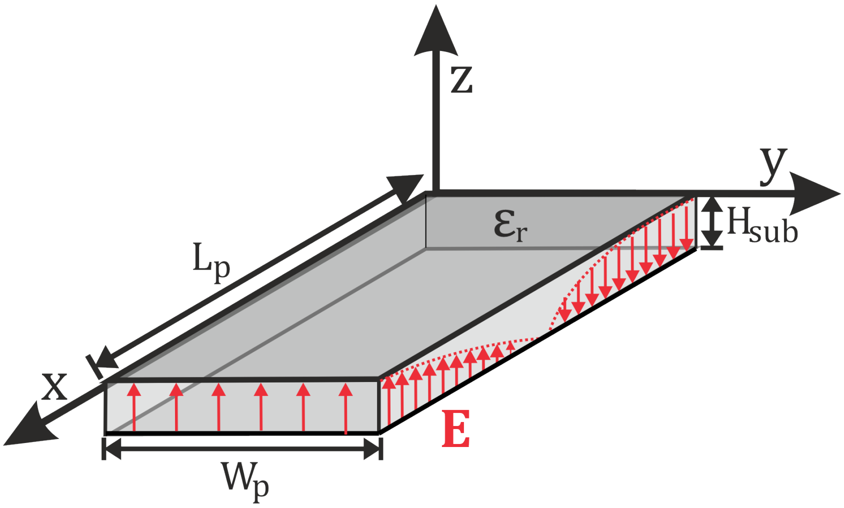

Figure 2.7: Idealised cavity model for a microstrip patch antenna of dimensions, patch width W_p, patch length L_p, and dielectric substrate height, H_{sub}. Demonstrating with the distribution of the electric field along the non-radiating edge, and no fringing fields.

is, $H_{sub} \ll \lambda$, the fields generated within the cavity are purely transverse magnetic (TM) as the fringing fields are practically zero where the electric field is normal to the surface of the cavity. The resonant frequency, F_r, of the patch can thence be derived through a vector potential approach to solving the wave equation, that is

$$\nabla^2 A_x + k^2 A_x = 0 \tag{2.23}$$

where k is the wavevector and A_x is the vector potential. Applying boundary conditions to the cavity such that the upper and lower patches are electrical conductors and the side walls are magnetic conductors, equates to [25]

$$k_x^2 + k_y^2 + k_z^2 = \left(\frac{m\pi}{H_{sub}}\right)^2 + \left(\frac{n\pi}{L_p}\right)^2 + \left(\frac{p\pi}{W_p}\right)^2 = \omega_r^2 \mu \varepsilon \tag{2.24}$$

with k_x, k_y, and k_z representing the wavenumbers along the x, y, and z directions, respectively, m, n, and p, refer to the resonance modes, and ω_r is the angular frequency. Equation 2.24 leads to the existence of a resonant frequency, F_r, given by

$$F_{r,mnp} = \frac{1}{2\pi\sqrt{\mu\varepsilon}} \sqrt{\left(\frac{m\pi}{H_{sub}}\right)^2 + \left(\frac{n\pi}{L_p}\right)^2 + \left(\frac{p\pi}{W_p}\right)^2}. \tag{2.25}$$

Here, the magnetic permeability is $\mu = \mu_0 \mu_r$, where μ_0 and μ_r are the permeability

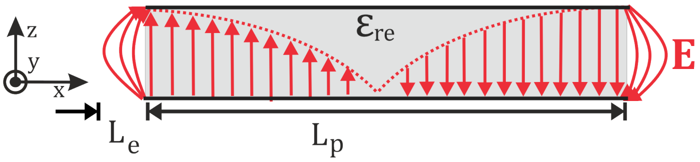

Figure 2.8: Side view of the Cavity Model with fringing fields that leads to the effective relative permittivity, ε_{re}. Leakage from these fields causes the antenna to radiate, and produces an effective length, L_e, additional to the patch length, L_p.

constant and relative permeability, respectively, and the permittivity is $\varepsilon = \varepsilon_0 \varepsilon_r$.

The lowest order resonant frequency is known as the dominant mode. For patch antenna geometries where $L_p > W_p > H_{sub}$, and by assuming that the permeability of the substrate is unity, this provides the lowest resonance at the dominant TM_{010} mode. Hence, the general formula for designing a patch antenna takes the form

$$F_{r,010} = \frac{c}{2L_{pe}\sqrt{\varepsilon_{re}}} \tag{2.26}$$

where c is the speed of light in a vacuum and the effective length, L_{pe}, accounts for the additional length due to fringing, that is, $L_{pe} = L_p + L_e$, and the additional fringing length, L_e, can be observed in Figure 2.8 and is calculated by [25]

$$L_e = 0.415 H_{sub} \frac{(\varepsilon_{re} + 0.3)(W_p/H_{sub} + 0.264)}{(\varepsilon_{re} - 0.258)(W_p/H_{sub} + 0.8)}. \tag{2.27}$$

By assuming that the medium above the patch is air, the existence of the fringing fields leads to an effective permittivity, ε_{re}, which is a combination of the permittivity of the air and the dielectric substrate, and can be approximated by [25]

$$\varepsilon_{re} = \frac{\varepsilon_r + 1}{2} + \frac{\varepsilon_r - 1}{2}\left(1 + 12\frac{H_{sub}}{W_p}\right)^{-1/2} \tag{2.28}$$

It is important to note that the TM_{010} mode is not the only possible dominant mode: depending on the antenna geometry, the resonant frequency can be a function of W_p, for example, if $W_p > L_p > H_{sub}$, then the TM_{001} mode is dominant and Equation 2.26 is updated to replace L_p with W_p. This occurs due to the simplifications on the tangential electric field distribution along the cavity walls; when $L_p > W_p$, the magnitude of the field varies along the long edge, L_p, and is constant along the short edge, W_p, as shown in Figure 2.7. However, when $W_p > L_p$, this configuration is reversed and W_p is the long edge, which defines the resonant frequency of the patch. It should also be stressed that, in order to simplify the calculation of F_r, it is assumed that there are no fringing effects along the long edges of the cavity. While such an assumption may lead to less precise calculations, computer simulations can be utilised to optimise antenna designs prior to fabrication. Through Equation 2.26, the resonant frequency of the antenna is a function of the permittivity of the dielectric cavity: employing a material that exhibits a dielectric anisotropy e.g., a nematic LC, will thence affect a reconfiguration of the resonant frequency proportional to the dielectric anisotropy.

2.3.2 Microstrip Line Theory

Microstrip lines are planar two-conductor transmission lines consisting of a conductive strip separated from a groundplane by a dielectric substrate. In this configuration, the electric field penetrates into the dielectric substrate and into the air above the microstrip line, as illustrated in **Figure 2.9**. Due to the interface of the dielectric with the air, fully transverse electromagnetic (TEM) modes cannot be supported; however, to simplify the analysis, propagation modes are generally considered to be pure TEM modes. Hence, the properties of the microstrip line can be evaluated by using closed form equations to account for the air/dielectric interface. The combination of the air and dielectric materials leads to an effective filling fraction, q, which then relates the effective dielectric constant, ε_{re} by [74]

$$\varepsilon_{re} = (1 - q) + q\varepsilon_r \tag{2.29}$$

For wide microstrip lines, that is, $W_s/H_{sub} > 2$,

$$\begin{aligned} q = 1 - \frac{1}{d}\ln\frac{d+b}{d-b} + \frac{0.732}{d\varepsilon_r}\left[\ln\frac{d+b}{d-b} - \cosh^{-1}(0.358d + 0.595)\right] \\ + \frac{\varepsilon_r - 1}{d\varepsilon_r}\left[0.386 - \frac{1}{2(d-1)}\right] \end{aligned} \tag{2.30}$$

where, W_s is the width of the conductor, H_{sub} is the height of the dielectric substrate, $d = 1 + \sqrt{1 + b^2}$ and b can be found graphically from

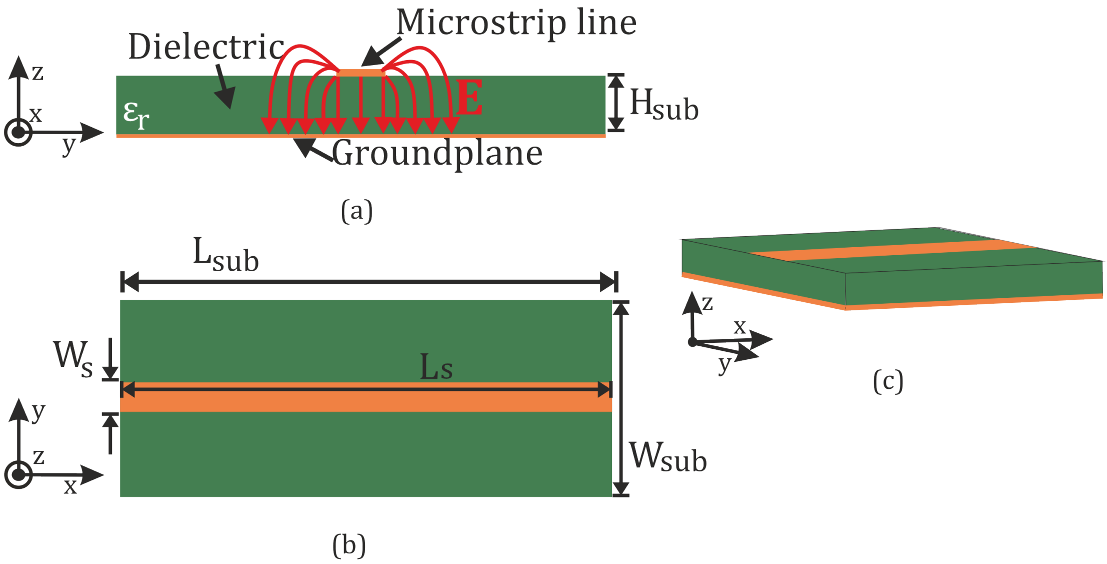

(a)

(b)

(c)

Figure 2.9: Microstrip line separated by a dielectric substrate. Where L_{sub}, W_{sub}, H_{sub} and ε_r, refer to the length, width, height, and relative permittivity of the substrate, respectively, and L_s and W_s refer to the length and width of the conductive strip, respectively. (a) end view, (b) top view and (c) 3D view.

$$\frac{\pi w}{2h} = b - \sinh^{-1} b \tag{2.31}$$

Hence, for microstrip lines with $W_s/H_{sub} > 2$ the relative permittivity of the substrate, ε_r can be related to the effective permittivity using Equation 2.29, 2.30 and 2.31. For $W_s/H_{sub} \leq 2$, then the effective permittivity in Equation 2.28 suffices. The resonant frequency for a microstrip line device is also described by Equation 2.26.

2.4 Transparent Conductive Films

Transparent conductive films (TCFs) are oxide-doped semiconductors that are deposited to form a thin-film between 100 nm - 500 nm and exhibit excellent transparency in the optical domain and are electrically conductive at RF, albeit with reduced conductivity, compared to some alloys. Typically, the TCF employed is indium-tin oxide (ITO), however, ITO can be doped with other alloys such as zinc or silver.

ITO is a semiconductor material, with a band gap of approximately 3.8 eV, in which indium oxide is doped with tin oxide to produce a film that is both electrically conductive and optically transparent. The window of transparency is limited at high photon energies (short wavelengths) by the plasma frequency, which must correspond to wavelengths shorter than ≈400 nm, and is limited by lower photon energies relating to wavelengths of ≈ 1 mm. Hence, the transparency window includes the range of visible wavelengths. To maximise the transparency, the material can be doped to create a low free-electron density, n_e, although this is detrimental to the electrical conductivity. For a fixed free electron density, the electron mobility of the ITO layer can be increased to its maximum of $\mu_e \approx 50$ cm^{2}V^{-1}s^{-1}, to improve both the conductivity and transparency [38]. This conflict between electrical conductivity and optical transparency can be distilled into the trade-off between sheet resistance, R_s, and optical transparency, T, as illustrated in Equations 2.32 and 2.33:

$$R_s = \frac{1}{n_e e \mu_e t} \tag{2.32}$$

$$T \approx \exp \frac{-2n_e t}{\alpha} \tag{2.33}$$

where t is the thickness of the TCF, e is the electron charge and α is a constant that includes the physical properties of the material. Consequently, maximising n_e will reduce the sheet resistance, whereas minimising n_e will improve the optical transparency.

Equations 2.32 and 2.33 also show that a trade-off in film thickness is required, which in turn leads to consideration of the skin effect: the skin depth, δ, is the depth into a conductor at which the surface current has reduced by approximately two thirds and is described by

$$\delta = \sqrt{\frac{2}{\omega\mu\sigma}}\sqrt{\sqrt{1+(\rho\omega\varepsilon)^2}+\rho\omega\varepsilon} \tag{2.34}$$

where, σ and ρ are the material's electrical conductivity and resistivity, respectively. For conductors in general, efficiency is reduced with increasing frequency due to resistive losses; however, this is not the case with ITO films where an increase in operational frequency of the antenna results in a reduction of the skin depth, bringing it closer to the film thickness and increasing the efficiency of the TCF [37].

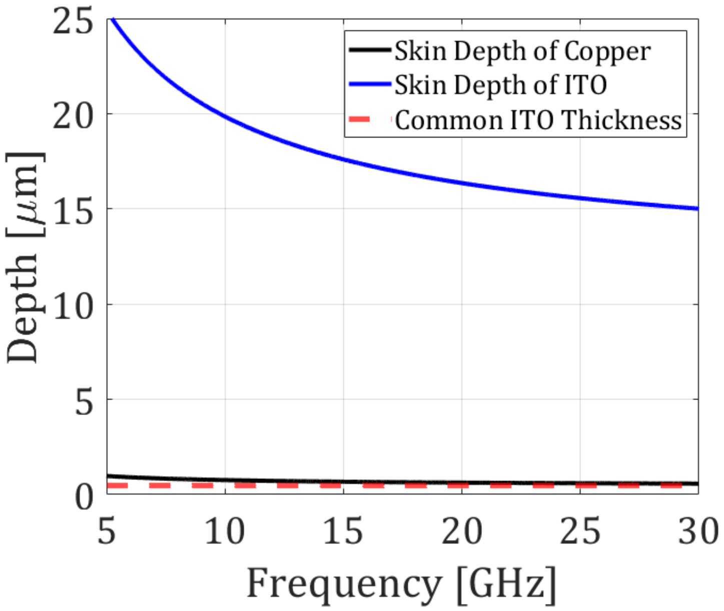

Figure 2.10: Skin depth of copper and ITO across a range of frequencies, including ITO film thickness of 500 nm for reference.

The general advantage of using ITO is that it features a high-level of transmittance, $> 90\%$ between wavelengths of 400 nm - 800 nm. On the other hand, the major drawback with ITO is that the electrical conductivity is lower than that of copper, with $\sigma_{copper} \approx 6 \times 10^7$ S/m and $\sigma_{ITO} \approx 6 \times 10^5$ S/m [37], and is often printed in thin films of 100 nm – 500 nm thickness: this induces ohmic losses in the TCF due to the skin effect and high sheet resistance, since $R_s \propto 1/t\sigma$. The difference in skin depth between copper and ITO is illustrated in **Figure 2.10**: at 10 GHz, $\delta_{copper} = 0.76$ μm, whereas at the same frequency $\delta_{ITO} = 20$ μm, which is above the typical film thickness, illustrating the drawback of ITO. Hence, the thin film of ITO does not have sufficient thickness to encompass the skin depth and as such, cannot maintain the same levels of current as a copper conductor. In practice, employing ITO as the conductor for RF devices, for example a microstrip antenna, will likely lead to reduced efficiency of the antenna, compared to a copper-based antenna.

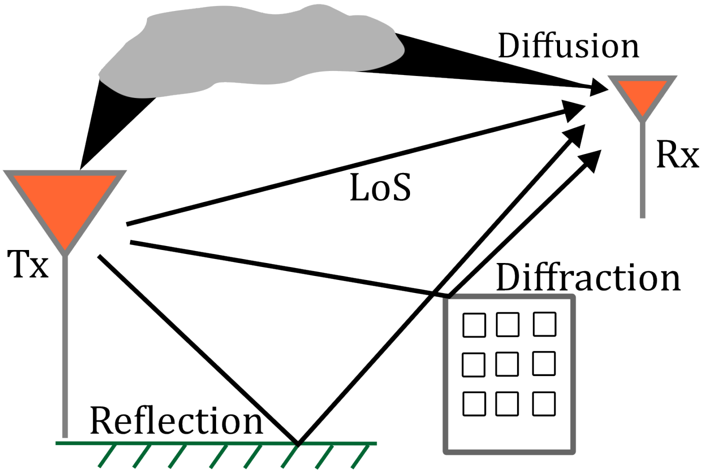

Figure 2.11: Multipath fading between the transmitted (Tx) and receiver (Rx) caused by reflections, diffusion, and diffraction.

2.5 Communication Theory

2.5.1 The Wireless Channel

The wireless channel is the impulse response of a linear time-varying communication link over the system bandwidth. Signals that propagate through the wireless channel undergo various deleterious effects that cannot easily be determined for all cases: the channel varies over long time scales, due to deterministic path loss between transmitter (Tx) and receiver (Rx) and random shadowing (attenuation due to obstacles) also known as slow-fading. It simultaneously varies over short time scales, due to constructive and destructive interference from small movements in position of the Tx or Rx, or multipath effects, known as fast-fading, or a frequency selective channel. The effects on the propagation of EM waves through this environment are demonstrated in **Figure 2.11**, and are characterised by approximations that seek to capture the behaviour of the wireless channel through empirical or statistical models.

By assuming that the transmitted EM wave can be represented by a single 'ray', the two-ray propagation model, which considers the direct line of sight (LoS) signal and a single reflected ray, assuming a reflector with known dielectric properties, can then be used to estimate the channel. In this two-ray approximation, the ratio of power received, P_r, to power transmitted, P_t, not accounting for noise, is [75]

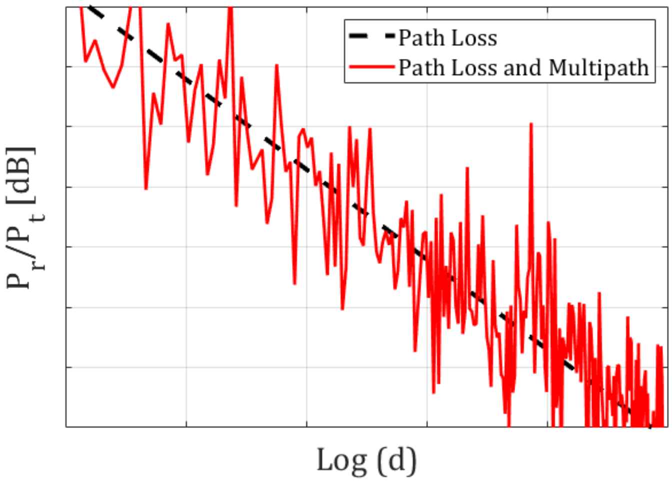

Figure 2.12: Ratio of received power to transmitted power (P_r/P_t) as a function of distance between the transmitter (Tx) and receiver (Rx), showing the case for just path loss as well as both path loss and multipath fading.

$$\frac{P_r}{P_t} = \left(\frac{\lambda}{4\pi d}\right)^2 \left|\frac{\sqrt{G_r G_t}}{d} + \frac{\Gamma\sqrt{G_r}e^{-j\Delta\phi}}{a_1 + a_2}\right|^2 \tag{2.35}$$

where a Tx and Rx are separated by a distance, d, with the phase difference between the LoS and reflected signals given by $\Delta\phi = 2\pi(a_1 + a_2 - d)/\lambda$, and $a_1 + a_2$ is the distance travelled by the reflected wave, G_r and G_t are the gain of the Rx and Tx antennas, respectively, and, Γ, is the complex reflection coefficient of the reflector. In most cases, the distance between the Tx and Rx is large so that $d \approx a_1 + a_2$ and by Equation 2.35 the received power becomes $P_r \propto 1/d^4$, whereas for the single ray case $P_r \propto 1/d^2$.

Ray tracing can be extended by by adding additional rays as the multipath effects increase; however, this is a deterministic model which is not used in practice. Instead, statistical models are employed that capture the changes in time, frequency, distance, and multipath effects. The two dominant wireless channel models are Rayleigh fading and Rician fading, which are employed in urban and rural environments, respectively.

If the delay spread of the channel (the time between the first and last resolvable multipath component) is much less than the inverse of the channel bandwidth, B^{-1}, then the channel is said to be narrowband (frequency-flat). Conversely, if the delay spread is comparable to or greater than B^{-1}, the channel is wideband (frequency-selective). **Figure 2.12** demonstrates the effects constructive or destructive interference at the receiver, including path loss, and path loss with multipath fading.

The classic model of a narrowband channel, assuming a single-input single-output (SISO) and single user channel is defined as

$$y = \sqrt{E_s} hx + n, \tag{2.36}$$

where the time-index is discarded for simplicity, y, is the received signal, E_s is the energy per transmitted symbol, $h \sim \mathcal{CN}(0, \sigma_h^2)$ is a complex circular Gaussian random variable that denotes the channel from Tx to Rx, x is the unit power information symbol, and $n \sim \mathcal{CN}(0, \sigma_n^2)$ models the channel noise, typically additive white Gaussian noise (AWGN), and σ_h^2 and σ_n^2 are the variance relating to the distribution of the channel and channel noise, respectively.

In any communications system there are three fundamental quantities that can be interchanged to improve performance or reduce costs; bandwidth, transmit power and data rate. For example, increasing bandwidth allows the transmit power to be reduced while maintaining the same data rate. In general, bandwidth is highly restricted and determined by regulators, and it is desirable to keep the Tx power to a minimum, while maintaining a data rate high enough to prevent outages. The channel capacity is the maximum amount of information that can reliably be transmitted over a channel. The maximum rate, R, or capacity, for a SISO channel taking

$$R = \log_2 \left(1 + \frac{E_s |h|^2}{\sigma^2} \right) \tag{2.37}$$

where σ^2 is the noise power. The right-hand expression within the brackets above can also be denoted as the signal-to-noise ratio i.e., $SNR = E_s |h|^2 / \sigma^2$ and the general term for capacity is $R = \log_2(1 + SNR)$, which is the famous Shannon-Hartley theorem.

2.6 RIS Operation

Reconfigurable intelligent surfaces (RISs), sometimes termed in the literature as Intelligent Reflecting Surface or software-controlled metasurfaces, offer the opportunity to passively exert a degree of control over the wireless channel, as an aid to improving the communications link between transmitter and receiver. The aim of a RIS is to reflect the

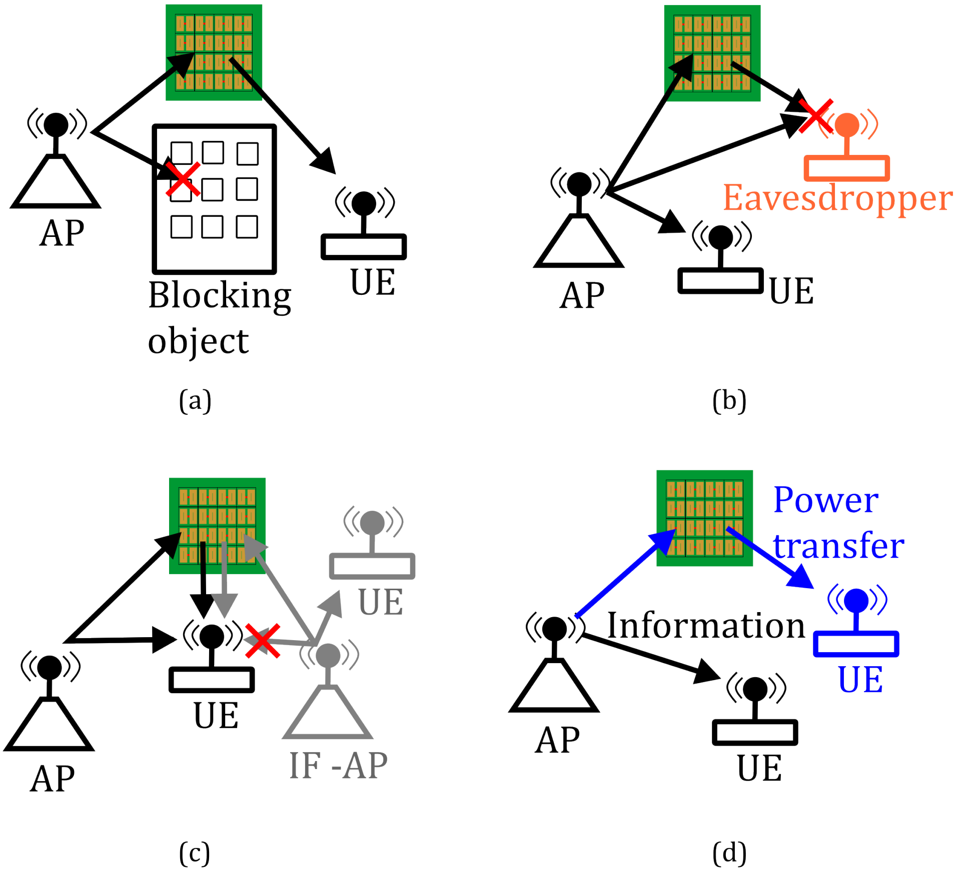

Figure 2.13: Use-cases for the RIS-assisted wireless channel. (a) the LoS path between the access point (AP) and user equipment (UE) is blocked, (b) the signal of an eavesdropper is nullified through destructive interference, (c) enhancement of desired signals and/or cancellation of interference (IF) signals, and (d) wireless power transfer.

impinging EM waves, utilising sub-wavelength phase-shifting elements to independently modulate the phase of the wave, such that all reflected signals are in-phase when arriving at the Rx, or in-phase with the LoS signal (if there is one). This passive control produces constructive interference which results in a higher SNR at the Rx, without requiring any increase in the gain of the signal, as seen in an active system such as a relay.

Figure 2.13 details several use-cases for RIS deployment. The most commonly considered scenario is depicted in Figure 2.13(a), where there is no LoS path between the access point (AP) and the user equipment (UE) due to a blocking object. This scenario is particularly pertinent for millimetre-wave (mm-wave) communications channels where the signals are easily attenuated. Another use-case is demonstrated in Figure 2.13(b) where an eavesdropper exploits a weakness in wireless communications by sitting in the

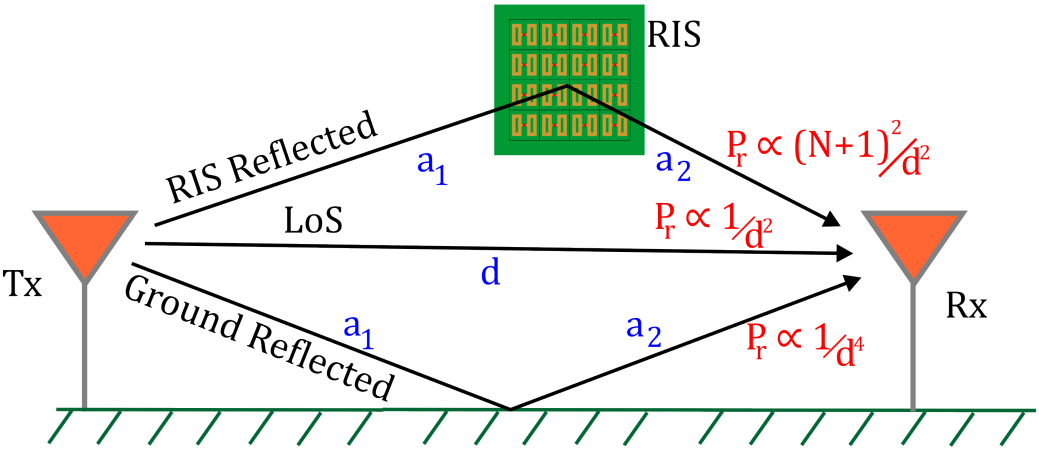

Figure 2.14: Two-ray model with a RIS.

coverage area of the AP. Here, the RIS can be deployed to enhance the physical layer security by adjusting the phase-shift of reflected signals to nullify the signal received by the eavesdropper. In Figure 2.13(c) the UE is situated at a cell edge and is subject to significant interference from a neighbouring AP. The RIS can be deployed to simultaneously enhance the desired signals and nullify the interference signals, eliciting an improvement in the signal-to-noise plus interference ratio (SNIR) of the UE. The final demonstrated use-case is in Figure 2.13(d), where the UE benefits from wireless power transfer aided by the RIS. This could apply to low-energy devices and allow them to become more self-sufficient.

2.6.1 RIS-Assisted Wireless Channel

Considering again the two-ray model in Equation 2.35, with the two-ray scenario illustrated in **Figure 2.14**, it can be observed that the received power falls off proportionally to $1/d^4$. However, if the reflected path is now via a RIS with N independent phase-shifting elements, by the generalized Snell's law, the element imposes a linear phase gradient that modifies the reflected wavefront, enabling precise beamsteering of the reflected signal. Hence, the two-ray model in Equation 2.35 is now [56]

$$\frac{P_r}{P_t} \approx (N+1)^2 \left(\frac{\lambda}{4\pi d} \right)^2 \tag{2.38}$$

assuming that $d \approx a_1 + a_2$ and that the phase of each reflected path from the RIS is ideally aligned to the LoS path. This reveals two important conclusions: 1) the received power now decays by the inverse of the distance squared, instead of the fourth power and 2) the received power increases proportionally to the number of RIS elements, N. However, this depends on the ability to apply an ideal phase-shift at each of the elements.

For a RIS supported channel, the received signal model from Equation 2.36 is now encapsulated by [2]

$$y = (h_{tr} + \mathbf{h}_{ts}^T \mathbf{\Theta} \mathbf{h}_{sr}) \sqrt{E_s} x + n \tag{2.39}$$

with, $h_{tr} = h$ relating to the LoS path between Tx and Rx, $\mathbf{h}_{ts} \in \mathbb{C}^{N \times 1}$ denoting the channel between Tx and RIS, $\mathbf{h}_{sr} \in \mathbb{C}^{N \times 1}$ denoting the channel from RIS to Rx, $\mathbf{\Theta} = \nu \text{diag}\left(\exp^{j\theta_1}, ..., \exp^{j\theta_N}\right)$, where $0 \leq \nu < 1$ is the amplitude reflection coefficient and $\theta_1, ..., \theta_N \in (0, 2\pi]$ are the phase-shift variables that the RIS seeks to optimise. For a RIS-assisted channel, the maximum capacity from Equation 2.37, is updated to encapsulate the RIS and is given by [2]

$$\begin{aligned} R_{RIS} &= \max_{\theta_1,...,\theta_N} \log_2 \left(1 + \frac{E_s |h_{tr} + \mathbf{h}_{ts}^T \mathbf{\Theta} \mathbf{h}_{sr}|^2}{\sigma^2}\right) \\ &\approx \log_2 \left(1 + \frac{E_s |h_{tr}| + \nu \sum_{n=1}^{N} |h_{ts,n} h_{sr,n}|^2}{\sigma^2}\right) \end{aligned} \tag{2.40}$$

It is clear from Equation 2.40 that the maximum achievable rate is dependent on $\mathbf{\Theta}$, that is, the phase-shifts, θ_N which the RIS must control to produce an in-phase reflected wave. To achieve the maximum rate, the RIS must produce phase-shifts according to

$$\theta_n = \begin{cases} \overbrace{\arg(h_{tr}) - \arg(h_{ts,n} h_{sr,n})}^{\text{for the continuous case}}, & \forall n \\ \overbrace{\arg\min_{\psi \in \mathcal{F}} |\theta_n - \psi_n|^2}^{\text{in the discrete case}}, & \forall n \end{cases} \tag{2.41}$$

where, ψ_n is the value taken from $\mathcal{F} = \{0, \Delta\theta, ..., (L-1)\Delta\theta\}$, the set of discrete phase-shift values, $\Delta\theta = 2\pi/L$ and $L = 2^b$ is the number of discrete levels produced by a b-bit system. For example, a 1-bit system would produce $\mathcal{F} = \{0, \pi\}$ and a 2-bit system would provide $\mathcal{F} = \{0, \pi/2, \pi, 3\pi/2\}$ from which the minimum square error, between the ideal

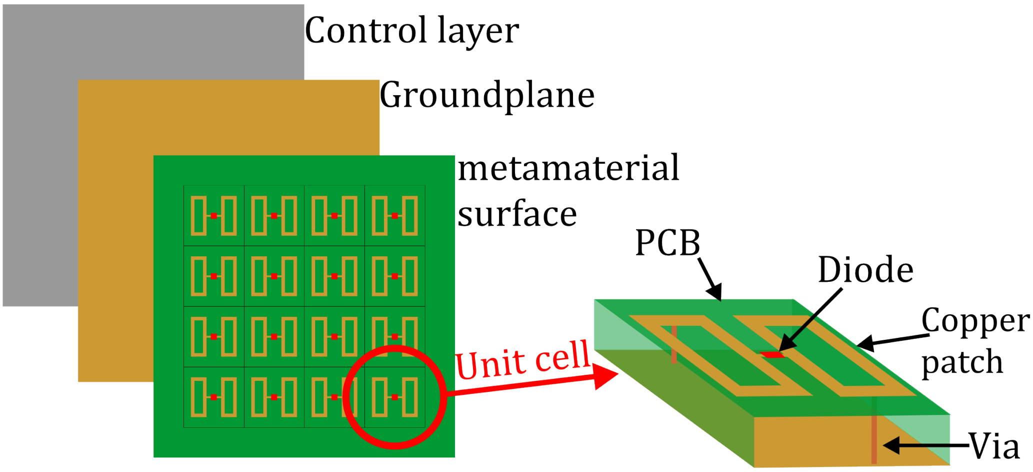

Figure 2.15: Structure of a RIS and the unit cell.

phase-shift and the set of discrete phase-shifts, is found. This assumes that the RIS has full channel state information to provide the ideal phase-shift value.

2.6.2 Typical RIS Hardware and Structure

The construction of a RIS enables it to behave as a metasurface, which is a metamaterial that interacts with incident EM waves in a manner that is controlled by designers. The geometry of the metasurface elements governs the response to those impinging EM waves which induce surface currents in the elements: in a RIS the elements can be arbitrarily altered to affect the surface current and thus adjust the phase of the reflected EM waves.

The physical construction of the RIS typically consists of three layers; the top layer contains of an array of metallic patches that interact with the RF environment, a groundplane layer, and a bottom layer consisting of control circuitry. Each element of the RIS has the ability to independently adjust the phase of a reflected wave. The typical structure of a single element, for example in [76], contains two metallic patches on a PCB connected through a single diode. The control layer is connected to the metallic patches with a via that allows the diode to be switched on or off, thus affecting a 1-bit, adjustment in the phase of the reflected signals. The size of the element is related to the signal wavelength, with typical values of $\lambda/2$-$\lambda/8$. A diagram featuring the typical RIS construction and an example of a unit element is depicted in **Figure 2.15**.

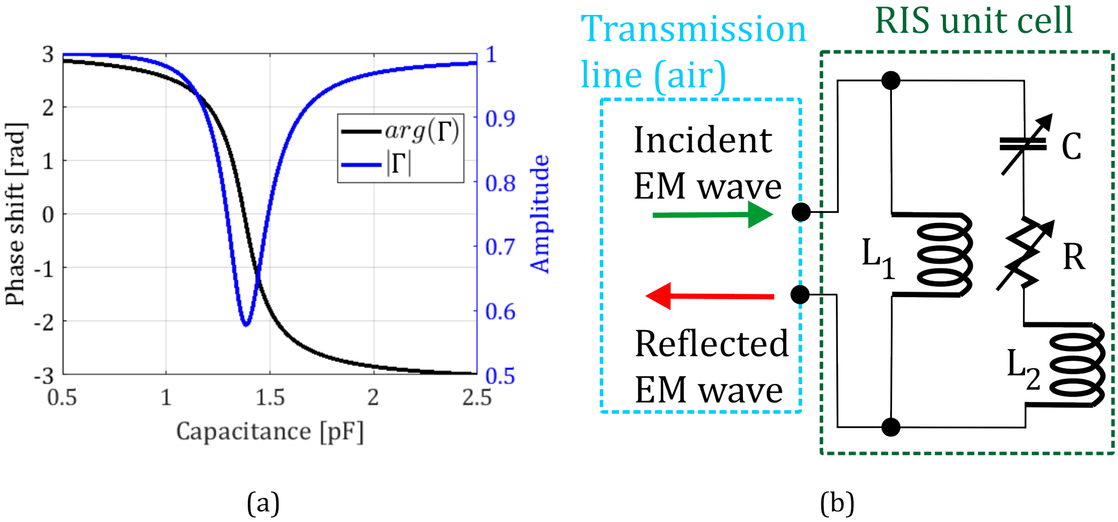

(a) (b)

Figure 2.16: (a) Phase-shift (left-hand y-axis) and amplitude (right-hand y-axis) applied by an element in a RIS as a function of the capacitance, C using representative values for the inductance and resistance. (b) Equivalent circuit for a RIS unit element.

2.6.3 RIS Equivalent Circuit Model

The structure of a RIS unit cell typically features metallic patches connected by a diode which is controlled through an external bias voltage to affect a phase-shift on reflected EM signals. This unit cell has an associated capacitance from the diode, resistance from the metallic patch, and inductance due to the high-frequency current producing a magnetic field. Hence, the response can be modelled using an equivalent circuit that characterises the achievable phase-shift, independent of the particular geometry [77].

The equivalent circuit is shown in **Figure 2.16**(b), where the unit cell is modelled by parallel and series lumped elements, and the transmission line model is used to model free space. The impedance of the parallel resonant circuit is given by [78]

$$Z(C,R) = \frac{j\omega L_1(j\omega L_2 + 1/j\omega C + R)}{j\omega L_1 + (j\omega L_2 + 1/j\omega C + R)}, \tag{2.42}$$

where, L_1, L_2, R, C represent the bottom layer inductance, top layer inductance, effective resistivity, and effective capacitance, respectively, and are depicted in the circuit diagram in Figure 2.16(b), and ω is the angular frequency of the incident EM wave.

The complex reflection coefficient, Γ, can be calculated by

$$\Gamma = \frac{Z(C,R) - Z_0}{Z(C,R) + Z_0}, \tag{2.43}$$

where Z_0 is the free space impedance. The phase-shift applied by a particular element in the RIS is thence calculated by plotting Γ for a range of capacitance values. An example, with representative values for the inductance and resistance [78], is depicted in Figure 2.16(a). The plot in Figure 2.16(a) demonstrates that a continuous phase-shift can be achieved by a single RIS element: the effective capacitance can be continuously tuned by varying the bias voltage over the varactor, and modulated by the RIS control layer. However, this requires complex circuitry and control signals for each element. Instead, 1-bit RISs have been developed that employ a diode in place of the varactor that exhibits two states: on and off [3]. This discrete control in turn provides only two states for the phase-shift, typically 0° and 180°

2.7 Conclusions

This Chapter has outlined the most relevant background topics for the research conducted in this Thesis. In particular, the general behaviour of dielectrics was considered and then the dielectric properties specific to a nematic LC was elaborated on, which will aid in the discussions on LC materials throughout this Thesis. The characteristic and governing equations for microstrip patch antennas and microstrip lines were described, before detailing the physical properties of TCFs, including their advantages and disadvantages, which will be used in Chapters 4, 5, 6 and 7 to design and understand the behaviour of the devices described in those chapters. Finally, the general behaviour wireless communications channel was introduced and then developed to specify the inclusions of a RIS-assisted channel, and the typical structure of the RIS was delineated, which will aid in understanding the operation of RIS technologies for Chapters 7 and 8, where RIS unit cells will be described.

Chapter 3

Materials and Experimental Methods

In this Chapter, the materials commonly employed throughout this Thesis to construct the bespoke liquid crystal (LC)-based devices, and the experimental methods for fabricating and measuring these devices are detailed. To facilitate the fabrication and measurement of such devices for the 1 GHz - 40 GHz frequency range, it was necessary to develop a range of bespoke methods and techniques, for example; applying LC device preparation techniques used for indium tin oxide (ITO)-coated glass substrates to copper-clad FR-4 substrates, etching complex geometries into the ITO-coated glass, or establishing the necessary apparatus to conduct measurements in the radio frequency (RF) domain. Parameters for the full-wave electromagnetic (EM) simulations, and other measurement equipment frequently employed in this work will also be discussed.

The main contributions of this Chapter are as follows:

- the reliability of the LC alignment layer when applied to copper surfaces is assessed;
- methods for etching complex geometry from ITO films are investigated;
- a bespoke anechoic chamber for conducting RF measurements of LC devices is designed and constructed; and,
- the properties of materials commonly used in this work are measured, or reported values presented.

Additionally, the typical methods for fabricating LC devices are detailed, and the general measurement apparatus are specified.

The remainder of this Chapter is assembled thusly: the properties of dielectric and conductive materials employed in this work are outlined in Section 3.1, then in Section 3.2 the standard LC device preparation, and deviations necessary for RF applications, are delineated. Following this, in Section 3.3 two techniques for patterning ITO are explored and their merits determined. The equipment used to facilitate physical measurements in the RF and optical domains is described in Section 3.4 and the EM simulation software for comparing with the RF measurements is presented in Section 3.5.

3.1 Materials

There were several materials, and techniques for processing them, used in multiple research Chapters in this Thesis. Those most commonly employed were:

- FR-4: a copper-laminated material used for prototyping printed circuit boards (PCBs). Designs were imported to Pulsonix PCB software and printed using a LPKF PCB fabricator.
- Rogers RO 4350B: a copper-laminated PCB material used for high-frequency applications. Designs were created in Pulsonix and fabricated externally.
- ITO-coated glass: soda lime float glass with one side coated in ITO. Purchased from Ossilla with the ITO patterned using either the chemical or laser etching methods detailed in this Chapter. The ITO layer was 100 nm thick and the conductivity measured at d.c. as 0.667 MS/m using a 2-point probe.
- Polylactic acid (PLA): 3D printed material used to fabricate antenna mounts. Designs were made in Solidworks and printed using a Bambu P1S 3D printer.
- Nematic LCs: the nematic LC mixture known as E7 (Synthon Chemicals) was typically used, except for in Chapter 7, where the nematic LC mixture ZOC-A019XX (JNC Corporation) was utilised.

Parameters for the dielectric materials are detailed in **Table 3.1**. The dielectric parameters for ITO-glass and copper-laminated FR-4 were measured using the resonance

Table 3.1: Parameters for selected the dielectric materials used in this work. Measured values were obtained in this work, unless otherwise stated. All measurements were conducted at a temperature of 20°C.

Name	Material Type	Height [mm]	ε_r	$\tan\delta$	Freq [GHz]
FR-4	Fibreglass/epoxy resin composite	1.54	4.54 4.43 4.23	0.014 0.016 0.01	5 10.95 16.76
RO 4350B	Fibreglass/ ceramic composite	0.5	3.48	0.0037	10 [79]
Glass	Soda lime, float glass	1.1	5.9 5.54	0.08 0.1	3.6 9.8
Antenna mounts	Polylactic acid	various	3.47	0.073	10 [80]

method: for FR-4, this was achieved by using the LPKF PCB machine to cut a microstrip line into double-sided copper-clad FR-4; whereas for the ITO-coated glass the microstrip line was initially patterned using the laser etching technique with colloidal silver spin-coated onto the reverse to act as the groundplane and onto the microstrip to improve the conductivity of the device. The copper-clad FR-4, and silver-coated glass microstrip lines were 15 mm and 20 mm long, respectively, and designed to exhibit an impedance of 50 Ω. SMA connectors were attached to each device and the S-parameters measured using a Rohde & Schwarz VNA between 1 GHz - 20 GHz, each measuring several resonance peaks. Examples of the devices and the measured S-parameters of the silver/glass device are shown in **Figure 3.1**.

3.2 Fabricating Liquid Crystal-based Devices

There exists a myriad of ways to fabricate an LC-based device; while this Thesis will consider LC devices for use at RF, specifically 1 GHz - 40 GHz, the basics of LC device preparation for general applications will be described here. LC devices can be categorised into 'commercial' and 'homemade'. Commercial devices are fabricated to a high-degree of precision and are typically employed in the optical domain i.e., 400 nm - 800 nm. Such devices have been utilised in this Thesis, however, the majority of the research

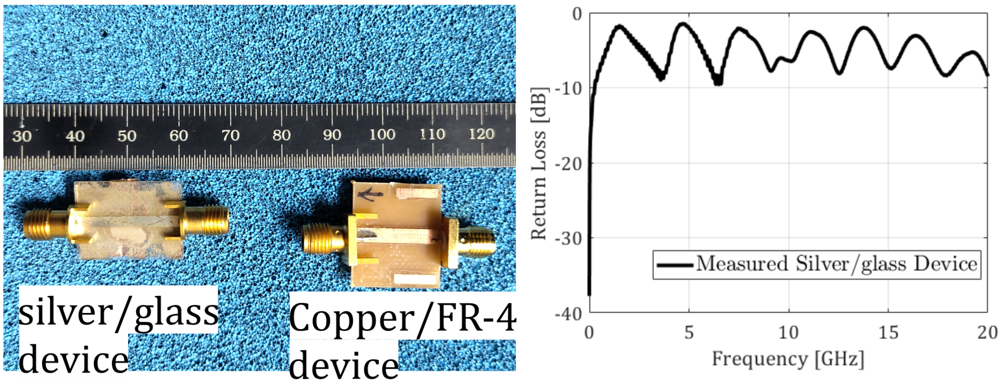

(a) (b)

Figure 3.1: (a) Photograph of silver/glass and copper/FR-4 microstrip line devices. (b) Measurement and simulation results of the return loss as a function of frequency for the silver/glass device.

conducted herein necessitated the use of bespoke homemade LC devices that provided a greater range of flexibility. The fabrication methods described in this Section are utilised for devices constructed in; Chapter 4, for creating a LC device from copper-clad FR-4 in a bowtie antenna; Chapter 5, for fabricating a LC-based microstrip line device from ITO-coated glass; Chapter 6 for producing a transparent reconfigurable antenna from ITO-coated glass; and in Chapter 7, for constructing a reconfigurable intelligent surface unit cell using copper-clad RO 4350B.

LC devices are typically constructed from two overlapping substrates, that each incorporate an electrode, separated by spacers to produce a small air gap into which the LC material can be filled. An electric field can be applied across the gap to affect a reorientation of the LC director: these gaps generally range from a few micrometers (e.g., for optical applications/display devices) to several hundred micrometers or more (e.g., RF applications). To control the reorientation direction of the LC director upon the application of an external electric or magnet field, a LC alignment layer is typically applied to the substrates. This produces a pre-tilt angle of the LC director at the interface of the substrate and LC, ensuring each LC molecule will rotate in the same direction, in line with the applied field. An example of an LC device is illustrated in **Figure 3.2**. The fabrication steps employed to produce this 'homemade' device are:

- place an ITO-coated glass substrate into an ultrasonic bath of isopropyl alcohol

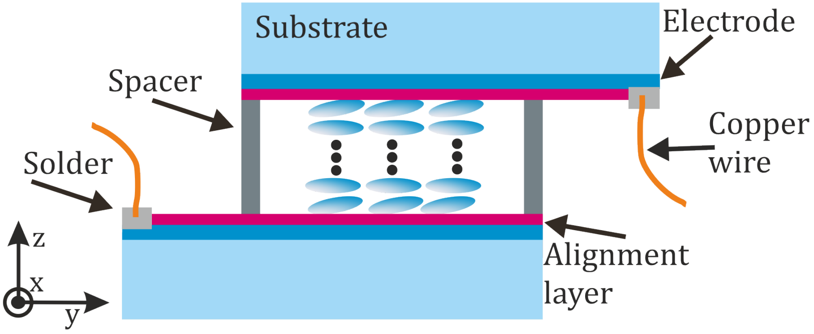

Figure 3.2: Schematic of a typical LC device used in this thesis.

(IPA) for 5 minutes before using a nitrogen gas pump to dry the substrate.

- Apply an alignment layer by depositing the alignment material onto the ITO-coated side of the substrate and spin-coat for 30 seconds at 1000 rpm.
- For a homogeneous (planar) alignment layer, mechanically rub the substrate to produce a pre-tilt angle.
- Apply a spacer to each of the long edges of the substrate.
- Add a second substrate, which has also been cleaned and has an alignment layer applied, such that the two substrates are overlapping but separated by the spacers.
- Infiltrate UV-curable glue at the edges of the device and place it in a UV oven until the glue has cured.
- Solder conductive wires onto the ITO electrodes.
- Capillary fill the LC into the air gap between the two substrates.

Prior to the application of an electric (or magnetic) field across the LC material, LC molecules are subject to thermal fluctuations that could cause them to rotate either clockwise or anti-clockwise, depending on the fluctuation at the instant a field is applied, in a mathematical process known as bifurcation. This leads to undesirable effects and the bifurcation is counteracted through the application of an alignment layer to define the angle of the LC molecules/director at the interface of the substrate and LC, ensuring the molecules/director rotate in a controllable and uniform manner.

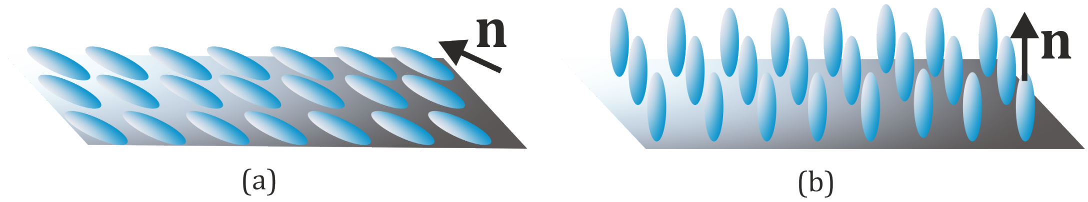

Figure 3.3: (a) Homogeneous alignment layer and (b) a homeotropic alignment layer on glass substrates. Including the LC director orientation, **n**.

The LC alignment layer can be homogeneous, homeotropic, or hybrid, that is, one substrate with a homogenous layer and one substrate with a homeotropic layer. To produce a homogeneous alignment layer, 1 wt.% of polyvinyl alcohol (PVA) was dissolved in distilled water and deposited onto the substrate, followed by spin-coating and a mechanical rubbing process to produce a pre-tilt angle of $1° - 5°$. The tilt angle was not measured directly but a successful homogeneous alignment was confirmed by observing the completed device through a polarising optical microscope (POM). When two substrates featuring a homogeneous alignment are combined, the substrates can be orientated such that rubbing directions are in opposition (planar antiparallel alignment) or in the same direction (planar parallel alignment). To achieve a homeotropic alignment layer, 0.1 wt.% of lecithin is combined with IPA followed by spin-coating to produce a pre-tilt angle of 90° to the substrate. **Figure 3.3** depicts the homogeneous and homeotropic alignment types.

3.2.1 Copper-based Devices

The previous discussion on device preparation assumed that the substrate was ITO-coated glass. However, for LC-based devices in the RF regime, copper-clad FR-4, or other PCB materials were commonly employed. One pre-requisite for applying the LC alignment layer was that the surface exhibits a certain level of smoothness: this is not strictly defined but is generally considered to be on the sub-micrometer scale. Hence, it was necessary to understand various degrees of surface roughness exhibited by copper-based substrates and the effect, if any, this has on the LC alignment layer, and importantly, the variation in the LC permittivity, $\Delta\varepsilon_r$. For example, if the surface roughness of the copper was such that it prevented the LC alignment layer from having any effect, this could reduce the range of $\Delta\varepsilon_r$ (since the LC director would no longer be planar aligned), which would be detrimental to the application of any LC-based device. To test this effect, an experiment was devised to apply homogeneous antiparallel alignment layers to different types and states of a copper substrate, producing a comparison between each of them. The two types of copper used were copper-clad FR-4 and bulk copper (samples were cut from a sheet of pure copper between 1 mm - 2 mm thick).

Three pieces of FR-4 and three pieces of bulk copper (referred to commonly as ’copper substrates’ henceforth) were mechanically cut to be 20 mm × 15 mm × 1.544 mm (length × width × height) as this matched the dimensions of the ITO-coated glass substrates. The following states of the substrate were produced:

- copper substrate with no polishing and no alignment layer,
- copper substrate with no polishing and with a homogeneous alignment layer, and
- copper substrate with polishing and a homogeneous alignment layer.

To allow observation under a microscope, each of these samples were constructed with one copper substrate and one ITO-coated glass superstrate, also featuring a homogeneous alignment layer.

Copper Polishing

For each of the copper substrates that were polished, the same procedure was followed, applied directly after the substrates were cut to the relevant size and before the cleaning and alignment deposition process. The polishing was conducted in the following steps:

- Powdered bakelite was placed into pressurised machine to produce a mount ≈ 40 mm in diameter and 20 mm in height.
- A crystal wax adhesive was utilised to attached the mount to the copper substrate.
- The copper substrate was initially polished on a sandpaper covered turntable, rotating at 100 rpm, by holding it in place by hand with the bakelite mount.
- The grit level of sandpaper was increased by:
    - 600/1200/2400 for 5 minutes at each stage for bulk copper, and

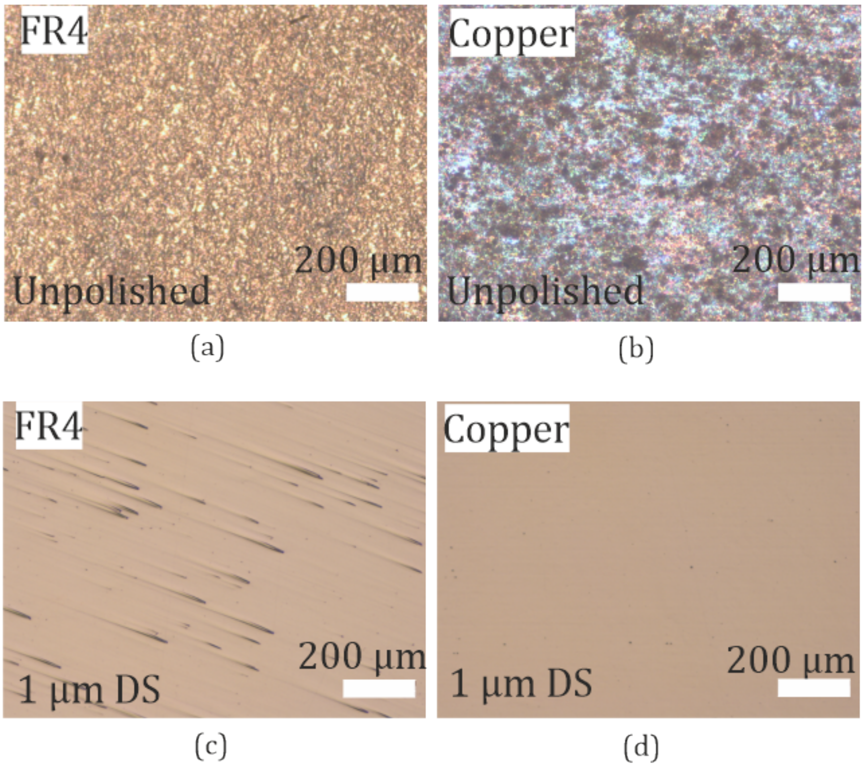

Figure 3.4: Microscope images (taken in reflection) at 4× magnification of the (a) unpolished copper-clad FR-4 and (b) copper substrates, and at 1 μm diamond suspension (DS) for (c) FR-4 and (d) copper.

  - 1200/2400 for 5 minutes at each stage for FR-4.

- A polishing pad was then placed onto the turntable and covered with diamond suspension in water featuring:
  - 6 μm diamond particles for 5 min for both samples, followed by
  - 1 μm diamond particles for 5 min for both samples.
- The mount was removed from the copper substrates by dissolving the wax adhesive in acetone.

The grit levels 600, 1200 and 2400 translate to 30 μm, 15 μm and 7 μm, respectively. The copper laminate on the FR-4 board was 36 μm thick, hence the 600 grit was not used. Images from different stages of the polishing process, taken under a reflection mode microscope at 4× magnification, are presented in **Figure 3.4**.

Surface Roughness

To gauge the effectiveness of the polishing process, the copper substrates were characterised using a Nanosurf CoreAFM atomic force microscope (AFM) before and after polishing. The measurement was conducted for a 100 μm $\times$100 μm grid of $N \times M$, where $M = N = 256$, discrete measurement points of height, z_{ij}, representing the surface height at the point (x_i, y_j) in the xy-plane. The Nanosurf CoreAFM yields a precision of $\pm 0.01\%$ of the sample height [81]. The raw measurement data produced by the AFM was analysed using the open source software Gwyddion. The surface roughness was quantified using R_a, that is, the average height deviation from the mean line ,as

$$R_a = \frac{1}{N} \sum_{i=1}^{N} |z_i - \bar{z}| \tag{3.1}$$

and by the surface roughness, S_a, that is, the difference in height for every measured point compared to the mean of the surface, defined as

$$S_a = \frac{1}{MN} \sum_{i=1}^{M} \sum_{j=1}^{N} |z_{ij} - \bar{z}| \tag{3.2}$$

Figure 3.5 displays the results from the AFM measurement for the copper substrates. The unpolished copper laminate on the FR-4 had a mean surface roughness of $S_a = 430$ nm, compared to $S_a = 140$ nm for the polished copper laminate. The range from maximum peak to minimum trough for unpolished copper laminate was 180 nm, which was reduced to 110 nm when polished.

The results from the AFM measurement for the bulk copper are presented in Figure 3.5(b). The unpolished bulk copper had a mean surface roughness of $S_a = 180$ nm, compared to $S_a = 50$ nm for the polished bulk copper. The range from maximum peak to minimum trough for unpolished was 900 nm, which was reduced to 20 nm for polished bulk copper.

Hence, the polishing process was successful in reducing the surface roughness of the bulk copper and FR-4 substrates. The average height for both cases was reduced to below 100 nm, which was expected to be suitable for applying an LC alignment layer.

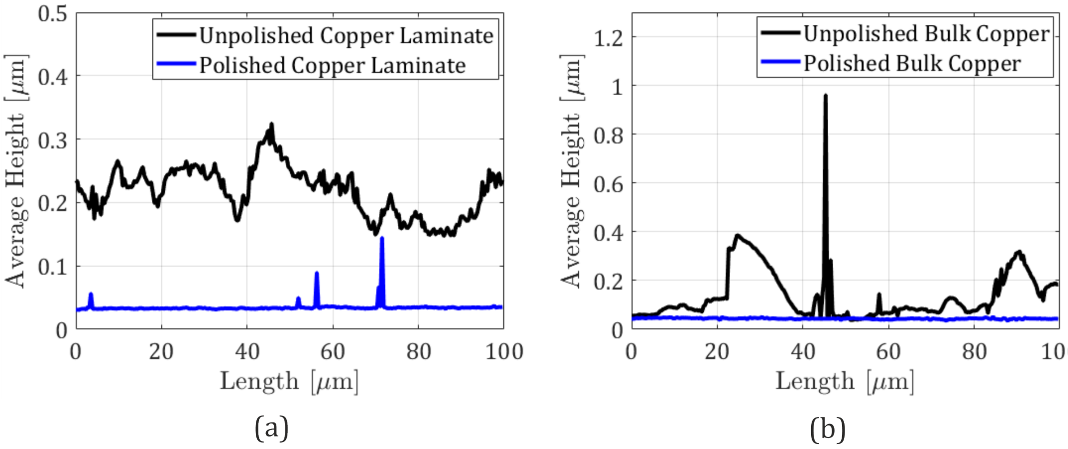

Figure 3.5: The average height deviation from the mean line (R_a) of the polished and unpolished (a) copper-laminated FR-4 substrates and (b) bulk copper.

Dielectric Properties

Following the polishing process, each copper substrate was then cleaned and the homogeneous alignment layer applied in the same manner as previously described. A glass superstrate was used to sandwich the LC and also featured a homogeneous alignment layer. Two 25 μm spacers were fixed to the copper substrates before attaching them to the glass superstrate. UV-curable glue was infiltrated at the edges of the device and placed into a UV oven for 10 minutes. Finally, copper wires were soldered to the devices. Images of an FR-4/glass and copper/glass device are shown in **Figure 3.6**.

The copper/glass devices were analysed using a POM in reflection mode with an external voltage applied across the nematic LC layer, to observe the effects on the LC birefringence with increasing voltage. However, due to the colour of the copper distorting the interference colours, these results were inconclusive and were disregarded. To observe and compare the effects of the homogeneous alignment layer on unpolished and polished copper substrates, the LC devices were characterised using an inductance-capacitance-resistance (LCR) multibridge to measure the capacitance with an applied voltage increasing from 0 V - 20 V, at 1 kHz, in an empty device (at 0 V only) and then with the device filled with the nematic LC known as 'LC10' (provided by Samsung). From this, the relative dielectric permittivity $\varepsilon_{r,\perp}$ was found by dividing C_{air}/C_{LC} at 0 V, i.e., the capacitance of the cell before LC was infiltrated, C_{air}, and after the LC was infiltrated, C_{LC}.

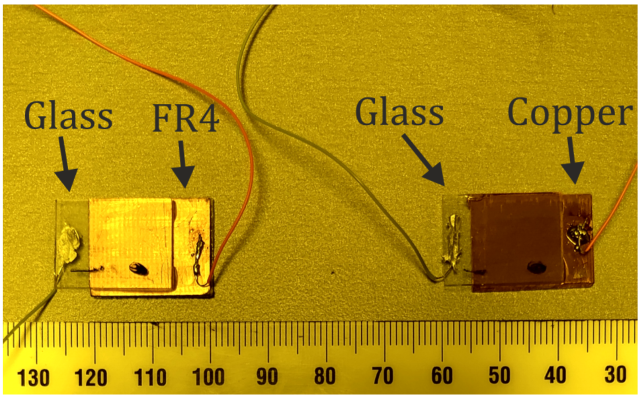

Figure 3.6: Photographs of fabricated FR-4/glass and copper/glass devices. Each device has a 25 μm spacer between the substrates, conductive wires soldered on, and was infiltrated with a nematic LC.

The value for the relative dielectric permittivity $\varepsilon_{r,\|}$ can then be found by extrapolating the Capacitance-Voltage plot to the limit of an infinite voltage, corresponding to the point where the LC director has aligned ideally parallel with the applied electric field (for the case of a positive dielectric anisotropy). Rearranging C_{LC} then enabled $\varepsilon_{r,\|}$ to be obtained. Having determined both $\varepsilon_{r,\perp}$ and $\varepsilon_{r,\|}$, it was then possible to obtain a value for the dielectric anisotropy, $\Delta\varepsilon_r$ at a given temperature.

Table 3.2 shows the results from the capacitance measurements, from which the relative dielectric permittivities, and dielectric anisotropy for each of the LC devices was estimated at a specific operating temperature of 20°C, with an applied voltage of 1 kHz between 1 V - 20 V. The biggest source of uncertainty in these measurements arose from thickness in the LC layer, defined by polymer spacers, with empirical evidence suggesting the actual thickness was ±5% of the ideal value. For both of the bulk copper and copper-laminated FR-4 results, applying a homogeneous alignment layer improved the accessible dielectric anisotropy compared to the devices where no alignment layer was present. However, there was little difference in the anisotropy for the polished and unpolished devices. These results also suggested that even in the case where no alignment layer was applied, the LC was only 'pseudo-random' in that it was only random in the planar dimension. Hence, this study indicated that the copper polishing prior to the application of a homogeneous alignment layer provided little discernable difference to the unpolished case, and therefore, will not be conducted for copper-based LC devices employed in this Thesis.

Table 3.2: Dielectric permittivities ($\varepsilon_{r,\parallel}$ and $\varepsilon_{r,\perp}$) and dielectric anisotropy ($\Delta\varepsilon_r$) for nematic LC LC10, filled into devices consisting of a range of different substrates and alignment layers. Each device featured an LC layer thickness of 25 μm and measurements were conducted at 20°C and at 1 kHz frequency in applied voltage.

Substrate/Superstrate	Polish Level	Alignment	$\varepsilon_{r,\perp}$	$\varepsilon_{r,\parallel}$	$\Delta\varepsilon$
FR-4/Glass	None	Random planar	2.5	5.6	3
Copper/Glass	None	Random planar	2.9	6.6	3.4
FR-4/Glass	None	Homogeneous	2.5	6.6	4.1
Copper/Glass	None	Homogeneous	2.5	6.4	3.9
FR-4/Glass	1 μm	Homogeneous	3.6	7.7	4.1
Copper/Glass	1 μm	Homogeneous	3.5	7.6	4.1

3.3 Etching ITO

ITO-coated glass substrates were used for several applications in this Thesis in which complex patterns from the ITO layer were required: erstwhile methods for etching ITO in the research group facilitated only simple patterns, such as straight lines. This chemical etching technique was also difficult to control, could not produce narrow features (e.g., < 500 μm), and the resulting structures were not precisely delineated. Hence, it was necessary to develop an etching process to reliably fabricate complicated geometric shapes. To achieve this, improvements were made to the chemical etching process, while simultaneously developing a novel laser etching technique. The two methods will be described and compared forthwith.

The patterns considered in each process were for a microstrip patch antenna, portrayed in **Figure 3.7**(a), where; W_p and L_p are the patch width and length, respectively; W_t and L_t are the impedance transformer width and length, respectively; and W_f and L_f are the antenna feed width and length, respectively. The ITO-coated glass substrates were 20 mm × 15 mm × 1.1 mm (length × width × height) with a 100 nm thin film of ITO entirely covering one side.

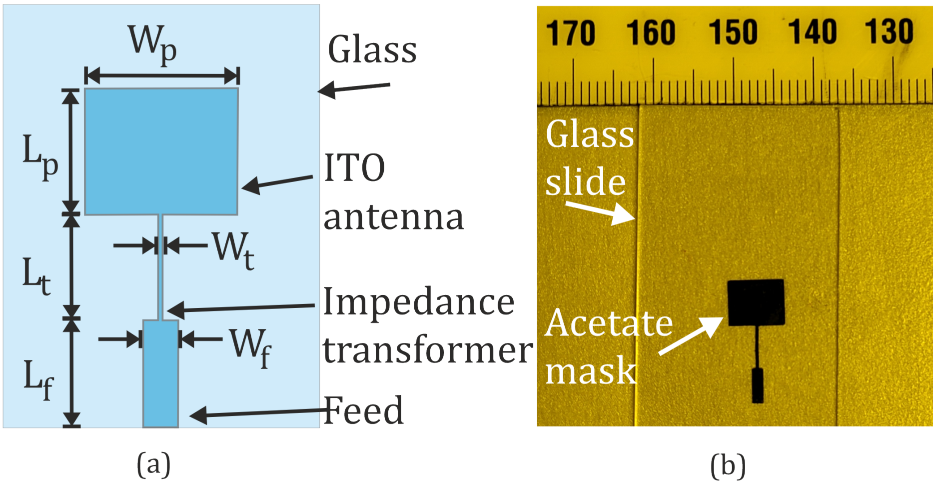

Figure 3.7: (a) Schematic showing the geometry of the microstrip patch antenna. (b) Photograph of a photomask cut into acetate tape using a laser cutter.

3.3.1 Chemical Etching

To facilitate the chemical etching, a photomask was produced for the photolithography stage. Here, a positive photoresist material was used, that is, the geometry of the photomask relates to the area of ITO that will remain at the end of the etching process. Prior to this work, the photomask used was a simple stencil that allowed for the etching of straight lines of various thicknesses, however, this was not suitable to produce complex shapes such as an antenna.

For the chemical etching process the antenna was designed with values (all in mm): $W_p = 7.5$, $L_p = 6$, $W_t = 0.22$, $L_t = 5$, $W_f = 1.66$, $L_f = 5$. To fabricate an accurate photomask using the antenna parameters, the 2D geometry of the antenna was exported from computer modelling software and uploaded to a Trotec Speedy 360 laser engraving machine featuring a 130 W laser. Black acetate tape was loaded into the machine and cut into the required pattern, before fixing it to a glass slide to produce the photomask, shown in Figure 3.7(b).

The photolithography and etching procedures were conducted in the following steps:

- Spin-coat SP1813 positive photoresist (PR) onto an ITO-coated glass substrate for 50 s at 4000 rpm.
- Hard bake the substrate for 60 s at a temperature of 120°C.

- Affix the photomask to the substrate and subject them to 50 $\mathrm{mW/cm^2}$ of ultraviolet light for 60 s.
- Dip the substrate into Microposit MF-319 developer for 60 s.
- Produce a 3 mol solution of hydrochloric acid (HCl) and deionised water, then submerge the substrate into the solution for 2.5 hours at 40°C.
- Remove the substrate from the HCI bath and clean away the remaining PR.
- Measure the resistance across the substrate and remaining ITO to confirm the removal and presence of ITO in the relevant areas.

The HCI solution may be heated to above 40 °C to decrease the etching time, however, this caused the ITO region to be poorly delineated. This process can take between 6 - 8 hours from start to finish. The results of the photolithography and etching processes are displayed in **Figure 3.8**, including an image of the glass substrate with the unwanted ITO removed to form the antenna (a), and a microscope image under ×4 magnification of the transition from the antenna feed to impedance transformer (b).

Examination of the microscope image revealed that the ITO was not precisely delineated at the edges of the antenna structure. These imperfections were on the order of $\approx$ 100 micrometers across and may not be significant when considering that the wavelength of the antenna was $\approx$ 3 cm. Comparing the measured values of the feed width and transformer width, 1330 μm and 216 μm, respectively, with the desired values, detailed here for convenience, $W_f = 1660$ μm and $W_t = 220$ μm, respectively, and considering the precision of the photolithography and etching processes, the results were generally in good agreement with the design parameters.

It is important to stress that this successful result came after several unsuccessful attempts without alteration of the process: the photolithography and chemical etching techniques suffer from poor repeatability, likely due to thermal effects in the HCI mixture. For example, **Figure 3.9** show results where the HCI had cut through the PR layer and disconnected the antenna feed from the radiating element, which has rendered the antenna useless. Successful devices were produced in around 30% of the experiments.

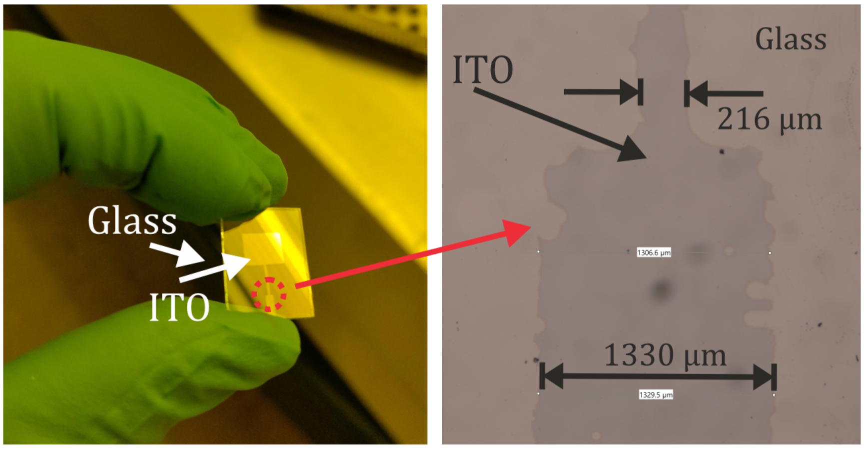

(a)

(b)

Figure 3.8: Results of etching ITO from the glass substrate. (a) a Photograph of the entire substrate. (b) the region of etched ITO as viewed under a microscope at ×4 magnification (dimensions showing where the ITO has been removed are labelled).

3.3.2 Laser Etching

The laser etching process, on the other hand, was more streamlined and could be completed in several minutes. The same 2D file of the device geometry used to cut out the photomask was imported to the laser PC, however, the input parameters to control the laser required adjusting to etch ITO. To assess these parameters, 2 mm wide strips were etched along the width of the ITO-coated glass, with five strips per substrate. The laser power, speed and dots per inch (DPI) were adjusted for each strip, while the frequency was maintained at 1000 Hz. Once the laser control parameters were optimised, the ITO-coated glass was loaded into the laser engraver, using a 3D printed mould to hold the glass and ensure it was correctly aligned. The time for etching the ITO for these antennas was around 1 minute.

The laser etching results, after optimisation of the laser parameters, are portrayed in **Figure 3.10**, by an image of the antenna (a) and the antenna under a microscope with ×4 zoom (b). For this test, the laser etching process realised excellent delineation of the antenna outline; furthermore, once the laser parameters were fixed, the optimised process exhibited ideal repeatability and speed. The regions where the ITO was removed exhibited minor damage to the glass, caused by the laser. Attempts to avoid this by reducing the laser power resulted in the ITO region not being fully removed. To demon-

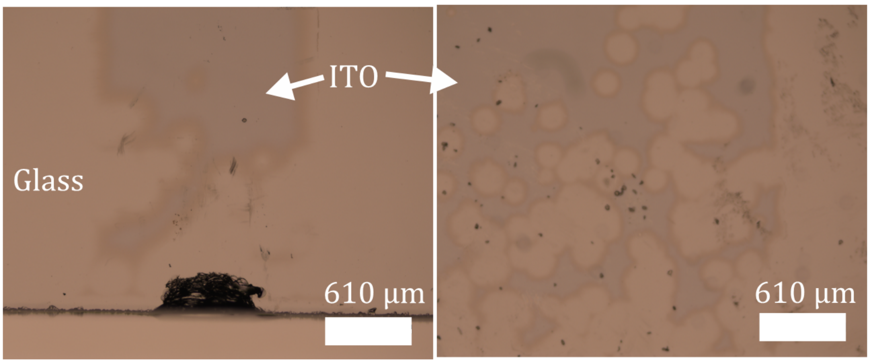

(a) (b)

Figure 3.9: Results of chemically etching ITO from the glass as viewed under a microscope at ×4 magnification with the ITO removed in undesirable locations. (a) a region at the edge of the glass, (b) a section of the microstrip line.

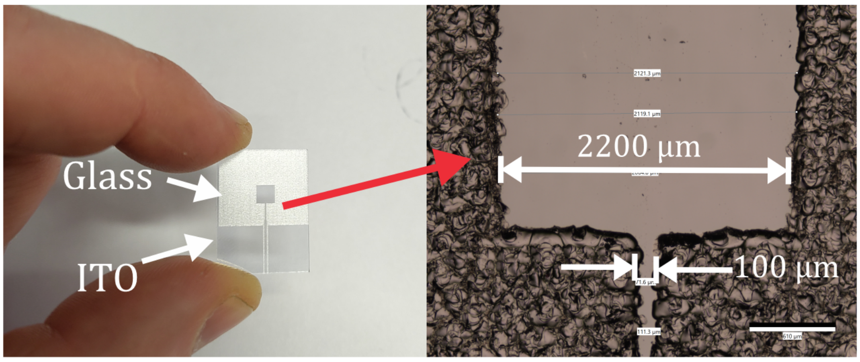

(a) (b)

Figure 3.10: Results of laser etching ITO from an ITO-coated glass substrate. (a) Photograph of the antenna and (b) the ITO-region of the antenna when viewed under a microscope at ×4 magnification.

strate the precision of the laser etching, an antenna with smaller features was designed, with values (all in mm): $W_p = 2.2$, $L_p = 3.3$, $W_t = 0.1$, $L_t = 2.68$, $W_f = 0.4$, $L_f = 8.6$, depicted in Figure 3.10.

3.3.3 Comparison

Comparing the microscope images for the chemically and laser etched antennas, in Figures 3.8 and 3.10, respectively, underlined the ability of the laser to produce well-defined and precise features, whereas the chemical etching exhibited poor delineation between the ITO/glass boundary and a discrepancy between the desired and resulting geometry.

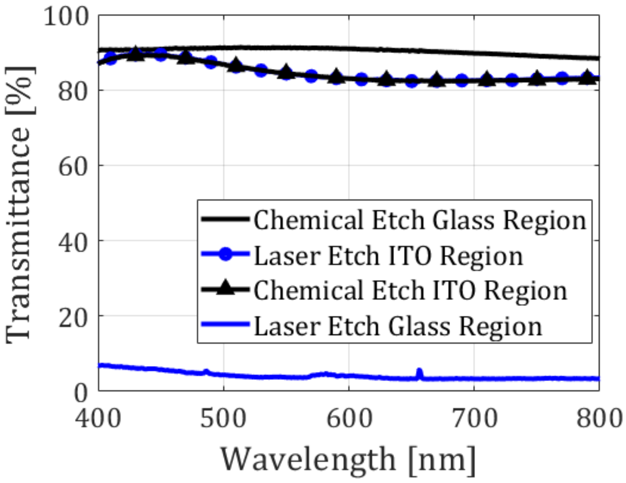

Figure 3.11: Transmittance spectra for ITO-coated glass that has been etched using either laser or chemical etching techniques.

For example, there was a disparity of 20% between the desired and resulting values of W_f in the chemically etched antenna, compared to 5% for the laser etched device.

The transmittance was subsequently recorded for a wavelength range of 400 nm - 800 nm for the glass region and the ITO region in both devices. The transmission spectra were obtained using an Agilent Technologies Cary 8454 UV-Vis spectrometer and the results are presented in **Figure 3.11**. The transmittance results for these devices indicated that the ITO region for both methods was unaffected. As was suggested from the visual images, the glass region was damaged from the laser etching process. However, for the applications of transparent devices in this Thesis the damage to the glass was of little concern since these were prototype devices and there may be industrial fabrication techniques that can negate this problem.

The Nanosurf CoreAFM was again utilised to characterise the surface features that were produced from each etching process. **Figure 3.12** illustrates the average height recorded over a 100 μm $\times$ 100 μm grid for both the laser etched and chemically etched substrates, with the grid located to include the glass/ITO boundary. It was clear that the laser etching process ablated the glass by $\approx$ 8 μm, roughening the glass surface and causing the reduction in transmittance observed in Figure 3.11. The results for the chemically etched ITO showed little variation in surface profile.

3.3.4 Summary of the Etching Processes

Both of the etching procedures have produced functioning substrates that were suitable for the intended application, i.e., a transparent antenna. Each have advantages and disadvantages which may steer the chosen etching process for any particular application, summarised for the chemical etching by:

- **Advantages**
  - Did not require specialist equipment, e.g., a laser engraver.
  - Did not ablate the region below the ITO, or make the glass opaque.
  - Materials were low-cost and available in the SMP group lab.
- **Disadvantages**
  - Process was time consuming and required hazardous chemicals.
  - Failure rate was high, around 70%.
  - Geometric patterns were poorly delineated and often contained small features where the ITO was undesirably removed.

and for the laser etching process:

- **Advantages**
  - Process was fast and repeatable with no failures (after the laser settings had been optimised).
  - Produced small features, ≈ 100 μm across that were within 5% of the desired width.
  - Geometric patterns could be exported directly from modelling software into the laser etching software.
- **Disadvantages**
  - Area where the ITO was removed damaged the glass, leaving it almost completely opaque.
  - Required expensive equipment (available in the Engineering department).

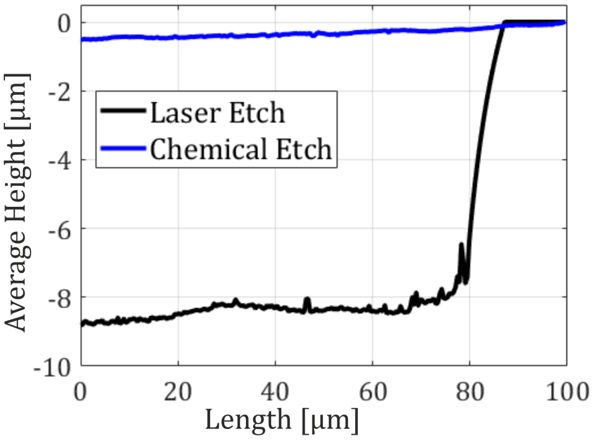

Figure 3.12: Results from AFM for the average height change between the ITO and ITO-removed areas, with the 100 μm × 100 μm grid covering the glass/ITO boundary.

3.4 Experiment Characterisation Systems

Measurements carried out in this Thesis were considered to fall into one of two main categories: either optical frequency measurements, that is, between 400 nm - 800 nm in wavelength, and RF measurements between 1 GHz - 40 GHz. Other equipment used to fabricate or characterise devices in this Thesis will be introduced where relevant.

3.4.1 Optical Frequency Measurements

The transmittance is the fraction of incident energy transmitted through a device and was employed to gauge the optical transparency of LC-based devices. Transmittance was measured using an Agilent Technologies Cary 8454 UV-Vis spectrometer between wavelengths of 400 nm - 800 nm. From the transmittance results, the interference pattern could be used to infer the distance between two glass substrates, when filled with air i.e., prior to infiltrating a nematic LC into the device. This was used to provide an accurate value for the gap between the two substrates, as this could often differ slightly from the prescribed thickness of the spacer.

An Olympus BX51 polarising optical microscope (POM) was used to record images of LC devices in transmission. The source for this microscope was a halogen white light that passed through an initial polariser, a device under test, and then a second polariser (the analyser). The POM featured a range of microscope objectives including a 4×

magnification objective lens with a numerical aperture (NA) of 0.1, a 20× magnification objective lens with 0.45 NA, and 50× magnification with an NA of 0.7.

3.4.2 Radio Frequency Measurements

At the outset of this Thesis, there were no facilities available to conduct the required RF measurements of the LC-based antennas and/or RIS elements that were to be investigated. Hence, the equipment necessary to fabricate and measure devices was either purchased, sourced from within the department, or manufactured in-house. A 2-port Rohde & Schwarz ZNB43 vector network analyser (VNA) that operates from 100 kHz - 43 GHz, two phase-stable 50 Ω RF cables, and a 50 Ω open, short, match, through calibration kit were purchased to facilitate scattering parameter (S-parameter) measurements. The VNA was (unless otherwise stated) calibrated with 1601 frequency points over a range of 10 GHz, around a frequency of interest, for each measurement presented in this Thesis. That results in an error of ±3.12 MHz, or ±0.03%.

S-parameters are a measurement technique for characterising electrical networks as a function of frequency and require a VNA. S-parameters measure the ratio of voltage returned to voltage transmitted, assuming a 2-port system, in the following configurations:

- $S11$ - energy delivered to a device from port 1 reflected back to port 1 i.e., wasted energy;
- $S22$ - energy delivered to a device from port 2 reflected back to port 2;
- $S21$ - energy transmitted to port 2 from port 1 i.e. useful energy, and
- $S12$ - energy transmitted to port 1 from port 2.

In general, it is assumed that $S11 = S22$ and $S21 = S12$ for identical ports. By defining the voltage emitted from ports 1 and 2 ans a_1 and a_2, respectively, and the voltage reflected back to ports 1 and 2 as b_1 and b_2, respectively, then the S-parameters can be described mathematically as

$$S11 = \frac{b_1}{a_1}, \quad S21 = \frac{b_2}{a_1}, \quad S12 = \frac{b_1}{a_2}, \quad S22 = \frac{b_2}{a_2} \tag{3.3}$$

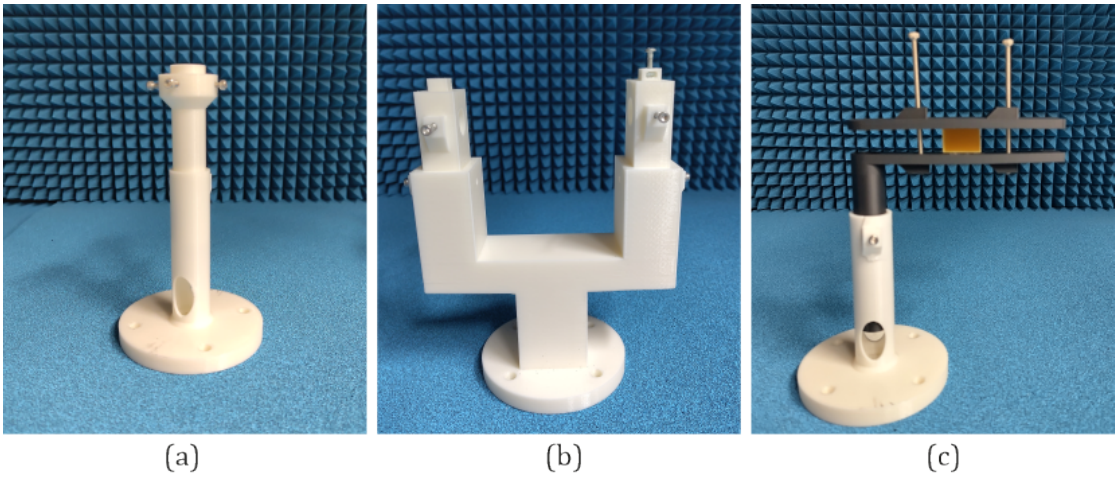
(a) (b) (c)

Figure 3.13: 3D printed antenna mounts for measuring radiation patterns in (a) the E-plane, (b) the H-plane, and for (c) phase reflection measurements.

For testing of the LC-based antennas and RIS elements, two pairs of pyramidal horn antennas were also purchased. One pair of double-ridged horn antennas, DRH30 from RF Spin, operated between 2.5 GHz - 30 GHz with an average voltage standing wave ratio (VSWR) of 1.25. The second pair, H-A40 pyramidal horn antennas from RF Spin, operated between 26.5 GHz - 40 GHz with an average VSWR of 1.15. As it was necessary to apply voltages above 30 V across the LC devices, a high voltage broadband bias-tee (SHF BT45R) and DC block (SHF DC45R) were purchased. Both operated up to 200 V and between 0 - 45 GHz.

A mechanical turntable with 360° rotation was used, and three antenna test mounts were designed and 3D printed, as presented in **Figure 3.13**; two antenna mounts were used to measure the radiation pattern of an antenna device under test (DUT), specifically the E-plane shown in Figure 3.13(a), and H-plane shown in Figure 3.13(b); and one mount for phase reflection measurements shown in Figure 3.13(c).

To provide a quiet RF environment for antenna and RIS element testing, a bespoke anechoic chamber (BAC) was designed and built. The outer dimensions for the chamber were 1340 mm × 610 mm × 730 mm (length × width × height). The dimensions were made with consideration of the far-field, FF, region of the antenna DUT, which is $FF > 2D^2/\lambda$, where D is the largest dimension of the antenna and λ is the wavelength relating to the test frequency. For testing LC-based devices with the RF Spin DRH30

Table 3.3: Typical Reflectivity for RF absorbent foam at three different frequencies [82].

Name	3 GHz	12 GHz - 18 GHz	18 GHz - 40 GHz
WAVASORB VHP-2	-20 dB	-40 dB	-45 dB
WAVASORB AN-72	No data	-11 dB	-11 dB
WAVASORB AN-77	-15 dB	-15 dB	-15 dB

(the largest of the two test antennas), which has a width of 70 mm, $FF \approx 1200$ mm at 40 GHz, decreasing as the test frequency decreases. Hence, the BAC was designed to accommodate testing of antennas and RIS elements in the far-field region up to 40 GHz.

The inner walls and ceiling of the BAC were covered with pyramidal RF absorbent foam, WAVASORB VHP-2, whereas the floor was covered with flat RF absorbent foam WAVASORB AN-72 and AN-77, all from Emerson & Cuming. The combination of RF absorbent foams provided a reflectivity of < -15 dB at frequencies above 3 GHz, improving to < -26 dB above 12 GHz. These measurements were provided by Emerson & Cuming [82] and full details are provided in **Table 3.3**. Two holes were drilled into the side of the BAC to insert the phase-stable cables from the VNA. The walls of the BAC and foam were arranged to limit any gaps in the foam and one of the walls was detachable to allow the measurement configuration to be assembled, and replaced during tests.

The BAC offered several advantages over a standard anechoic chamber including; ability to locate noisy electronic equipment, such as the VNA, voltage generator and amplifier, outside of the chamber, while still utilising phase-stable cables; its low cost, and the ability to reconfigure for different arrangements as required. An image of the BAC, including different measurement configurations, is presented in **Figure 3.14**. The outside of the BAC, with the detachable wall in-place, voltage source and cable holes is shown in Figure 3.14(a), the inside of the BAC, VNA and antenna measurement visible in Figure 3.14(b), in Figure 3.14(c) the E-plane measurement with a DRH30 horn antenna and DUT are shown, and in Figure 3.14(d) the phase reflection measurement of a RIS unit cell is demonstrated, with the H-A40 horn antennas.

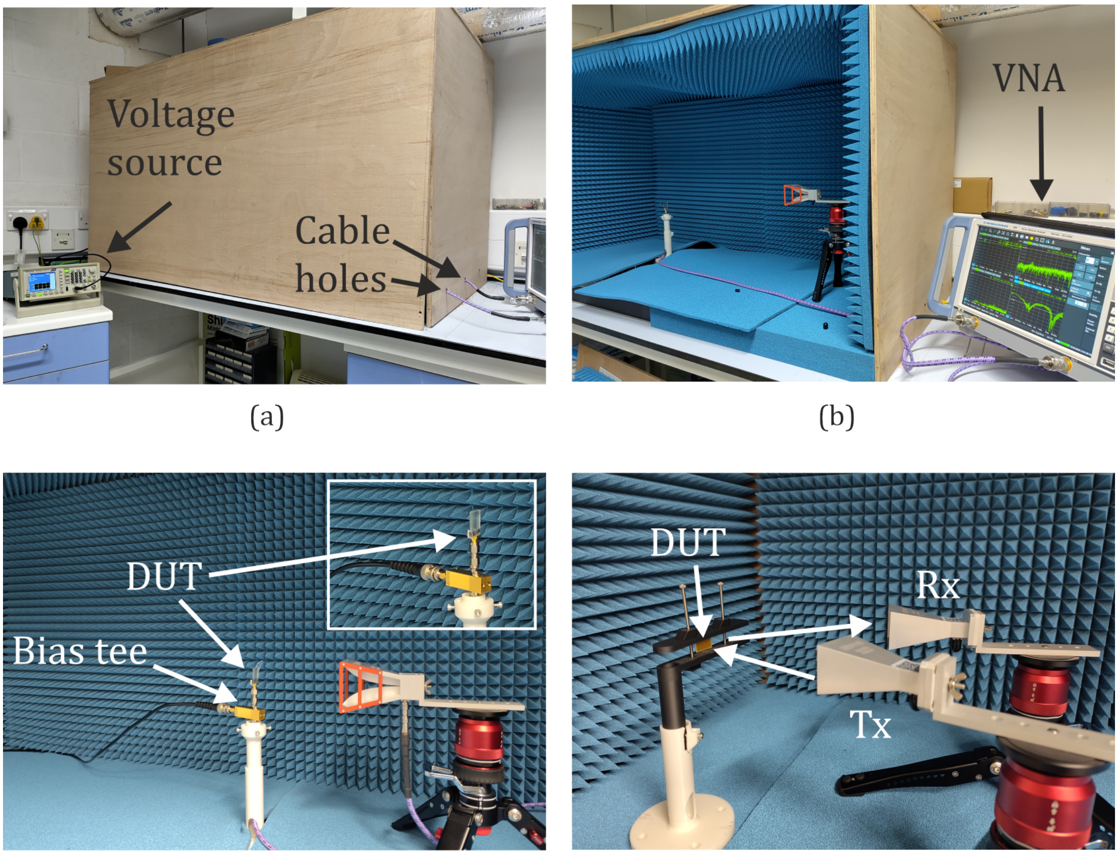

(a) (b)

(c) (d)

Figure 3.14: Bespoke anechoic chamber (BAC) and associated equipment designed and constructed in this work. (a) Photograph showing the outside of the BAC with voltage generator cables fed into the BAC. (b) Photograph of the VNA and inside of the BAC with antenna. (c) Photograph showing a close-up of an antenna measurement system. (d) Photograph showing a close-up image of a phase reflection measurement arrangement.

3.5 EM Simulations

Full-wave EM simulations were computed using the commercially available CST Studio Suite. When designing the LC-based devices for this Thesis the approach was to use analytical expressions, e.g., Equation 2.26, to provide approximate values for the dimensions of the antenna, then to import these into CST to optimise the design. Devices were then fabricated, the dimensions accurately measured using a microscope and the RF behaviour tested. The original simulation parameters were adjusted to account for fabrication errors, and fitted to the measurement data by making small adjustments to specific parameters that could not be measured definitively (e.g., material losses). Simulations used the library parameters where applicable, e.g., when simulating copper conductors. Where library values were not available, e.g., for simulating LCs, initial values were input directly and optimised over a range of values to match physical measurements. The boundary conditions were open in the positive and negative x, y and z-planes, except for where waveguide ports were used, which featured an electrical boundary. Local mesh properties were refined for final simulations to ensure accurate results.

For most simulations, the time domain (TD) solver in CST was used, except for characterisation of a unit cell in Chapter 7, where due to the higher frequency range, it was more computationally efficient to use a frequency domain (FD) solver (since the TD method attempts to solve time-dependent equations). Both methods define a bounding box in which the finite space is discretised into mesh cells and then approximate the solution by solving the integral form of Maxwell's equations using different techniques; TD uses the finite integration technique with a hexahedral mesh, whereas FD employs the finite element method and a tetrahedral mesh. Nevertheless, both methods provide similar results. To assess the simulation parameters that were fittest to the experimental data, a microstrip patch antenna was fabricated from copper-laminated FR-4 and measured. The geometry of this antenna is well understood and there are many examples e.g., [25], to compare results with. The antenna was designed to operate at 14 GHz and the S11 was measured in the BAC. The measurement and simulation results are exhibited in **Figure 3.15**, where the measured and simulated S11 are compared, using both the TD and FD approaches, with the default number of mesh cells in Figure 3.15(a) and with the number of mesh cells increased by a factor of 5 in Figure 3.15(b).

For both the TD and FD measurements with the default mesh settings, the S11 results at the resonant frequency were reasonably close to the measured antenna, although the Q-factor for each simulation was poor. When the number of mesh cells was increased, the S11 results for TD and FD both exhibited improvements in terms of comparisons with the measurements, as did the Q-factor. However, the penalty for this was the simulation time increasing exponentially with mesh density. It should also be mentioned that the input parameters to the CST simulations such as conductivity, dielectric permittivity and material losses are constant and do not vary with frequency, whereas each of these may do in practice. The simulations employed in this Thesis featured an increase in

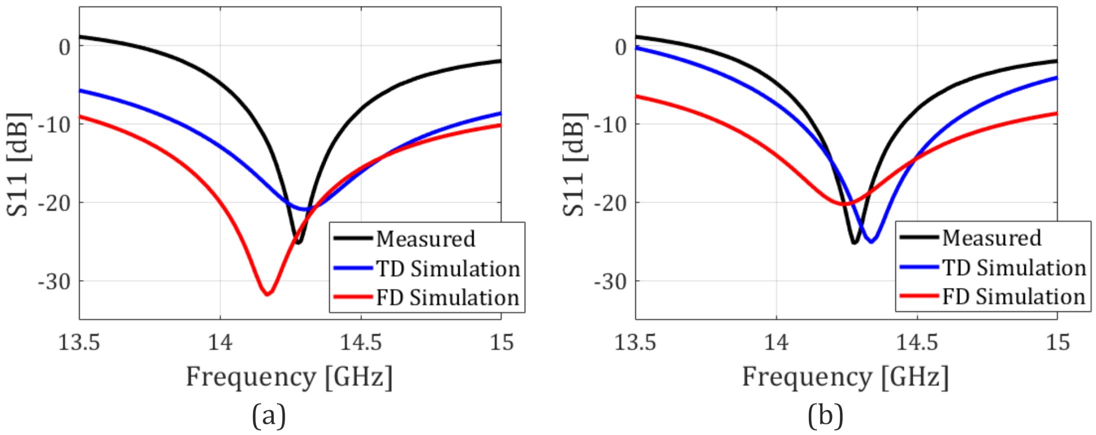

Figure 3.15: Measurements and simulations of a microstrip patch antenna to demonstrate the differences in the TD and FD solvers used in CST Studio Suite (a) using the default number of mesh cells (b) mesh cells increased by a factor of 5.

the number of mesh cells for the presented simulations and were less accurate further away from the operational frequency of the devices. Hence, the comparisons between measurements and simulations will focus on the operational frequency of the devices.

3.6 Summary

In this Chapter, the materials and techniques employed to fabricate bespoke LC-based RF devices, measurement equipment utilised to characterise the RF and optical properties of these devices, and the simulation packages employed to assist with device design and validation were presented. Additional materials, fabrication methods and characterisation methods will be detailed in the relevant Chapters. The techniques for constructing copper-based LC devices will be used in Chapter 4 where the design and characterisation of a reconfigurable bowtie antenna are described, and Chapter 7 where a RIS unit cell is described. The ITO etching procedures will be implemented for forming the optically-transparent microstrip devices in Chapters 5 and 6, and the EM simulations will be used in each of those four chapters. The BAC measurement system was key in testing the LC-based RF devices described throughout this Thesis and some element of the BAC, and/or ancillary equipment, was used for each research chapter presented herein, except for Chapter 8.

Chapter 4

Reconfigurable Bowtie Antenna

This Chapter details the design, simulation, fabrication, and measurement of a reconfigurable bowtie antenna operating at 2 GHz, featuring a nematic liquid crystal (LC), employed to induce a continuously tunable frequency response in the operating frequency of the antenna. Reconfigurable antennas allow for reversible modifications of the antenna parameters, such as radiation pattern, frequency, or impedance, commonly achieved through changing the state of the antenna input network, to produce a set of discrete frequencies that the antenna could be tuned to. Reconfiguration can be used to mitigate congested radio frequency (RF) channels, or allow frequency-hopping and anti-jamming techniques, without the requirement for multiple antennas.

The design equations for a microstrip patch antenna, described in Chapter 2 will be developed to aid the design of the bowtie antenna. Methods detailed in Chapter 3 will be employed to fabricate the antenna, which was printed onto two separate and overlapping copper-based substrates, each fed with a microstrip network, with nematic LC infiltrated between the substrates. An external heat source was used to control the dielectric permittivity of the LC and alter the operation frequency of the antenna, negating the requirement for an external magnetic or electric field. Additional modelling, employed in conjunction with data obtained on two alternative LC mixtures with properties tailored specifically for the radio frequency (RF) band, was also carried out to demonstrate improved frequency tuning performance of the reconfigurable antenna.

A microstrip bowtie antenna was selected due to the desirable characteristics of microstrip antennas; ease of printing, minimal weight and potential for incorporation with

LC. Moreover, the properties of the bowtie antenna such as broadband frequency response and high directivity, along with the well understood design process, also contributed to its selection. A thermotropic nematic LC was employed as increasing the temperature within the nematic mesophase increases random fluctuations in the LC molecules. This leads to a change in the dielectric permittivities due to a decrease in the order parameter, S, but the average orientation of the LC director does not change.

Measurements of this temperature variation in the relative permittivities, that is, parallel and perpendicular to the director, given by $\varepsilon_{r,\parallel}$, and $\varepsilon_{r,\perp}$, respectively, and the effect on the dielectric anisotropy, $\Delta\varepsilon_r$, are demonstrated in **Figure 4.1**, for the nematic LC mixture 'E7' (Synthon Chemicals Ltd.). This mixture exhibits a clearing temperature of $T_c \approx 62°\text{C}$, above which the LC transitions from the nematic mesophase to an isotropic liquid phase and no further substantial change in dielectric permittivity is possible. Although E7 was used here, the trend exhibited in Figure 4.1 is applicable to any thermotropic nematic LC with a positive dielectric anisotropy, however, the exact values for permittivity and clearing temperature may be different.

The results in Figure 4.1 can also be compared with other works that have measured the variation of the dielectric properties of E7 with temperature. For example, in [83], measurements at 45°C, and at a frequency of 1 kHz, give $\varepsilon_{r,\parallel} = 16.5$ and $\varepsilon_{r,\perp} = 5.5$, with an uncertainty of ±1. In Figure 4.1, the corresponding values are $\varepsilon_{r,\parallel} = 16$ and $\varepsilon_{r,\perp} = 6$, with the same uncertainty. At 55°C, [83] reports values of $\varepsilon_{r,\parallel} = 15$ and $\varepsilon_{r,\perp} = 6.5$, whereas Figure 4.1 shows values of $\varepsilon_{r,\parallel} = 15.5$ and $\varepsilon_{r,\perp} = 6$. A small discrepancy is observed in the clearing temperature of the LC: [83] reports a value of approximately 58°C, while Figure 4.1 indicates a clearing temperature of approximately 62°C. This difference can be attributed to uncertainties in temperature measurement (approximately ±0.5°C in each setup), as well as minor variations in batch formulation or the presence of small impurities in the LC mixture. Hence, both measurements are congruent in terms of the measured values, trends of the permittivity with temperature variations, and clearing temperature, with a minor discrepancy accounted for.

Increasing the temperature of a nematic LC is thence a technique often used to alter the relative permittivity of the LC, without the need for applying an external electric or magnetic field, commonly employed in optoelectronic devices. This chapter aims to

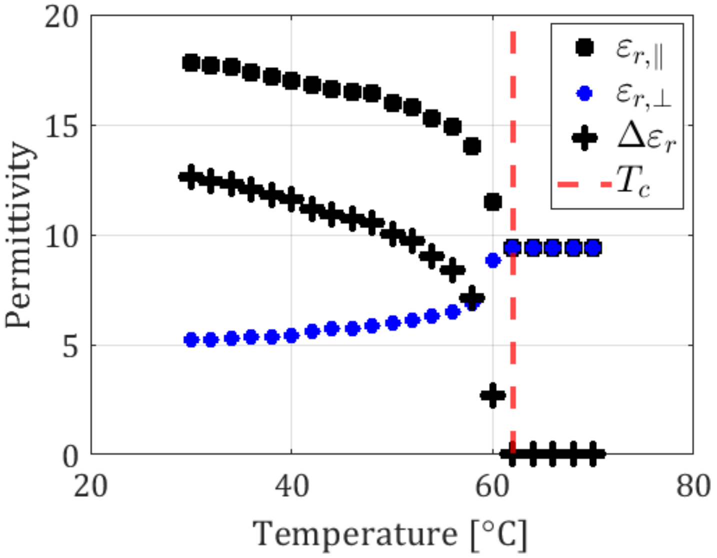

Figure 4.1: Variation in the relative dielectric permittivity with temperature for the nematic LC mixture E7. Measured at an applied frequency of 1 kHz.

establish whether such a method could be applied to a reconfigurable antenna in the RF band.

The main contributions in this Chapter are as follows:

- a bowtie antenna design is developed that incorporates a nematic LC in a manner that elicits frequency reconfiguration in the antenna;
- it is demonstrated that thermal tuning of a nematic LC can be utilised to produce a reconfigurable antenna, and;
- additional simulations indicate how the performance of a thermally tuned reconfigurable antenna can be optimised in the future.

The remainder of this Chapter is arranged as follows: in Section 4.1, background theory pertaining to the design of a bowtie antenna is outlined, including the design and fabrication of the bowtie antenna. This is followed by the measurement and simulation results of the reconfigurable bowtie antenna in Section 4.2. Additional simulations of an optimised reconfigurable bowtie antenna are then presented in Section 4.3. This Chapter is then concluded in Section 4.4. This work was published in the 2023 IEEE Conference on Antenna Measurements and Applications, and an oral presentation was given at the conference.

4.1 Bowtie Antenna Design

The biconical antenna is an extension of a simple dipole antenna that exhibits frequency-independent characteristics by linearly increasing the width of the conductor moving away from the centre of the antenna, where the feed is situated, to produce a cone-shaped radiating element that is infinitely long. Thus, the biconical antenna geometry is defined by its (usually symmetric) cone angles. In the case where the inner angle of the bowtie lobes is zero, the antenna simplifies to that of a dipole.

In practice, the length of the radiating element, L, is not infinite but designed to be much longer than the wavelength of operation, λ, causing the surface currents to dissipate before reaching the limit of the structure. If the length of the radiating element becomes small relative to the wavelength, the radiation pattern becomes similar to that of a dipole. Hence, between these two regions, that is, $\lambda/4 < L < 10\lambda$, is where performance can be exploited by designers through changes to the shape of the structure.

Microstrip bowtie antennas are a planar realisation of a biconical antenna, typically a thin conducting sheet of two triangular elements shaped in the fashion of a bowtie, with the geometry of the antenna governing the operational mode. Rather than follow the design procedure for a biconical antenna, however, the design equations for a microstrip patch antenna, as detailed in Chapter 2, can be adapted to the bowtie structure. In this case, the resonant frequency for the dominant TM_{010} mode is given by [84], [85]

$$F_r = \frac{1.152c}{2R\sqrt{\varepsilon_{re}}L} \tag{4.1}$$

where,

$$R = \frac{L[(W + 2\Delta l) + (W + 2\Delta l)]}{2(W + 2\Delta l)(S + 2\Delta l)} \tag{4.2}$$

and

$$\Delta l = \frac{0.412(\varepsilon_{re} + 0.3)(W_i/H_{sub} + 0.262)}{(\varepsilon_{re} - 0.258)(W_i/H_{sub} + 0.813)} \tag{4.3}$$

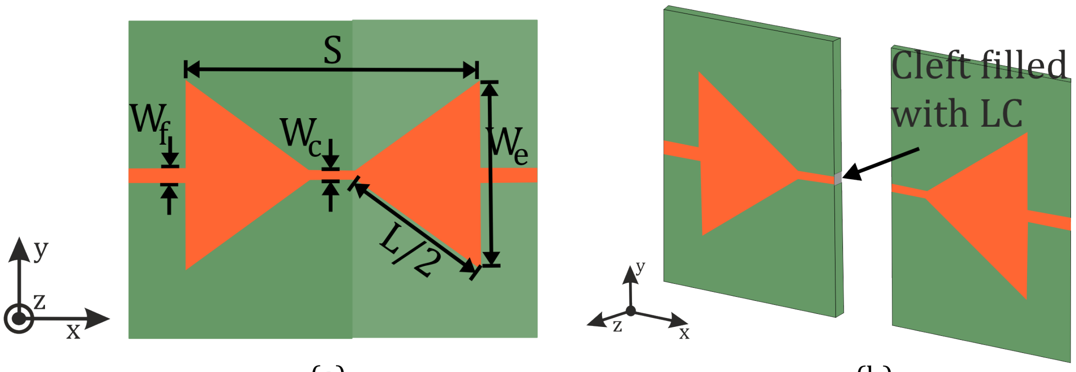

(a) (b)

Figure 4.2: (a) Geometry of the updated (Version 2) bowtie patch antenna and (b) exploded view to display the LC section that was infiltrated between the conductive strips of the upper and lower substrates.

$$W_i = \frac{W_e + W_c}{2} \tag{4.4}$$

and ε_{re} is the effective permittivity of the substrate (outlined in Equation 2.28), with c referring to the speed of light in a vacuum and H_{sub} representing the substrate height. The parameters relating to the large element width, W_e, separation between elements, S, small element width W_c, and element length L, are shown in **Figure 4.2**. Alteration of the operating frequency can be obtained via modifications to L and W_c, with W_e typically constant to ensure the area of the element is not substantially changed.

The first iteration of a reconfigurable bowtie antenna developed in this work was a microstrip bowtie antenna, fed by a balun network, printed on copper-clad FR-4 and designed to operate at 2 GHz according to Equation 4.1. To induce a reconfigurable frequency response from the bowtie version 1 (V1) the fringing fields inherent in a microstrip device were exploited by depositing a nematic LC around and on top of the bowtie elements. Hence, the effective permittivity of the antenna, which governs the frequency response according to Equation 4.1, was not a combination of the FR-4 substrate and air, but instead the substrate and the LC. To alter the relative permittivity of the LC, the antenna was placed on top of a hotplate, which was subsequently heated to 50°C. However, this failed to elicit any reconfiguration, and the design was discarded.

To address the deficiencies of the first version of the reconfigurable bowtie antenna, the design was updated to produce a more substantial frequency shift: this was achieved

Table 4.1: Reconfigurable Bowtie Version 2 Antenna parameters.

W_e [mm]	S [mm]	L [mm]	W_f [mm]	W_c [mm]	L_c [mm]	H_c [mm]	Z_f [Ω]
42	55	60.2	3.2	2	10	0.9	50

by electrically connecting the two narrow ends of the bowtie elements with conductive strips, between which the nematic LC was infiltrated. In this case, the balun network was removed from the design and, instead, two separate feeds were used, with one feed connected to each of the bowtie elements. Each of the bowtie elements was printed on a separate copper-clad FR-4 substrate such that the conductive strips overlapped when the substrates were placed together and the FR-4 between them was removed to form a cleft: this created a parallel plate capacitive effect between the two conductive strips with the cleft initially filled with air, and then with a nematic LC that was thermally varied to provide the reconfigurability in the antenna's frequency response. The reverse side of each substrate featured a copper groundplane; however, for the upper substrate the ground plane below the conductive strip was removed. The geometry of the updated bowtie antenna, including a diagram of the cleft, is illustrated in Figure 4.2. The dimensions of the bowtie elements and the feed network are detailed in **Table 4.1**.

The bowtie V2 antenna geometry was imported into CST Studio Suite to confirm the antenna behaviour, before a physical version was fabricated using an in-house PCB printer. The region below the conductive strip of the upper substrate was removed via a milling process to 1) provide a cleft to infiltrate the LC and 2) maximise the effect of the LC by ensuring a minimal amount of FR-4 (i.e., non-tunable dielectric) between the two conducting strips. The cleft was milled to have width equal to W_c, height, H_c, and length, L_c.

A homeotropic alignment mixture was deposited onto the top of the conductive strip (lower substrate) and bottom of the cleft (upper substrate) to align the LC parallel to the electric field between the two conductive strips: the largest tuning range between two different temperatures was realised when the LC director was aligned parallel to the electric field to provide dielectric permittivity $\varepsilon_{r,\parallel}$ at temperature $T1 = 20°\text{C}$, that is, $\varepsilon_{T1} = \varepsilon_{r,\parallel}$, and then heating the LC to $T2 = 50°\text{C}$. The effect of heating a nematic

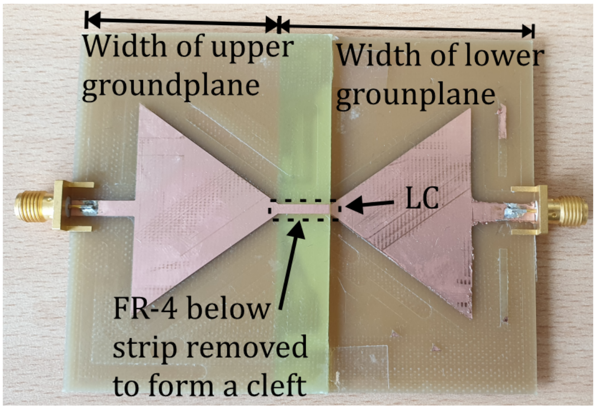

Figure 4.3: Photograph of the fabricated bowtie antenna with the different segments of the antenna highlighted.

LC, demonstrated in Figure 4.1, was that the permittivity became an average of the two ideal states, when the temperature was increased, that is, $\varepsilon_{T2} = \varepsilon_{r,av}$, where $\varepsilon_{r,av} = \left(2\varepsilon_{r,\perp} + \varepsilon_{r,||}\right)/3$. Hence, the dielectric anisotropy for thermally tuning the LC was $\Delta\varepsilon = \varepsilon_{T1} - \varepsilon_{T2} = \varepsilon_{r,||} - \varepsilon_{r,av}$. The LC layer thickness was defined by the height of the cleft, that is, $H_c = 0.9$ mm, hence, the alignment will not be ideal throughout the bulk of the LC: instead it was likely that at $T1 = 20$°C there was realised permittivity situated between $\varepsilon_{r,\perp}$ and $\varepsilon_{r,||}$.

The LC used was a bespoke nematic mixture referred to as ’LC10’ (provided by Samsung). The parallel and perpendicular relative permittivity for LC10 were $\varepsilon_{r,||} = 13$ and $\varepsilon_{r,\perp} = 4$, respectively, and the dielectric anisotropy was $\Delta\varepsilon_r = 9$, measured at 100 kHz using LCR multibridge method described in Chapter 3. The clearing temperature, $T_c = 120$°C, was measured by infiltrating LC10 between two glass substrates and placing the LC cell into a ’hot stage’ while increasing the temperature and observing the effect through a polarising optical microscope, until the isotropic phase was reached.

The two printed bowtie antenna substrates, with the cleft milled out and before any LC was infiltrated, were sandwiched together such that the two conductive strips overlapped entirely, with the lower strip seated into the cleft of the upper substrate. An ultraviolet (UV)-cured glue was then applied to the joint and the two substrates clamped together and placed into a UV oven for 10 minutes to cure the glue. An SMA connector was soldered onto the feed network of each substrate to connect with two coaxial cables leading to the VNA. The final fabricated device is pictured in **Figure 4.3**.

4.2 Results and Discussion

4.2.1 Antenna Performance: Frequency Tuning

For the measurements, A 2-port Rohde & Schwarz ZNB vector network analyser (VNA) was calibrated using open, short, matched and through standards measuring 1601 frequency points between 500 kHz - 6 GHz, providing a step size of 3.4 MHz. To heat the LC, a voltage-controlled silicon heating pad (HP) was fixed to the FR-4 substrate and the temperature of the LC section of the antenna was measured using a digital thermometer. The purpose of the silicon HP was to provide a more focussed delivery of the heat, compared to a hotplate. The measurement system is shown in **Figure 4.4**. Measurements for the reconfigurable bowtie V2 antenna that were taken included;

- the antenna only,
- the antenna with the HP attached at 20°C,
- the antenna with the HP attached at 50°C,
- the antenna with the HP and LC infiltrated into the cleft between the conductive strips at 20°C, and
- the antenna with the HP and LC infiltrated between the conductive strips at 50°C.

Figure 4.5 compares the measured and simulated S11 of the bowtie antenna, without any LC or a heating pad, between 1.4 GHz – 2.4 GHz. The bowtie antenna exhibited a resonant frequency of 1.9 GHz which was within 5% of the designed frequency, had an antenna reflection efficiency $e_r = 99.9\%$ and a -10 dB bandwidth of $BW = 80$ MHz. The simulation results matched the measurement in terms of centre frequency; however, it was not congruent with the reflection efficiency of the antenna.

The results for each of the measurements with the heating pad attached as demonstrated in Figure 4.4(b), including simulations, and a comparison of all of the measured results, are presented in **Figure 4.6**. Figure 4.6(a) displays the measured and simulated S11 of the bowtie antenna, with a heating pad fixed to the FR-4 but without any LC, between 1.4 GHz – 2.4 GHz. The measurement was conducted without inducing any heat into the pad at an ambient temperature of 20°C. The addition of the silicon heating

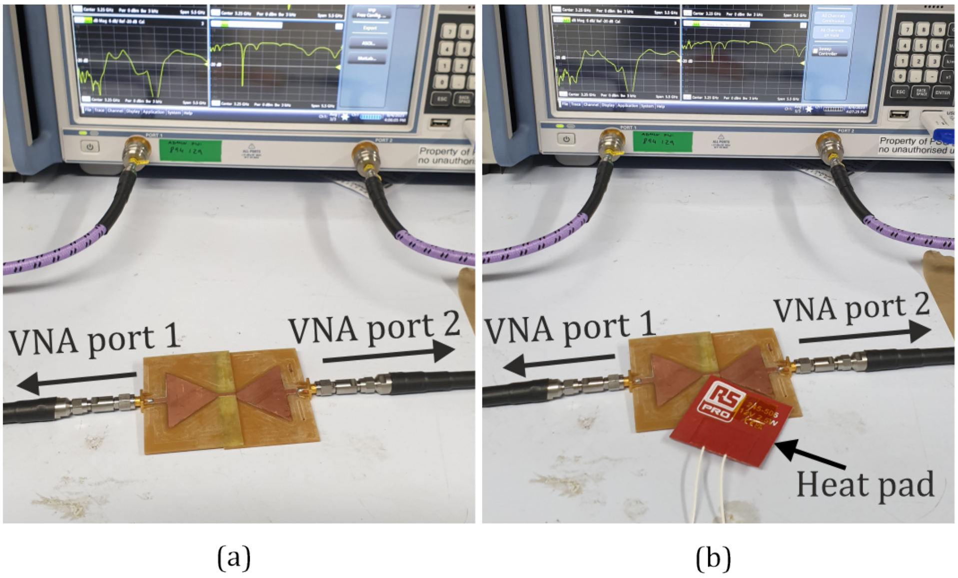

Figure 4.4: Measurement system (a) without the heating pad and (b) with the heating pad attached.

pad altered the resonant frequency of the bowtie antenna to 1.96 GHz and the antenna efficiency was diminished to 87.5%, suggesting the heating pad was introducing significant material losses into the system. The simulation result, which included the silicon heating pad, was in good agreement with the measurement, with the resonant frequency and S11 values of the simulation both within 2% of the measured results.

The effect of inducing heat into the antenna, measured using a digital thermometer to be 50°C, is portrayed in Figure 4.6(b). The resonant frequency of the antenna was reduced somewhat to 1.9 GHz and the reflection efficiency was again degraded, to 78.7%. The simulation was updated to account for the increased heat by adjusting the loss tangent of the silicon heating pad, with the assumption that increased heat will induce additional material losses. This assumption was tested by calculating the material losses $\tan\delta = 1/Q$, where Q is the quality factor of the antenna. For the measurement at 20 °C, $\tan\delta = 0.033$, whereas at 50°C, $\tan\delta = 0.065$, demonstrating that the material losses have almost doubled when inducing heat into the antenna, which indicates that the assumption was valid.

Figure 4.6(c) compares the measured and simulated S11 of the bowtie antenna, with a heating pad attached and with LC infiltrated between the conductive strips, in the range

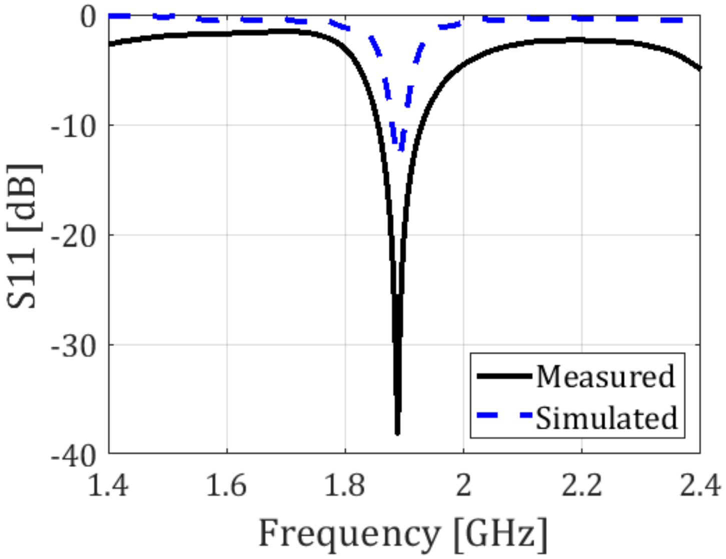

Figure 4.5: Measured and simulated result of the bowtie V2 antenna without a heating pad or LC infiltrated.

1.4 GHz – 2.4 GHz. The measurement was conducted without inducing any heat into the HP, at an ambient temperature of 20°C. The introduction of the nematic LC mixture LC10 into the cleft between the conductive strips shifted the resonance down in frequency by 65 MHz to 1.9 GHz (compared to the 20°C measurement of the antenna without LC), while the antenna efficiency was 83%. The simulation was again in good agreement with the measurements, with the reflection efficiency and resonant frequency in agreement to within 2% of the measurements. The presence of the nematic LC was accounted for in the simulations by including the dielectric material in the relevant position and adjusting the relative permittivity and material losses, based on a range of values that are typical for a nematic LC at 2 GHz [70], and then optimising those values to align the simulation with the measurements. From the input parameters that elicited the best fit between simulation and measurement, the relative permittivity of LC10 at 20°C and 1.9 GHz was indirectly estimated to be $\varepsilon_{r,20} = 1.9$ with $\tan\delta_{20} = 0.058$. However, due to the large LC layer thickness, it was unlikely that $\varepsilon_{r,20}$ equated to $\varepsilon_{\perp}$ in this case.

In Figure 4.6(d) the measured and simulated S11 of the bowtie antenna, with a heating pad attached and with LC infiltrated between the conductive strips, in the range 1.4 GHz – 2.4 GHz are presented. The heating pad was heated to increase the temperature to 50°C in the LC section, measured using a digital thermometer. Increasing the temperature of LC10 shifted the resonant frequency by 80 MHz to 1.817 GHz: accounting for changes induced by heating the antenna without LC (i.e., results in Figure 4.6(b)), suggested that using thermal means to affect the relative permittivity of the LC elicited a frequency response in the antenna of 21 MHz. This was a decrease in frequency from the measurement at 20°C which can be compared with the change of LC dielectric permittivity with temperature as depicted in Figure 4.1, indicating that the large thickness of the LC layer did indeed produce a dielectric permittivity between $\varepsilon_{r,\perp}$ and $\varepsilon_{r,\|}$ which increased slightly with temperature, causing the resonant frequency of the antenna to decrease in accordance with Equation 4.1, that is, $F_r \propto 1/\sqrt{\varepsilon_{re}}$. The antenna efficiency was again reduced when increasing the temperature of the LC region in the antenna, to 72%. As with previous results, the simulation parameters were aligned with the experimental measurements to within 2% in term of reflection efficiency and resonant frequency. The same procedure of trialling a range of values for permittivity and material losses of the LC suggested that the relative permittivity of LC10 at 50°C and 1.82 GHz was $\varepsilon_{r,50} = 2$, with $\tan \delta_{50} = 0.1$.

Comparing these two simulated values for the dielectric permittivity, that is, $\varepsilon_{r,20} = 1.9$ and $\varepsilon_{r,50} = 2$, and for material losses, that is, $\tan \delta_{20} = 0.058$ and $\tan \delta_{50} = 0.1$ aligned with the previous supposition that the relative permittivity and material losses of LC10 would increase with temperature. These values were not unreasonable, when compared to other nematic LCs at this frequency e.g., [70]. The dielectric anisotropy, however, was noticeably lower: this likely stemmed from the relatively large thickness of the LC layer causing the LC director orientation to stray from the intended direction elicited by the homeotropic alignment layer. As such, the relative permittivity that would be evinced from an ideal alignment of the LC director was reduced to a value somewhere between $\varepsilon_{r,\|}$ and $\varepsilon_{r,\perp}$. This was compounded by the effect on the dielectric properties when heating the nematic LC, illustrated in Figure 4.1, where the permittivity becomes an average between the two ideal states, that is, $\varepsilon_{r,av}$.

In Figure 4.6(e) the measured S11 results from Figures 4.6(a)-(d) are combined to display the effect of introducing LC to the antenna at 20°C and then heating the LC to 50 °C. The effect of heating the antenna to 50°C without LC is also included for reference. These measurements established that the bowtie antenna operating at 1.9 GHz could be

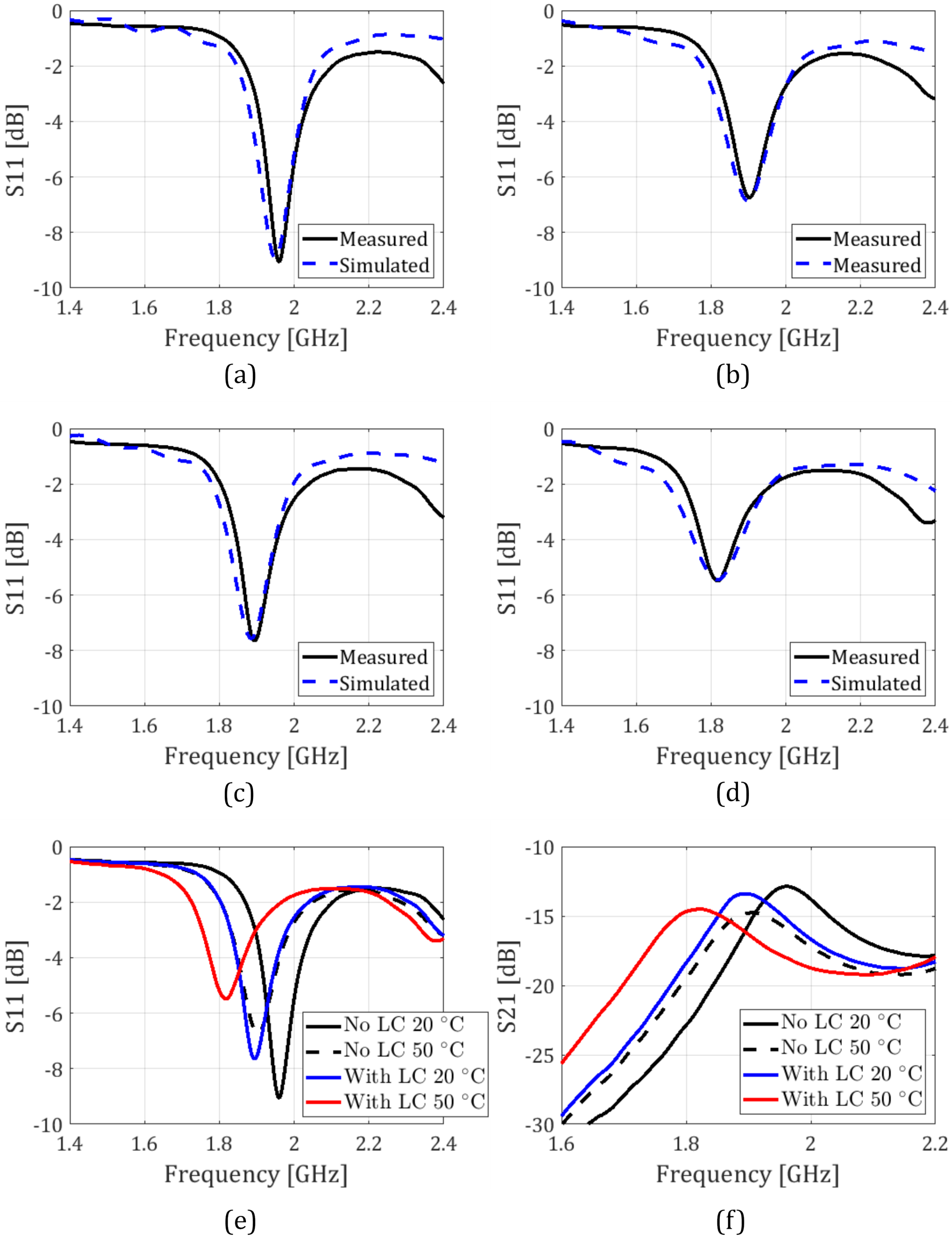

(a) (b) (c) (d) (e) (f)

Figure 4.6: Measurement and simulations results for (a) bowtie antenna with heat pad at 20°C, (b) bowtie antenna with heat pad at 50°C, (c) bowtie antenna with LC and heat pad at 20°C, (d) bowtie antenna with LC and heat pad at 50°C, (e) S11 comparison of all measurements and (f) S21 comparison of all measurements.

Table 4.2: VSWR of bowtie V2 antenna.

Antenna Only	Antenna with HP at 20 °C	Antenna with HP at 50 °C	Antenna with LC at 20 °C	Antenna with LC at 50 °C
1:1	2.1:1	2.7:1	2.4:1	3.2:1

reconfigured using LC10 in a range of 21 MHz, which was 1.1% of the operating frequency, with the use of a nematic LC allowing the antenna to be reconfigured continuously in this range using thermal means.

As the design of the reconfigurable bowtie V2 antenna featured two input networks, the S21 for the antenna at 20°C and 50°C, and the antenna with LC10 at 20°C and 50°C, could be determined, which is presented in Figure 4.6(f). Each of the resonant peaks for the S21 correspond to the same frequency as the S11, indicating the antenna was well matched in terms of reflection and transmission efficiency at each frequency. As with S11, S21 exhibits a controllable frequency response when thermally tuned, with the same shift of 21 MHz observed.

Table 4.2 details the voltage standing wave ratio (VSWR), where $VSWR = (1 + |\Gamma|)/(1 - |\Gamma|)$, and Γ is the S11 value converted to linear form, and is a measure of how well the feed of the antenna is matched to the coaxial cables that connect the antenna to the VNA. For each entry, the VSWR was recorded at the relevant resonant frequency. Satisfactory values are typically $1 < VSWR < 3$, hence the VSWR for the bowtie without the HP exhibits excellent matching of the feed network; however, the introduction of the HP and the application of heat has diminished the VSWR, which was further reduced with the addition of the nematic LC.

Measurements of the reconfigurable bowtie V2 antenna demonstrated that a reconfigurable frequency shift was achieved through thermal stimulation of the LC, aligning with predictions of the effect on relative dielectric permittivity when heating the LC, as outlined in Figure 4.1, and with the resonant behaviour of the bowtie antenna, described in Equation 4.1. However, the performance of the antenna, in terms of reconfigurability, material losses and reflection efficiencies, was generally found to be relatively poor. In practice, using the 2.4 GHz WiFi band, which has four 20 MHz channels, would mean the 21 MHz reconfiguration of this antenna could only operate at and switch between two of those channels. This is only one example, however, and while there are many possible applications that do not use 2.4 GHz WiFi, the example illustrates a need for further enhancements. The basic antenna performance metrics that have been outlined; reflection efficiency, VSWR, Q-factor and material losses, were excellent for the antenna alone; however, adding the heating pad to the antenna has denigrated these metrics to decrease the overall performance. That said, the performance was still within the limits of what is commonly considered acceptable for microstrip antennas.

The switching time of the LC when employing a thermal variation was relatively slow compared with that observed with the application of an electric field. The time required to heat the LC was a function of the speed at which heat was induced into the system, and experimental observations suggest this was in the range of 1 s - 2 s per °C for the system developed herein. However, cooling of the LC was 10 s - 20 s per °C.

4.2.2 Antenna Performance: Radiation Pattern

Due to the construction of the bowtie antenna, specifically, the location of the two antenna feeds at either edge of the structure, it was not possible to measure the radiation in the bespoke anechoic chamber, and a measurement chamber that features a moveable test antenna was required. Therefore, only the simulated radiation pattern will be presented here. This was achieved by utilising the far field calculation in CST Studio for the simulations presented in Figure 4.6(d) and (e), that is the bowtie antenna and heat pad at 20°C with $\varepsilon_{r,20} = 1.9$ and $\tan\delta_{20} = 0.058$, and the bowtie antenna and heat pad at 50°C with $\varepsilon_{r,50} = 2$ and $\tan\delta_{50} = 0.1$, respectively. As there was a frequency shift of only 21 MHz between the measurements at each temperature, the radiation pattern was simulated the same frequency, 1.9 GHz, for each.

The far field calculation allowed the simulation of the E-plane and H-plane of the bowtie antenna, demonstrated in **Figure 4.7**. For the E-plane, the half power beam width (HPBW) was 57° and the antenna gain, $G_a = -1.75$ dB with a directivity, $D_a = 3.9$ dB, suggesting an antenna efficiency of $e_a = 27\%$, where $e_a = G_a/D_a$, using linear values. For the H-plane simulation, the HPBW was 67°, the antenna gain was -1.92 dB with a directivity of 3.74 dB, suggesting $e_a = 27\%$. For both the E-plane and H-plane

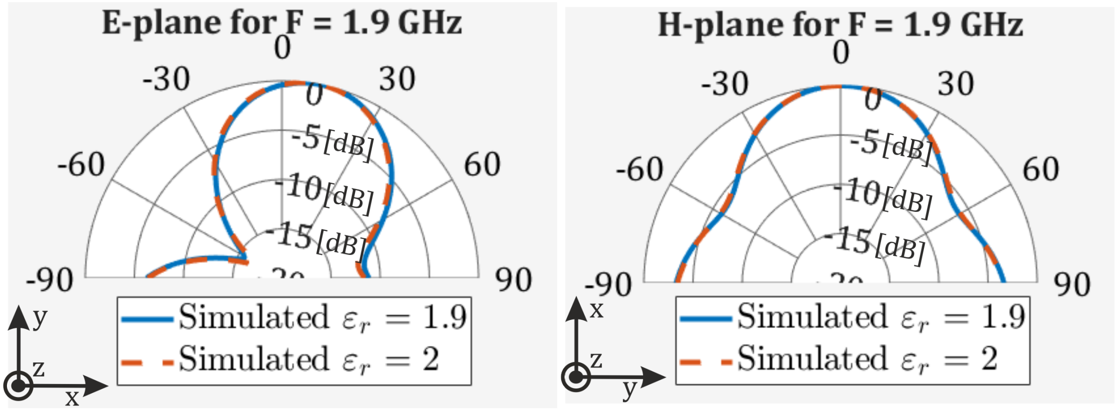

(a) (b)

Figure 4.7: Simulated radiation pattern results for (a) E-plane and (b) H-plane.

results, there was little difference between the simulations with $\varepsilon_{r,20}$ and $\varepsilon_{r,50}$. Both the E and H-plane measurements exhibited a high level of directivity from the antenna, as is common for bowtie patch antennas. The antenna efficiency was slightly lower than is typical for microstrip bowtie antennas, which was likely due to the lossy substrate, LC and heat pads.

4.3 Simulations of RF-optimised Nematic LCs

The simulation model developed in this work produced results that were in good agreement with the experimental measurements, both with and without LC, and at increased temperatures, as demonstrated in Figure 4.6(a)-(d), where it is shown that there was only a small mismatch in the resonant frequency and S11 value. However, the physical performance of the antenna was hindered by: using an LC material (LC10) that was not tailored for RF applications, a large LC layer reducing the achievable dielectric anisotropy, and the addition of the heating pad. Hence, the simulation model was subsequently used to predict the performance of the antenna when incorporating different types of nematic LC mixtures that exhibit more desirable properties at RF, in particular, over the range 1 GHz - 20 GHz.

In [70], an overview of the properties of numerous LCs at RF was reported. Of particular interest were the nematic LC mixtures 'GT3-23001' and 'Merck-MixB'. The mixture 'GT3-23001' exhibited low material losses, with $\tan\delta < 0.02$ and 'Merck-MixB'

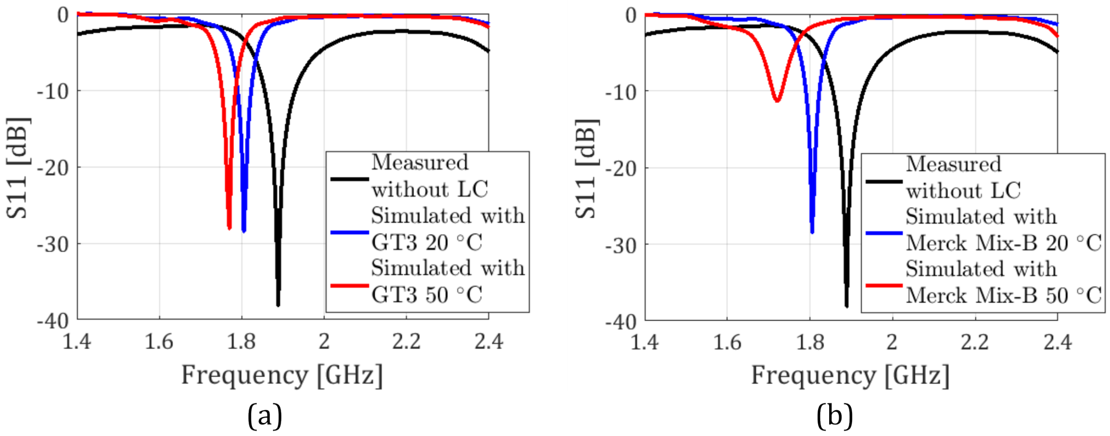

Figure 4.8: Measurement and simulations results for (a) the LC mixture 'GT3-23001' and (b) the LC mixture 'Merck-MixB'.

provided a desirable tuning range with $\Delta\varepsilon_r = 1.32$. The results of simulating 'GT3-23001' in the bowtie V2 antenna are shown in **Figure 4.8**(a) and for 'Merck-MixB' in Figure 4.8(b). The effect of the HP was removed from this simulation, as it induced significant electrical losses, to predict the best-case scenario for the antenna's performance. The simulation also assumed that the full range of dielectric anisotropy, as measured in [70], was achievable.

By employing 'GT3-23001' in the bowtie V2 antenna the simulation suggested that this LC could produce a reconfiguration in the antenna of 30 MHz with a reflection efficiency of 99%, even when the LC was heated to 50°C. With 'Merck-MixB', the range was 85 MHz; however, the efficiency was reduced to 93% when heated to 50°C. Hence, for the nematic LC mixture 'Merck-MixB', it was possible to employ the reconfigurable antenna to operate within the 2.4 GHz WiFi band, which features four 20 MHz channels, as an example of its practicability. **Table 4.3** summarises the results from simulations of the bowtie antenna for the three nematic LC mixtures (LC10, GT3-23001, Merck-MixB) considered in this study.

4.4 Conclusions

In this work, a reconfigurable bowtie antenna featuring a nematic LC and operating at 2 GHz was designed, simulated, fabricated and characterised. An initial experiment

Table 4.3: Results for the bowtie from measurements and simulations.

	F_r [GHz]	e_r [%]	$\varepsilon_{r,LC}$	$\tan\delta_{LC}$
Bowtie at 20 °C	1.96	87.5	N/A	N/A
With LC10 at 20 °C	1.896	83	1.9	0.04
With LC10 at 50 °C	1.817	72	2	0.1
Change with LC10	**0.021**	**11**	**0.1**	**0.06**
With GT3 at 20 °C	1.805	99	2.41	0.014
With GT3 at 50 °C	1.77	99	3.18	0.004
Change with GT3	**0.03**	**0**	**0.77**	**0.01**
With MixB at 20 °C	1.805	99	2.62	0.02
With MixB at 50 °C	1.72	93	3.94	0.07
Change with MixB	**0.085**	**6**	**1.32**	**0.05**

produced a bowtie antenna with a balun network, while this antenna exhibited desirable properties, the design was not able to evince any meaningful frequency reconfigurability from the presence of a nematic LC. The design was subsequently updated to include a capacitive strip electrically connecting the two bowtie elements. Further measurements demonstrated that the bowtie V2 antenna achieved a modest frequency shift of 21 MHz when increasing the temperature of the LC region via an external heating pad. However, this heating pad also negatively impacted the antenna performance of the device, from a highly desirable level to one that was just about acceptable. CST simulations were used to model the antenna, heating pad, LC, and a change in temperature, and were found to be congruent with the measurements, with simulated results within 2% of measurements.

Subsequent simulations, based on the model developed and refined against a series of measurement data, and separate measurements of LCs that are suitable for RF, suggest that LCs with lower losses and/or large tuning ranges can produce an antenna with a wider range in which it can be reconfigured or minimise losses in antenna efficiency. The mixture ’GT3-23001’, in particular, may provide a reconfigurable range of 30 MHz without altering the efficiency, whereas ’Merck-MixB’ could produce a tunable range of up to 85 MHz with a drop in efficiency of just 6%.

The method of thermally tuning the LC negates the use of an external electric or magnetic field, however, the dielectric contrast between the two different states is reduced and, importantly for the application of this antenna, increases the switching time. Hence, this design could only be employed in frequency switching scenarios that align with the slow switching times. Alternatively, the antenna could be employed to react to a changing environment, e.g., in a 'smart greenhouse', where the temperature changes can be monitored through changes to the antenna's reconfiguration, while still employing the antenna to send and receive information.

The work in this chapter was useful in determining the work in subsequent research chapters, for example, the simulation of the effects of large LC layers in Chapter 5, and the need to use substrate materials where the LC layer thickness is not as large, by sandwiching the LC between glass substrates in Chapter 6, or utilising thinner PCB materials in Chapter 7.

Chapter 5

Characterisation of Liquid Crystal Dielectric Properties for RF Applications

In this Chapter, the behaviour of a nematic LC mixture operating in the radio frequency (RF) band will be investigated. Firstly, the dielectric properties of a nematic liquid crystal (LC) will be characterised at frequencies of 4 GHz and 5 GHz. In particular, the chapter reports the design, simulation, fabrication, and measurement of an optically-transparent microstrip line device that exploits the resonance technique to estimate the complex dielectric permittivity of the LC both parallel and perpendicular to the director. Secondly, the behaviour of a nematic LC layer with a relatively large thickness, that is $\geq$ 100 μm, will be simulated using an LC director profile model that is based upon continuum theory, which also attempts to account for the effect of thermal fluctuations on the individual LC molecules, both with and without the application of an electric field. The experimental work on characterising a nematic LC was published in the 2025 IEEE 20th International Symposium on Antenna Technology and Applied Electromagnetics, with an oral presentation given at the conference.

From the discussion in Chapters 1 and 2, it is clear that characterisation of the frequency-dependent complex dielectric permittivity of an LC material is paramount in understanding the behaviour of any device that utilises LCs. Previous work in this area has largely focussed on the use of conventional printed circuit board (PCB) materials, such as FR-4 and copper. To support research on optically-transparent RF antennas and metasurface elements in this Thesis, and other work on transparent LC-based devices for RF applications [53], the dielectric characterisation detailed here will be conducted using an optically-transparent microstrip device formed from indium tin oxide (ITO)-coated glass. The frequencies of 4 GHz and 5 GHz were selected as they are situated within the frequency range outlined in the scope of this Thesis, and because the resonant frequency was proportional to the length of the microstrip line, which was limited by the dimensions of the ITO-glass that was available.

The structure of a device used to incorporate LCs into the geometry of the antenna, or metasurface element, presents a further consideration to the microstrip line model, and equations for effective permittivity described in Chapter 2. The effective substrate permittivity is integral to the operation of the device, and assumes the dielectric substrate interfaces with air; however, for the LC-based RF devices in this Thesis, in particular Chapter 6, the LC substrate interfaces with a glass superstrate. This causes undesirable effects in the device operation, especially on the operating frequency. Exploiting the simple geometry of a microstrip line will realise an improved understanding of the effective dielectric behaviour between the LC and glass materials, while the structure of the characterisation device will closely match the antenna demonstrated in Chapter 6.

When fabricating LC devices for display technologies, the thickness of the LC layer is typically < 100 μm, where the surface alignment can be reliably maintained through the bulk of the LC material and voltages ≈ 10 V are sufficient to fully reorientate the LC director parallel to the applied electric field (assuming positive dielectric anisotropy). However, to enable sufficient modulation in the RF domain, the LC layer needs to be 100 μm - 700 μm, as shown, for example, in [19], [53], [86]. At these thicknesses, the effects of the surface alignment layer and applied electric field on the LC molecules can be counteracted by perturbations from thermal fluctuations, that is, random molecular motion due to thermal energy. These perturbations are rarely considered in RF LC devices and it is generally assumed that the LC director behaves in the same way whether the LC layer is 10 μm or 300 μm. However, such an assumption does not capture the precise nature of the LC.

The main contributions in this chapter are as follows:

- An optically-transparent microstrip line device is designed, and fabricated from ITO-coated glass, such that it can incorporate a nematic LC and resonate at a desired frequency;
- LC dielectric properties, including dielectric anisotropy and material losses, are characterised at 4 GHz and 5 GHz using a resonance based technique. The effects of the dielectric contribution of the glass substrates on the material losses and effective permittivity, compared to FR-4 and copper, are also discussed.
- An updated LC director model that attempts to encapsulate the effects of thermal noise in the LC bulk is presented. This model is employed in LC director simulations to show the effects on large LC layers.

The remainder of this Chapter is organised as follows: in Section 5.1 the dielectric properties of a nematic LC are investigated, including the design and measurement results of an optically-transparent microstrip line device. Then, in Section 5.2, the simulation parameters for the LC director model are delineated, with results for three different LC layer thicknesses presented. Finally, the key findings in this chapter are summarised in Section 5.3.

5.1 Characterisation of a Nematic LC at 4 GHz and 5 GHz

5.1.1 Microstrip Design

A microstrip line device was employed due to the suitability of its geometry for etching ITO-coated glass and the corresponding analysis of its electrical properties. The resonant frequency, F_r, of the line was calculated using

$$F_r = \frac{c}{2L_{se}\sqrt{\varepsilon_{e,sub}}} \tag{5.1}$$

where L_{se} is the effective length of the conductive microstrip line (Equation 2.27) and $\varepsilon_{re,sub}$ is the effective dielectric permittivity of the substrate (Equation 2.28), in this case the substrate was a nematic LC. The device was constructed by etching ITO-coated glass

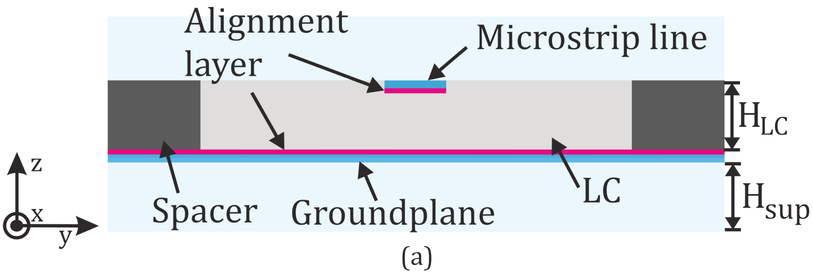

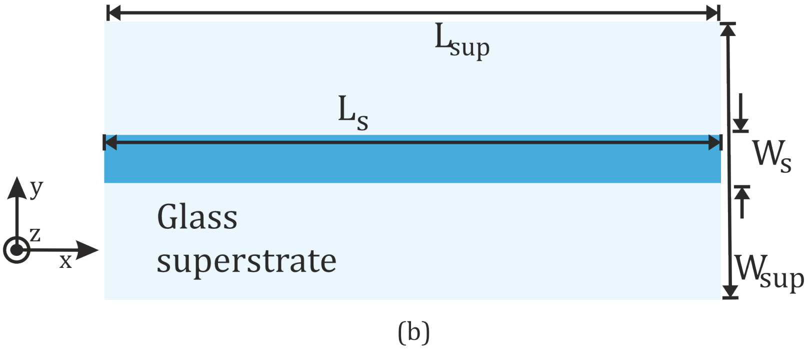

Figure 5.1: Microstrip line geometry with values detailed in Table 5.1. (a) end view, (b) top view. The device features a nematic LC acting as the dielectric substrate, with the ITO-coated glass employed to provide the conductive strip and groundplane. The ITO-coated glass also enabled the application of a voltage across the LC layer.

to produce the microstrip line, with a second piece of ITO-coated glass (unetched) to act as the groundplane. A homogeneous alignment layer was applied to the ITO-covered regions of the glass samples. Two 300 μm spacers were utilised to separate the two pieces of glass into which a nematic LC, 'E7', was infiltrated. Hence, the device featured ITO as the conductive microstrip line and groundplane, separated by the LC acting as the dielectric substrate. For clarity, the glass will be termed as the top and bottom superstrate.

The geometry of the resonant device - microstrip line width and length, and LC layer thickness, W_s, L_s and H_{LC}, respectively; glass superstrate width, length and height and dielectric permittivity, W_{sup}, L_{sup} and H_{sup}, $\varepsilon_{r,sup}$, respectively; characteristic impedance of the strip, Z_f, are defined in **Figure 5.1** with values detailed in **Table 5.1**.

The next step was to create a CST Studio Suite microwave simulation based on these device parameters to confirm the microstrip line operational frequency and impedance. A second device using copper-clad FR-4 to replace the ITO-coated glass, with the same

Table 5.1: Microstrip line, superstrate, and LC parameters. The values for $\varepsilon_{r,sup}$ were measured in Chapter 3.

Device	W_s [mm]	L_s [mm]	H_{LC} [mm]	W_{sup} [mm]	L_{sup} [mm]	H_{sup} [mm]	$\varepsilon_{r,sup}$	Z_f [Ω]
Transparent V1	1.7	15	0.3	15	20	1.1	5.6	30
Transparent V2	1.7	20	0.3	15	20	1.1	5.6	30
FR-4 V1	1.7	15	0.3	15	20	1.56	4.3	30

parameters as in Table 5.1 was also fabricated using a LPKF PCB cutting machine to etch the microstrip line geometry. The FR-4/copper device was constructed and simulated in the same configuration as the ITO-coated glass device to compare the results; that is, for the device shown in Figure 5.1 copper clad FR-4 replaced the ITO-coated glass superstrates, with all other parameters and fabrication steps unchanged.

The laser etching parameters described in Chapter 3 produced desirable results, portrayed in **Figure 5.2**, by an image of the microstrip line (a) and the device observed on a microscope with ×4 magnification (b). From the images, it was clear that the features of the microstrip line were well delineated, with the average strip width as measured on the microscope being 1750 μm, compared to the desired width of 1700 μm. The glass beneath the regions where the ITO was removed was damaged and became opaque. However, for this application, the minor damage/opaqueness was not a concern.

5.1.2 S-parameter Measurement Results

S-parameter measurements were conducted using a calibrated Rohde & Schwarz ZNB43 vector network analyser (VNA), with a SHF BT45R broadband bias-tee and a SHF DCB45R broadband DC-block inserted either side of the transparent microstrip line device. A voltage generator was used to apply a 1 kHz square wave up to 100 V across the LC layer, using the microstrip line and groundplane as electrodes. The measurement configuration is shown in **Figure 5.3**.

Measurement and simulation results for the first transparent microstrip line device are provided in **Figure 5.4**. From the measurement results it was clear that applying an electric field across the LC region shifted the resonance frequency of the microstrip line

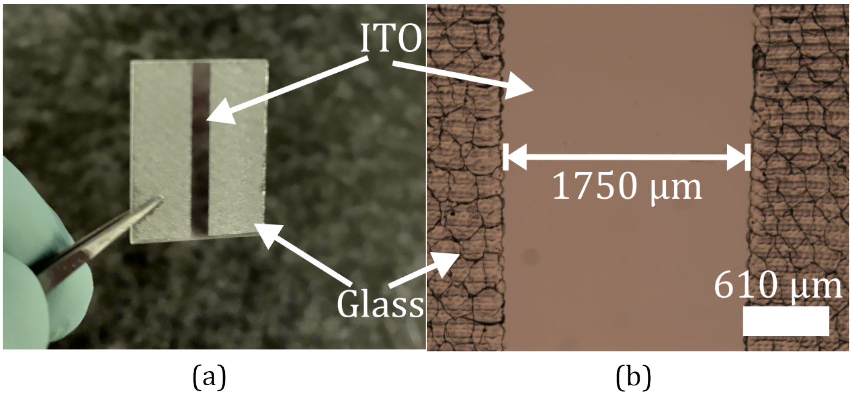

(a) (b)

Figure 5.2: Results of laser etching ITO from the glass. Image of the etched ITO (a) and viewed under a microscope at ×4 magnification in (b).

from 5.4 GHz down to 5.2 GHz, a shift of 200 MHz, which was a deviation of 3.7% from the initial resonance frequency. This downshift was congruent with the expected results since $F_r \propto 1/\sqrt{\varepsilon_{e,sub}}$, and applying a voltage across the LC layer will induce an increase in the dielectric permittivity for a positive dielectric anisotropy nematic LC mixture, such as E7.

By observing the resonant frequencies of the measured device, Equation 5.1 was then used to calculate the effective permittivity of the LC: at 0 V this equated to $\varepsilon_{e,\perp} = 3.39$, and at 100 V $\varepsilon_{e,\parallel} = 3.64$, providing a dielectric contrast between the two states of $\Delta\varepsilon_e = 0.25$. However, as outlined in Chapter 2, the effective permittivity is formed by contributions of the electric field penetrating the substrate material, here the LC, and into the region above the microstrip line, typically air. The effective permittivity of a dielectric substrate with relative permittivity ε_r and air is $1 < \varepsilon_e < \varepsilon_r$, since the permittivity of air is ≈ 1. However, in this case the LC interfaced with the glass superstrate, with a relative permittivity of 5.9 at 3.6 GHz (measured in Chapter 3). Hence, it was likely that the effective permittivity was higher than the relative permittivity of the LC i.e., $\varepsilon_{r,sub} < \varepsilon_{e,sub} < \varepsilon_{r,sup}$. Another consideration was that the dielectric anisotropy between the two states (at 0 V and 100 V) was reduced due to the LC layer thickness being as large as 300 μm, thereby reducing the integrity of the surface alignment through the bulk of the LC. The 300 μm thickness was needed in order to accommodate the feed from the SMA connector into the microstrip line device, which was 250 μm.

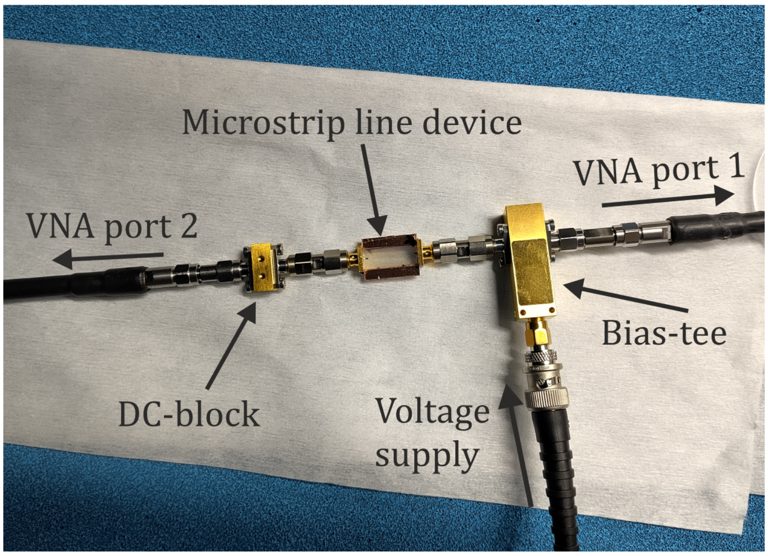

Figure 5.3: Measurement configuration of the S-parameters for the microstrip line devices presented herein, with each component labelled.

Attempts to calculate the relative permittivity from the measured effective values, using the closed form expressions for filling fraction in Chapter 2 Equation 2.29, or the effective permittivity also in Chapter 2 in Equation 2.28 did not yield results that were reasonable when compared with similar works, such as those detailed in a comprehensive review of LC dielectric properties at RF in [70]. For example, Equation 2.29 yielded results 163% greater those found through the method described below, and Equation 2.28 gave values 153% greater. This was likely due to the assumption in both of these equations that the effective permittivity is a combination of the substrate (i.e., the nematic LC) and air, whereas in this case it was a combination of the substrate and the glass superstrate. Hence, the relative permittivities were estimated using CST Studio simulations to model the transparent microstrip line device.

A range of values for $\varepsilon_{r,\perp}$ and $\varepsilon_{r,\|}$, based on previously reported works, were input to the CST simulations and assessed, then optimised to find simulated results that matched the measurements. The resulting resonant frequencies are presented alongside the measurements in Figure 5.4. The simulated resonant frequencies were found to be congruent with the measurements to within 2%, at both the 0 V and 100 V measurements. This led to the estimated relative permittivity values of $\varepsilon_{r,\perp} = 2.9$ and $\varepsilon_{r,\|} = 3.2$, at 0 V and 100 V, respectively, and a dielectric anisotropy of $\Delta\varepsilon_r = 0.36$ between the two states.

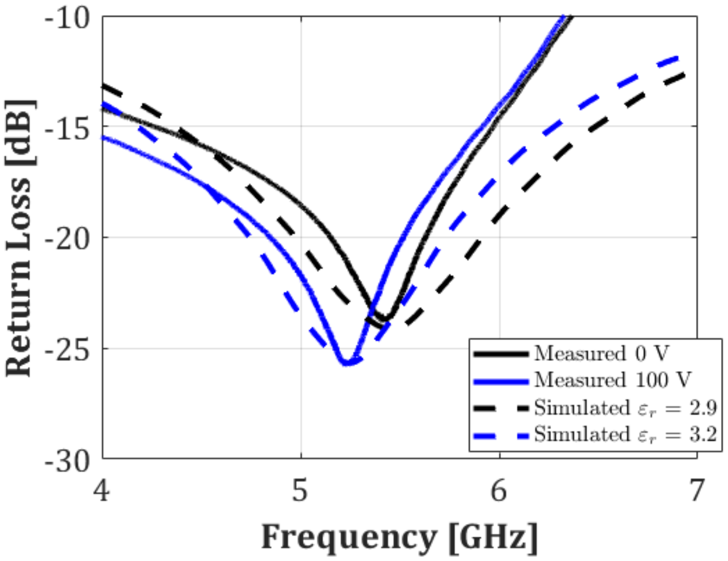

Figure 5.4: Measured and simulated resonant frequency for the transparent V1 device, with and without a voltage applied. Conducted at a temperature of 20°C.

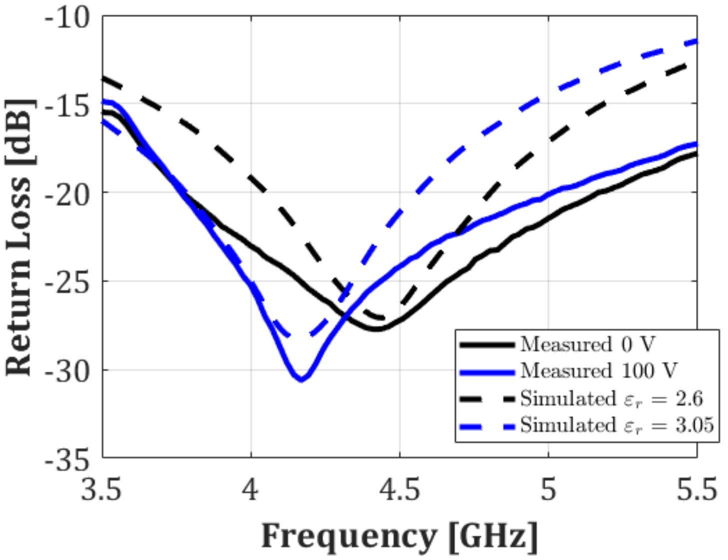

Figure 5.5: Measured and simulated resonant frequency for the transparent V2 device, with and without a voltage applied. Conducted at a temperature of 20°C.

It should be noted that the values estimated here for $\varepsilon_{r,\perp}$ and $\varepsilon_{r,\parallel}$ were not strictly $\varepsilon_{r,\perp}$ and $\varepsilon_{r,\parallel}$. Because of the large LC layer thickness, the LC director was not ideally aligned with the pre-tilt angle in the case of the 0 V measurement due to the effects of thermal fluctuations through the LC bulk. For the 100 V measurement, the respective E-field strength was not sufficient for fully align the LC director parallel with the applied field. In Section 5.2 the effects of large LC layers are characterised and discussed further.

The material losses, $\tan\delta_{\perp}$ and $\tan\delta_{||}$, for the 0 V and 100 V measurements, respectively, were estimated by $\tan\delta = 1/Q$, where Q is the Q-factor of the resonance. Calculating the Q-factors for the resonance frequencies at 5.43 GHz and 5.2 GHz gave material losses as $\tan\delta_{\perp} = 0.072$ and $\tan\delta_{||} = 0.087$, respectively. These values were not unreasonable but somewhat higher than those reported in [70]. This could be due to the material losses of the glass superstrate, and ohmic losses of the ITO conductor contributing to the measured material losses. The microstrip line impedance, Z_0, detailed in Table 5.1 could also reduce the Q-factor due to a mismatch with the 50 Ω coaxial cables that connect to the VNA.

A second transparent microstrip line device was fabricated using the transparent V2 parameters detailed in Table 5.1. The difference between the V1 and V2 devices was only in the resonant strip length, L_s, which produced the two different resonant frequencies of 5 GHz and 4 GHz, respectively. The measurement and simulation results for the transparent V2 device are depicted in **Figure 5.5**. Again, there was a high-degree of agreement between the measured and simulated values, with results accurate to within 5%. The effective permittivity values, calculated directly from the measured S-parameters were $\varepsilon_{e,\perp} = 2.9$ and $\varepsilon_{e,||} = 3.23$, at 0 V and 100 V, respectively. The same procedure for estimating the relative permittivity and material losses was used for the Transparent V2 device, with the results detailed in **Table 5.2**. As in the previous measurement, the estimated values for $\varepsilon_{r,\perp}$ and $\varepsilon_{r,||}$ did not correspond to the ideally aligned states.

A third device was constructed and simulated, using the parameters for the FR-4 V1 in Table 5.1, from copper-clad FR-4 in order to compare the results with the ITO-coated glass devices. This device was fabricated using the same processing steps as the Transparent V1 and V2 devices: the copper clad FR-4 device was used as a benchmark to compare the method of characterising the LC dielectric permittivity with the ITO-coated glass devices with traditional PCB materials. The FR-4 device exhibited three modes of resonance, with the second order resonance frequencies exhibiting the most prominent results, displayed in **Figure 5.6**.

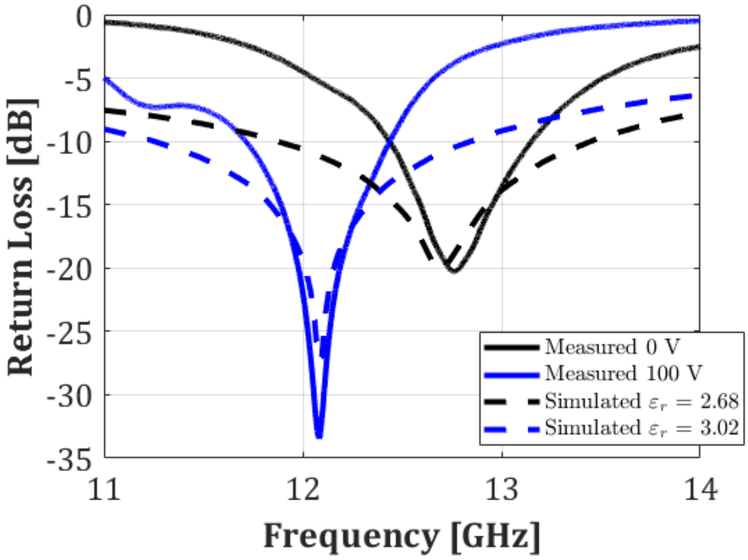

Figure 5.6: Measured and simulated second order resonant frequency for the FR-4 V1 device, with and without a voltage applied. Conducted at a temperature of 20°C.

For the purposes of comparison, values extracted for the LC dielectric permittivities, losses, and resonant frequencies are presented in Table 5.2 for the two transparent devices and the FR-4/copper device presented here, along with values reported from other published works. As the FR-4/copper device displayed high-quality resonance peaks at multiple modes, these results have also been included in Table 5.2.

The measurement results for both of the transparent (ITO-coated glass) devices provided effective permittivity values that, when used to estimate the values of relative permittivity using closed-form equations (e.g., Equations 2.28 and 2.29) were noticeably higher than relative permittivity values estimated through simulations. An average increase in the relative permittivities of $\approx 15\%$ between the closed-form equations and simulation/measurement results was attributed to the glass superstrates. Higher $\tan\delta$ losses were attributed to the combination of the glass material losses and ohmic losses from the ITO. The results for the FR-4/copper device revealed that the effective permittivity was also slightly higher than predicted by the closed-form equations, with an increase of $\approx 6.5\%$ on average. The increase here was less than with the glass substrates, likely because the relative permittivity of the FR-4 superstrate was lower than the glass superstrate.

Table 5.2: Measured properties for the nematic LC mixture, E7, using both transparent (ITO-coated) and FR-4 microstrip line devices (this work), and values reported from other other published works.

Device	$\varepsilon_{r,\perp}$	$\varepsilon_{r,\parallel}$	$\Delta\varepsilon_r$	$\tan\delta_\perp$	$\tan\delta_\parallel$	$F_{r,\perp}$ [GHz]	$F_{r,\parallel}$ [GHz]
Transparent V1	2.9	3.2	0.36	0.072	0.087	5.4	5.23
Transparent V2	2.6	3.05	0.38	0.12	0.053	4.43	4.17
FR-4 V1 (1st order)	2.16	2.46	0.3	0.032	0.034	6.37	6.1
FR-4 V1 (2nd order)	2.68	3.02	0.34	0.019	0.034	12.7	12
FR-4 V1 (3rd order)	2.63	3.1	0.35	0.017	0.014	18.76	17.46
[19]	2.18	2.62	0.44	0.039	0.012	4.32	4.06
[87]	2.87	3.11	0.24	0.05	0.02	3	3

Encouragingly, the relative permittivity results for the two transparent devices using the combination of measurements and simulations, were congruent with other published works that characterised the dielectric properties of the nematic LC mixture E7 at similar frequencies, for example, those detailed in Table 5.2. For the FR-4 microstrip line device fabricated and characterised herein, there is excellent agreement with previous works that have measured the properties of E7 at each of the three resonance modes as detailed in Table 5.2. Combined, these results provide a high-level of confidence that the microstrip line design employed here, adapted to allow the nematic LC to be incorporated between the microstrip line and groundplane, and the method of estimating the dielectric permittivity through simulations, yields reliable results that compare well with reported values.

5.2 LC Director Simulations for RF Devices

5.2.1 Thick Liquid Crystal Layers

In this Section, the effect of thick LC layers will be considered. The approach will be to consider only the effects of these thick LC layers on the LC director, and the consequences this might have for the design and operation of RF devices in general, i.e., not specific to any particular device.

LC dielectric permittivity measurements, and applications thereof, in the RF regime require that the thickness of the LC layer is one or two orders of magnitude greater than is typically required for traditional LC display devices. However, historically, studies of LC materials and devices at microwave frequencies reported in the literature often make assumptions on the LC director that, in general, over-simplify the behaviour and do not provide the full picture [19], [53], [86]. These assumptions are:

1. the surface anchoring effects of the LC alignment layer continue through the bulk of the LC;
2. the voltage applied to fully reorientate the LC director across a 10 μm LC layer is sufficient to fully reorientate the LC director for an LC layer > 100 μm thick; and
3. there are no thermal fluctuations in the LC.

While points one and two are certainly true for an LC layer on the order of 10 μm, it is not the case for LC layers > 100 μm, for example. Regarding the third point, thermal fluctuations can be ignored in devices that are ≈ 10 μm as the elastic interactions dominate. It is important to note that there is no defined point at which these assumptions cease to be accurate, but that they become less valid with increasing thickness of the LC layer.

The cause of these effects is thermal fluctuations that act on individual molecules in the LC layer: over short distances, e.g., ≈ 10 μm, elastic interactions dominate over thermal fluctuations, stabilising the director field. Whereas over larger scales, e.g., $\geq$ 100 μm, thermal fluctuations can accumulate and lead to significant distortions of the director field, in particular for materials with weak elastic constants. The effect of this for LC-based RF devices is that as the device thickness increases, the achievable dielectric anisotropy, $\Delta\varepsilon_r$ reduces due to the inability of the surface alignment to maintain uniform alignment through the device, i.e., the LC director is not parallel to the plane of the device, and, if the applied voltage is not sufficient to fully align the LC director, then it is not reoriented parallel to the applied electric field.

5.2.2 Liquid Crystal Director Simulation Parameters

It is not only the Frank-Oseen free energy, as described in Equation 2.9, but also external influences that affect the director distribution: e.g., surface interaction, external fields and thermal fluctuations all contribute to the resulting director profile. To consider these external effects, a model of the LC director was developed in MATLAB using an iterative approach to minimise the total free energy density in the LC, u_T. Equations 2.9 and 2.14, are repeated here for convenience

$$u_T = \underbrace{\frac{K}{2}\left[(\nabla \cdot \mathbf{n})^2 + (\nabla \times \mathbf{n})^2\right]}_{u_F} - \underbrace{\frac{1}{2}(\mathbf{D} \cdot \mathbf{E})}_{u_e}$$

where u_F and u_e are the free-energy density and dielectric-energy density, respectively. u_T was integrated over the volume of the LC layer to produce the total energy in the system, U, according to

$$U = \int_v u_T \; dv = \int_0^{H_{LC}} u_T(z, \theta, \partial/\partial x) \; dz \tag{5.2}$$

where H_{LC} is the thickness of the LC layer. The energy terms were restricted to be a function of position, z, angle, θ, and gradient, $\partial\theta/\partial z$, and the angle of the director was simplified to only rotate in the zx-plane, although the position of any molecule was a function of the xyz-plane i.e., $\theta(x, y, z)$. The Euler-Lagrange equation was applied to the total energy according to

$$F = \frac{\partial U}{\partial \theta} - \frac{\partial}{\partial z}\left(\frac{\partial u}{\partial\left(\frac{\partial \theta}{\partial z}\right)}\right) \tag{5.3}$$

which enabled the director distribution to be determined by minimising the result from the Euler-Lagrange equation, achieved by

$$F = F_F + F_E = \underbrace{K\frac{\partial^2 \theta}{\partial z^2}}_{\text{torque from } u_F} + \underbrace{\frac{\Delta\varepsilon_r \varepsilon_0}{2}\frac{V^2}{H_{LC}^2}\sin 2\theta = 0}_{\text{torque from } u_e} \tag{5.4}$$

Many LC director models assume the minimisation of elastic and dielectric energy will suitably capture the behaviour of the LC; however, here a more encompassing model was developed to account for thermal fluctuations on LC molecules that cause deviations

Table 5.3: Parameters used in the LC director simulation for the nematic LC E7.

L_z [μm]	L_x [mm]	L_y [mm]	T_s [rad]	$\Delta\varepsilon_r$	K [pN]
10, 100, 300	1.2	1.2	0.07	11	18

in angle from the surface alignment layers, and the electric field. Hence, a thermal noise term, N, was subsequently added to the LC director model to account for these effects and Equation 5.4 was then updated to

$$F = F_F + F_E + N \tag{5.5}$$

with N representing random fluctuations in the $xyz-$plane on any particular LC molecule within the structure. This was implemented by introducing a random rotation in the range $[-\pi, \pi]$ weighted by a scalar value to represent random thermal perturbations. The value of the scalar weight was determined by observing the resulting effect on the LC director. For example, if the LC director in the 10 μm LC layer was not aligned with the pre-tilt angle in the 0 V simulation, that is, there were observable perturbations of the LC molecules, this was an indicator the scalar weight (and therefore, the thermal noise effect) was too large, whereas if the LC director in the 300 μm thick LC layer was ideally aligned with the pre-tilt angle at 0 V, this was an indicator that the weight (or thermal noise effect) was too low. Hence, empirical results through repeated simulations produced a scalar weight from 0.3 - 0.8, with the value at the upper end of this range for thicker LC layers, to account for the cumulative effect of the thermal noise. **Table 5.3** includes the parameters used in the simulation, where; L_z, L_x, and L_y, refer to the dimension of the LC in the z, x and y-directions, respectively; T_s is the pre-tilt angle; and $\Delta\varepsilon_r$ and K are the low-frequency dielectric anisotropy and the elasticity coefficient for the nematic LC mixture, E7, respectively. The elasticity constant $K = K_{11}$ as only splay deformations were relevant in this simulation.

5.2.3 Liquid Crystal Director Simulation Results

The LC director profile simulation was run over three variations in LC layer thickness; 10 μm, 100 μm, and 300 μm, and for three variations in applied voltage; 0 V, 10 V,

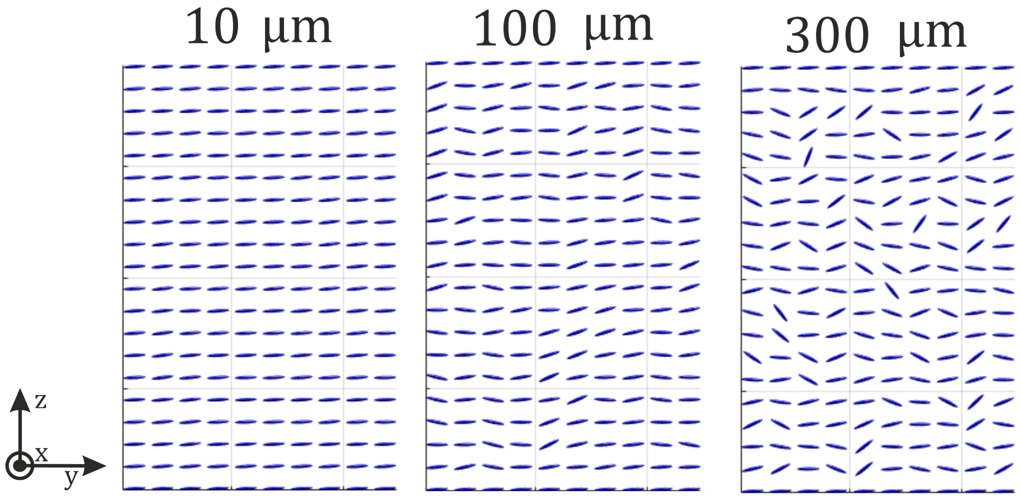

Figure 5.7: Simulations of the director profile in the yz-plane for three different LC layer thicknesses with no voltage applied.

and 100 V. The free energy minimisation term in Equation 5.5 was calculated using an iterative approach to find the minima at each node. There were 20 nodes in the z-plane and 10 nodes in the x and y planes, and the thermal noise was applied independently at each node. The results for each LC layer thickness at 0 V, that is with the F_E term in Equation 5.5 set to zero, are shown in **Figure 5.7**, where each blue oval is a node, representing the local LC director.

The results from this simulation demonstrate that the anchoring effects for the 10 μm LC layer are sufficient to continue through the entire layer, which was predicted to happen due to the elastic interactions dominating the thermal noise term with the lower layer thickness. Hence, this particular result suggests that the strength of the thermal noise used in the simulation was not too high. At 100 μm LC layer thickness some deviation away from the pre-tilt angle can be seen, and for the 300 μm case the surface alignment has exerted little effect through the bulk of the LC. These two results demonstrate an increase in the randomness of the local LC director orientation, suggesting that the strength of the thermal noise term in the experiments was not too low.

The average magnitude of the deviation from the pre-tilt angle demonstrated in Figure 5.7 was measured at each node in the z-direction, that is, an average magnitude of the angles in the xy-plane, and is plotted for the three LC layers in **Figure 5.8**. There was

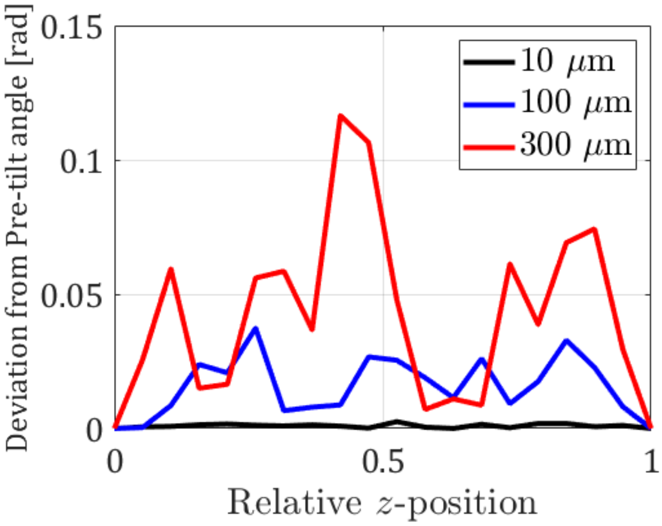

Figure 5.8: Average magnitude of the deviation of the LC director (along the z-axis) from the the pre-tilt angle of 0.07 radians at three different LC layer thicknesses, with no voltage applied.

an observable increase in the deviation from the pre-tilt angle as the LC layer thickness increased, further illustrating the thermal effects on the LC director.

In **Figure 5.9**, the simulation parameters were updated to apply 10 V across each LC layer in the z-plane. Again, the thermal fluctuations had little effect on LC director in the 10 μm LC layer, which had almost fully reoriented to match the direction of the applied E-field. This was not the case for the 100 μm and 300 μm LC layers, however. In the 300 μm layer the thermal fluctuations dominated through the LC bulk and there was little difference observed in the director profile between the 0 V and 10 V simulations.

The average deviation of the LC director for the case with 10 V applied to the LC layer, is plotted in **Figure 5.10**. Here, the deviation was taken relative to the E-field direction, which was applied in the z-direction across the LC layer. The LC director profile for the 10 μm LC layer exhibited very little deviation from the E-field, whereas the 100 μm and 300 μm LC layers exhibited increasing deviation from the E-field, as observed in Figure 5.9. The deviation from the E-field that was observed at the upper and lower limits in the 10 μm and 100 μm LC layers was due to the surface alignment pre-tilt angle.

Next, the simulation was run with an increased voltage of 100 V and the results

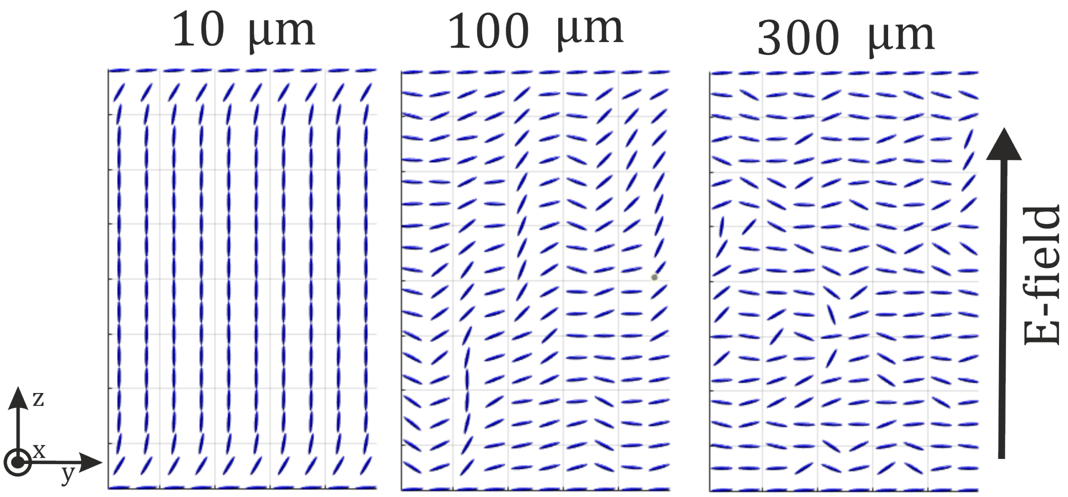

Figure 5.9: Simulations of the director profiles in the yz-plane for three different LC layers when 10 V was applied to the LC.

are presented in **Figure 5.11**. Now the LC director in the 100 μm LC layer had fully reoriented with the applied field, as had the 10 μm LC layer, whereas the director field in the 300 μm LC layer was almost fully aligned but still visibly affected by thermal fluctuations. **Figure 5.12** portrays the average deviation of the LC director from the applied electric field direction at 100 V for each case. Here, the 10 μm and 100 μm cases were almost ideally aligned, except for the pre-tilt angle. There remained some average deviation from the E-field for the 300 μm LC layer, although this was significantly reduced from 1.5 radians in the 10 V case (shown in Figure 5.10), to 0.5 radians.

The final simulation was run for the 300 μm LC layer only, with the applied voltage increased to 300 V, depicted in **Figure 5.13** with the simulated results for LC director field in (a) and the deviation from the E-field direction in (b). Here the voltage was increased such that electric field strength was equivalent to 10 V across the 10 μm LC layer and 100 V across the 100 μm layer, that is, 1 MV/m, demonstrating that the thermal fluctuations in large LC layers can be overcome with a sufficient E-field strength.

5.2.4 Comparison to Measurements

Following the LC director profile simulation, it was prudent to relate these results back to the S-parameter measurement results for the transparent V1, V2 and FR-4 devices. The LC director profile simulations suggested that for increasing LC layer thickness, the

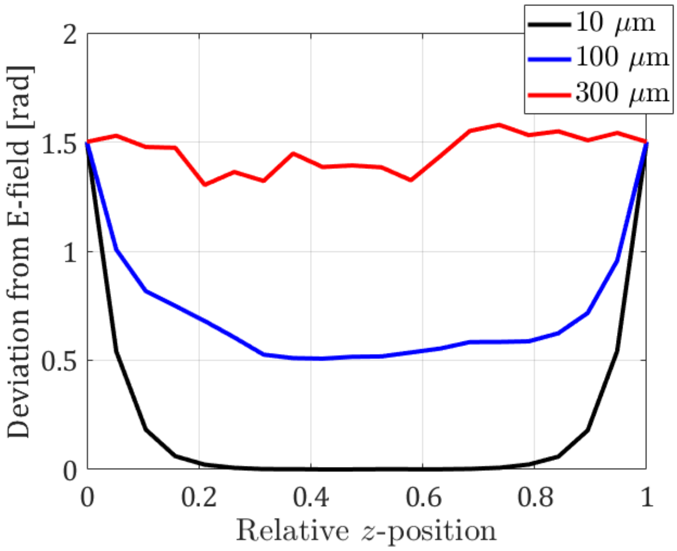

Figure 5.10: Average deviation of the LC director (along the z-axis) from the the electric field direction, with 10 V applied across each LC layer.

thermal perturbations would lead to the measured permittivity becoming an average permittivity, $\bar{\varepsilon}_r$, between the two ideal states, that is, $\varepsilon_{r,\perp} < \bar{\varepsilon}_r < \varepsilon_{r,\parallel}$. To facilitate this, the average angle of the simulated local LC director, $\bar{\theta}$, was translated to an average permittivity by calculating $\bar{\varepsilon}_r = \varepsilon_{r,\parallel} \sin^2 \bar{\theta} + \varepsilon_{r,\perp} \cos^2 \bar{\theta}$. The values for the ideally aligned states were $\varepsilon_{r,\perp} = 2.7$ and $\varepsilon_{r,\parallel} = 3.3$, selected to align with the measurements in Section 5.1. The average angle was calculated by first finding the average angle over the xy-plane at each of the 20 nodes, and then finding the average angle of those 20 nodes in the z-plane, to provide the average permittivity across the LC layer. This was computed for the 10 μm, 100 μm, and 300 μm thick LC layers, at 0 V, 10 V, 100 V and 300 V and the results are shown in **Table 5.4**.

The results in Table 5.4 indicated that the thermal fluctuations did indeed relate to a disparity between the ideal and calculated permittivity values for the thicker LC layer. For the 10 μm LC layer simulation, the difference was 0.1% from the ideal value at 0 V, and 1.8% at 100 V, this minor disparity was due to the tilt-angle in the simulation, which was maintained at 0.07 radians throughout. For the 100 μm simulation, the effective permittivities were 1.5% away from the ideal value at 0 V, and 3.6% at 10 V, however, at 100 V, the disparity matched that of the 10 μm device. Finally, for the simulation of the 300 μm thick LC layer, there was a difference of 10.4% at 0 V, 10.3% at 10 V and

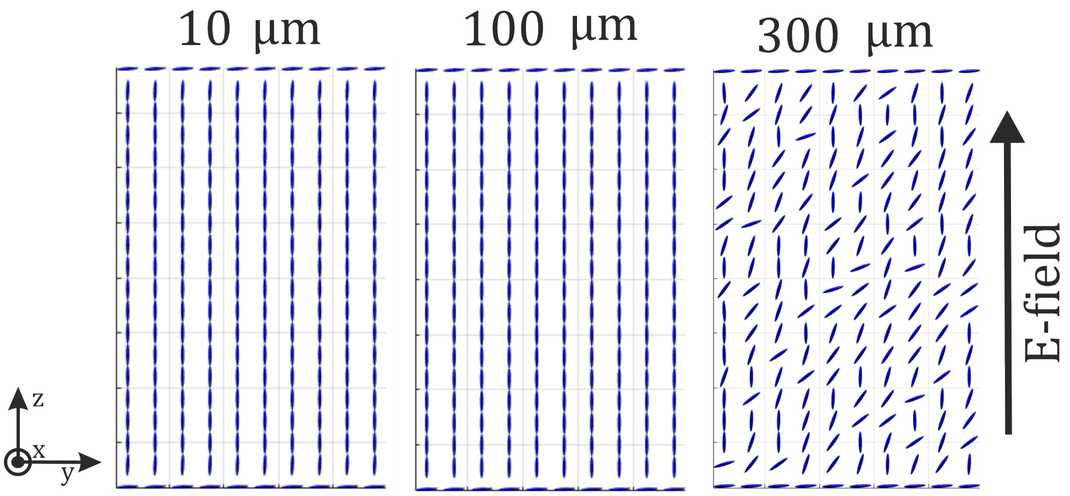

Figure 5.11: Simulation of the director profile for three different LC layers in the *zy*-plane, with 100 V applied.

Table 5.4: Calculated average permittivities for the simulated LC layers. Change from the ideal value in parenthesis.

Average permittivity	10 μm	100 μm	300 μm
$\bar{\varepsilon}_r$, 0 V	2.703 (+0.1%)	2.74 (+0.15%)	2.93 (+10.4%)
$\bar{\varepsilon}_r$, 10 V	3.22 (-1.2%)	3.18 (-3.6%)	2.96 (-10.3%)
$\bar{\varepsilon}_r$, 100 V	3.24 (-1.8%)	3.24 (-1.8%)	3.23 (-2.12%)
$\bar{\varepsilon}_r$, 300 V	3.24 (-1.8%)	3.24 (-1.8%)	3.24 (-1.8%)

2.12% at 100 V. At 300 V, the 300 μm layer matched the 10 μm and 100 μm results.

Hence, for LC devices that are $\approx$ 100 μm, the effect on the achievable dielectric permittivity is minor and can in part be mitigated by applying a larger voltage across the device. However, for LC layers $\geq$ 100 μm, theses results suggest there is a significant disparity between the achievable and ideal permittivities. Again, this can be in part addressed by applying a larger voltage, with 100 V seemingly sufficient, and little gained by applying 300 V.

Comparing the results for the Transparent V1 device and the average permittivities in Table 5.4 suggests that the measured value for the device at 0 V of $\bar{\varepsilon}_r = 2.9$ would relate to an ideal value of $\varepsilon_\perp = 2.7$ and measured at 100 V of $\bar{\varepsilon}_r = 3.2$ would relate to to an ideal value of $\varepsilon_\| = 3.3$. Applying the same process to the Transparent V2 device

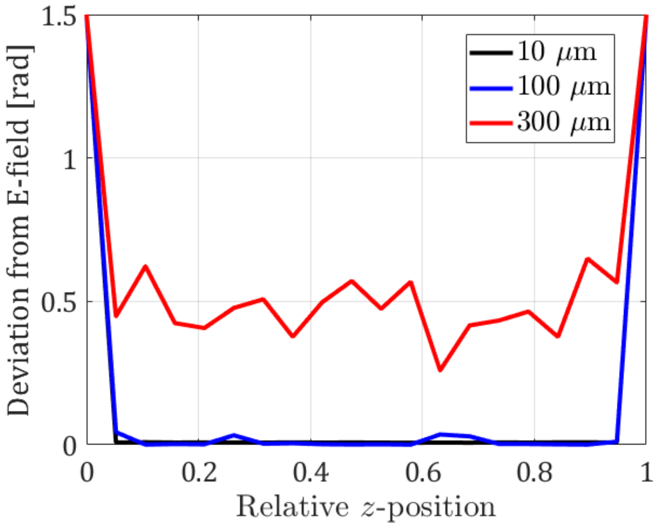

Figure 5.12: Average deviation (along the z-axis) of the LC director from the the electric field direction, with 100 V applied each LC layer, at three different LC layer thicknesses.

suggested that the ideal values were $\varepsilon_\perp = 2.42$ from $\bar{\varepsilon}_r = 2.6$ at 0 V, and $\varepsilon_\parallel = 3$ from $\bar{\varepsilon}_r = 3.05$ at 100 V.

5.3 Conclusions

This Chapter has been concerned with the characterisation of the dielectric properties of a nematic LC in the RF band in order to underpin the studies presented later in this Thesis. Firstly, the design, fabrication, measurement and simulation of an optically-transparent microstrip line device tailored to incorporate, and estimate the dielectric permittivity of a nematic LC at 5 GHz, was presented. EM simulations of these devices suggested that the measurements were accurate to within 5%. This device was also employed to observe the effects of effective permittivity, dielectric anisotropy and material losses and to assess the differences observed when using ITO-coated glass to copper-clad FR-4.

Accordingly, an FR-4 microstrip line device was constructed, with the same parameters as the ITO-coated glass devices, to compare the results. The main findings suggest that the optically-transparent device can be used, in conjunction with full-wave simulations, to reliably estimate the relative permittivity of a nematic LC. Furthermore, the effective permittivity, which governs the operational frequency of resonant devices,

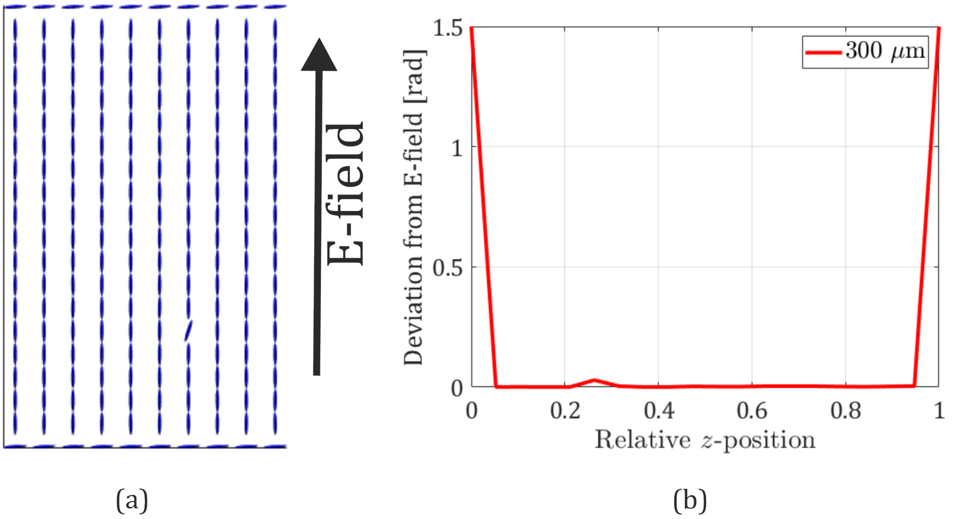

Figure 5.13: Average deviation of the LC director (along the z-axis) from the the E-field with 300 V applied over the 300 μm LC layer (a), and LC director simulation (b).

was found to be higher in ITO-coated glass devices, compared with copper-clad FR-4 of similar dimensions, likely due to the higher relative permittivity of the glass.

Following this, an updated model of the LC director was developed to understand the behaviour of nematic LCs that are employed in LC layers $\geq$ 100 μm. Simulations carried out using this model at 10 μm, 100 μm, and 300 μm demonstrate that weakening of the surface anchoring effects through the bulk of the LC material and deviations of the LC director from an applied E-field, are increase when the LC layer thickness is increased. While the latter concern can be addressed by increasing the applied voltage, there remains further work on how to address the reduction in surface anchoring. The LC director profile simulations indicate that there is no defined LC layer thickness at which elastic deformations overcome the thermal fluctuations, but it can be stated that for LC layers on the order of 10 μm elastic deformations dominate and for LC layers $\geq$ 100 μm, thermal fluctuations have an observable effect.

The combined results from the LC director profile simulations and LC relative permittivity measurements suggest that when employing devices featuring large LC layers, it is unlikely that the permittivity is measured with the LC director ideally aligned in either the parallel or perpendicular configuration. Instead, due to the effect of thermal fluctuations that propagate through the LC bulk, the ideal values for $\varepsilon_{r,\perp}$ and $\varepsilon_{r,||}$ cannot be reliably measured. Nonetheless, the combination of improvements in the updated LC director model can in turn be used to produce more accurate estimates of the relative dielectric permittivity in LC devices that require a layer thickness ≥ 100 μm.

In the following Chapter, a reconfigurable optically-transparent antenna is designed: this microstrip patch antenna is formed from ITO-coated glass with the nematic LC E7 employed to affect the operational frequency of the antenna. Hence, the work conducted here in characterising the effect that the LC/glass construction has on the effective permittivity, and therefore, the behaviour of the antenna, will be used to improve the design procedure. Furthermore, the results indicated by the LC director profile simulations will be utilised when considering the thickness of the LC layer employed, and the required voltage to extract the maximum frequency-shift performance from the antenna.

Chapter 6

Reconfigurable Optically-Transparent Antenna

In this Chapter, a proof of concept for a new class of optically-transparent antenna that is frequency reconfigurable via a nematic liquid crystal (LC) is presented. Optically-transparent antennas have garnered much attention in the literature due to their potential to have a transformative impact on the wireless communications sector: antennas are the largest physical constituent of a radio frequency (RF) transmitter/receiver and optical transparency unlocks previously unfeasible locations to place the antenna, such as windows in buildings and automotive vehicles as well as smartphone and laptop displays. Typical methods for antenna reconfiguration, for example, switching circuits, are unsuitable for use in transparent antennas due to their opaqueness. Hence, the incorporation of a nematic LC into an RF antenna, using the radiating patch and groundplane to apply an electric field across the LC layer, would be of significant interest. While there are a reasonable number of articles in the literature that address the fabrication of optically-transparent microstrip antennas, and there exists a myriad of published works that consider reconfigurable antennas, with several including nematic LCs [88], [89], there are currently none that study both reconfigurable and optically-transparent features.

In Chapter 2, the closed-form design equations for a microstrip patch antenna were described, and will be applied to design the optically-transparent antenna featured in this Chapter. The indium tin oxide (ITO) etching procedure that was developed in Chapter 3 will be employed in patterning the antenna geometry according to those closed-form equations. In the preceding Chapter on the characterisation of LC dielectric properties for RF devices, the effect on the resonant frequency elicited from constructing the optically-transparent device using ITO-coated glass superstrates, will be used to inform this design.

For the first time, we report a nematic LC deposited directly onto the radiating patch of the antenna via drop-on-demand (DoD) inkjet printing, to precisely control the coverage area and height/volume occupied by the LC, greatly reducing the amount of wasted LC, compared with infiltration methods. We employ an electrically conductive material that is transparent to visible wavelengths, ITO, due to its widespread availability, ease of fabrication and long-standing use in LC display devices. The aim here is present proof-of-concept for a reconfigurable optically-transparent antenna, and not to optimise erstwhile deficiencies present in non-reconfigurable transparent antennas. Specifically, this Chapter will consider; fabrication methodology, optimisation of the reconfigurability and optical transmittance, and characterisation of the antenna performance. The work presented in this chapter has been submitted for publication, and a patent has been filed for the methodology of fabricating the device.

The main contributions of this work are as follows:

- a DoD inkjet printing process is developed from printing droplets to form a contiguous patch of a desired length, width and height;
- A nematic LC is incorporated into an RF antenna using this DoD inkjet printing process; and
- frequency reconfiguration of the optically-transparent antenna is achieved by using an electric field to reorientate the LC director.

The remainder of this Chapter is organised as follows: In Section 6.1, the experimental methods required for this work - including the antenna's geometry and DoD inkjet printing techniques and a summary of the fabrication steps - are outlined. Results for the LC printing and ITO patterning are presented in Section 6.2, and characterisation of the antenna, including optical transmittance, reconfigurability and radiation pattern are presented in Section 6.3. Finally, this Chapter is concluded in Section 6.4.

6.1 Antenna Fabrication Methodology

6.1.1 Antenna Design

A patch antenna was selected for its simple design parameters and the ease of implementation with ITO-coated glass. The frequency of operation was selected to fit within the future mobile communications bands i.e., 6 GHz - 30 GHz [90], and by constraints of the materials and fabrication process. Once a desired operational frequency and substrate material were identified, these values were input to a MATLAB programme, developed in this work, which employed the use of patch antenna design methods detailed in [25], and then output the relevant antenna parameters. The increase in effective permittivity of the antenna substrate when using the combination of glass superstrate (containing the ITO-based antenna)/LC substrate/glass superstrate (containing the ITO groundplane) that was evaluated in Chapter 5 was also used to guide the design parameters. The geometry of the antenna was identical to that described in Chapter 3, repeated here for convenience: radiating patch width and length, W_p and L_p, respectively; microstrip line feed width, length, and impedance, W_f, L_f and Z_f, respectively; and impedance transformer width and length, W_t and L_t, respectively, are defined illustratively in **Figure 6.1** with values detailed in **Table 6.1**. A microstrip feed to connect the radiating patch of the antenna to the signal input was chosen as it was straightforward to fabricate and impedance match with the 50 Ω input to the antenna.

The next step was to create a CST Studio Suite simulation based on the patch antenna parameters to confirm the antenna operational frequency, efficiency, and impedance of the feed network. Additional parameters required for the simulation are detailed in Table 6.1, including the width, length, height and permittivity of the ITO-coated glass substrate and superstrate, W_{sup}, L_{sup}, H_{sup} and $\varepsilon_{r,sup}$, respectively, and the thickness and measured conductivity of the ITO coating, H_{ITO} and σ_{ITO}, respectively, were taken from the supplier datasheet [91]. The values for $\varepsilon_{r,sup}$ and σ_{ITO} were also measured experimentally. The LC thickness H_{LC} was selected as a design choice to optimise the trade-off between optical transparency and frequency reconfigurability, also accounting for the effect of thick LC layers on the surface anchoring detailed in Chapter 5. Once the geometry of the antenna and feed was confirmed, the ITO was patterned into the

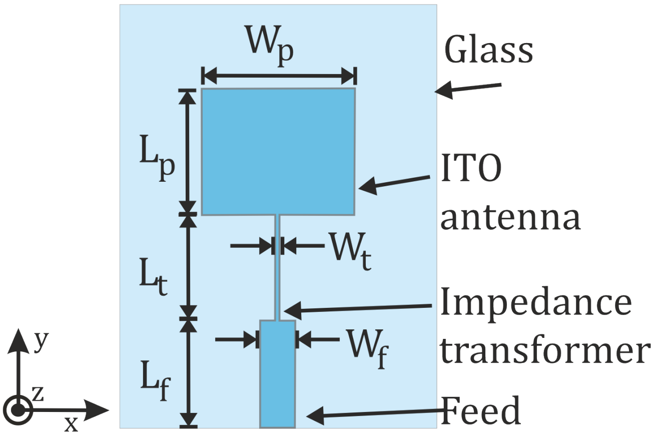

Figure 6.1: Parameters for the final patch design, with values detailed in Table 6.1.

Table 6.1: Antenna, substrate and LC parameters.

W_p [mm]	L_p [mm]	W_t [mm]	L_t [mm]	W_f [mm]	L_f [mm]	Z_f [Ω]	W_{sup} [mm]	L_{sup} [mm]
7.5	6	0.22	5	1.66	5	48	15	20
H_{sup} [mm]	$\varepsilon_{r,glass}$	H_{LC} [mm]	H_{ITO} [nm]	σ_{ITO} [MS/m]	$\varepsilon_{r,\perp}$	$\varepsilon_{r,\parallel}$	$\tan\delta_\perp$	$\tan\delta_\parallel$
1.1	5.9	0.1	100	0.667[a]	2.53[b]	2.98[b]	0.002[b]	0.009[b]

[a] Measured in this work [b] For E7 measured at 19 GHz [70]

desired structure using the photolithography and chemical etching processes as outlined in Chapter 3.

6.1.2 Drop-on-Demand Printing of Nematic Liquid Crystals

The next step in fabricating the reconfigurable optically-transparent patch antenna was to incorporate the LC into the antenna construction. This is typically achieved by infiltrating the LC between two sandwiched substrates. Infiltration, however, cannot offer precise control over the coverage of the LC within the antenna. Instead, in this work, we chose to use DoD inkjet printing to add the LC to the antenna: this allowed for accurate deposition of LC droplets onto the area where the LC is most effective; that is, precisely between the radiating patch of the antenna and the groundplane. DoD printing of the LC also reduced wastage of the LC as only the required material is used, thus lowering the cost. By considering the electric field distribution between the antenna patch and

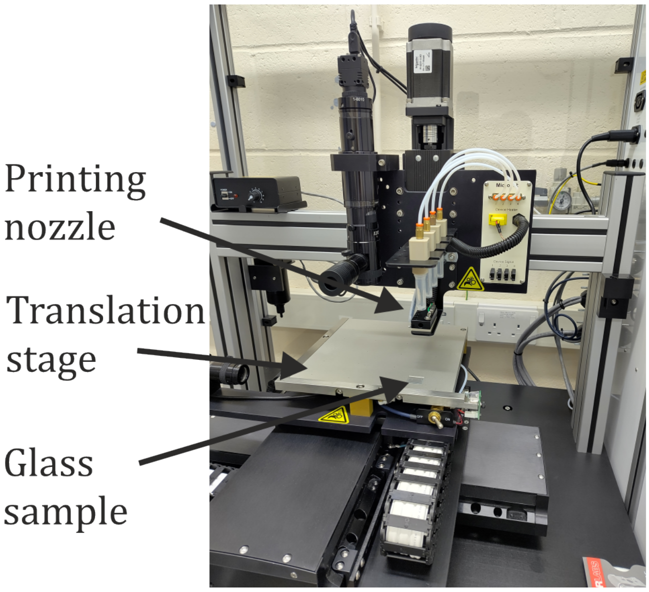

Figure 6.2: MicroFab inkjet printer setup.

groundplane, further reduction of the LC volume was feasible by only depositing droplets where the field is strongest; for example, at the edges of the patch where the fringing fields appear. This remains an option for future designs, in particular, for larger patches or antenna arrays that would require a significant volume of LC material.

The nematic LC mixture, E7, with measured parameters detailed in Table 6.1, was printed using a Jetlab II MicroFab inkjet printer to form a grid of droplets covering the entire area of the ITO-patterned radiating patch, which was previously coated with a homeotropic alignment layer. The Jetlab II system prints multiple individual drops, each with a volume of ≈ 150 pL, at the same coordinates, to build the height of a single droplet. The aim was to form a droplet height of 50 μm - 100 μm. To achieve this, the number of drops at each position in the grid was increased from 20 drops to 100 drops, in 20 drop increments, followed by further optimisation to find the number of drops that maximised the height of the LC droplet. The most favourable results were from 35 drops printed at each position: a larger number of drops would increase the diameter of the droplet, and not produce any increase in the height. As the LC was employed to induce a change in the antenna's frequency, it was necessary to print the droplets such that when the superstrate was added, they coalesced to form a contiguous film over the area of the antenna patch. **Figure 6.2** illustrates the DoD inkjet printing system with an

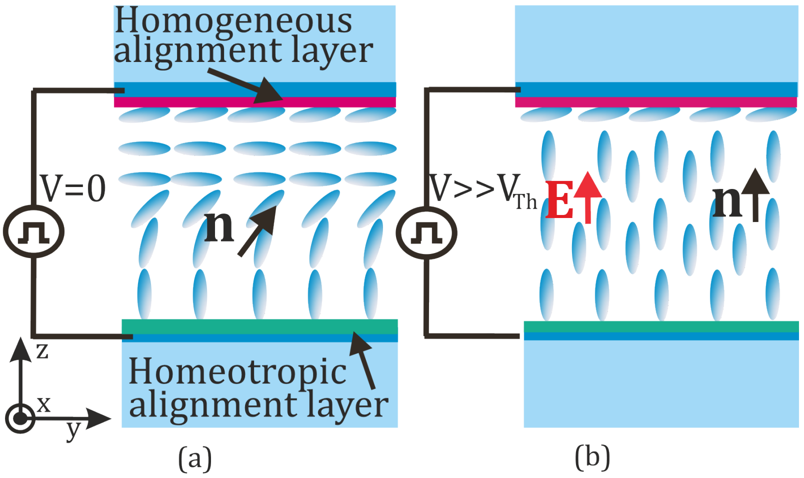

Figure 6.3: Illustration of an LC device featuring a hybrid alignment layer (a homeotropic layer on the inner surface of the substrate and a homogeneous layer on the inner surface of the superstrate). (a) without a voltage applied, (b) with a voltage applied.

ITO-coated glass substrate on the translation stage.

The MicroFab printer featured a piezoelectric-driven printhead comprising a 80 μm diameter nozzle, and a back-pressure pneumatic system employed to control the liquid meniscus. The printhead was driven by a waveform comprising a 100 V_{p-p}, 500 Hz square wave with a rise and fall time of 5 μs and 8 μs, respectively, and a dwell and echo time of of 13 μs and 8 μs, respectively. Drops were printed to form a grid of dimensions $L_p \times W_p$, with a centre-to-centre droplet separation of 0.5 mm in the x and y-planes. The printhead was maintained at a temperature of 62°C with the substrate at a temperature of 20°C.

A homeotropic alignment layer was required to print spherical-cap droplets that facilitate the numerous drops needed to increase the height. In contrast, using a homogeneous (planar) alignment layer typically caused the droplets to wet the substrate, reducing control over the thickness and coverage of the LC layer. However, applying a voltage across an LC layer with a fully homeotropic alignment would not induce any reorientation of the LC director when employing a positive dielectric anisotropy mixture such as E7. To address this, a homogeneous alignment layer was applied to the inner surface of the superstrate, forming a hybrid alignment, as illustrated in **Figure 6.3**.

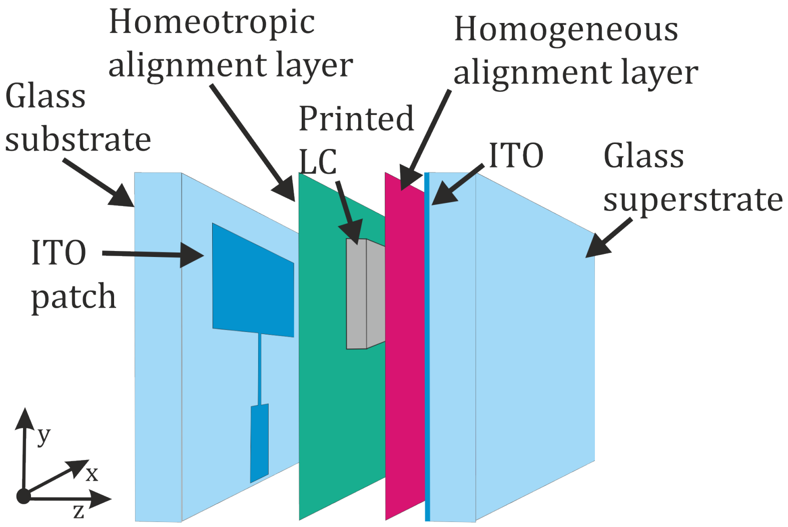

Figure 6.4: Exploded view of the constructed optically transparent LC antenna. For clarity, the adhesive spacers are not shown here.

6.1.3 Fabrication Scheme

The fabrication of a reconfigurable optically-transparent patch antenna was conducted in several phases, including; designing the antenna and feed structure, patterning the transparent electrode and inkjet printing a nematic LC. Each of these stages was subject to particular difficulties associated in combining the traditional antenna design and LC device fabrication processes, into a single artefact. An exploded view of the constructed antenna, including the individual layers, is depicted in **Figure 6.4**, and the step-by-step process of fabricating the full device is illustrated in **Figure 6.5**.

6.2 Fabrication Results

6.2.1 ITO Etching

The results of the photolithography and etching processes, described in Chapter 3 and in Figure 6.5(a)-(b), are repeated in **Figure 6.6**, which includes a photograph of the glass substrate with the unwanted ITO removed to form the antenna profile (a), and a microscope image under 4× magnification of the transition from the antenna feed to impedance transformer (b). A discussion of these results is related in Chapter 3. For convenience, a summary of this discussion will follow: the chemical etching process used

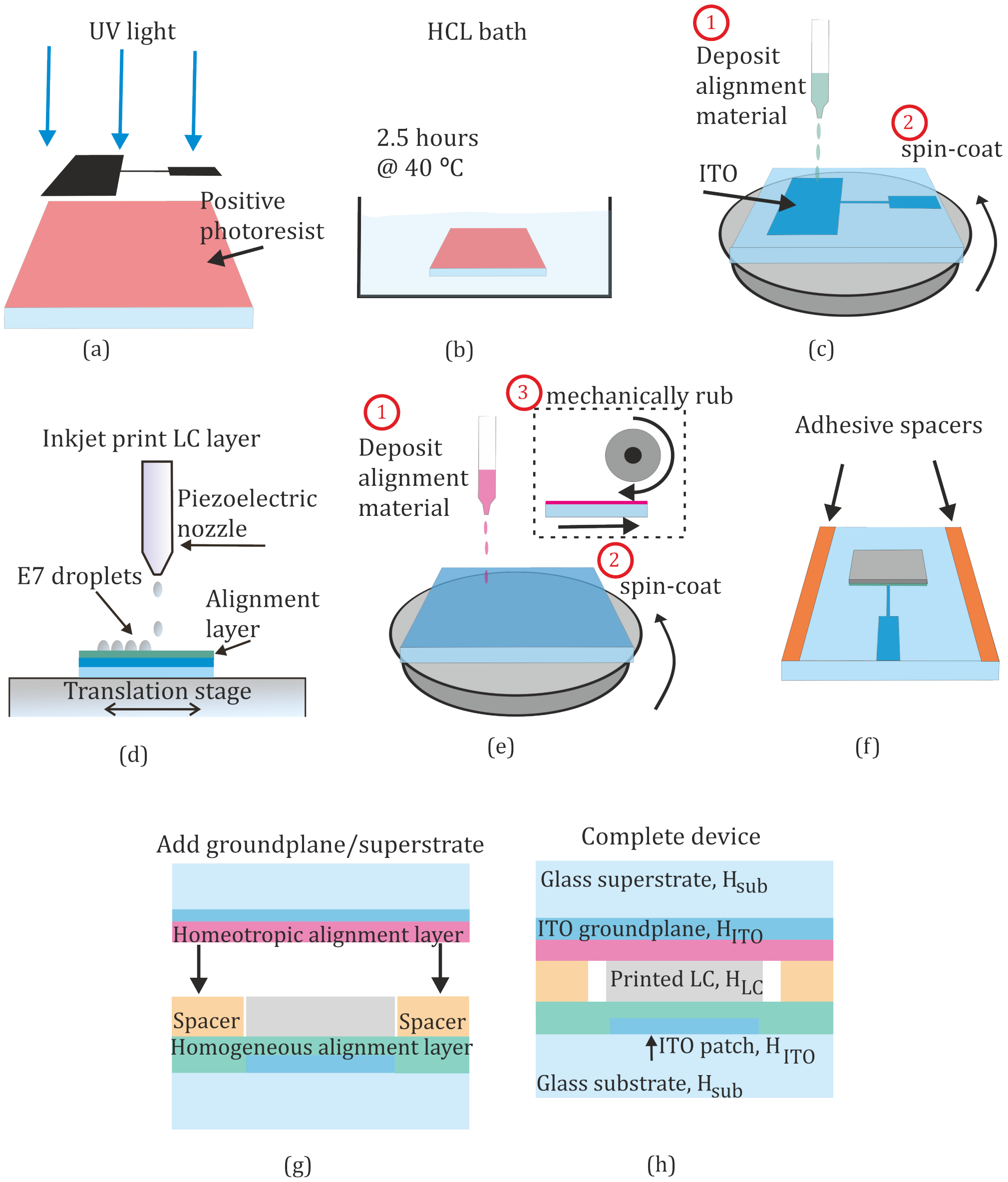

(a) (b) (c)

(d) (e) (f)

(g) (h)

Figure 6.5: Steps for fabricating the transparent antenna. (a) positive photoresist material was spin-coated onto an ITO-coated glass substrate. A photomask formed of the antenna's geometry was attached and then subjected to UV light. (b) the substrate was dipped in Microposit developer for 1 minute and then a HCI bath for 2.5 hours at 40°C, (c) the homeotropic alignment material was deposited onto the substrate and spin-coated. (d) the nematic LC (E7) was inkjet printed directly onto the antenna patch. (e) a second ITO-coated glass, the groundplane or 'superstrate', had a homogeneous alignment layer applied. (f) adhesive spacers were attached to the substrate. (g) the superstrate was combined with the substrate and (h) a cross-section of the complete antenna.

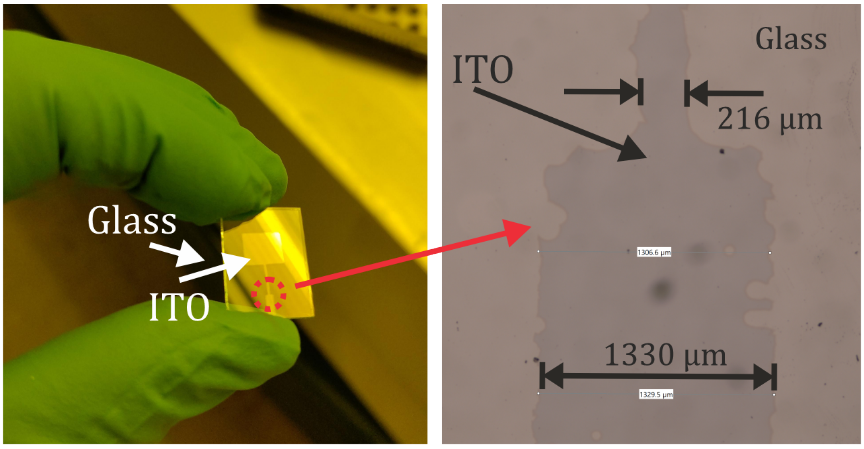

(a) (b)

Figure 6.6: Results of etching ITO from the glass with a photograph of the entire substrate (a), and the section highlighted by the red circle is viewed under a microscope at 4× magnification (b).

to form the geometry of this antenna produced several imperfections; however, the scale of these imperfections was not deemed to drastically impair the operation of the antenna and was generally congruent with the design requirements.

6.2.2 Liquid Crystal Droplet Configuration

Figure 6.7 demonstrates the nematic LC droplets printed onto the radiating patch of the antenna, without a superstrate, when viewed on a polarising optical microscope (POM) with 4× magnification and either crossed (a) or parallel (b) analyser and polariser. The results in Figure 6.7(a) show that the droplets have successfully been printed and a homeotropic alignment of the director was achieved from the dark cross visible in each droplet aligned with the analyser and polariser. The diameters of several droplets were measured in Figure 6.7(b) and the average value calculated as 455 μm with a standard deviation of 12 μm, and an average spacing between droplets of 40 μm with a standard deviation of 9.8 μm.

The height for an individual droplet was measured by taking an image of the droplet's side profile, before the superstrate was added, using a digital camera with a 12× magnification adapter (Navitar microscope) and a bright backlight. Imaging software was employed to fit a circle to the profile of the droplet to estimate the static contact angle,

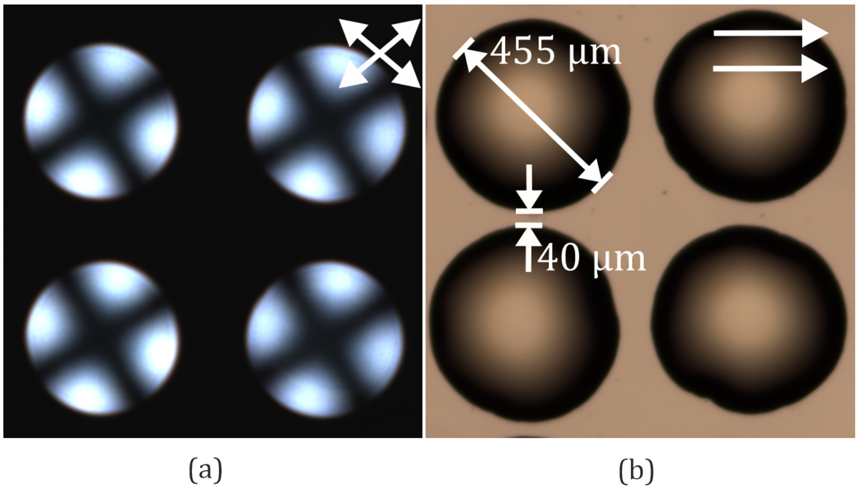

Figure 6.7: Nematic LC droplets printed on ITO-coated glass viewed on a polarising optical microscope at 4× magnification with crossed analyser and polariser (a) and parallel polarisers (b). The double-headed white arrows in (a) and the single-headed white arrows in (b) correspond to the orientations of the polariser and analyser.

θ_c, illustrated in **Figure 6.8**. The contact angle between the glass substrate and the LC droplet was $\approx 32°$, from this the height of the droplet was calculated to be $\approx 65\ \mu$m.

Upon combining the antenna and ITO-coated glass superstrate, it was necessary to confirm that the droplets had made contact (and wet) with the superstrate: the antenna was again placed on a POM, with the results displayed in **Figure 6.9**. These images confirmed that the droplets had made contact with the superstrate. By observing a single nematic LC droplet, it was clear that the LC alignment was indeed a hybrid alignment due to the smooth gradient between light and dark states of the polarised light. These printed droplets when combined with the superstrate had not coalesced to form a continuous film, as was desired. The upshot of this was that the area between the radiating patch and the groundplane was not entirely encompassed by LC, but instead with some areas containing air, which reduced the net variation in the dielectric permittivity.

6.2.3 Printed Liquid Crystal Patch

The reduction in the net dielectric permittivity variation produced from the gaps between LC droplets directly related to a reduced variation in the frequency tunability of the antenna: to address this the LC was printed such that it formed a contiguous film. The same printing conditions as described in Section 6.1.2 were employed, again printing

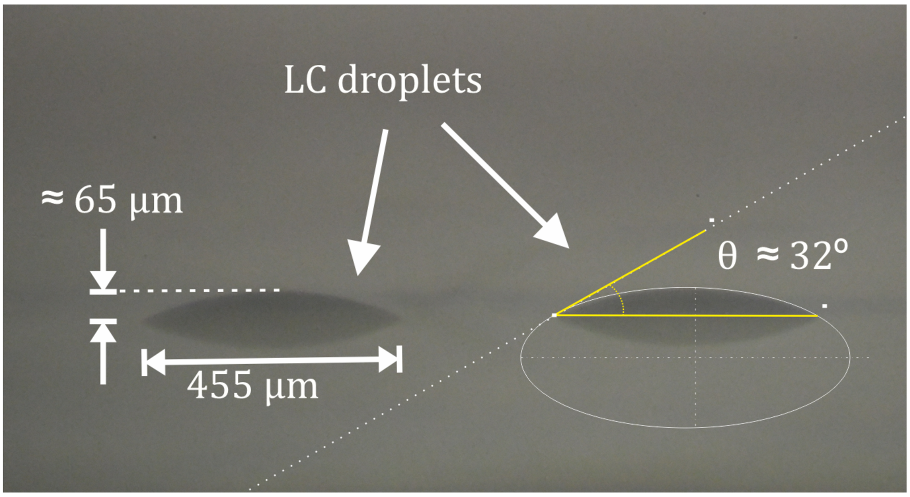

Figure 6.8: Nematic LC droplets printed on a glass substrate with a homeotropic alignment layer and imaged using a digital camera with 12× zoom. The substrate is not visible, however, it does cause a reflection of the droplet image in the horizontal plane.

the nematic LC mixture E7 in a grid directly over the area of the radiating patch of the antenna. However, to ensure the droplets coalesced, the spacing between printed droplets was reduced incrementally until the optimal distance was found. To successfully print a contiguous patch of nematic LC the centre-to-centre droplet spacing was reduced to 200 μm, until it appeared that the LC had formed a contiguous patch.

The effect on the LC alignment was assessed by placing the printed LC under a POM with 4× magnification and crossed polariser and analyser, with and without a superstrate, shown in **Figure 6.10**. In Figure 6.10(a), the section at the bottom right-hand side of the patch is shown, and the region between the LC and no LC was present, albeit not well delineated. There was also a gradient moving towards the centre of the patch that indicates the thickness of the LC layer increased towards the centre, likely due to the curvature of the LC patch. With the superstrate added in Figure 6.10(b), the border between the LC and air was well defined. Some additional LC spots can be observed, which were likely caused by the printhead during the deposition. The process of estimating the height of this contiguous LC patch was to print a single LC droplet adjacent to the patch and capture an image containing both. The droplet height was calculated using the contact angle approach and the number of pixels of the droplet height compared to that of the LC patch. The height of the LC patch was ≈ 105 μm.

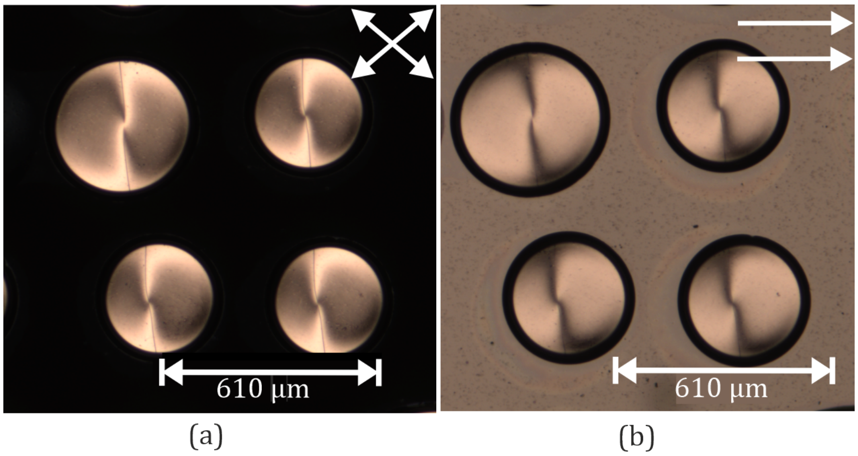

Figure 6.9: Printed nematic LC droplets sandwiched between a glass substrate and glass superstrate, viewed on a POM with ×4 magnification and crossed polarisers (a), ×4 magnification with parallel polarisers (b). The double-headed white arrows in (a) and the single-headed white arrows in (b) correspond to the orientations of the polariser and analyser.

6.2.4 Assembling the Antenna

The final step in the process was to construct the antenna by sandwiching the printed LC with an (unpatterned) ITO-coated glass superstrate, which simultaneously acted as the groundplane of the antenna and allowed an electric field to be applied across the device to reorientate the LC director. The groundplane was spin-coated with 1 wt.% PVA in distilled water and mechanically rubbed (Figure 6.5(e)) to produce a homogeneous alignment. The substrate and superstrate were separated with 100 μm double-sided adhesive spacers along each of the long edges, approximately 2.5 mm in width, positioned such that they do not come into contact with the conductive area of the antenna. Images of the printed LC patch and final device are presented in **Figure 6.11**.

6.3 Antenna Performance and Characterisation

6.3.1 Antenna Transparency

The transmittance was recorded between 400 nm - 700 nm for the following three devices: a single ITO-coated glass substrate, two ITO-coated glass substrates separated by 100 μm of air (i.e., the antenna without any LC or alignment layers), and the final antenna, featuring the ITO-coated substrate/superstrate and 100 μm thick layer of nematic LC

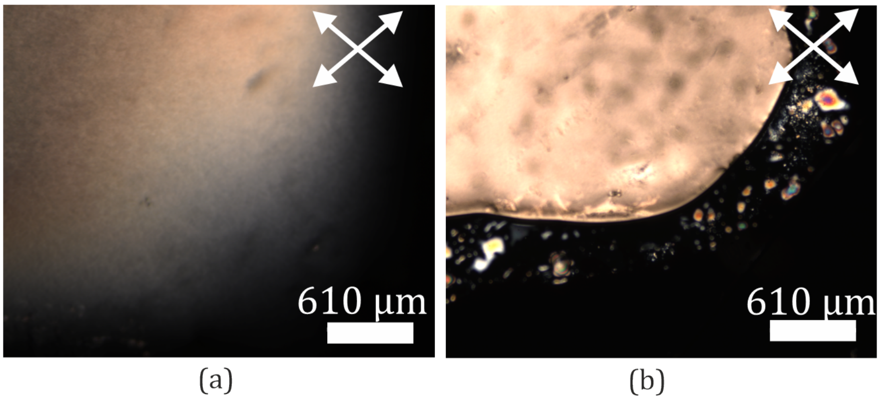

Figure 6.10: Nematic LC droplets printed onto ITO-coated glass with a homeotropic alignment layer to form a contiguous layer (a), and with a superstrate added (b). Viewed on a POM at ×4 magnification and with a crossed polariser and analyser. The double-headed white arrows in (a) and (b) correspond to the orientations of the polariser (P) and analyser (A).

and the LC alignment layers. These were measured using an Agilent Technologies Cary 8454 UV-Vis spectrometer and the results are shown in **Figure 6.12**.

The results demonstrate that the high level of optical transparency from a single ITO-coated substrate was reduced by the introduction of the glass superstrate, diminishing the transmittance by an average of 9% across the visible wavelengths, with the variation of transmittance with wavelength likely due to Fabry-Pérot effects arising from losses due to multiple Fresnel reflections, and scattering was also a probable contributor to the reduction in transmittance at short wavelengths. The addition of a nematic LC, and alignment layers, affected an average reduction of 14% across the measured spectrum. Although the substrate and superstrate were necessary to apply an electric field across the LC layer, one of these could be replaced by a thin-film, as is already the case in some smartphone displays. If this device were to be implemented in a window, two panes of glass would typically be present. Hence, in practice the effect of the LC on the transmittance (opposed to the effect of the glass) is a more important consideration.

The optical transmittance of the complete LC-based antenna was measured at 450 nm, 550 nm, and 650 nm for an increasing a.c. voltage, featuring a 1 kHz square wave, applied across the LC layer, which is presented in **Figure 6.13**. This result showed a slight reduction in the transparency at 1 V, followed by a sharp rise between 1 V - 5

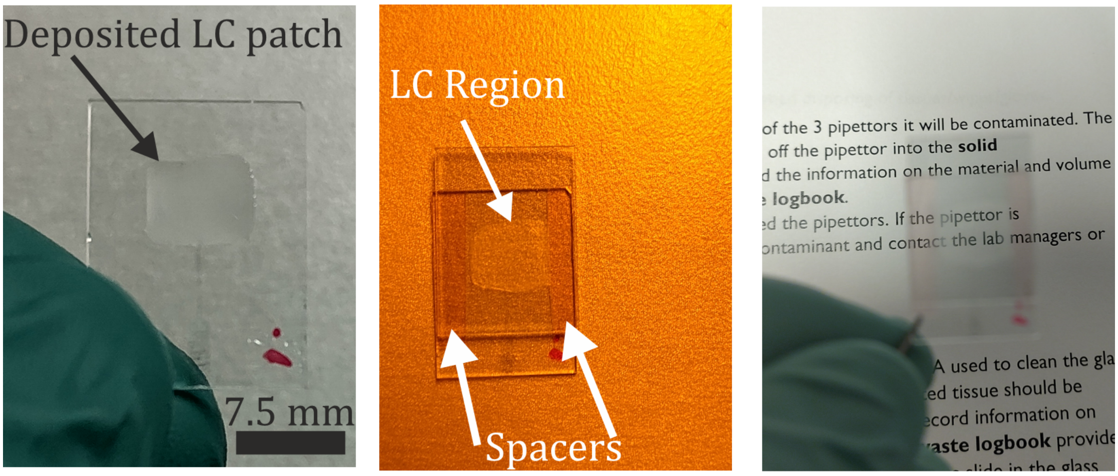

(a) (b) (c)

Figure 6.11: Photographs of printed nematic LC droplets. (a) LC droplets printed onto ITO-coated glass with a homeotropic alignment layer that form a contiguous layer across the patch. Antenna with the LC patch sandwiched between a glass substrate and a glass superstrate. 100 μm spacers have been included between the substrate/superstrate. (b) highlights the different regions and (c) demonstrates the optical transparency of the printed antenna

V, and a gentle increase beyond 5 V, at each of the three wavelengths. The variation in transmittance was likely caused by scattering losses that decreased as the voltage increased above the threshold voltage, V_{Th}, with the maximum scattering loss observed to be slightly below the threshold voltage.

6.3.2 Frequency Tuning

S-parameter measurements were conducted using a calibrated Rohde & Schwarz ZNB43 vector network analyser (VNA), with an SHF BT45R broadband bias tee inserted between the VNA and the antenna, and an 1 kHz a.c. voltage applied via the bias tee. Examining the plot of S11 in **Figure 6.14** revealed a desirable performance in terms of antenna reflection efficiency and frequency tunability: applying a bias voltage across the LC layer induced shift of 90 MHz in the operational frequency of the antenna, over a continuous range from 11.34 GHz to 11.25 GHz, which was a shift of approximately 1% of the operational frequency. The downshift in frequency was congruent with the expected results: aligning the LC director parallel to the applied field increased the dielectric permittivity of the LC (see Table 6.1), and hence lowered the operational frequency, as

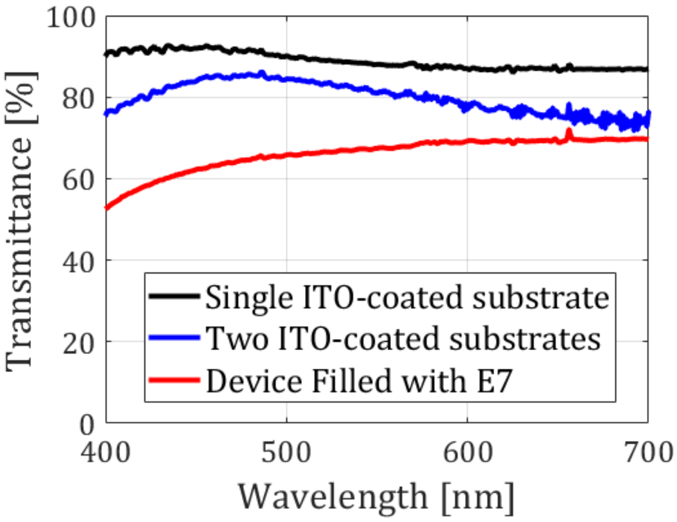

Figure 6.12: Transmittance as a function of wavelength of an ITO-coated substrate with homeotropic alignment layer and fabricated antenna both empty and with printed nematic LC layer of 100 μm, at optical wavelengths.

$F \propto 1/\sqrt{\varepsilon_{re}}$.

The nematic LC mixture used here, E7, exhibited a moderate degree of dielectric anisotropy at RF, whereas other mixtures, such as the GT series developed by Merck, could provide twice the level of dielectric anisotropy [70], and hence improve the frequency tuning range of this device. The dielectric anisotropy, and hence the frequency reconfigurability, was also reduced by the hybrid alignment layer causing an average relative permittivity, $\varepsilon_{r,av}$, seen by an impinging EM wave that is approximately $\varepsilon_{r,av} = \left(2\varepsilon_{r,\perp} + \varepsilon_{r,||}\right)/3$ when no electric field is applied, resulting in a slightly higher permittivity value than if the alignment were ideally planar, i.e., $\varepsilon_{r,\perp}$. This effect was evident from Figure 6.3, where the LC director was not aligned parallel to the substrate.

Considering the plot of measured S11 in Figure 6.14, the operational frequency of the antenna at 0 V was found to be 11.34 GHz and 11.25 GHz at 100 V. A voltage of 100 V was used here after the LC director profile simulation findings in Chapter 5 suggested that 100 V was required to fully re-orientate the LC director in a 100 μm thick LC layer. Re-arranging Equation 2.26, suggested the values for effective dielectric permittivity of the antenna are $\varepsilon_{re,\perp} = 4.14$ and $\varepsilon_{re,||} = 4.2$, at 0 V and 100 V, respectively. These values are somewhat higher than those reported for E7 [70]; however, the reported values

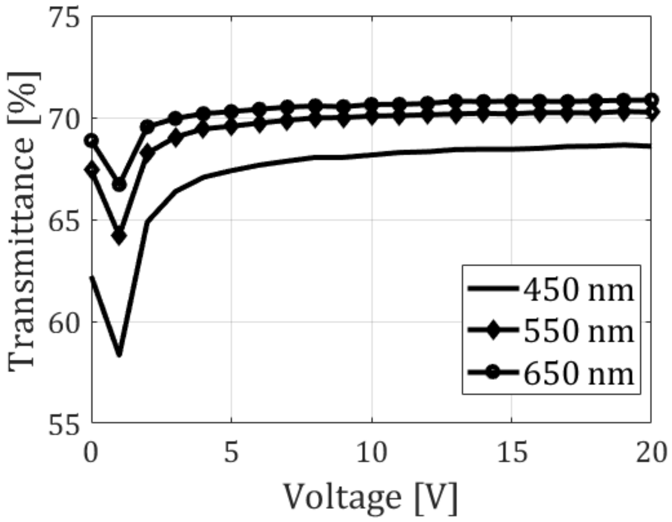

Figure 6.13: Transmittance of the final antenna with a 100 μm thick printed layer of E7 against an increasing voltage, at three different optical wavelengths.

are for the relative permittivity, whereas the effective permittivity of this antenna is a combination of the LC and the glass substrate and superstrate. The increase in effective permittivity observed here was likely because the relative permittivity of the glass is higher than E7. This increase was congruent with the experimental findings in Chapter 5. There was also a reduction in the dielectric anisotropy $\Delta\varepsilon_{re}$ between this antenna and the reported values, which can be attributed to the hybrid alignment employed here reducing the variation in permittivity.

Figure 6.14 also demonstrates the -10 dB bandwidth (BW) and antenna reflection efficiency, $e_r = 1-|\Gamma|^2$, where Γ refers to the conversion of the S11 value from dB to Volts. At 0 V the operational frequency was 11.34 GHz, with $e_r = 99.4\%$ and $BW = 780$ MHz, whereas at 100 V the operational frequency was 11.25 GHz, $e_r = 98.7\%$ and $BW = 740$ MHz. The reduction in reflection efficiency was likely due to the alteration of the LC permittivity when applying the bias voltage, causing a slightly greater mismatch between the antenna impedance and impedance of the microstrip feed. The decrease in BW was most likely caused by decreased material losses in the LC, which is congruent with the values for $\tan\delta$ in Table 6.1, causing the Q-factor to increase.

The switching times in Equations 2.19 and 2.20 can be calculated by assuming that the threshold voltage is $V_{Th} \approx 1$ V, and taking $K_{11} = 18 \times 10^{-12}$ N [92] and $\gamma_1 = 0.26$

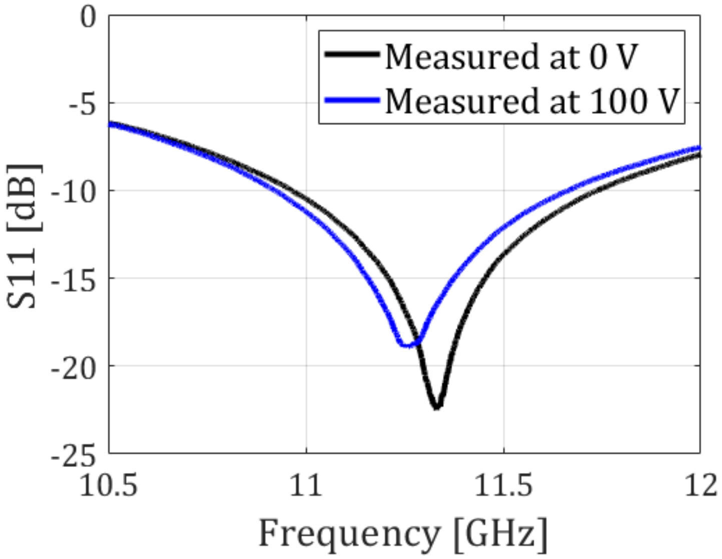

Figure 6.14: Measured S11 of the printed LC optically transparent antenna with a bias voltage of 0 V and 100 V applied to reorientate the LC director.

Pa·s [70] for the nematic LC mixture E7. In this case, the switch on time was estimated as $\tau_{on} \approx 6.5$ ms and the switch off time was $\tau_{off} \approx 23$ s. It is clear from Equation 2.19 that the switching on time can be reduced significantly by driving it with a high voltage. For example, increasing V_a to 250 V results in a switching on time of 0.37 ms, whereas τ_{off} can only be altered by reducing the LC layer thickness, or employing a dual-frequency nematic LC, as in [93], for example.

6.3.3 Comparison with Full-wave Simulations

Comparisons with the measured and simulated S11 of the antenna at 0 V and 100 V, are depicted in **Figures 6.15**(a) and (b), respectively. The antenna was simulated in CST Studio Suite using the parameters detailed in Table 6.1 for the glass substrate/superstrate and the antenna geometry. The LC parallel and perpendicular permittivity and loss tangents, detailed in Table 6.1, were used to guide the simulations: the measurements in [70] were not conducted at the operational frequency of this antenna, hence, a range of values for the relative dielectric permittivity and loss tangent, guided by those reported results, were tested in the simulation.

Values of $\varepsilon_{r,\perp} = 2.74$ and $\varepsilon_{r,\parallel} = 2.8$, relating to the 0 V and 100 V measurement,

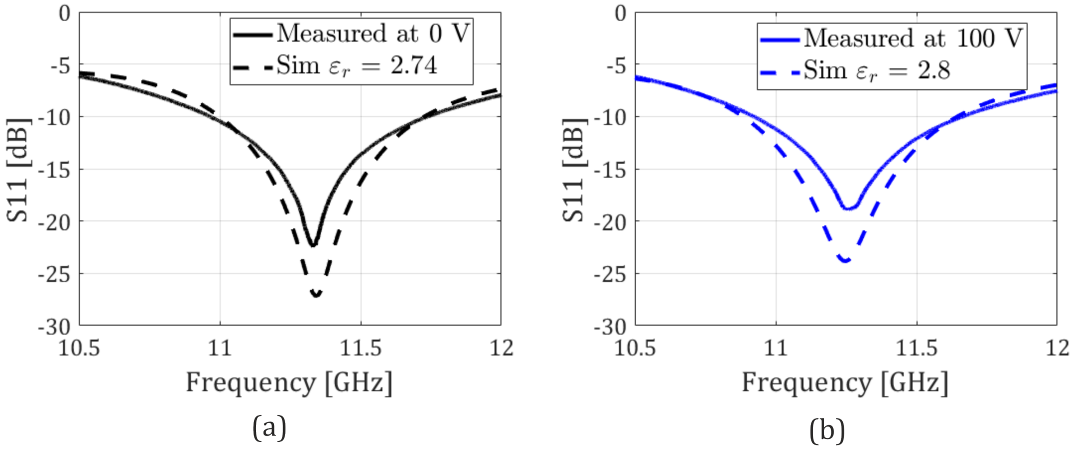

Figure 6.15: (a) Measured S11 of the optically transparent antenna with a bias voltage of 0 V and full-wave simulation with $\varepsilon_r = 2.74$. (b) Measured S11 of the optically transparent antenna with a bias voltage of 100 V with simulation parameter $\varepsilon_r = 2.8$.

respectively, provided the most accurate simulation results in terms of the operational frequency of the physical antenna, with only a 0.07% disparity between each measurement and simulation. Hence, using representative values for the relative permittivity of E7 reported in [70], have resulted in the simulated antenna exhibiting the same operational frequency as the measured antenna, and by Equation 2.26, the same effective permittivity, providing confidence that the increased values for $\varepsilon_{e,\perp}$ and $\varepsilon_{e,\|}$ are in fact due to the contribution from the glass substrate/superstrate.

The measured Q-factor of the antenna can be used to estimate the $\tan\delta$ losses by $Q = 1/\tan\delta$; however, this assumes a single dielectric substrate, whereas in this design, the material losses of the LC, glass substrate/superstrate, alignment layers, and the thin-film of ITO are combined. Hence, for the simulations, a range of values for the LC material losses was simulated. The most accurate results, compared to the measurements, in terms of the S11 value at the operational frequency were $\tan\delta_\perp = 0.022$ and $\tan\delta_\| = 0.009$, which were congruent with values reported in [70] for E7 at 19 GHz.

There was a noticeable disparity between the simulation and measurement results in terms of the S11 value at the operational frequency of the antenna, which was consistently lower in the simulated results. The most likely cause was a mismatch between the physical dimensions of the antenna structure, which contained minor imperfections in the geometry due to fabrication tolerances and variations in the width of the antenna feed due to the chemical etching process, and the ideal geometry which was used in the simulation. It was also possible that the material losses were not fully captured in the simulation. This could be mitigated by improving the impedance matching of the antenna to 50 Ω.

6.3.4 Radiation Patterns

The radiation pattern of the E-plane and H-plane of the optically-transparent patch antenna were measured by placing the device in the bespoke anechoic chamber (BAC) established in Chapter 3. The BAC was designed and fabricated specifically for the studies presented in this thesis. A 3D printed antenna mount was attached to a turntable to conduct the measurements, with the VNA connected to the antenna via a bias-tee to supply the external voltage across the LC layer. The test antenna was a DRH30 horn antenna, supplied by RF Spin. The inside of the BAC, measuring the E-plane of the antenna, is highlighted in Figure 3.14. The radiation pattern was measured by attaching the optically-transparent antenna to the antenna mount, orientated for either the E-plane or H-plane measurements, with the mount itself attached to a manual turntable. The turntable was rotated through 180°, in 2° increments, with the S21 recorded each time. The simulated radiation pattern was recorded using the same simulation setup for the S-parameter measurements, which automatically calculates the E and H-plane pattern.

Figure 6.16 depicts the measured and simulated radiation patterns for the E-plane of the reconfigurable antenna at frequencies of 11.25 GHz and 11.34 GHz, respectively, corresponding to applied voltages of 100 V and 0 V for the measured data and, $\varepsilon_r = 2.8$ and $\varepsilon_r = 2.74$ for the simulated data, respectively. The H-plane measurements for the same parameters are displayed in **Figure 6.17**. For both the E-plane and H-plane, there was reasonable agreement between the measured and simulated results. The discrepancies were likely caused by slight differences in fabricating the antennas and controlling the turntable by hand, compared to the idealised simulation parameters.

The E-plane measurements suggested peak directivity at 16° and a half power beamwidth of 56°. The gain comparison method was used to measure an antenna gain of -4.38 dBi, with little difference between the measurement at 0 V and that at 100 V. The reduction in gain, compared to a copper/FR-4 patch antenna, was due to the ITO conductor losses,

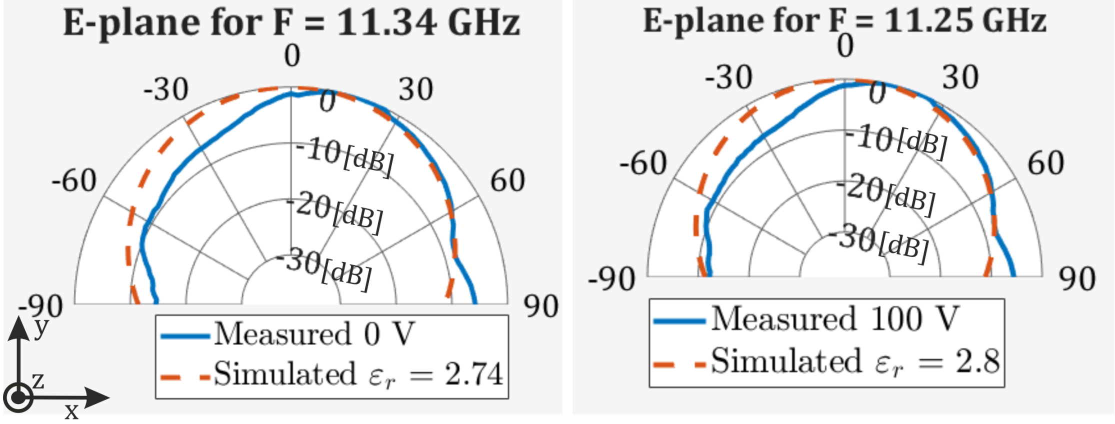

(a) (b)

Figure 6.16: Measured and simulated E-plane (xz-plane) radiation patterns of the printed optically transparent LC antenna for frequencies of (a) 11.34 GHz (no voltage applied) and (b) 11.25 GHz (100 V applied).

and the addition of the LC layer increasing dielectric losses. However, a transparent patch antenna that did not incorporate LC, reported in [48], was found to yield a similar value for the antenna gain, despite not being reconfigurable.

6.3.5 Voltage Standing Wave Ratio

The voltage standing wave ratio (VSWR) is a measure of how well the antenna is impedance matched to the transmission line, in this case a 50 Ω coaxial cable: the lower the VSWR the more power is delivered from the power source to the antenna. The VSWR is calculated by $VSWR = (1 + |\Gamma|)/(1 - |\Gamma|)$, and the ideal case is a VSWR of 1:1, and in practice 2:1 is acceptable. This metric was of particular interest here since the antenna was fabricated using ITO-coated glass, which is not a typical material combination for fabricating antennas. It also relied on a pressure connection from the copper SMA to the ITO conductor, which could not be soldered as for a PCB-based antenna.

Figure 6.18 demonstrates the VSWR for the optically transparent antenna, with and without a bias voltage applied. It is shown that the VSWR was not higher than 2:1 between 8.5 GHz - 12.5 GHz, and below 1.2:1 from 11 GHz - 11.5 GHz, indicating a high level of impedance matching at the operational frequency of the antenna for the different bias voltage conditions. There was little difference in the antenna matching performance for the 0 V and 100 V cases, particularly around the operational frequency:

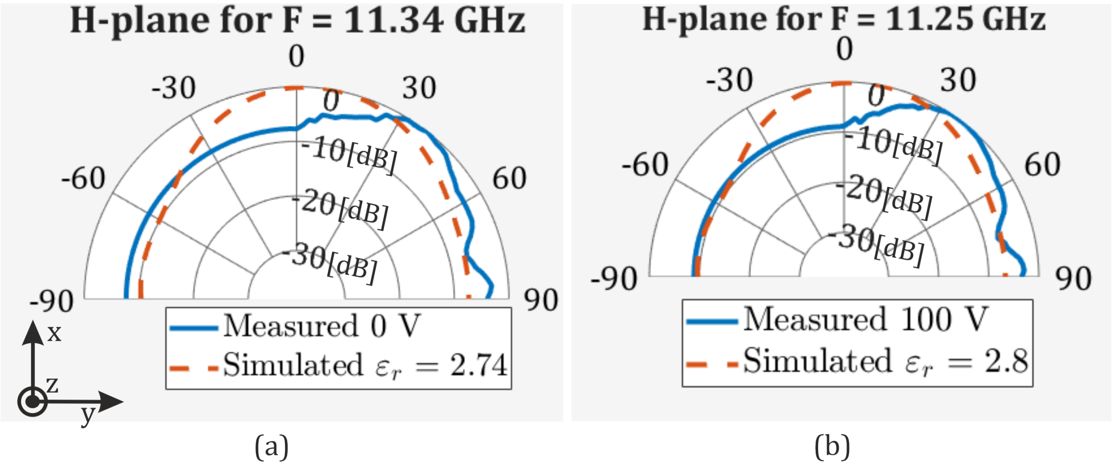

Figure 6.17: Measured and simulated H-plane (zy-plane) radiation patterns of the printed optically transparent LC antenna for frequencies of (a) 11.34 GHz (no voltage applied) and (b) 11.25 GHz (100 V applied).

Table 6.2: Comparison of this work and other optically-transparent patch antennas.

Ref	Material	Freq [GHz]	Transparency [%]	Gain dBi]
[47]	ITO	9.85	90	4.27
[49]	FTO	5	85	1.72
[48]	Cu Mesh	2.5	61	2.63
[48]	IZTO/Ag	2.5	81	-4.23
This work	ITO/LC	11.25 - 11.34	66	-4.38

this was expected as the tunable part of the antenna, i.e., the nematic LC, was printed directly above the radiating patch and not onto the antenna feed. Hence, these results demonstrate that using non-standard materials to fabricate the antenna has not caused a significant mismatch in delivering power to the antenna.

A summary of the results from this study and a comparison with several other works relating to optically-transparent antennas is provided in **Table 6.2**. The parameters achieved for this reconfigurable optically-transparent antenna match those previously reported for antennas that cannot be tuned, suggesting that the addition of a non-optimised nematic LC into the antenna has not degraded the fundamental antenna performance.

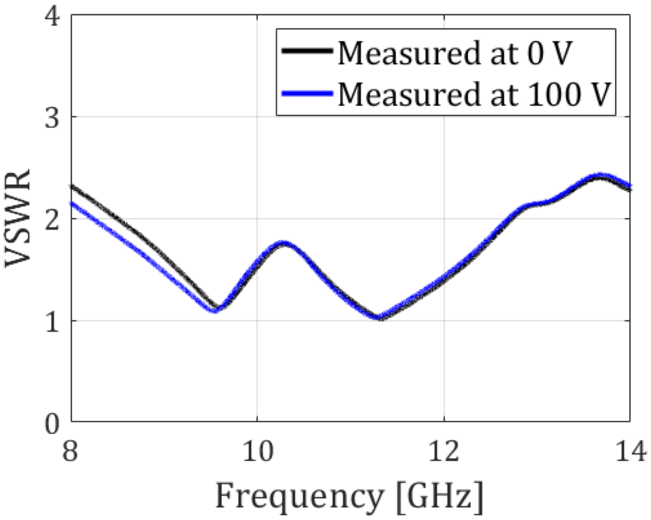

Figure 6.18: Measured VSWR of the optically transparent antenna.

6.4 Conclusions

This study has detailed the design, fabrication, simulation, and measurement of a reconfigurable optically-transparent patch antenna using a nematic LC. The focus of this work was to detail the method by which the frequency of an optically-transparent antenna could be tuned in a continuous and reversible manner, and to measure the degree of tunability, while maintaining the effectiveness of the antenna (i.e., the ability to radiate energy), and its optical transparency. Compared with previous works on transparent antennas, the antenna proposed here exhibits slightly diminished levels of transparency, efficiency, and gain, to those reported elsewhere, but with the additional ability of frequency tuning the antenna.

A method of precisely printing a nematic LC onto a radiating patch of an antenna, using a drop-on-demand (DoD) system to reduce wastage and maximise the tuning range, was also presented here for the first time. The DoD printing method could be optimised further and may be vital for larger antennas, or antenna arrays, in reducing the amount of LC that is required. The technology proposed in this study could be adapted into many applications, such as display technology, or smart windows, where LCs are already prevalent, or to alleviate frequency congestion where necessary.

Chapter 7

Liquid Crystal-Based Reconfigurable Intelligent Surfaces for Radio Frequencies

This Chapter details an investigation into the feasibility, benefits and limitations of utilising a nematic liquid crystal (LC) in the construction of a reconfigurable intelligent surface (RIS) unit cell. RIS technologies have been subject to a myriad of published literature over recent years, yet, there exist only a small number of well-cited articles that consider the design and fabrication of the RIS unit cell. There are currently no prominent works in which a nematic LC is featured in the RIS covering the 5G n257 band. The current state-of-the-art is to employ p-i-n diodes in the unit cell, restricting the phase values that the RIS can adopt to 1-bit, as demonstrated in Chapters 1 and 2. The motivation behind a RIS unit cell is the potential to impart a continuous phase-shift on radio frequency (RF) signals reflected by the RIS. This would be the ideal case. However, there exist cases in which the LC-based unit cell could still provide a benefit over the alternative options, for example, by dynamically increasing the number of phase values the RIS can adopt. The experimental methods for constructing LC-based devices on copper-clad substrates, detailed in Chapter 3 are applied here, along with measurements using the bespoke anechoic chamber (BAC) and CST Studio Suite simulations, also described in Chapter 3. Furthermore, the transmission line approximation of a RIS unit cell that was presented in Chapter 2, is be tested against the LC-based unit cells that are assessed in this chapter.

Cases for which the LC-based RIS can produce a benefit over the alternative options are articulated herein, including; the conditions necessary to meet each case, the unit cells designs to achieve this, the electromagnetic (EM) simulation techniques by which they will be assessed, and a discussion on the results and implementation strategy for an LC-based RIS. The unit cell designs that meet the stipulated requirements will thence be fabricated and tested using the BAC. These will be assessed against simulations carried out in this Chapter to assess the feasibility of an LC-based RIS. Work detailed in this chapter has been submitted to the IEEE 2026 International Conference on Communications.

In particular, the contributions of this Chapter are:

- a set of stringent requirements for an LC-based RIS unit cell is delineated, against which several candidate unit cell designs are evaluated using CST simulations;
- these simulations demonstrate a novel wideband LC-based unit cell that provides: up to 290° of continuous phase shift, a reflection magnitude above -3 dB and an angular stability of ±60°, across the entire n257 band, with a unit cell size of 0.3λ,
- the designs that meet the requirements are then fabricated and validated experimentally; and
- periodic boundary simulations and measurement results are used to make a final assessment of the LC-based RIS feasibility.

The remainder of this Chapter is organised as follows: In Section 7.1, the requirements for the LC-based unit cell are outlined, along with the four candidate designs that are considered. Periodic boundary simulations are then employed to support an assessment of these designs, including how an LC-based RIS could operate in Section 7.2. Then, in Section 7.3, the techniques used to fabricate the unit cell designs are described before experimental validation of each design is presented, which is followed by a discussion on the results and feasibility of an LC-based RIS unit cell. Finally, this Chapter concludes in Section 7.4.

7.1 Requirements for an LC-based RIS Unit Cell

Prior to evaluating the feasibility of an LC-based RIS unit cell, a set of requirements for the unit cell was first considered. This was important to 1) focus the scope of the investigation, 2) ensure the resulting artefact could realistically be employed in a RIS, and 3) provide a fair comparison with the leading alternative RIS technology. Two prominent works on the design and fabrication of RIS prototypes have demonstrated: a 1-bit phase shift between 5.5 GHz - 6 GHz using a varactor diode [3]; and a 1-bit phase-shift using a p-i-n diode between 24.5 GHz - 29.5 GHz, that is, the 5G n258 (24.25 GHz - 27.5 GHz) and n257 (26.5 GHz - 29.5 GHz) bands [4]. Employing a nematic LC in the lower frequency range was considered, however, this would require relatively thick LC layers and thereby an increase in the switching times and cost of the RIS, due to the increased volume of LC needed. Furthermore, the millimetre wave (mm-wave) 5G network infrastructure is an active research area and due to the increased attenuation of EM signals in this band, represents a more attractive option for the deployment of novel technologies. Hence, the work by Wang et al., [4], will serve as a benchmark for assessing the performance of an LC-based RIS, representing the leading alternative to the use of LC materials for a RIS technology in the mm-wave band.

The LC-based unit cell investigated here was subject to several practical requirements that were split into a set of general conditions and one of three benchmarks. These general conditions were:

- the technology needs to operate in the 5G n257 band (26.5 GHz - 29.5 GHz),
- exhibit low reflection losses, $>$ -5 dB, and
- possess a unit cell size $< 0.5\lambda$ (at 28 GHz $\lambda = 10.71$ mm).

A further three use-specific cases relating to the achievable phase-shift of the LC-based unit element will then be investigated, starting with the ideal case and moving towards the most basic case, to yield three benchmarks:

1. The LC-based unit element exhibits a continuous phase-shift in the range of $(0°, 360°]$ across the entire n257 band (outperforming the leading alternative).

2. The LC-based unit element exhibits a phase-shift ≥ 90° across the entire n257 band (matches or outperforms the leading alternative).

3. The LC-based unit element exhibits a phase-shift ≥ 90° across a single channel in the n257 bandwidth (matches or worse than the leading alternative).

Benchmark 1 represents the ideal case for an LC-based RIS. While there are practical barriers to employing a continuous phase-shift, such as channel overheads and precision, it is worth considering. Benchmark 2 was a more realistic condition and could be used to realise an LC-based RIS with multiple phase-levels, i.e., 2 or 4-bit, depending on the realised performance. The minimum phase-shift for benchmark 3 of 90° was selected somewhat arbitrarily: in a 1-bit system any two values can be selected, with the first being no phase-shift and the second commonly chosen as 180° to maximise the distance between the two values. This is not necessary as the phase-shifts of signals arriving at the receiver that the RIS is serving are random. However, there is an unavoidable error in applying the phase-shift, hence the value furthest from 0° is commonly applied. For benchmarks 1 and 2, the phase-shift must be applied across the entire n257 band, however, for benchmark 3 this condition was relaxed to a single channel: n257 channel bandwidths range from 50 MHz - 400 MHz, forming between 7 - 60 individual channels. In practice, this would mean an LC-based RIS can only operate at one of these channels, or require the RIS to be split into sections that relate to the channels, reducing the RIS performance gains.

The phase difference, also termed phase-shift, is defined as the difference in phase for reflected signals that is observed in simulations with $\varepsilon_{r\perp}$ compared to $\varepsilon_{\|}$, or the the case of measured data, the difference between the phase of reflected signals for measurements taken at 0 V and 100 V.

The structure of the LC-based RIS unit cell used in the periodic boundary simulations was comprised of; an upper layer featuring a metallic patch designed to resonate in the n257 frequency band, a layer of a nematic LC and a bottom layer featuring a metallic groundplane. The resonant patch and groundplane were attached to a Rogers 4350B dielectric substrate (RO 4350B), which is a PCB material designed to operate in the RF band. Hence, the order of the layers was; RO 4350 substrate, resonant patch, LC layer, groundplane, RO 4350B substrate. The investigation into the LC-based unit element

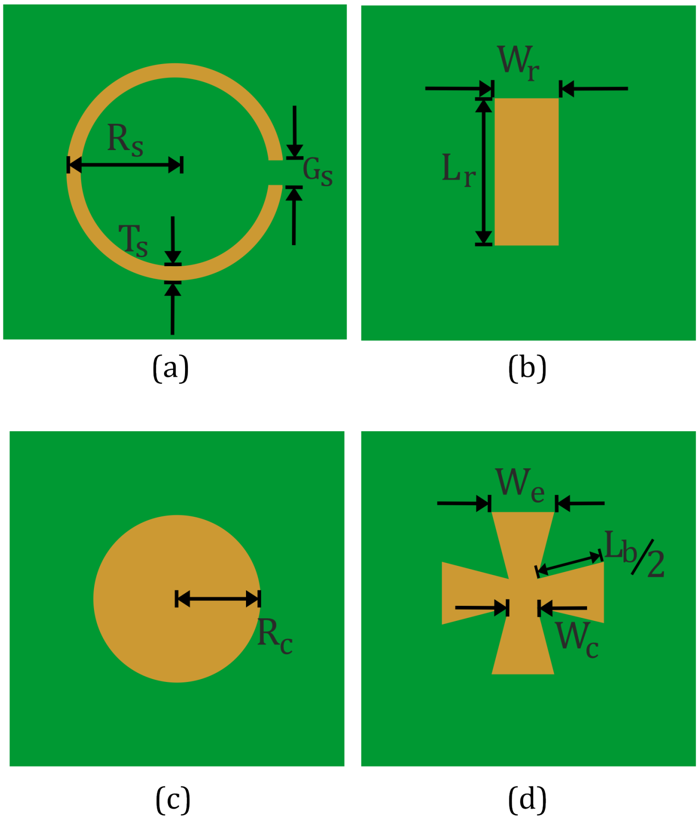

Figure 7.1: Geometric shapes for the LC-based unit cell: (a) split ring resonator with radius, ring thickness and gap width, R_s, T_s, and G_s, receptively. (b) rectangular patch with patch length and patch width, L_r, and W_r, respectively. (c) circular patch with radius R_c, and (d) double bowtie with large element width, element length and small element width, W_e, $L_b/2$ and W_c, respectively.

evaluated four designs for the metallic patch. The shapes were; a split ring resonator (SRR), a rectangular patch, a circular patch, and a double bowtie. These shapes are illustrated in **Figure 7.1**. Each of these shapes was selected for its well-known resonance frequencies and simple geometry for both the etching process and simulations.

The geometry for each shape that was investigated, illustrated in Figure 7.1, had specific values detailed in **Table 7.1** including; SRR radius, ring thickness and gap width, R_s, T_s and G_s, respectively; rectangular patch width and length, W_r and L_r, respectively; circular patch radius R_c and double bowtie large element width, element length and small element width, W_e, $L_b/2$ and W_c, respectively.

For each of the unit cell patch designs in Figure 7.1, the same substrate and LC materials were used, with parameters detailed in **Table 7.2**, including the height, H_{RO},

Table 7.1: Optimised simulated parameters for each design shown in Figure 7.1.

Shape	Parameters [mm]		
SRR	R_s 1.39	T_s 0.1	G_s 0.1
Rectangular patch	W_r 1	L_r 2.7	
Circular patch	R_c 1.6		
Double bowtie	W_e 3.45	$L_b/2$ 4	W_c 1

copper laminate thickness, T_{cop}, relative permittivity, $\varepsilon_{r,RO}$, and loss tangent, $\tan\delta_{RO}$, for the RO 4350B substrate; and height, H_{LC}, dielectric anisotropy, $\Delta\varepsilon_{r,LC}$ and loss tangent, $\tan\delta_{LC}$, for the nematic LC mixture known as 'ZOC-A019XX' (proprietary mixture provided by JNC Corporation). ZOC-A019XX is novel nematic LC mixture designed to exhibit a large dielectric anisotropy and low loss tangent in the mm-wave band, with specific characteristics, except those detailed in Table 7.2 protected as intellectual property of JNC and therefore cannot be published here. For clarity, when referring to the the parallel and perpendicular relative permittivities of ZOC-A019XX, instead of the specific values, the variables $\varepsilon_{r,\parallel}$ and $\varepsilon_{r,\perp}$ will be used, respectively. To further strengthen the case for an LC-based RIS, only readily available materials, such as the Rogers PCB and ZOC-A019XX nematic LC, were used in these simulations.

7.2 Assessment of RIS Unit Cell Candidates

7.2.1 Simulation Parameters

The geometry for each shape in Table 7.1 was initially found by calculating its respective resonant frequencies at 28 GHz, that is, using Equations 2.26 and 4.1 for the rectangular patch and bowtie shapes, respectively, and the resonance frequency for a circular patch is given by [25]

$$F = \frac{1.8412c}{2\pi R_c\sqrt{\varepsilon_{re}}} \tag{7.1}$$

where c is the speed of light in a vacuum, ε_{re} is the effective relative permittivity of the substrate and R_c is the radius of the circle. For the SRR, the resonance equation is based on the total capacitance and inductance of the shape, which are difficult to accurately calculate. Hence, CST Studio Suite simulations were used to find the resonant frequency by testing a range of designs. CST was then used to optimise the resonant frequencies of each shape, assuming that ε_{re} was the LC permittivity, with values in a range between $\varepsilon_{r,\perp}$ and $\varepsilon_{r,\|}$, producing the upper and lower resonant frequencies, respectively. These upper and lower resonant bounds were optimised to conform to the upper and lower bounds of the n257 frequency band.

The CST Microwave Studio model for each unit cell was configured using the Periodic Structure Template with unit cell boundary conditions in the x and y-planes; that is, the opposing faces of the model exhibit identical EM properties and repeat periodically across those faces. The positive and negative z-directions featured Floquet port excitations of two plane waves with orthogonal electric fields, TE_{00} and TM_{00} modes, with co-polar and cross-polar coupling between the modes, and both transmission and reflection parameters. The waves were incident at the unit cell structure at an azimuth angle of $\theta = 0°$ and elevation angle of $\phi = 0°$, assuming a spherical co-ordinate system, unless otherwise stated. Simulations were run using the frequency domain solver, between 20 GHz - 40 GHz, and with refined tetrahedral meshes for final measurements.

To assess the suitability of each of the four shapes presented in Figure 7.1, each was evaluated against the general conditions and the three benchmarks. CST Microwave studio simulations were conducted using the geometry for each shape defined in Table 7.1 and material parameters as detailed in Table 7.2. The relative permittivity of the LC was varied to produce a dielectric anisotropy $\Delta\varepsilon_{r,LC} = \varepsilon_{r,\|} - \varepsilon_{r,\perp}$. For each of the simulations, it was assumed that the dielectric properties measured by JNC at 28 GHz did not change across the range of the frequency domain solver. However, the frequency band of interest was 26.5 GHz - 29.5 GHz, i.e., ±1.5 GHz from the measured frequency of ZOC-A019XX, and hence there would be only minor deviations from the measured

Table 7.2: RO 4350B substrate and ZOC-A019XX LC parameters.

H_{RO} [mm]	T_{cop} [μm]	$\varepsilon_{r,RO}$	$\tan\delta_{RO}$	H_{LC} [mm]	$\Delta\varepsilon_{r,LC}$	$\tan\delta_{LC}$
0.51	36	3.66[a]	0.0037[a]	0.15	1.27[b]	0.006[b]

[a]Measured at 10 GHz [79]. [b]Measured at 28 GHz by JNC.

values. It was also assumed that the temperature in the simulation did not vary from the measurement temperature of 20°C. For each result, the reflection magnitude and phase difference were taken as the TE_{00} co-polarised reflection S-parameters from the periodic boundary simulation.

7.2.2 Simulation Results

Figure 7.2 and **Figure 7.3** present simulation results for the reflection magnitude and phase difference for all four designs shown in Figure 7.1 (SRR, circular patch, rectangular patch and double bowtie antennas), with the n257 frequency band illustrated by the region in light blue. In Figures 7.2(a) and (b), the SRR reflection magnitude and phase difference, respectively, are presented. With regard to the three general conditions defined previously; the SRR structure elicited a phase-shift that peaked within the n257 frequency band and featured a unit cell size of 0.28λ; however, the reflection magnitude at 29.7 GHz was -8.19 dB, which decreased as the LC relative permittivity increased to -10.8 dB, resulting in a value that was >3 dB below the stated target. Nevertheless, the design met the 2nd benchmark, i.e., a phase-shift of more than 90° across the entire bandwidth of the n257 band. SRRs are, by design, highly resonant structures, and in particular due to the narrow ring gap, are efficient at energy storage and hence the strong resonance exhibited in Figure 7.2(a) was unsurprising, yet resulted in this structure being discounted from further investigation as a RIS unit cell. However, the sharp resonance exhibited by this shape may be of use for other reconfigurable metasurface designs; for example, in a reconfigurable frequency-selective surface.

The reflection magnitude and phase difference produced by the circular patch unit cell are presented in Figures 7.2(c) and (d), respectively. This structure attained each of the three general conditions defined earlier; encouragingly, the phase difference peaked

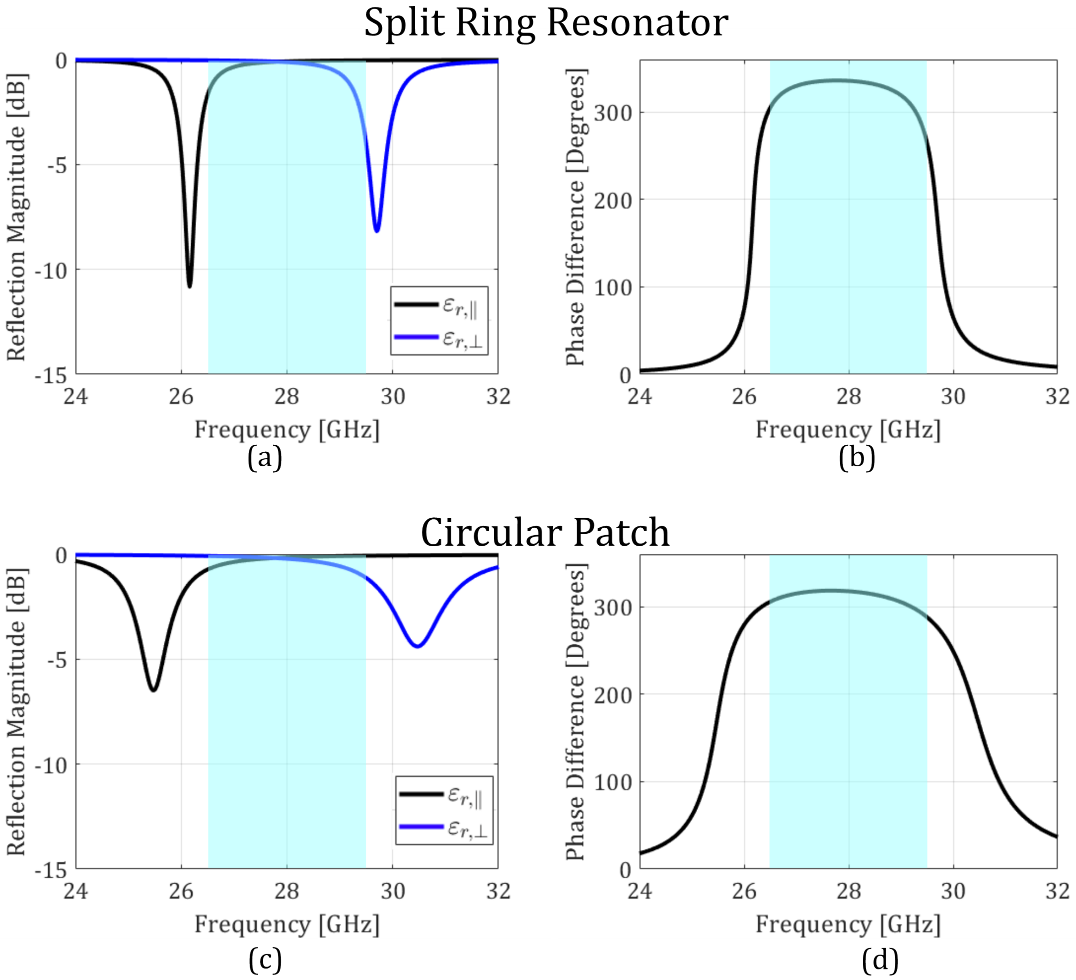

(a) (b) (c) (d)

Figure 7.2: Simulation results for the four unit-cell designs presented in Figure 7.1. For the reflection magnitude plots, results are presented for $\varepsilon_{r,\|}$ and $\varepsilon_{r,\perp}$. Reflection magnitude and phase difference for the SRR (a) and (b); circular patch (c) and (d). The n257 frequency band is shown in light blue.

in the n257 frequency band, the reflection magnitude was above, or only slightly below, -5 dB, and the unit cell size was 0.31λ. The phase difference between 26.5 GHz - 29.5 GHz was 290°, meeting the 2$^{\text{nd}}$ benchmark. The assessment of the circular patch unit cell, against the general conditions and benchmarks, indicated that it could be a suitable candidate for an LC-based unit cell and thus warranted further investigation through experimental validation.

Even though the phase-shift only reached 290°, this could provide superior performance over a p-i-n diode. The RIS demonstrated in [4], for example, yielded a ±20° phase error. Employing the phase-shift of up to 290° achieved in Figure 7.2(d), corresponds to a maximum phase error of ±35°, that is, a desired phase value of 225° would result in the maximum error of 35° from both 290° and 360° (which is equivalent to 0°). This in turn indicates a 10-level RIS: in practice this would be rounded down to 8-levels (3-bit), with 45° separation between each level, and could be altered in real-time e.g., reduced to 1-bit. Furthermore, implementing this configuration would require no additional materials or resources, other than channel state information (CSI) overhead. To achieve 8 phase-levels in a p-i-n diode-based RIS would require the number of p-i-n diodes to be quadrupled during manufacture of the RIS, at a significant additional cost.

Figures 7.3(a) and (b) present the reflection magnitude and phase difference, respectively, for the rectangular patch unit cell. The maximum dimension of the unit cell yielded a size of 0.25λ, the phase difference was centred within the n257 band, and the reflection magnitude was greater than -3.3 dB across the entire band, meeting the three general requirements. The phase-shift across the target bandwidth was at least 260°, which was congruent with the 2nd benchmark. Hence, the initial assessment of this shape demonstrated that it was also suitable for further investigation.

Lastly, the simulation results for the double bowtie antenna are shown in Figures 7.3(c) and (d), where the reflection magnitude and phase difference are demonstrated, respectively. The unit cell size was 0.76λ, the phase difference peaked in, and extended past the n257 band, and the reflection magnitude was -15 dB, decreasing to -25 dB as the LC permittivity increased. There was also a double resonant peak present for the simulation with $\varepsilon_{r,\perp}$, which could cause further losses. The phase difference throughout the target bandwidth was 346°, reaching the 1st benchmark with an allowance for up to a ±7° phase error. While the double bowtie demonstrated an excellent phase-shift, it did not meet the general condition on reflection losses, and was slightly larger than the target unit cell size. As such, the bowtie antenna design was not considered further. However, the potential to elicit a continuous phase-shift across the entire n257 frequency band may warrant further investigation in the future, where techniques to reduce the reflection magnitude, such as rounding the edges of the bowtie lapels, could be considered.

These four designs were not the only ones that were considered and simulated during this investigation, others including the following: concentric SRRs, and multi-patch unit cells were tested to create multiple resonant frequencies where a phase-shift was exhibited,

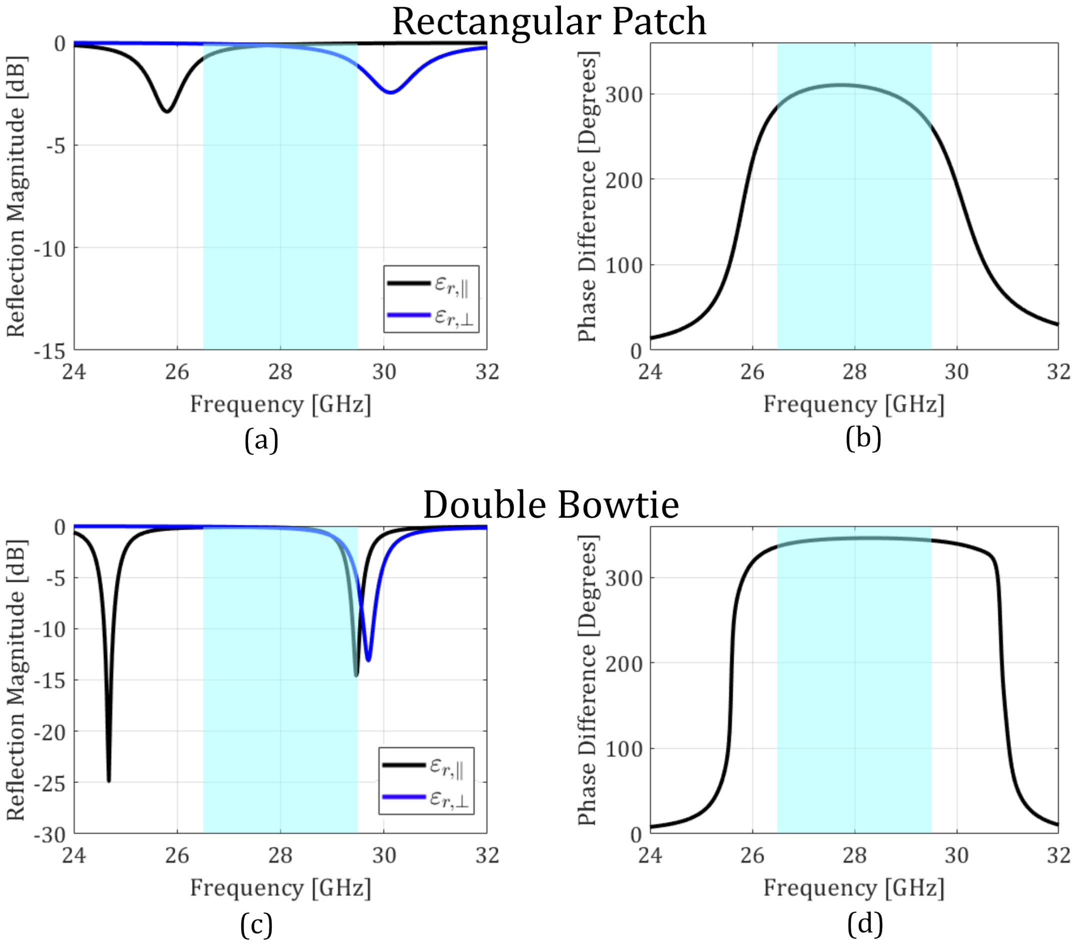

(a) (b)

(c) (d)

Figure 7.3: Simulation results for the unit-cell designs presented in Figure 7.1. For the reflection magnitude plots, results are presented for $\varepsilon_{r,\parallel}$ and $\varepsilon_{r,\perp}$. Reflection magnitude and phase difference for the rectangular patch (a) and (b); and double bowtie (c) and (d). The n257 frequency band is shown in light blue.

or to extend the phase-shift at the main resonant point; a single bowtie, and more complicated shapes such as; spirals or meandering transmission lines, were all gauged for their suitability in a RIS unit cell. None of these exhibited performance improvements over the four designs detailed in Figure 7.1 and therefore are not included in this Chapter.

However, the multi-resonant unit cell, where two, or three, rectangular patches were placed next to each other such that they produced a phase-shift over multiple frequency bands, for example the n258 and n259 (39.50 GHz – 43.50 GHz) bands were feasible. The downside to this approach was that each individual resonant patch required its own bias line to independently apply a voltage across each resonant patch. If only one bias line was used, the phase-shift could only be controlled in one band at a time. Avoiding this limitation would double the number of bias lines required, complicating a full RIS structure containing 100s of unit elements. Nonetheless, the idea could be investigated in the future.

In the previous discussion, each of the unit cell designs featured the same LC layer thickness of 0.15 mm. This value was not selected arbitrarily but after an assessment of varying the LC thickness in the unit cell. The results for this simulation, using the rectangular patch unit cell design, and all other parameters unchanged, are detailed in **Figure 7.4**, where the LC thickness was tested at 0.1 mm, 0.15 mm, 0.2 mm, and 0.3 mm, for both $\varepsilon_{r,\perp}$ and $\varepsilon_{r,\parallel}$. The phase difference for the 0.1 mm case was notably improved over the other values, reaching 335° over a bandwidth larger than the n257 band. The range was slightly shifted up in frequency, although this could be corrected by adjusting the length of the patch, L_r.

Despite the improved phase-shift performance, the 0.1 mm LC thickness was not chosen due to the strong resonance demonstrated in Figure 7.4(a), which was observed to be between -6 dB to -10 dB. Increases of the LC thickness above 0.15 mm led to a diminished phase difference in terms of both the peak value and bandwidth. This was caused by the capacitive effect between the unit cell rectangular patch and groundplane, which is increased as the LC thickness decreased, causing a greater phase delay and increased bandwidth.

To further characterise the behaviour of the LC-based RIS unit cell, the azimuth and elevation angles of the Floquet port excitation waves were varied. In a practical RIS deployment, RF waves are incident at the RIS from any arbitrary azimuth angle and therefore, the angular response required evaluation. In wireless communications systems it is typically assumed that the elevation angle is zero. Nonetheless, a range of elevation angles were also tested.

Figure 7.5 demonstrates the angular stability of the rectangular patch design, with the effect of varying the azimuth and elevation angle on reflection magnitude and phase difference for a range of angles. The angular stability of the unit cell remained near constant for an azimuth angle of 30°, for both reflection magnitude and phase difference

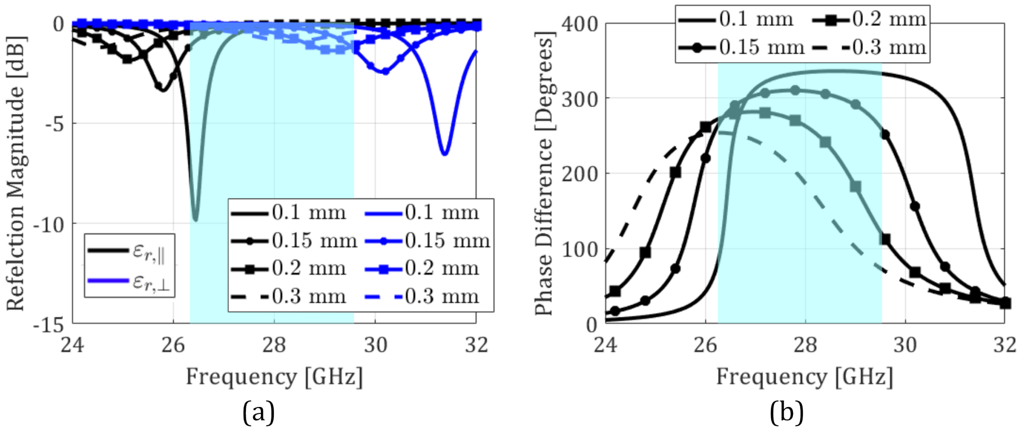

Figure 7.4: Simulation results for five different LC layer thicknesses in the rectangular patch unit cell design. (a) reflection magnitude and (b) phase difference as a function of frequency. The n257 frequency band shown in light blue.

(Figures 7.5(a) and (b)) and was subject to a minor increase in phase difference for $\theta = 60°$. However, when the azimuth angle was increased to $\theta = 85°$, there was no phase difference when varying the LC permittivity and the reflection magnitude was below -10 dB. Evaluating the angular stability for variations in the elevation angle of the incident waves in Figures 7.5(c) and (d) suggested that the phase difference and reflection magnitude was consistent up to $\phi = 30°$ but negative effects in the phase difference and reflection magnitude were observed for an elevation of $\phi = 60°$.

The initial increases in phase difference, corresponding to increases in the azimuth and elevation angles to $\theta = 60°$ and $\phi = 30°$, respectively, were likely due to the incident EM wave taking a longer path through the LC material. The lack of phase difference when the azimuth angle was $\theta = 85°$ and elevation angle was $\phi = 60°$ suggested that the incident EM waves were not penetrating into the LC region due to the large angle of incidence. For a practical RIS, this alteration of the phase difference for increased arrival angles could produce a mismatch in the desired phase-shift and actual phase-shift and as such, should be considered for any future development of a practical RIS.

Figures 7.6(a) and (b) present the reflection magnitude and phase difference, respectively, for the rectangular patch design with the achievable variation in dielectric permittivity increased incrementally to the maximum value of $\Delta\varepsilon_r = 1.27$. This can be considered as equivalent to an increase in applied voltage in a measured device. Of

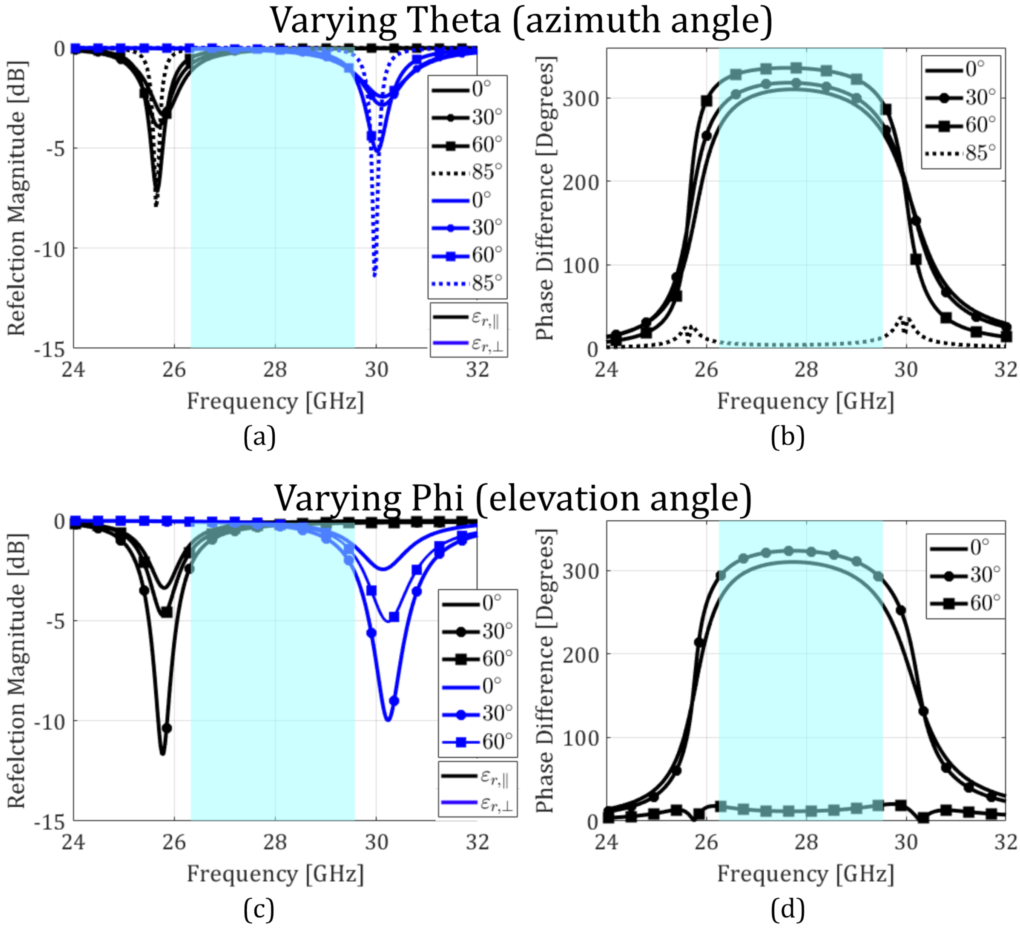

(a) (b)

(c) (d)

Figure 7.5: Simulation results for varying the angle of arrival for incident EM waves, using a spherical co-ordinate system, for the rectangular patch unit element. Theta (azimuth angle); reflection magnitude (a), phase difference (b), and for phi (elevation angle); reflection magnitude (c), phase difference (d). n257 frequency band shown in light blue.

particular interest here is the alteration of the phase difference plot as the variation in permittivity increases. The n257 frequency band contains a 3 GHz bandwidth with individual channel bandwidths of 50 MHz, 100 MHz, 200 MHz or 400 MHz, producing 60, 30, 17, or 7 individual channels, respectively. Hence, to apply a phase shift of, for example, 200° at 29 GHz, will require lower $\Delta\varepsilon_r$ value, compared to 27 GHz.

The problem is illuminated further in **Figure 7.7**(a) and (b), where the phase value and phase difference are plotted against the maximum achievable dielectric anisotropy for ZOC-A019XX, respectively. Again, the increase in dielectric anisotropy in this simulation is equivalent to an increase in applied voltage for a physical measurement. Assuming a

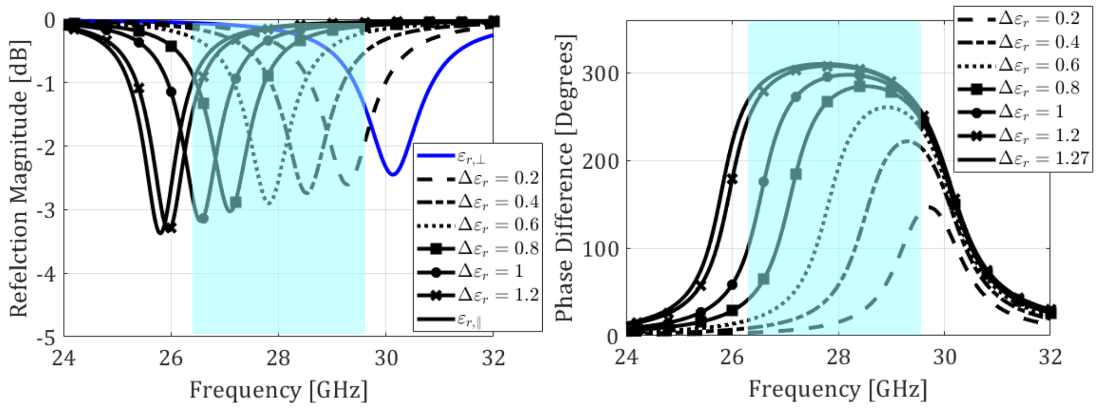

(a) (b)

Figure 7.6: Simulation results for increasing variation in relative permittivity (to the maximum achievable value for ZOC-A019XX) for the rectangular patch unit element. (a) reflection magnitude and (b) phase difference as a function of frequency of the EM wave. n257 frequency band shown in light blue.

200 MHz channel bandwidth and the carrier frequency centred in that band, the lower, mid, and upper n257 channels operate at a centre frequency of 26.6 GHz, 28 GHz, and 29.4 GHz, respectively, each of which is considered in Figure 7.7. The dashed lines in both plots represent possible phase values for an LC-based RIS that operates using a 2-bit, or 4-level, phase-shift. Hence, by Figure 7.7(a), if a RIS unit cell was required to apply a phase of -100° to a reflected wave, it was apparent that the dielectric anisotropy, and therefore, the applied voltage level, would be different depending on the particular carrier frequency of the n257 channel that was in use. In practice, the most simple and reliable way to implement this would be through characterising the phase-shift at each n257 channel for a given LC material. Another strategy could operate by describing the change of phase using an analytical expression, as a function of frequency and dielectric permittivity of the LC material. This is likely to be less accurate than measurements but could be applied more generally i.e., at different frequencies or LC materials.

A desirable feature of employing an LC-based RIS is that the number of phase-shift levels could be dynamically altered, depending on channel conditions, e.g., if a user was experiencing a low signal-to-noise-ratio (SNR). This is not possible for a RIS utilising p-i-n diodes: an increased number of phase-shift levels could only be achieved during manufacture at a significant cost increase, and could not be reduced thereafter.

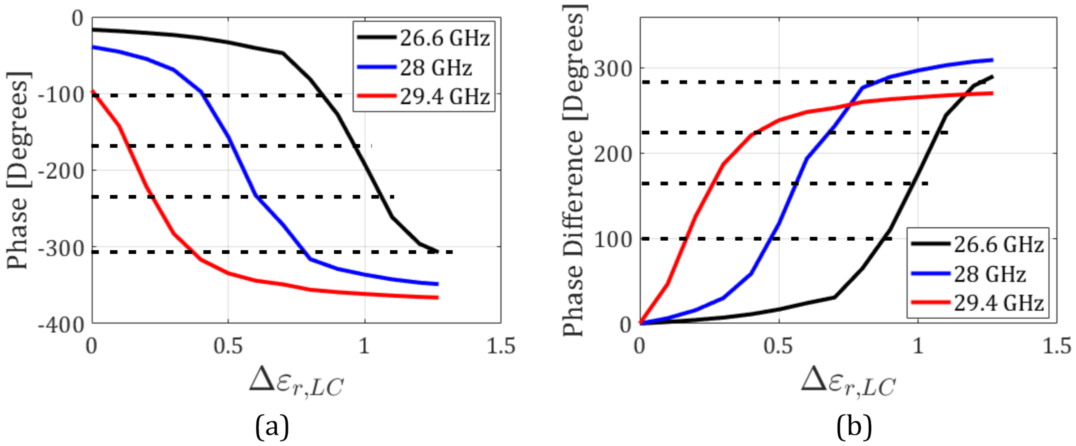

Figure 7.7: Simulation results of phase as a function of increasing relative dielectric anisotropy, at three discrete frequency points, for the rectangular patch unit element. (a) phase value and (b) phase difference. Dashed lines represent potential phase values for a RIS that applies a 2-bit (4 level) phase-shift to incident signals.

Furthermore, due to the phase errors inherent in a p-i-n diode RIS, e.g., ±20° in [4], there is an upper limit on the number of phase levels that could be reliably implemented, whereas nematic LCs are not as susceptible to this issue.

In Chapter 2, the behaviour of a RIS unit cell was described using a transmission line (TL) model, with the unit cell modelled by a capacitance between the reflective patch and groundplane, C, bottom layer inductance L_1, top layer inductance L_2, and resistance R. This model was employed using a nematic LC in place of the variable capacitance and plotted alongside the CST simulation results for comparison, displayed in **Figure 7.8**. For the TL model, the capacitance was calculated using the parallel plate method, assuming a rectangular patch unit cell with the geometry described in Table 7.1, and dielectric permittivity value that was representative of the nematic LC mixture, ZOC-A019XX. Specific values for the model were; $L_1 = 1.8$ nF, $L_2 = 0.9$ nF and $R = 1.2\ \Omega$. The results for reflection magnitude are congruent with the simulated values, with a disparity of 3% at each of the resonant points. The results for phase, however, were slightly less accurate, with the peak difference in phase values being 64° at 29 GHz. However, differences between a lumped-element model and a full-wave EM simulation are expected and there is enough agreement between the two to suggest that the TL model described in Chapter 2, holds for an LC-based unit cell, although some

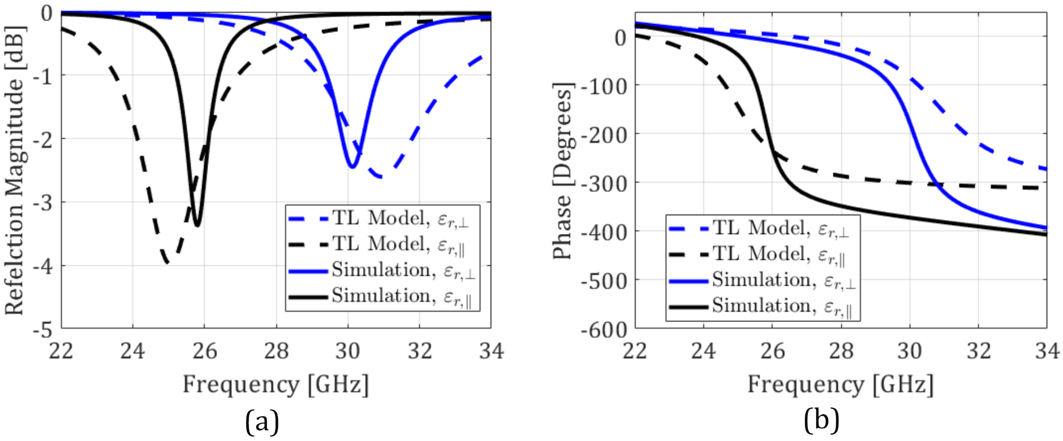

Figure 7.8: Plots of the reflection magnitude (a) and phase difference (b) as a function of the frequency of the EM wave for the rectangular patch unit element. Results from the Transmission line (TL) model and CST Simulations are presented.

further refinements are required.

7.3 Unit Cell Fabrication and Characterisation

7.3.1 Fabrication of Unit Cell

Once the geometry and performance of each RIS unit cell design were characterised using the periodic boundary simulations in CST, a computer-aided design file (specifically a Gerber file) was created to fabricate a PCB for those designs that were selected for further investigation, namely the rectangular and circular patches, as highlighted in the previous sections. The PCB was produced externally by Newbury Electronics as the materials and precise etching process were not available in-house. Since the PCB manufacturing process was likely to yield minor inaccuracies, three versions of each shape were printed; one with the exact values in Table 7.1, one with a 0.05 mm increase in size and one with a 0.05 mm decrease in size. Bias lines from the patch and ground plane to the side of the PCB were also included to enable an electric field to be applied across the LC layer, once it was incorporated into the unit cell. A photograph of the PCB containing a circular patch, alongside the groundplane, is shown in **Figure 7.9**.

To construct the RIS unit cells from the PCB the following steps were taken:

- two LC filling holes, with a diameter of 2 mm and 1 mm, were drilled into opposing

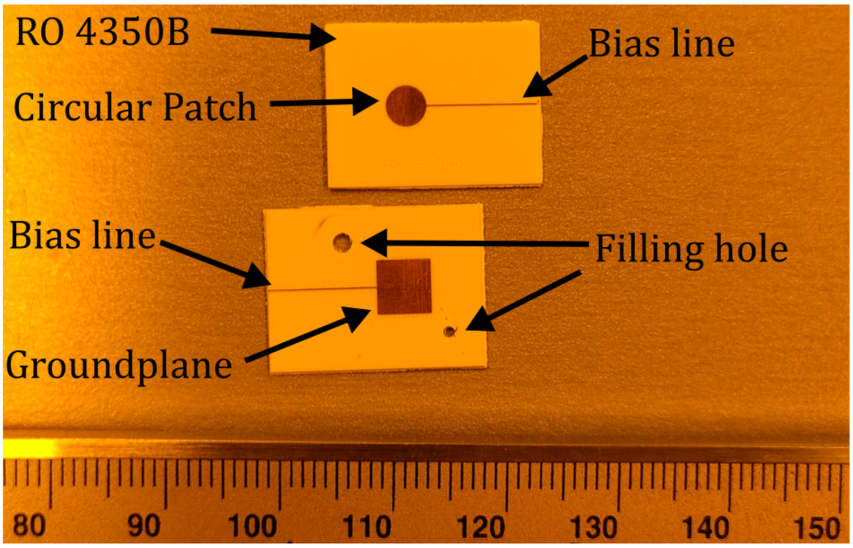

Figure 7.9: Photograph of the fabricated circular patch unit element and corresponding groundplane. Key features are labelled.

corners of the groundplane substrate.

- The groundplane and patch substrates were cleaned, and a homogeneous alignment layer was applied (both as described in Chapter 3) to the copper areas of the patch and groundplane.
- Double-sided adhesive spacer tape was applied to each of the outer edges of the groundplane substrate, forming a square with the filling holes on the inside. The tape was positioned to prevent escape of the LC (see Figure 7.10(b)) .
- The groundplane and patch substrates were combined and fixed together by the adhesive tape (see Figure 7.10(c)).
- the nematic LC ZOC-A019XX was injected into one of the filling holes until the cavity was completely filled with the material, and the holes were covered with black tape to prevent any LC from escaping.
- Small solder pads were added using copper tape, and copper wires were soldered onto the pads.

Figure 7.10 demonstrates three of the steps in the fabrication process; the PCBs as received from the manufacturer, the groundplane with filling holes and spacer tape, and

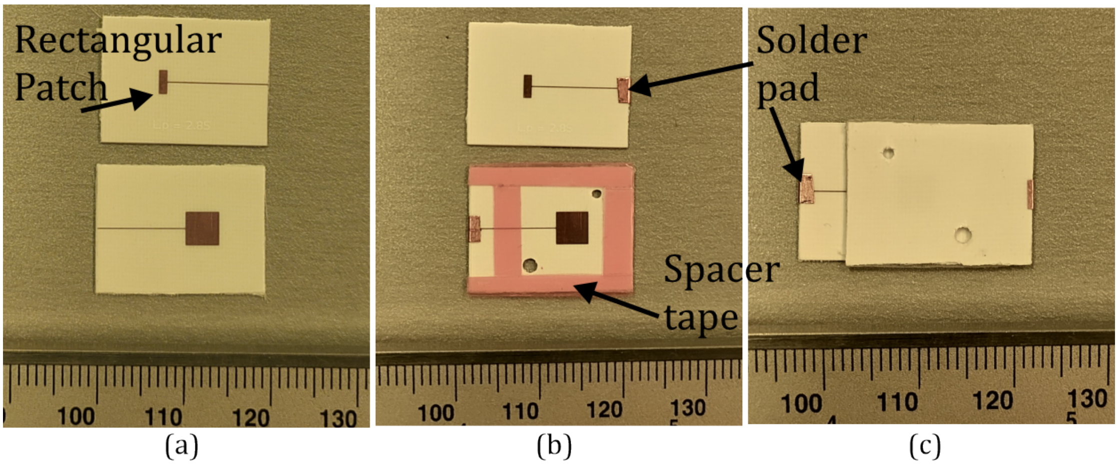

Figure 7.10: Photographs highlighting three key unit cell construction steps: (a) the rectangular patch and ground plane PCBs, (b) the filling holes, soldering pads and spacer tape added, and (c) patch and groundplane substrates combined.

the two PCBs combined such that the patch and groundplane overlap on the inside of the unit cell. Bias lines were included as the most simple way to apply an electric field across the LC layer; however, other methods such as using a via could be used in the future. The adhesive spacer tape was 200 μm thick, which effectively defines the thickness of the LC layer. As the copper thickness was 36 μm for the patch and groundplane, the LC layer thickness was $\approx$ 130 μm. An illustration of the unit cell, featuring the rectangular patch, location of the LC filling holes, bias line and spacers, is portrayed in **Figure 7.11**.

7.3.2 Measurement of Unit Cell Dimensions

To observe any disparities between the desired values for each shape that was discerned in the Gerber file, and the actual fabricated lengths, each version of the rectangular and circular patches was measured through illumination from the reflection arm of a polarising optical microscope under a 4× magnification, with the results for the rectangular patch displayed in **Figure 7.12**. Measurements for all patches are detailed in **Table 7.3**, with the desired values included in brackets. The tolerance for the PCB fabrication was stated by the manufacturer (Newbury Electronics) as ±0.1 mm, with each measured parameter in Table 7.3 congruent with that value.

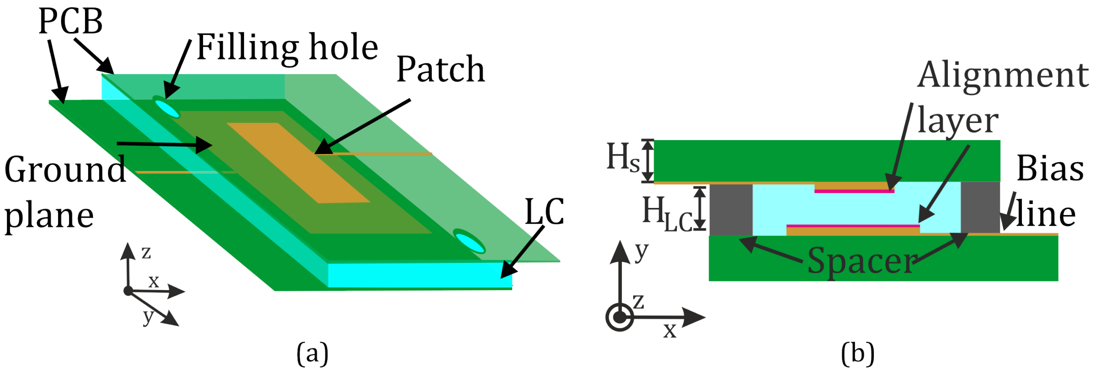

Figure 7.11: Architecture of the LC-based unit cell: (a) 3D isometric view with the upper PCB made transparent and no spacers visible for illustrative purposes, (b) an end-on view.

7.3.3 Measurement and Simulation of Unit Cells

To characterise the RIS unit cells that met the general conditions and benchmarks outlined in Section 7.1, the BAC experimental system described in Chapter 3 was utilised, specifically the phase reflection measurement portrayed in Figure 3.14(d). The vector network analyser (VNA) was calibrated between 20 GHz - 34 GHz and each of the two ports were connected to a H-A40 horn antenna (RF Spin). Unit cells were positioned 30 cm from the pair of antennas to ensure they were in the far-field, where it could therefore be assumed that the radiated wave incident at the unit cell was a plane wave. Because of the distances involved, the reflection magnitude results, both measured and simulated, presented in this Section were normalised, that is, scaled to between 0 and 1, then converted to dB. A voltage source was connected to the copper wires attached to the unit cell, providing a 1 kHz frequency square wave. A 3D printed mount was used to hold the unit cell in place with an initial measurement taken with no unit cell present, to record and remove any reflections of EM energy from the mount.

The physical process of conducting a measurement was thus; an RF signal was emitted from the transmit horn antenna via the VNA, this signal propagated through the wireless channel, into the far-field, and was incident at the unit cell; this RF energy was absorbed at the unit cell and re-radiated back to the horn antenna. An initial measurement was conducted with no voltage applied to the LC layer in the unit cell, which was used as a reference for the signal phase. Then, a voltage was applied to the LC layer, inducing the LC director to begin to align with the electric field, altering the relative dielectric

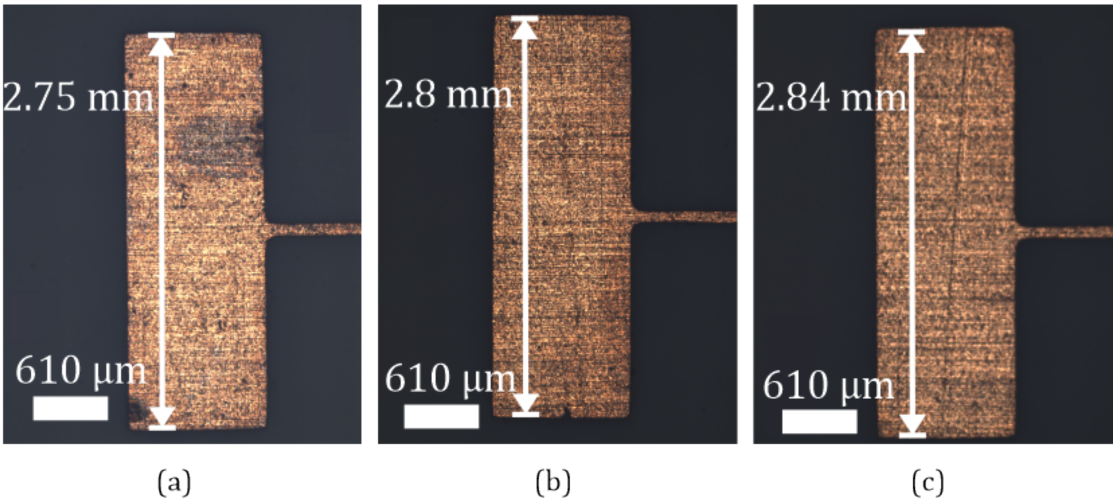

Figure 7.12: Photographs of the different rectangular patches obtained on an optical microscope operating in reflection. The three fabricated rectangular patches are shown for a 4× magnification as follows: (a) patch V1, (b) patch V2, and (c) patch V3.

permittivity of the LC. Now in a subsequent measurement, when the RF signal from the transmit horn antenna arrived at the unit cell, the phase of the signal reflected by the unit cell was shifted, compared to the reference, due to the change in LC permittivity. It was expected that increasing the voltage across the LC layer would lead to an increase in the phase-shift, from the 0 V (reference case).

In previous notable literature published on RIS construction, e.g., [2], [4], periodic boundaries and Floquet ports are utilised in EM simulation packages to characterise and optimise the RIS unit cells before constructing and measuring the complete RIS. However, a full RIS measurement was outside the scope of this Thesis and, instead, only the unit cell was measured. As the simulations presented in Section 7.2 assumed a periodic structure, they were not valid for the measurements of a single unit cell. Instead, it was necessary to develop a simulation model in CST that incorporated the full experimental arrangement described above, that is, a pair of H-A40 horn antennas and the relevant unit cell, positioned 30 cm away. This simulation will henceforth be referred to as the 'unit cell' simulation configuration. This type of configuration was not well-suited for CST Studio due to the very large boundary required, and hence necessitated a coarse mesh and restricted optimisation of the results. Nonetheless, it was necessary to perform this simulation to provide a link between the physical measurements of the unit cell and

Table 7.3: Measured parameters for each patch shape obtained using microscope with ×4 magnification in reflection mode. The desired values are shown in parenthesis.

Shape	Parameters [mm]	
Rectangular patch V1	W_r 0.96 (1)	L_r 2.75 (2.8)
Rectangular patch V2	W_r 0.96 (1)	L_r 2.8 (2.85)
Rectangular patch V3	W_r 0.97 (1)	L_r 2.84 (2.9)
Circular patch V1	R_c 1.72 (1.75)	
Circular patch V2	R_c 1.75 (1.8)	
Circular patch V3	R_c 1.82 (1.85)	

CST simulations.

Of the four unit cell candidates that were assessed in in Section 7.2, only the rectangular and circular patches met the requirements outlined at the start of this Chapter. Three versions of each, with minor alterations to the dimensions governing their resonant frequencies, as described in Table 7.3 were tested. **Figure 7.13** demonstrates the BAC measurements for the rectangular patch V2, including the reflection magnitude and phase difference with no voltage, and with 100 V applied across the LC layer. The LC layer thickness for the rectangular patch V2 unit cell was $\approx 130\ \mu$m, which was determined by the thickness of the double-sided adhesive spacer tape and copper thickness, and measured using digital calipers. The normalised reflection magnitude results show that the unit cell operating bandwidth was shifted down in frequency to 24.5 GHz - 28.2 GHz, and therefore did not align with the n257 band. However, the measured bandwidth, that is, the distance between the lower and upper resonant points, was 3.7 GHz, and therefore sufficient for the n257 band. The reflection magnitude was > -5 dB for both the 0 V and 100 V measurements. For the 100 V measurement there was an observable drop-off in reflection magnitude below 26 GHz, as this was outside the ideal operating frequency range of the H-A40 antennas and the antenna gain was reduced. The unit cell size was 0.26λ, below the general requirement of 0.5λ.

A phase-shift was observed between 24 GHz - 27.8 GHz, with an average value of 20°. The phase-shift frequency range matched with expectations from the periodic boundary simulations but the phase value was markedly denigrated. This was attributed to the periodic assumption of the periodic boundary simulation, where the adjacent unit cells have a sub-wavelength separation and hence contribute to the realised phase-shift through mutual coupling. The use of bias lines and imperfections from fabricating the unit cell by hand, also likely contributed to the denigration in phase-shift performance.

The 'unit cell' CST simulation results for the normalised reflection magnitude were in reasonable agreement with the measurements: there was a slight discrepancy in the resonant frequency between the measurement at 0 V and simulation at $\varepsilon_{r,\perp}$, indicating a slightly increased relative permittivity from the measured unit cell, likely due to the inability of the surface anchoring effects to maintain an ideal alignment through the 130 μm thick LC layer. The depth of the simulated resonant peaks was significantly increased compared to the measurements. The 'unit cell' simulation results for the phase difference are again in reasonable agreement with the measured results, except for the two peaks occurring at the edges of the phase-shift bandwidth and corresponding to the sharp resonant frequencies in the simulated reflection magnitude plot. The disparities between the 'unit cell' simulation and BAC measurements, most noticeably the sharp resonant peaks and phase-shift peaks, were likely caused by either fabrication imperfections, slight differences in the BAC measurement compared to the 'unit cell' configuration, or because the mesh cells were too coarse, which was necessary due to the large bounding box required. Nonetheless, these differences were not a major concern as there was otherwise reasonable agreement between the simulated and measured performance in terms of the resonant frequency of the reflection magnitude, with the minor disparity between the measurement at 0 V and simulation at $\varepsilon_{r,\perp}$ accounted for.

A comparison between the normalised reflection magnitude of the BAC measurement and 'unit cell' simulation, of the rectangular patch V2 unit cell for a varying voltage and dielectric anisotropy, respectively, is presented in **Figure 7.14**. The measurement results

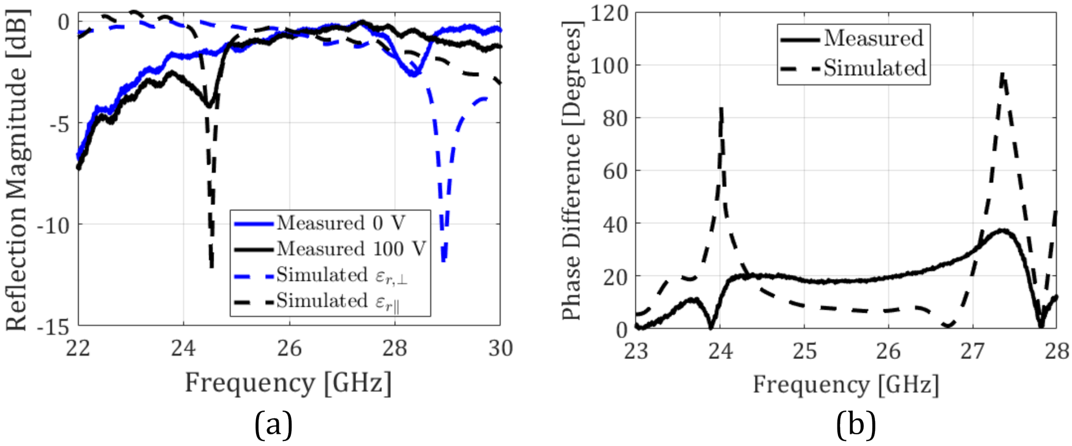

Figure 7.13: Results from measurements and simulations for the rectangular patch V2 unit cell. (a) reflection magnitude and (b) phase difference as a function of frequency.

show that half of the frequency shift occurred below 20 V and most of it had occurred at 60 V, although there was still a further 200 MHz of frequency shift after applying 100 V. This effect was mirrored in the 'unit cell' simulations, where increasing the contrast between the dielectric permittivities with and without an applied voltage increased the frequency deviation. For example, the frequency shift at 26 GHz corresponds to an applied voltage of 20 V and $\Delta\varepsilon_r = 0.85$. The measurement results in Figure 7.14 are congruent with the pattern in the periodic boundary simulations in Figure 7.6; for example, in both simulations, a variation of the LC relative permittivity of $\Delta\varepsilon_r \approx 0.8$ elicits a frequency shift of ≈ 3 GHz.

In **Figure 7.15**, the measured phase difference is plotted against increasing voltage for three separate frequency points; 27.5 GHz, 26 GHz, and 24.5 GHz, which were selected as they sit in the bandwidth of the measured rectangular patch V2 unit cell. The results follow a similar shape to the periodic boundary simulations for phase difference against dielectric anisotropy in Figure 7.7, forming an approximate 's'-shaped curve. The measurements of phase as a function of applied voltage were subject to fluctuations due to phase drift, which was mitigated by removing the voltage and re-measuring the 0 V case after each time the voltage had been increased; however, there remained some unwanted variability in the results. This was worsened further by the reduced range of the phase difference, making a phase drift of just 1° - 2° more noticeable.

Figure 7.16 portrays the BAC measurements for the circular patch V1 unit cell,

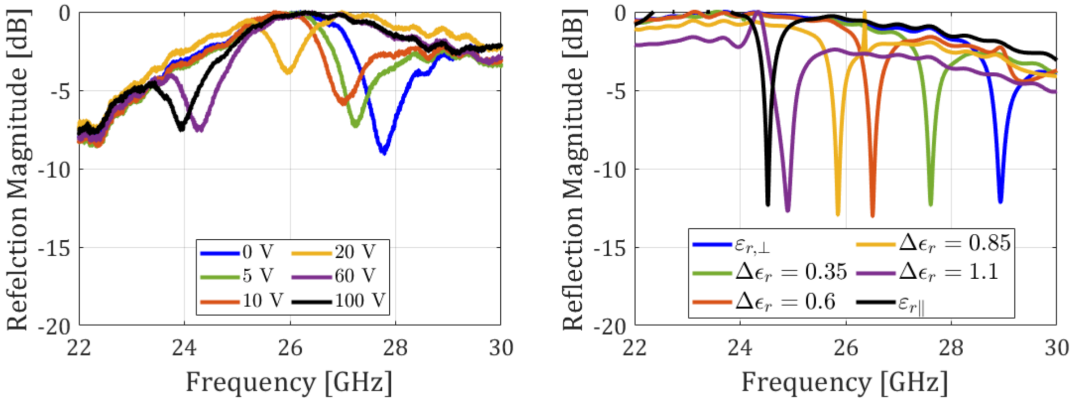

(a) (b)

Figure 7.14: Results for the rectangular patch V2 unit cell showing the reflection magnitude as a function of frequency for (a) measurements for different applied voltages and (b) simulations for different values of $\Delta\varepsilon_r$.

showing the normalised reflection magnitude and phase difference with no voltage, and with a 100 V applied across the LC layer. The LC layer thickness for the circular patch V1 unit cell was ≈ 130 μm. The normalised reflection magnitude results demonstrated that the unit cell operating bandwidth was unaligned with the n257 band, being shifted down in frequency to 23.05 GHz - 27.5 GHz, whereas the measured bandwidth was 3.45 GHz which was sufficient for the n257 band. The normalised reflection magnitude was above -5 dB for both the 0 V and 100 V measurements, accounting for the drop-off in reflection magnitude below 26 GHz, due to the reduced antenna gain. The unit cell size was 0.16λ, below the requirement of 0.5λ.

An average phase difference of 15° was observed between 23 GHz - 27.8 GHz. As with the rectangular patch V1 measurements, the phase value for the circular patch measurements was markedly denigrated compared with the phase-shift achieved in the periodic boundary simulations. This was again expected due to the periodic assumption of those simulations creating mutual coupling between the unit cells, bias lines and imperfections from fabricating the unit cell.

The 'unit cell' CST simulations corresponding to the circular patch V1 unit cell for the normalised reflection magnitude were congruent with the BAC measurements, although there was a minor mismatch in the resonant frequency between the measurement at 100 V and simulation for $\varepsilon_{r,\parallel}$, indicating a slightly reduced relative permittivity from the

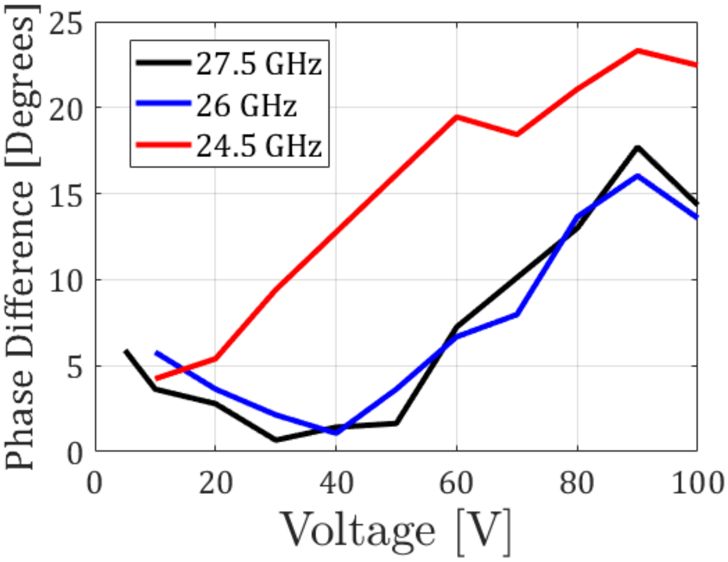

Figure 7.15: Measured phase difference as a function of voltage at three discrete frequencies for the rectangular patch V2 unit cell.

measured unit cell. Furthermore, the depth of the simulated resonant peak for $\varepsilon_{r,\|}$ was slightly increased compared to the measurement at 100 V. Both of these artifacts could have been caused by fabrication errors and/or misalignment between the measurement and 'unit cell' simulation configurations. The 'unit cell' simulation results for phase difference were again in reasonable agreement with the measured results, with the two peaks occurring at the edges of the phase-shift bandwidth as was observed in Figure 7.13.

Figure 7.17 compares the results for the normalised reflection magnitude of the BAC measurement with the 'unit cell' simulation for the circular patch V1 unit cell. Results are presented for a range of different applied voltages and corresponding dielectric anisotropies. The behaviour indicated in Figures 7.17(a) and (b) suggested that the effect of increasing voltage across the LC layer for the measured unit cell corresponded to an increase in accessible dielectric anisotropy in the LC of the simulated unit cell. The measurement results established that the majority of the frequency shift occurred below 20 V and only a further 100 MHz of frequency shift was achieved by applying a larger voltage of 100 V.

Table 7.4 details the results for the BAC measurements of the rectangular V1, V2, V3, and circular V1, V2 and V3 patches, alongside an 'ideal' case which corresponds to

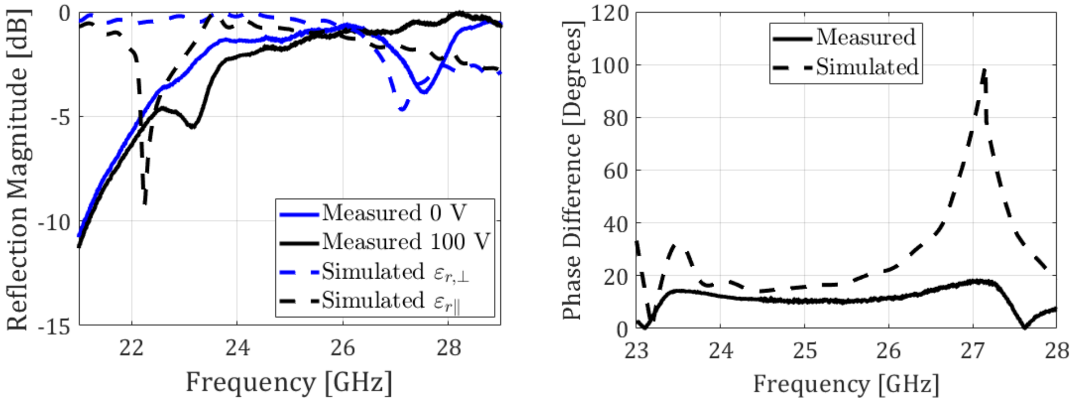

(a) (b)

Figure 7.16: Comparison of measured and simulated results for the circular patch V1 unit cell: (a) reflection magnitude, (b) phase difference.

the requirements delineated in Section 7.1, and results that were demonstrated via the periodic boundary simulations in Section 7.2. Two of the devices, the rectangular patch V1 and circular patch V3 failed during fabrication, that is, they were damaged and not repairable. The thickness of the LC layer was tested at 30 μm, 130 μm, and 230 μm to gauge the effect of varying the LC layer thickness.

Evaluating the measurement results for each unit cell design against the requirements set out in Section 7.1 indicated that none of the unit cells operated in the n257 band; however, this could be easily rectified by adjusting the geometry of the rectangular or circular shape. More importantly, these unit cells exhibit sufficient bandwidth (>3 GHz) to operate in the n257 band. Moreover, each of the cells meets the requirement of reflection losses above > -5 dB, and they are all below 0.5λ in size.

In terms of the phase-shift requirements, none of the unit cells have met the benchmarks set out in Section 7.1. The consistency of the denigrated phase difference in the 'unit cell' simulations and BAC measurements suggested that this was caused by the lack of mutual coupling between unit cells, which was present in the periodic boundary simulations, and not to a particular fabrication error. However, it also could be caused by a consistent error in the BAC measurement arrangement. The simplest way to address this would be to fabricate a periodic unit cell; for example, a PCB with a 3 × 3 grid of unit cells, each addressed by the same voltage. This would produce a result more

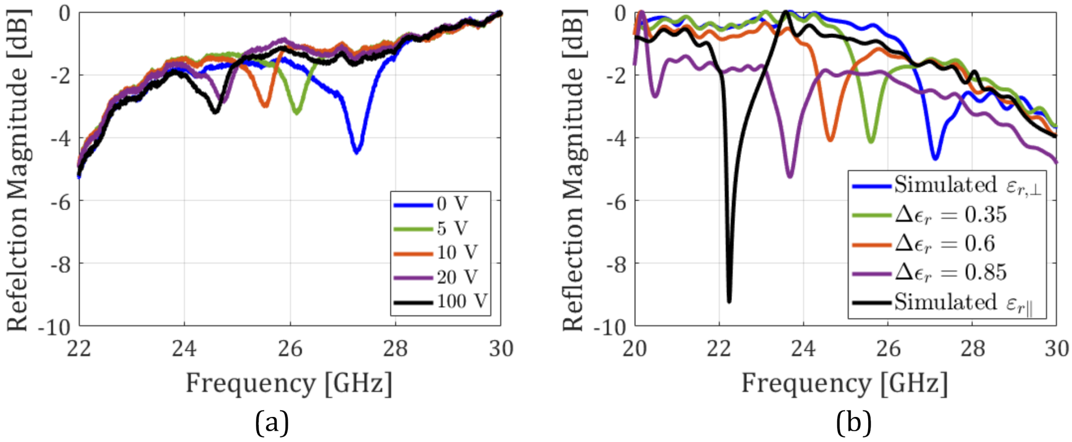

(a) (b)

Figure 7.17: The reflection magnitude as a function of frequency for the circular patch V1 unit cell. (a) measurements obtained by varying the magnitude of the applied voltage and (b) corresponding simulations whereby the change in applied voltage is accounted for by a change in the magnitude of the $\Delta\varepsilon_r$.

closely aligned with the periodic boundary simulation and negate the need to develop a complete RIS.

One metric not thus-far considered is the LC switching times. The nematic LC mixture used here, ZOC-A019XX, featured a rotational viscosity twice that of E7 [70]. Coupled with the large LC layer thickness, switch-on times for the unit cells were found to be in the region of 1 s, whereas switch-off times were on the order of 10 s. This would be difficult to implement in a 5G network due to the low-latency requirements. However, several published works have sought to reduce LC switching times, most successfully through the use of dual-frequency LCs and specially designed bias signals that have demonstrated a reduction in switch-on and switch-off times to the order of milliseconds, although this could reduced the tunability of the LC [68].

7.4 Conclusions

This Chapter has detailed an investigation into the feasibility of employing a nematic LC to enable direct control of the phase-shift in a RIS. A set of stringent requirements was first defined for an LC-based RIS such that it would be suitable for implementation into a 5G network operating in the n257 band, performing at least as well, or better, than a leading competitor using p-i-n diode RIS technology. An initial assessment using the

Table 7.4: Summary of results from experiments. Ideal values refer to the periodic boundary simulation results from Section 7.2. PD refers to phase difference and RM refers to reflection magnitude.

Shape	H_{LC} [μm]	F_1 [GHz]	F_2 [GHz]	ΔF [GHz]	Peak PD [Degrees]	RM [dB]
Ideal	**150**	**26.5**	**29.5**	**3**	**360**	**-5**
Rectangular patch V1	Device Failed					
Rectangular patch V2	130	24.5	28.5	3.7	20	-4.2
Rectangular patch V3	30	24.3	29.3	5	10	-2.7
Circular patch V1	130	23.05	27.5	3.45	10	-8.1
Circular patch V2	230	22	25	3	40	-5.1
Circular patch V3	Device Failed					

academic standard of a periodic boundary simulation of four different unit cell designs (an SRR, a rectangular patch, a circular patch, and a double bowtie) led to the SRR and double bowtie being evaluated as not suitable due to their poor reflection losses in the operational bandwidth. However, simulations of both the rectangular and circular patch met each of the conditions and exhibited superior phase-shift performance over the leading competitor.

The circular and rectangular unit cells were subsequently fabricated and tested using the BAC system developed for experimental evaluation. Both designs met the requirements in terms of frequency range (bandwidth), reflection magnitude and unit cell size; however, neither attained the most basic requirement for phase-shift. Even though the phase-shift measurements did not meet requirements, this was accounted for by the mutual coupling effect produced by the period boundary assumption in the simulation, and the LC-based RIS unit cell was able to conform to each of the other stipulated requirements. Of particular interest was the large frequency shift exhibited by using a bespoke nematic LC mixture, ZOC-A019XX. These requirements were designed to benchmark an LC-based RIS against a leading alternative. Periodic boundary simulations, which were employed by the alternative, indicated that the LC-based unit cell can indeed exhibit superior performance. A further advantage of utilising a nematic LC is the ability to dynamically increase the number of phase levels that can be employed by the RIS: a feature that cannot be easily achieved using p-i-n diodes. Increasing the number of phase values in a p-i-n diode-based RIS, to a 2-bit configuration, for example, necessitates twice the number of p-i-n diodes as a 1-bit RIS, representing a substantial cost increase. The main disadvantage of using LC for a 5G RIS unit cell is the switching times, which could limit the RIS from responding to the required phase adjustments in real-time. However, this problem has been mitigated in other published works through the use of dual-frequency LCs. Alternatively, applications where the LC switching time would not inhibit the RIS performance, such as satellite communications, could be explored.

Lastly, the performance established from the periodic boundary simulations, much of which is supported by the results from measurements, has demonstrated that an LC-based unit cell, using either the circular or rectangular patch design, would be suitable for use in an LC-based RIS operating in the n257 5G band. To address the undesirable phase-shift observed in the experiments, a 3×3 array of unit cells could be tested before proceeding with a full RIS.

Chapter 8

Dual-Mode Reconfigurable Intelligent Surface Unit Cell for Visible Light Communications

This Chapter extends the development of a liquid crystal (LC) unit cell for reconfigurable intelligent surfaces (RIS) technology tailored for the radio frequency (RF) band to a RIS unit cell designed for use in the 400 THz - 800 THz band, that is, the visible portion of the electromagnetic (EM) spectrum. This is motivated by the recent research focus on RIS for visible light communications (VLC) systems coupled with the significant capabilities of nematic LC technologies at optical wavelengths. Furthermore, to date, previous reports have been concerned with the study of channel models and simulations, merely alluding to potential element designs, without actually realising any physical structures.

The objective of this Chapter, therefore, is to demonstrate a novel RIS unit cell for VLC that operates in a dual-mode, that is, both transmission and reflection modes, by exploiting the reflection band of a chiral nematic LC to reflect impinging light signals, with an electric field applied across the chiral nematic LC to unwind the helix and allow the transmission of optical signals. The chiral nematic LC is combined with an additional layer in the unit element that contains a nematic LC that is employed to impart a phase-shift of up to 2π on light signals incident at the RIS. This design provides a route towards a RIS constructed of many independent phase-shifting elements that would be able to elicit beam steering and direct light signals from the RIS to a user that does not have line of sight (LoS) access to the VLC access point (AP), or to improve the performance of the link by utilising the EM energy incident at the RIS, that would otherwise be wasted. A manuscript for this work is in preparation.

The main contributions in this Chapter are:

- a novel unit cell for a LC-based VLC RIS that can operate in both transmit and reflect mode is proposed.
- For the first time, a VLC RIS unit cell is constructed and experimentally validated, with LC director profile simulations to compare the results.

The remainder of this Chapter is arranged as follows: in Section 8.1, an introduction to VLC systems and RIS for VLC, along with a literature survey is presented. Then in Section 8.2 the background theory pertaining to chiral nematic LCs and VLC is discussed, followed by the dual-mode unit cell design in Section 8.3. Section 8.4 details the experimental methods used to investigate the unit cell, before the results, including the reflection band of the chiral LC device and full unit cell, are demonstrated in Section 8.5. Finally, conclusions are discussed in Section 8.6.

8.1 Introduction

With the ever-increasing demand for faster data rates and the growing number of interlinked wireless devices, researchers have sought to develop novel communication techniques to expand bandwidth capabilities, for example, in the millimetre-wave (mm-wave) or terahertz frequency bands. VLC is an optical wireless communication (OWC) technology that exploits the visible portion of the EM spectrum to simultaneously transmit data and illuminate an enclosed indoor space. With the further advantage of the visible portion of the spectrum, specifically 400 THz - 800 THz, being currently unlicensed, VLC is expected to be a key enabler for sixth-generation (6G) systems that will integrate air, space, and underwater with terrestrial networks and thus require high data rates, with speeds of up to 15 Gb/s achieved in a VLC system [94].

VLC can be utilised to complement existing RF networks, for example in WLANs, or employed in its own right to reduce the load of RF networks in industrial or home environments, or to replace RF in settings such as healthcare or aviation to negate interference between RF emissions and sensitive equipment [95]. 6G networks will comprise myriad nodes: smart watches, smart glasses, pacemakers, and health monitoring sensors will all be employed to collect and transmit sensitive data. VLC can enhance the physical layer security by its natural inability to penetrate though walls and thereby prevent eavesdroppers from capturing this personal data [96].

A typical VLC system comprises a light source at the transmitter, a convex lens with a photodiode (PD) at the receiver, and a wireless channel that the light emission propagates through. In a VLC link the transmitter and receiver can suffer from a narrow field of view (FoV), when compared to RF antennas. Furthermore, the optical wireless channel introduces path loss and shadowing, with the latter particularly severe for VLC. Hence, RISs have been proposed to improve the link by manipulating incident light towards the target PD, navigating dead zones when there is no line of sight (LoS), or reducing the required transmitter power, in a dynamic scheme that can trade user requirements for data rate and illumination [97].

However, due to the differences between RF and VLC links there remains challenges to meet in delivering RIS for VLC such as; RIS construction and deployment, VLC channel models and estimation, improving the PD FoV, and optimisation of energy efficiency or data rates. A comparison between two RIS structures, a metasurface with independent phase-shifting elements and an array of mirrors with independent adjustments of orientation in two degrees of freedom was made in [98]. Simulation results suggested that both RIS schemes improved the link performance by a factor of five against the LoS only case, with little difference between the two methods. In [99], low-cost 2-D beam-steering for an OWC link was achieved by using polarisation gratings with a nematic LC to change the polarisation via an externally applied voltage. The FoV was increased when using beam-steering at the transmitter and receiver, over transmitter beam-steering alone, without denigrating the data rate. The authors in [100] addressed LoS blockages alongside random receiver orientation and random blockages, with a rate maximisation algorithm proposed to find the optimum orientation of a RIS mirror array. Simulations in [100] showed that the RIS mirror array improved the data rate by a factor of two when compared to a wall, and the outage performance was also improved by a factor of two when considering random blockers in a non-RIS versus RIS scheme.

Channel estimation for optical RIS cannot be achieved in the same way as for an RF RIS; the Lambertian wave model was adopted for VLC, opposed to planar or spherical wave models for far and near-field RF, respectively, and because the VLC RIS unit elements are not sub-wavelength, the specular reflector approximation must be applied, rather than the diffuse reflector [101]. The behaviour of a RIS-assisted VLC channel was assessed, specifically comparing a metasurface and a mirror-array, and deriving the continuous-time impulse response for both in [102]. The upper and lower bounds of the delay spread for each reflector was also derived, with simulations suggesting these bounds became tighter with a smaller source area. In [47], a channel estimation process involving joint space-time sampling was proposed. A codebook created to dynamically control the angle of each reflector in the RIS mirror array and estimation was achieved by splitting the RIS into sub-divisions and measuring the channel state information (CSI). The precise CSI for each element was then estimated through interpolation.

The first LC-based VLC RIS was proposed in [103], where an LC-based RIS was positioned at the VLC receiver in place of an optical concentrator/lens. The LC device was employed to condition the incoming light via stimulated emission before it reached the PD. The unit cell design utilised a photoconductive chiral compound with the terthiophene, 3T-2 MB LC, mixed with a 0.1 wt% concentration of trinitrofluorenone, to alter the transmittance of incident light. Experiments showed that increasing the concentration of the dopant reduced transmittance at 0 V to 70%, however, when a voltage was applied across the LC cell the transmittance was increased by up to 230%, compared to the case where no LC cell was present. The dopant also affected the transition phase temperature, order parameter and diffraction properties of the LC. The same idea was tested again in [104], with an LC-based RIS at the receiver used to steer and amplify the intensity of incident light. A channel model and rate optimisation algorithm based on a LC RIS was proposed with simulations suggesting the achievable rate could be increased by a factor of three, although this was only simulated at discrete wavelengths. In [105], a mirror array in the channel and a LC-based RIS at the receiver were proposed with a rate maximisation algorithm to jointly optimise the two, assuming random blockers in the LoS. Simulations suggested that the joint technique might achieve a three-fold improvement in rate, and up to a threefold improvement in energy efficiency, compared to the LC-only system in [100] but only a minor improvement over the system in [104]. A multi-user RIS system that used simultaneous transmit and receive (STAR) was proposed in [106]. Two multiple access strategies were tested, rate-splitting multiple access (RSMA) and non-orthogonal multiple access (NOMA), with the system model accounting for the LoS/non LoS paths and the refractive index of the LC. Simulations suggested that the RSMA scheme produced enhanced results over NOMA in terms of sum rate at a given transmit power, or number of users, and energy efficiency for a given number of RIS elements. However, no results were presented to assess the LC-based STAR RIS scheme against an alternative scheme e.g., an LC-based RIS without STAR. No design of the LC unit cell was proposed, and due to the construction of the RIS, the total number of elements must be divided, with some elements for transmission mode and some for reflection mode. No assessment was made into the optimal way to do this.

Spatial light modulators (SLMs) operate in a similar manner to a RIS unit cell in a VLC system, in that the SLMs are employed to modulate the phase or amplitude of light signals using a nematic LC. For example, in, [107], an SLM was used at the transmitter to combine time division multiple access (TDMA) and optical beamforming to direct the optical signal between two users. However, there are several key differences between an SLM and RIS for VLC applications: SLMs are most commonly utilised at the transmitter to modulate or steer/focus the optical signals, requiring LoS; whereas, RISs operate in the optical wireless channel to extend signal coverage when the is no LoS, directing the light signals to the user. The financial cost of a RIS is also substantially lower than for an SLM.

8.2 Background

8.2.1 Chiral Nematic LCs

Nematic LCs can be distorted through the introduction of a chiral material that imparts a macroscopic helical twist in the LC director resulting in a chiral nematic LC phase (CLC), which was historically known as the cholesteric phase [72]. The chiral nematic and nematic LC mesophases are locally similar: both exhibit orientational order along a

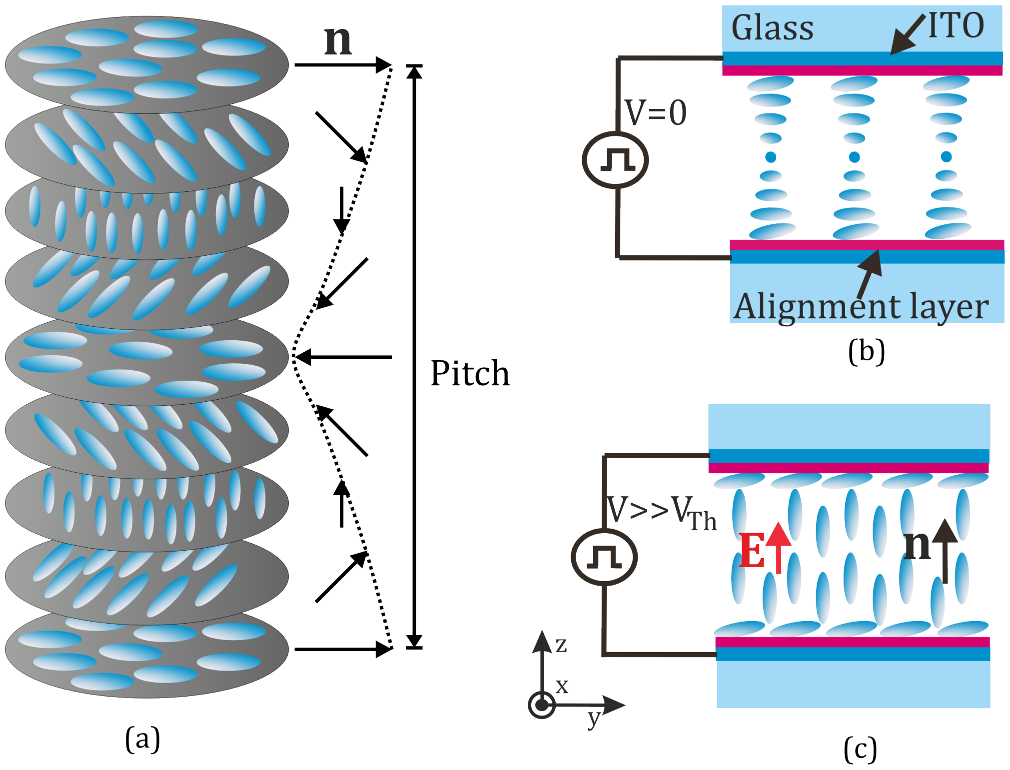

Figure 8.1: (a) Chiral nematic LC (CLC) and the definition of the pitch. (b) CLC in a device with homogenous alignment at 0 V, forming a Grandjean texture, and (c) a CLC in the same device with a large voltage applied, thereby unwinding the helix.

preferred axis, given by the LC director $\mathbf{n}$, and no long-range positional order. However, for chiral nematic LCs the preferred conformation is helical, with the director rotating about the helical axis, and a full 360° rotation defined as the pitch, p, as illustrated in **Figure** 8.1(a). Since $\mathbf{n} = -\mathbf{n}$, the periodicity, L, of the helical structure along the helical axis is $L = p/2$. The direction of rotation of the helix can be either right-handed or left-handed, with the direction defined by the molecular structure/handedness of the chiral dopant.

The pitch of a chiral nematic LC can be tuned by temperature, external fields, and in some cases, light for chiral additives that are sensitive to optical wavelengths, and exhibit a trans-cis conformation change. For the case of an external electric field, and for a nematic LC host with a positive dielectric anisotropy, a sufficiently strong field can fully unwind the helix, as demonstrated in Figure 8.1(b) and (c). Upon removal of the electric field, the chiral nematic LC will return to its helicoidal geometry. The electric field strength required to fully unwind a chiral helix is given by [72]

$$E = \frac{\pi}{p}\sqrt{\frac{K_{22}}{\Delta\varepsilon_r\varepsilon_0}} \tag{8.1}$$

where, K_{22} is the constant of elasticity related to a twist deformation, and the dielectric constant is at the frequency of the applied field.

Furthermore, the pitch can also be altered by varying the concentration of chiral dopant in the nematic LC host. For high concentrations, the pitch can be made to be comparable with optical wavelengths, and hence, result in Bragg reflection of light propagating along the parallel to the helical axis. For an incident light beam of wavelength, λ, Bragg reflection will occur in a chiral nematic LC with a bandwidth $\Delta\lambda = p\Delta n$, where $\Delta n = n_{\parallel} - n_{\perp}$, where $n_{\perp}$ and $n_{\parallel}$ are the LC refractive index perpendicular and parallel to the local director, respectively. Depending upon the magnitude of the birefringence and the helical pitch, the reflection bandwidth can be of the order of $\approx$ 50 nm - 100 nm. However, broadband reflection covering the entire visible spectrum has been demonstrated in [108], where the gradient of the helical pitch was increased by diffusing a combination of pitch-tightening cholesteric monomers and pitch-widening nematic monomers during polymerisation. This produced a chiral nematic LC with a graduated pitch that reflected 98% of incident light in the visible spectrum.

Two important observations on the polarisation of the reflected light must be considered [72]: the light reflected by the CLC is circularly polarised, and if the direction of the polarisation matches that of the helix, it is strongly reflected, if it is in the opposite direction the light is transmitted without significant reflection.

8.2.2 Visible Light Communications

A high-level comparison of a RIS-assisted wireless channel between RF and VLC yields many similarities between the two systems; however, there are several key differences between the two:

- RF systems employ antennas at the transmitter and receiver that are typically omnidirectional and can operate over large distances and can penetrate walls. Whereas VLC systems are deployed indoors and commonly utilise LEDs at the transmitter, which are also required to illuminate the room, with the receiver a PD with a restricted FoV.

- RF systems operate in duplex, whereas VLC is typically simplex, although full duplex systems have been demonstrated [109].
- The frequencies for RF systems are typically < 6 GHz, with 28 GHz systems in development. For VLC, the frequency range is 400 THz - 800 THz and as such, benefits from substantially larger bandwidths.
- In the wireless channel, both systems suffer from noise, interference, path loss and shadowing, however only RF systems are subject to multipath. In a VLC link, the interference arises from other sources of light, and the most significant sources of noise are thermal and Poisson (shot) noise.
- The transmitted RF signal can be complex and both positive and negative, whereas a VLC signal must be positive and real. This dictates the type of modulation schemes used for VLC, for example, OFDM cannot be directly applied (variations have been proposed). Standard modulation schemes for VLC include; on-off keying, colour shift keying and variable pulse position modulation.
- Pertaining to RIS, the primary disparity is the hardware: in RF RISs the unit cell is comprised of solid metallic patches and only optimises the phase-shift of the reflected signal. VLC RISs have been proposed that are formed of mirrors or LCs and must consider communication and illumination performance. The deployment for VLC RISs is closer to the AP and UE, covering distances of several meters.

The VLC system features an LED source as the access point, although a laser source could also be used, and operates unidirectionally in an indoor downlink system that can serve multiple users, however, here a single user equipment (UE) will be considered. To compensate for inherent dead zones in the environment, or shadowing caused by blockers (this includes random blockages from people or self-blocking), a RIS consisting of many unit elements can be employed to cause a 2π phase-shift on the light impinging at each independent unit element to steer the reflected light towards the desired user.

The RIS design proposed here in this chapter can operate in either transmission or reflection mode with each unit cell able to operate in both modes, switching between the two with the application of a voltage. The general case will include two rooms with a window between them, or a room and a corridor. **Figure 8.2** illustrates four specific use-cases for this LC-based RIS: the use-cases are split into transmission/reflection mode and into wide/narrowband helical pitch from the CLC. In Figures 8.2(a) and (b) a broadband helical pitch is assumed, that is, the entire range of the visible spectrum is reflected by the chiral nematic LC device. The RIS works in transmission mode (Figure 8.2(a)) by applying a phase-shift at each independent element to beam-steer the signal towards UE, which is in an adjoining room/corridor, with no AP, and may be subject to blockages, with the RIS embedded into a window connecting the two spaces. Figure 8.2(b) illustrates the RIS in reflection mode, addressing blockages between the AP and the UE by reflecting the signal from the AP to the UE, as well as inducing a phase-shift on the incident optical signals.

For Figures 8.2(c) and (d), a narrowband helical pitch in the CLC is assumed, with the reflection bandwidth designed to operate at wavelengths that encompass red light. In Figure 8.2(c) the RIS acts as a filter, preventing a narrowband of wavelengths from penetrating into the adjoining room, while also applying a phase-shift to the wavelengths that do penetrate. Figure 8.2(d) presents the final use-case, where the same narrowband of wavelengths are now reflected into the room with a phase-shift applied. Red light is used here for illustrative purposes but any continuous band in the visible range could be filtered in this way, subject to the achievable reflection bandwidth from the CLC.

8.3 Unit Cell Design

8.3.1 Chiral LC Reflector

To produce a single RIS unit element that could operate in both reflection and transmission mode in a VLC system, a CLC with the pitch tuned so that it reflects visible light was required. A further constraint was applied by the wavelength of the laser that was used to experimentally validate the unit cell, which operated at $\lambda = 633$ nm. To form the narrow reflection band CLC mixture, the nematic LC, E7 (Synthon chemicals Ltd), was

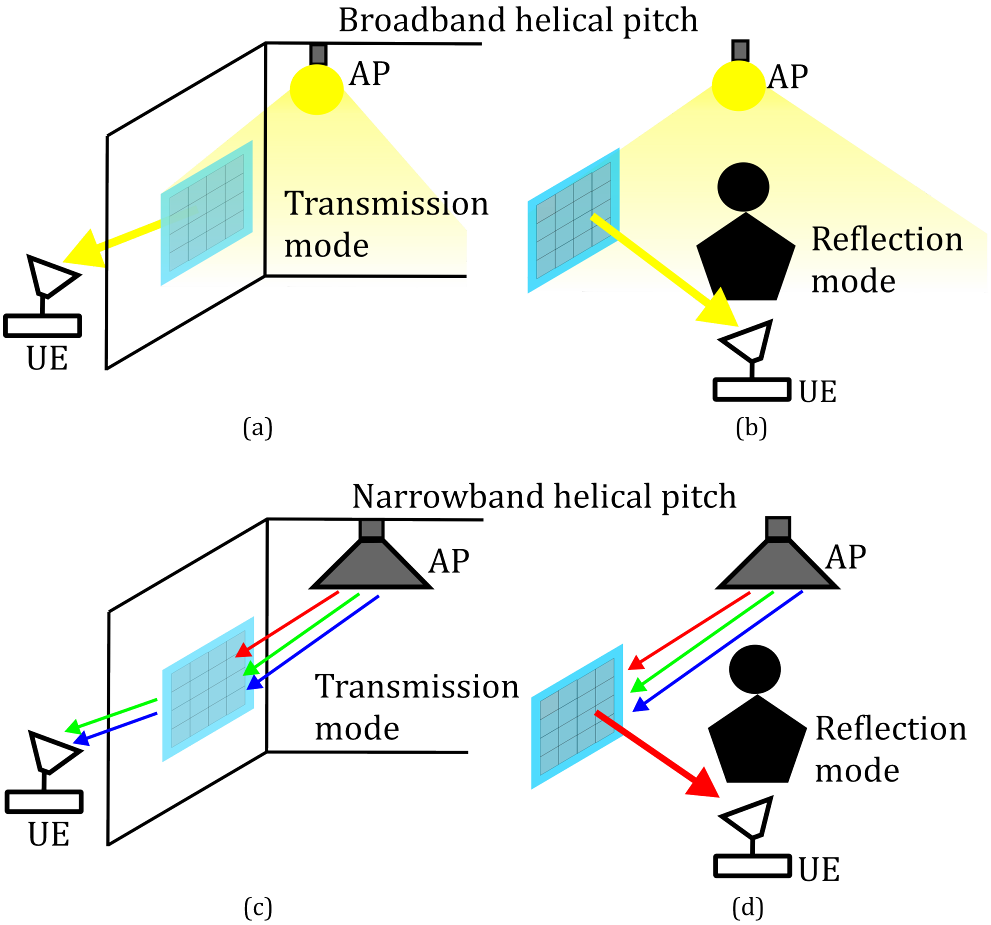

Figure 8.2: Potential use-cases for the VLC RIS technology proposed in this thesis. Assuming a broadband helical pitch and (a) RIS in transmission mode, and (b) RIS in reflection mode with a blockage between the UE and AP. A narrowband helical pitch for (c) transmission mode and (d) reflection mode with a LoS blockage.

combined with the chiral dopant R5011 (Merck KGaA). E7 was selected due to its nematic phase at room temperature and well-known values for refractive index, $n_{\parallel} = 1.747$ and $n_{\perp} = 1.522$ at $\lambda = 589$ nm and a temperature of 20°C. R5011 (right-handed twist) was chosen because of its strong helical twisting power (HTP) of $\approx 115\ \mu\text{m}^{-1}$ [110].

The pitch of the CLC can be calculated by

$$p = \frac{1}{C \cdot HTP} \tag{8.2}$$

where C is the weight concentration of the chiral dopant. As the central wavelength of the Bragg reflection band is $\lambda = np$ and the target wavelength was centred around 633 nm, the average refractive index i.e., $(n_{\parallel} + n_{\perp})/2$, was used to estimate the pitch, providing $p = 388$ nm. Equation 8.2 was then used to estimate the required concentration of R5011. The CLC mixture was prepared by combining 2.23 wt.% of R5011 with 97.76 wt.% of E7 and heating the mixture to 80°C for 24 hours. Achieving the correct ratio of R5011 to E7 required several attempts due to the particularly small weight of R5011 required (≈ 60 mg), with multiple batches made and the reflection band was tested to ensure it was located at the desired frequency range. The CLC was then infiltrated into an LC cell provided by Samsung, which had an air gap of 5 μm and homogeneous alignment layers. The cell featured an ITO layer on the two inner glass surfaces, which were connected to two copper wires in order to apply a voltage across the device.

8.3.2 The Complete RIS unit cell

To impart a phase shift of 2π onto the optical signals, a nematic LC device (5 μm air gap, Samsung) with homogeneous alignment layers, infiltrated with E7, was constructed. Copper wires were also connected to the ITO electrodes to facilitate the application of an electric field. As previously discussed, to fully reflect the incident light using a CLC, the incident light must be circularly polarised with the same handedness as the CLC: this was addressed by the addition of quarter-wave plates (QWP) both in-front and behind the CLC device. The final unit cell structure is illustrated in **Figure 8.3**.

The intended operation of the dual-mode unit cell is thus: in reflection mode, linearly polarised light signals penetrate through the nematic LC layer, where the phase modulation is controlled via an externally applied voltage; the light signal will then pass though the QWP and convert from linear polarisation to right circular polarisation (RCP) before arriving at the CLC device (with no voltage applied): due to the Bragg effect, and the chiral-dopant being right-handed, the RCP light is reflected from the CLC device and back through the QWP, again becoming linearly polarised. Finally, the linearly polarised light will exit via the nematic LC where the phase is modulated further.

In transmission mode, linearly polarised optical signals enter the nematic LC layer where the phase of the signal is modulated by an external electric field. The CLC device will have an external electric field applied such that it exceeds the threshold required to unwind the helix, given in Equation 8.1, which will reorient the LC director to align

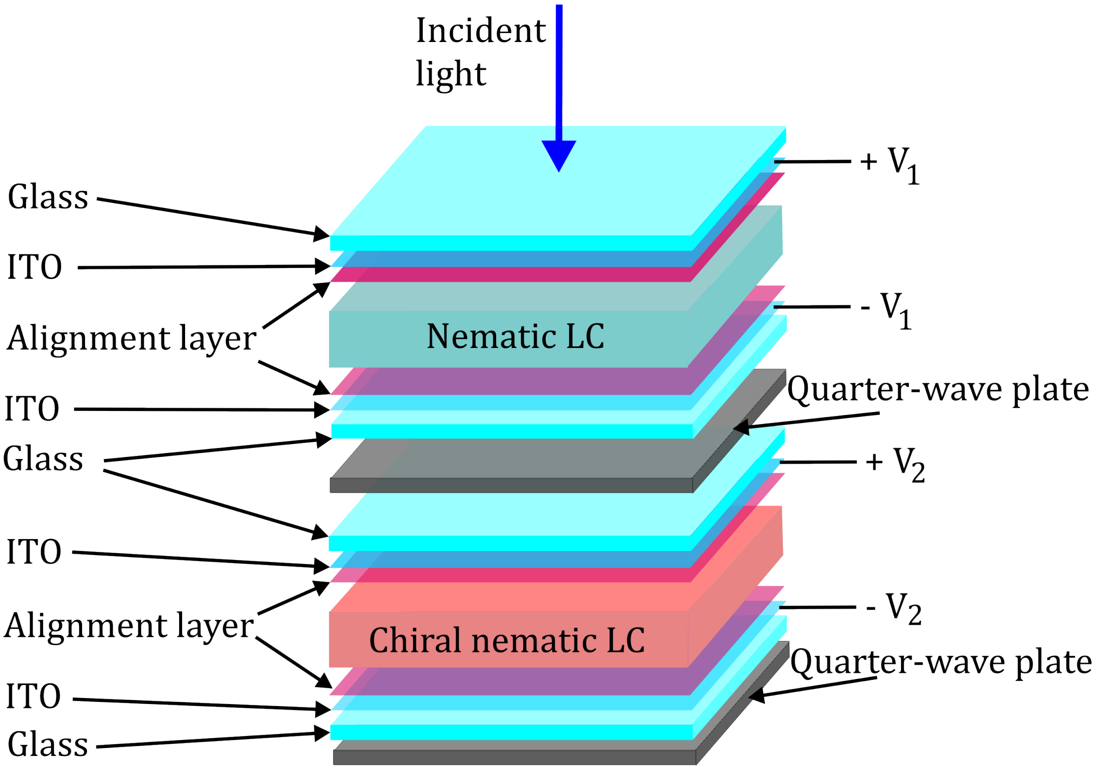

Figure 8.3: Structure of the dual-mode VLC RIS unit cell. In transmission mode, an a.c. voltage, V_1 controls the phase of the incident light signals passing through the nematic LC layer and a large voltage i.e., $V_2 \approx 50$ V is applied across the CLC layer to unwind the helix. In reflection mode, V_1 controls the phase, accounting for two passes of the light signals, and $V_2 = 0$ V.

with the electric field, conforming to the homeotropic state (as in Figure 8.1c)), allowing the transmission of light. Since the light signals will pass through the first QWP and become RCP, which is required to maximise the reflection mode capability, a second QWP was included after the CLC device, converting the RCP light signals back to linear polarisation.

One of the main assumptions for the operation of the dual-mode unit cell is that the incident light is linearly polarised. However, most VLC sources, in particular those that use an LED, emit unpolarised light. This can be addressed by targeting those VLC systems that use polarised light, for example, with a laser diode source, or by employing an additional linear polariser in the unit cell, although this would negatively affect the intensity of the emitted light. It is also the case that the CLC device will reflect unpolarised light, although it will not be as strongly reflected. A further assumption is to negate any angular effects. In practice, the reflect band of a CLC exhibits a strong angular dependence. These effects will not be measured for the operation of the dual-mode unit cell, however, methods to mitigate the angular dependence will be discussed.

8.4 Experimental Methods

8.4.1 Transmission Measurement

To characterise the unit cell in transmission mode, a phase-shifting Mach-Zehnder interferometer was established with the dual-mode unit cell placed in the test path, as depicted in **Figure** 8.4. The measurement equipment included a helium-neon (He-Ne) laser operating at $\lambda = 633$ nm (Thorlabs, HNL050L) passing through a non-polarising beam-splitter, directing the light into the reference path and test path. The reference path featured an acoustic optic frequency shifter (AOFS) that provided a continuous phase shift at 40 MHz, which created the phase-shifting interferometer. The dual-mode unit cell was placed in the test path. Before the unit cell, a half-wave plate (HWP) was positioned in the test path to match the polarisation of the reference path, which was inverted by the AOFS. A polariser was placed either side of the unit cell to ensure the intended polarisation state was measured.

The CLC device was controlled by a function generator (Tektronix AFG2021) that output to a voltage amplifier to produce up to 100 V, and the nematic LC device was controlled with a second function generator (Multicomp PRO, MP750510). The two paths were combined at a second non-polarising beam splitter and reflected by two mirrors. The extended path from the beam splitter was to mitigate stray light caused by the AOFS, improving the interference measurement. At the end of the extended path the light signals were received by a PD (DET10A/M Si based detector). Hence, the received signal at the PD was a combination of the phase-shifted light from the reference path and the test path with the optical phase shift from the nematic LC cell.

8.4.2 Reflection Measurement

To experimentally validate the VLC RIS unit cell in reflection mode, a phase-shifting Twyman-Green interferometer was constructed, with the unit cell placed in the test path

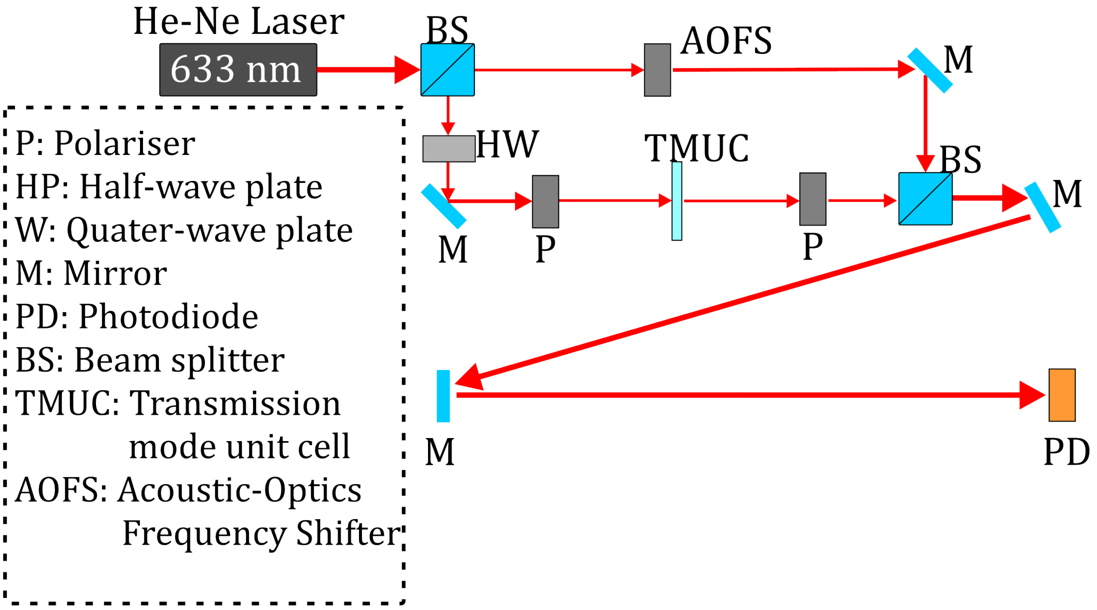

Figure 8.4: A phase-shifting Mach-Zehnder interferometer constructed to characterise the RIS unit cell in transmission.

as depicted in **Figure** 8.5. A He-Ne laser emitting at $\lambda = 633$ nm was again utilised, with the light passing through a non-polarising beam splitter to divide the laser signal into the test path, featuring the dual-mode unit cell, and the reference path. For the test path, light passed through a polariser and then the nematic LC device, before entering a QWP that converted linearly polarised light to RCP. At the end of the test path, standard Twyman-Green interferometer measurements would feature a mirror to reflect the signal; however, for this measurement, the mirror was replaced by the CLC device to reflect the RCP light via Bragg reflection.

The nematic LC device was connected to a function generator (Tektronics AFG2021) to apply a voltage across the device. For the reference path, the light passed through a QWP, rotating HWP, another QWP, and was then reflected by a mirror. Rotation of the HWP was controlled via a motor (PRM1Z8/M) rotating 90° every 4 s, eliciting a continuous phase-shift in the reference path that completed a 360° phase-shift every 4 s. The signals from the two paths were then recombined in the same beam splitter and passed through a lens to enlarge the beam pattern received by the PD (Thorlabs, PDA36A-EC, Si-amplified detector).

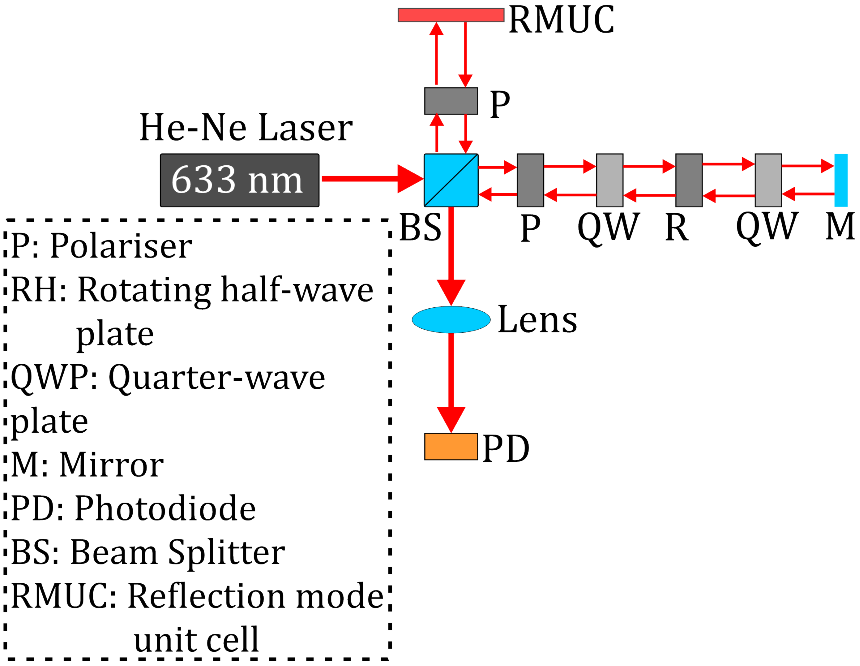

Figure 8.5: A phase-shifting Twyman-Green interferometer constructed to characterise the RIS unit cell in reflection.

8.5 Results

8.5.1 CLC Device Characterisation

To characterise the CLC device, the reflection band was recorded using a UV-Vis spectrometer (Agilent Technologies Cary 8454) and the results are portrayed in **Figure** 8.6. The transmittance was measured at 0 V to record the reflection bandwidth; at 50 V, to observe the helix unwinding; and a second time at 0 V to confirm the device returned to its initial state. The first measurement at 0 V showed that the reflection bandwidth was $\Delta\lambda = 80$ nm, with the laser wavelength situated close to the middle of the band, with an upper and lower limit of 601 nm and 681 nm, respectively. It also exhibited a reflectance of $\approx 45\%$, assuming that the scattering losses can be estimated as 15% from the average reduction in transmittance, T, observed in the 50 V measurement, and by taking reflectance, $R = 1 - T$ for the 0 V measurement. This is in agreement with the theoretical behaviour of the reflections: as the light from the UV-vis was unpolarised and not RCP, the maximum theoretical reflectance is 50%. However, even with unpolarised light, almost half of the incident light was reflected, suggesting the unit cell could still be

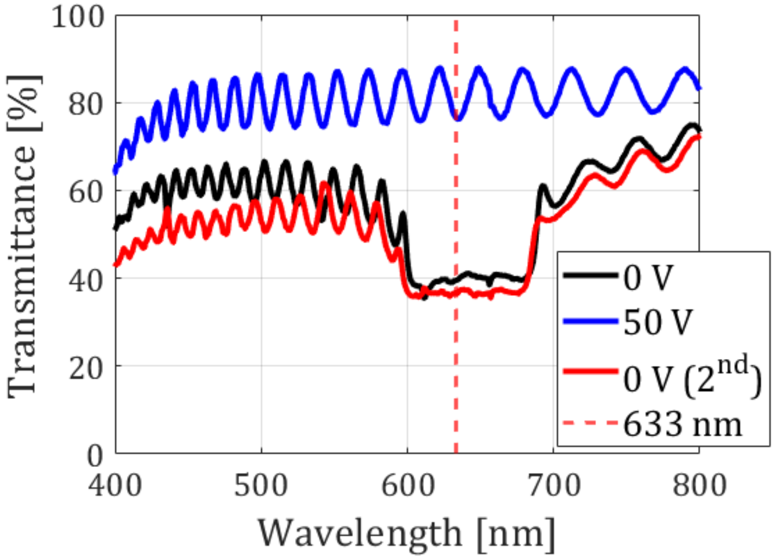

Figure 8.6: Transmittance as a function of wavelength for the CLC device with and without a voltage applied.

useful without the QWP or in a VLC system with an unpolarised light source. At 50 V, the transmittance was 86% on average, providing confidence that the helical pitch was fully unwound. Upon removing the voltage across the CLC device, the reflection bandwidth returned to its initial state, in terms of the reflection bandwidth and amplitude, providing assurance that applying a large voltage to the CLC device would not destroy or deteriorate the helical structure.

To further investigate the behaviour of the CLC device, it was observed under a polarising optical microscope (POM) at ×20 magnification under crossed analyser and polariser, shown in **Figure 8.7**. As before, the device was characterised at 0 V, 50 V, and 0 V for a second time, after the voltage was removed. The POM image in Figure 8.7(a) demonstrates the typical Grandjean texture associated with a CLC. In Figure 8.7(b), with 50 V applied, no light was able to pass into the microscope camera, indicating that the helix was indeed unwound and the LC had assumed a homeotropic nematic LC alignment. Upon removing the voltage, in Figure 8.7(c), the device returned to the Grandjean state, although the number of defect lines had increased somewhat. However, this was not expected to cause any issues for the RIS unit cell operation.

The switching time of the CLC device was measured using a modified version of the

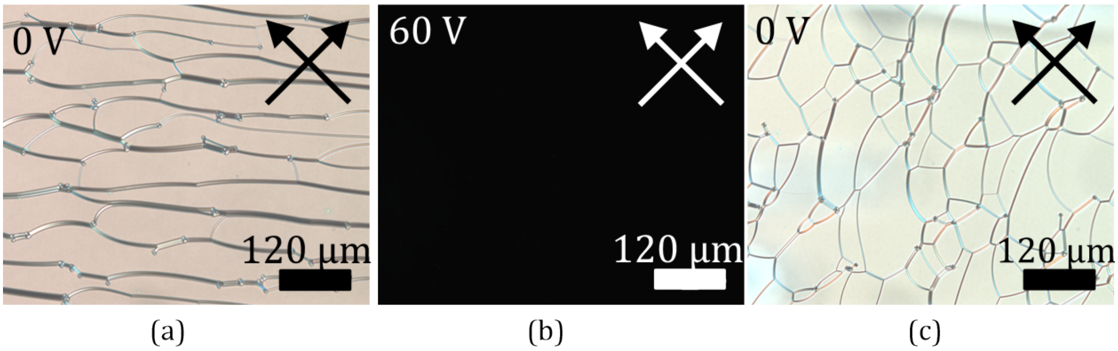

Figure 8.7: Chiral nematic LC device observed under a POM at ×20 magnification and crossed analyser and polariser at (a) 0 V, (b) 50 V, and (c) 0 V after the 50 V was removed. The single headed white or black arrows in the images indicate the orientations of the polariser and analyser.

Mach-Zehnder interferometer whereby the reference path was blocked, such that only the test path was recorded at the PD. A 1 kHz, 50 V a.c. voltage signal was applied across the CLC device for a duration of 5 s, after which the voltage was turned off for 5 s, then back on for 5 s, and so on. By recording the data for the test path only, the PD received signals from the laser when the unit cell was in transmission mode, and weak signals when it was in reflection mode, that is, with the voltage and without the voltage applied, respectively. **Figure 8.8** demonstrates the 'switch on' and 'switch off' times for the device. By defining the 'switch off' time, τ_{off} as the time taken for the voltage to drop from 90% to 10% of its maximum value, and the 'switch on' time, τ_{on}, as the time taken to go from 10% to 90% of its final value, the switching times were calculated as: $\tau_{on} = 1.21$ ms and $\tau_{off} = 56$ ms.

The response times for the nematic LC device was calculated using Equations 2.19 and 2.20 to be $\tau_{on} = 0.54$ ms and $\tau_{off} = 53.4$ ms, assuming a rotational viscosity of 237 mPa·s, and a splay elastic constant of 11 pN. The 'switch on' time for the CLC device was slightly longer, despite the applied voltage being 5 times greater than for the nematic LC. This could be explained by the additional time for the helix to fully unwind in the CLC device, since the helical structure introduces additional elastic energy, specifically, a twist deformation energy, that the applied voltage must overcome. The 'switch off' time for the CLC device was also slightly longer, with the extra time required to reform the helical structure compared to the nematic LC device.

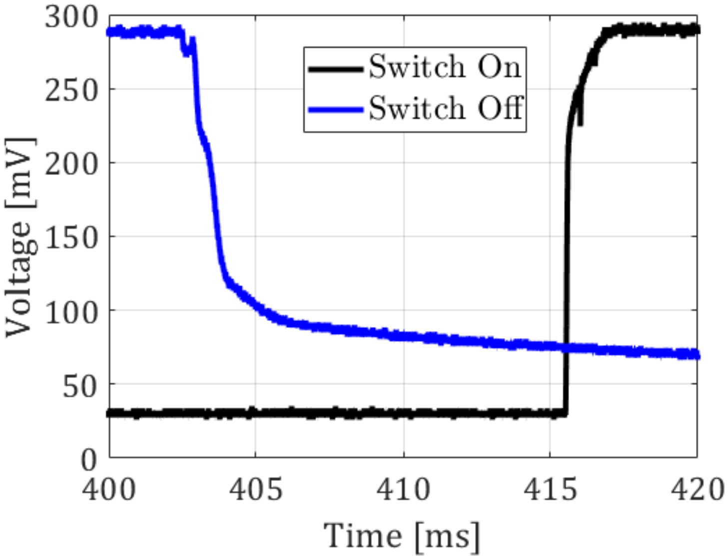

Figure 8.8: Switching times of the CLC device.

CLCs exhibit considerable angular dependence of the reflection band: at oblique incidence, the reflected wavelength shifts towards shorter wavelengths angles. The use of gradient pitch CLCs, as described in [108], could be explored to mitigate this concern, and research has been conducted to further reduce this problem by doping the CLC with a nematic LC that exhibits zero birefringence at 575 nm, 600 nm, and 625 nm, increasing the angular range to 80° [111]. Furthermore, in [112], a 100° viewing angle with no wavelength shift was exhibited. The angular independent state was achieved by a stable disturbed planar texture in a surface-treatment free LC device.

8.5.2 Transmission Mode Phase-Shift

The optical phase information was extracted by setting up an oscilloscope with two channels; one channel measured the 40 MHz sine wave that was applied to the AOFS and taken as the reference signal, and the other channel was connected to the PD, which contained the phase modulation information from the test path containing the unit cell. A 1 kHz square wave was applied to the nematic LC device and the difference in phase between the reference and the signal paths was calculated directly from the oscilloscope. This was achieved by initially applying a low voltage across the nematic LC device (< 1 V) to observe a minor difference in the phase of the reference and test signals. The

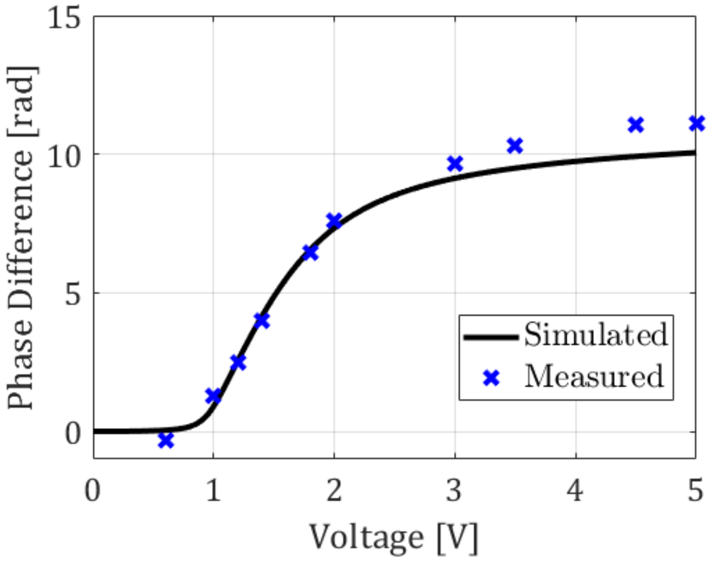

Figure 8.9: Measurement and simulation results for the phase-shift as a function of voltage for the nematic LC in transmission mode.

amplitude of this voltage was increased incrementally to allow the phase difference to be tracked, in particular, to observe when the phase difference approached, and surpassed, 2π, to prevent phase wrapping errors. To mitigate against phase drift, the voltage was removed after each measurement to ensure it returned to the reference position, and each increment of the voltage amplitude was measured five times, with the average value recorded. For the duration of the transmission measurement, a 50 V, 1 kHz square wave, was applied across the CLC device.

A simulation of the director profile for the Fréedericksz device was computed using the parameters for E7. This simulation used the same energy minimisation process described in Equation 5.3. **Figure 8.9** exhibits the measured and simulated phase-shift achieved in the unit cell by applying an increasing voltage to the Fréedericksz device. The measurement demonstrated a $> 2\pi$ phase shift with a low voltage applied, approximately 1.8 V, and there was excellent agreement between the measured and simulated results, across the range of voltages. This result was not unexpected due to the short wavelength of the laser compared to the thickness of the LC device.

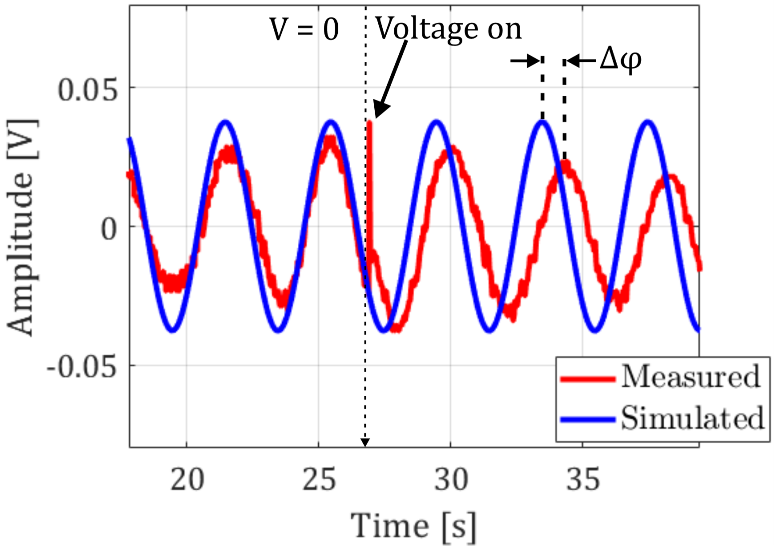

Figure 8.10: Extraction method for determining the phase-shift for the reflection mode measurements.

8.5.3 Reflection Mode Phase-Shift

The optical phase-shift in reflection mode was measured using the Twyman-Green interferometer configuration illustrated in Figure 8.5, with the sinusoidal signal received at the PD an interference pattern of the reflection and test paths. Data received at the PD was recorded for a duration of 1 minute to capture four periods of the sine wave, which was observed on an oscilloscope, without any voltage applied to the nematic LC device, then applying a 1 kHz square wave across the device until a further four cycles of the received sine wave were recorded, before turning off the voltage and recording a final four periods of the received sine wave. This was repeated with incremental increases of the voltage applied to the nematic LC device for each measurement. When the voltage across the nematic LC device was switched on, there was a clear spike in the received waveform denoting the point at which the phase of the received signal shifted. This modulation of the phase by the nematic LC layer was extracted by plotting all twelve cycles of the recorded data alongside a simulated sinusoidal wave that overlapped with the measured data at 0 V, then measuring the phase difference between the simulated sinusoid and measured data with the voltage applied. This extraction technique is portrayed in **Figure 8.10**.

The LC director profile simulation was again used, with the phase-shift values from the transmission measurement doubled to account for the light making two passes through the nematic LC device when in reflection mode. **Figure 8.11** displays the measured and simulated results for the unit cell in reflection mode, again yielding excellent agreement between the measured and simulated data and easily achieving the required 2π phase-shift, with only ≈ 1.4 V$_{RMS}$

8.5.4 Comment on Phase-Shift Strategy

It was previously assumed that the phase shift applied at the RIS was any value in the range $(0,2\pi]$, i.e., a continuous phase-shift. This is often the assumption for theoretical considerations of RIS technology; however, in practice, a discrete phase-shift, commonly two values, that is, on or off, is applied due to 1) imperfect CSI, 2) component costs and 3) increased overhead in control signals for transmitting more than two phase values. Since increasing the number of phase-shift levels using a nematic LC does not incur additional component costs, increasing to four or eight levels could be achieved with only a minor increase in signalling overhead. To achieve this, the phase values would need to be related to a specific voltage level; for example, for a phase-shift of π, 1.3 V would be required in transmission mode, or 1.5 V in reflection mode (this would equate to 3π but due to to phase wrapping the result would be a net shift of π). These voltage values would need to be measured for specific LC materials and thicknesses. For four distinct phase values, a 2-bit binary number could be transmitted to the RIS, with this relating to one of the four voltages, which could be different for each of the RIS elements.

It is also worth commenting on the strategy for switching between transmission and reflection modes in the dual-mode RIS elements. The time to switch between modes was measured as 53.4 ms for switching off and 0.54 ms for switching on, and requires only a binary on/off control signal. The entire RIS does not need to be in the same mode as each unit cell can be controlled individually, although, this would increase overhead compared to the case where the entire RIS is in the same mode. The strategy for switching between modes could be based upon need, or through an optimisation protocol, for example.

8.5.5 RIS Unit Cell Transmittance and Reflectance

The modified Mach-Zehnder interferometer was employed to calculate the combined transmittance of the VLC RIS unit cell: this was achieved in the same manner as de-

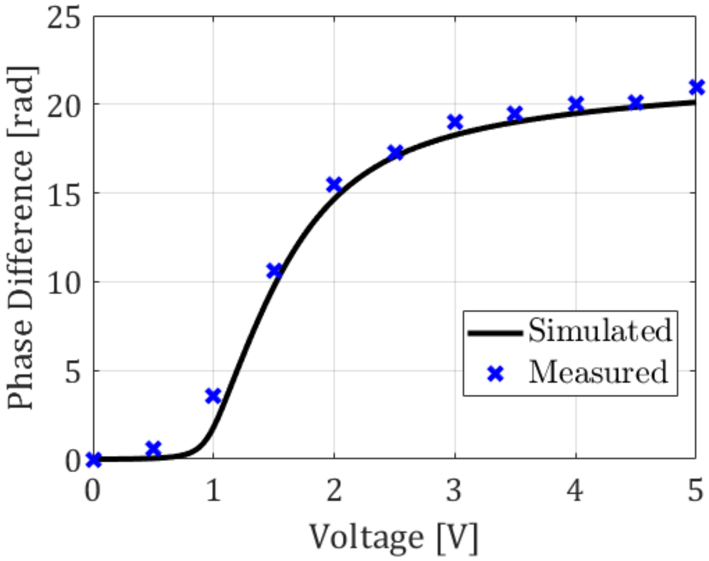

Figure 8.11: Measurement and simulation results for phase-shift against voltage in reflection mode.

scribed for calculating the CLC device switching time (the reference path was blocked). An initial measurement was conducted without the unit cell in the test path to assess the received signal voltage at the PD, which was $V_{max} = 355$ mV. Thence replacing the unit cell, the transmittance was measured by recording the received voltage when the CLC device had 50 V applied across the cell, V_T. The transmittance was again measured by recording the received voltage when the CLC device was in reflection mode, V_R, i.e., no voltage applied. The total unit cell transmittance in transmission mode was calculated as $T_T = V_T/V_{max} = 82\%$, and in reflection mode as $T_R = V_R/V_{max} = 7\%$.

The transmittance of the RIS unit cell in transmission mode was slightly diminished from the UV-Vis measurement in Figure 8.6 due to the addition of the Fréedericksz device, which was not present for the UV-Vis measurement. Nonetheless, the transmittance of the unit cell remained high. The reflection mode transmittance was substantially improved over the UV-Vis measurement due to the QWP converting the light to RCP before entering the CLC device.

To gauge the reflectance of the entire unit cell in transmission and reflection mode, three further measurements were conducted using an adjusted Twyman-Green interferometer configuration, where the reference path was blocked leaving only the light signals from the signal path received by the PD. The intensity of light received at the PD was recorded with the unit cell in the test path with either 50 V or 0 V applied across the CLC device, i.e., in transmission mode and reflection, respectively. The measurement was conducted again after removing all components of the unit cell and replacing it with a mirror. This provided the total reflectance of the unit cell in reflection mode, $R_R = 75\%$, and the reflectance in transmission mode of $R_T = 0.5\%$, likely due to some scattered light from the CLC device holder entering the detector. It should be noted that the reflectance was measured with respect to the reflectance of a mirror, and not the power transmitted directly from the He-Ne laser. This was considered as a fair comparison since when using the unit cell in a VLC RIS, there is not expected to be a LoS signal from the AP to the UE, and the main competitor for the RIS structure in a VLC system is an array of mirrors.

The transmittance and reflectance were both denigrated by the design of the unit element, in particular due to the extra layers of glass from using two LC cells, rather than a hybrid design to reduce the glass layers, or reduce the thickness of the nematic LC or CLC layers. This would increase the intensity of light emitted from the element and thus increase the reflectance and transmittance of the unit element in reflection and transmission mode, respectively.

8.6 Conclusions

In this Chapter, a novel concept for a dual-mode VLC RIS was proposed, and for the first time, a unit cell for a VLC RIS system was constructed and tested. The dual mode concept was enabled through exploiting the reflections of a chiral LC device that was switched between transmission and reflection modes using an externally applied voltage. Initial investigations into the experimental performance of the dual-mode RIS VLC unit element demonstrated that it was capable to operate as intended: the device reflected 75% of incident light in reflection mode and transmitted 82% in transmission mode, with a switching time between the two modes of 1.21 ms and 56 ms, respectively, and was able to impart a full 2π phase shift on the light incident at the element. The CLC device was subjected to numerous transitions between the two modes, with the chiral helix returning to the Grandjean state each time, although long-term stability analysis may be necessary.

Four use-cases for the dual-mode VLC RIS concept were presented to relate the possible scenarios in which the system could elicit a performance improvement in a VLC link. However, further work to model the RIS-assisted VLC channel in each of these scenarios is needed to evaluate the benefits of this concept. The dual-mode unit cell was characterised at a discrete wavelength, defined by the operation of the laser source and reflection bandwidth of the CLC, rather than across the entire range of the visible spectrum. The aim here was to demonstrate the feasibility of this design, and it has been established in many other published works that CLCs with a broadband reflection encompassing the visible portion of the EM spectrum can be produced. Hence, this work represents a proof of concept indicating both the viability of the approach and a clear route forward to deliver this technology.

Chapter 9

Conclusions and Future Work

In this Thesis, an investigation into the feasibility and utility of employing nematic liquid crystals (LCs) to effect alterations in the basic the properties of reconfigurable intelligent surfaces (RISs), and reconfigurable antennas (RAs) in the radio frequency (RF) and optical domains has been presented. Reconfiguration of these properties, such as the frequency of operation or the phase of reflected electromagnetic (EM) signals, allows the RA, or RIS, respectively, to dynamically respond to a degradation in the performance of the wireless communications channel, thereby improving the quality of service, with only a minimal increase in additional hardware and/or power consumption. To facilitate this, several experimental methods, and techniques to characterise both the RF and optical properties, were developed to evaluate the RIS and RA devices investigated in this Thesis. This Chapter will summarise the key findings for each of the research Chapters, and will discuss any relevant future work that would improve either the performance of the device or develop its technical readiness.

9.1 Materials and Experimental Methods

In Chapter 3 the materials, alongside the experimental methods, utilised to construct the RA and RIS devices in this Thesis were described. The basic steps used to build a LC-based device were outlined, and then a method to apply this to copper-clad substrates was detailed. Two methods to etch complex patterns into indium-tin-oxide (ITO)-coated glass substrates were presented and each was assessed for its advantages and disadvantages. Finally, the construction of a bespoke anechoic chamber (BAC), and ancillary equipments, that were integral to the Thesis and facilitated the RF performance testing for the LC-based devices, was reported.

With regards to the development of optically-transparent devices, the laser etching technique produced the fastest and most reliable results; however, the process of removing the ITO caused noticeable damage to the glass surface. That was not a problem for the prototype devices demonstrated here, however, further optimisation of this process could be done to reduce, or completely negate this damage. Furthermore, larger ITO-coated substrates could be used to allow larger devices to be fabricated, such as antenna arrays.

The BAC, while suitable for the measurements in this Thesis, required some compromises due to budget and time constraints. To improve the BAC, the mechanical, hand-turned, turnable could be replaced by an automatic system. This could be achieved in an inexpensive way using a small motor programmed with a microprocessor, improving the accuracy and reducing the time needed for antenna measurements.

9.2 Reconfigurable Bowtie Antenna

In Chapter 4, a reconfigurable bowtie antenna was presented. The classic bowtie antenna design was updated to incorporate a nematic LC in a way that produced a change in the operational frequency of the antenna, when changing the dielectric properties of the LC. Here, the alteration of the LC dielectric properties was achieved by thermally tuning the nematic LC, rather than using an electric field, as is common. The thermal tuning resulted in a modest 21 MHz shift in the operational frequency of the antenna, however, subsequent CST Studio simulations suggested that this could be increased to 85 MHz using a bespoke nematic LC mixture tailored for operation at RF. The main drawbacks of the bowtie V2 antenna were the heating pad affecting the efficiency of the antenna and the lack of frequency reconfigurability, stemming from the thickness and suitability of the LC mixture that was used for these demonstrations. The drawbacks could be addressed by:

- investigating more targeted heating of the LC layer,
- reducing the thickness of the LC layer,

- incorporating a nematic LC tailored for use at RF.

For example, the bowtie antenna could incorporate the nematic LC mixture ZOC-A019XX, with small Kapton polyimide heating systems, to improve the tunability, and address the poor efficiency, respectively. It should be stressed that this mixture was not available when the reconfigurable bowtie antenna was being developed and tested. Alternatively, the operation of the antenna could be reconsidered; for example, by employing the antenna in an environment that is sensitive to changes in heat, such as a greenhouse, with changes to the operational frequency monitored, and communicated using the antenna, to discern thermal variations in the greenhouse.

9.3 Characterisation of Liquid Crystal Dielectric Properties for RF Applications

Chapter 5 related the behaviour of a nematic LC mixture, E7, at frequencies of 4 GHz and 5 GHz, utilising an optically-transparent microstrip line device to observe the effect of glass substrates on the effective dielectric properties of the device. By characterising the LC permittivity at 4 GHz and 5 GHz, it was demonstrated through both measurements and EM simulations that the effective permittivity of the microstrip device, where the effective permittivity included dielectric permittivity contributions from the glass superstrate and LC substrate, was increased by 15% over the value predicted from closed-form equations. As this behaviour governs the operation of the device, the characterisation was then used to inform the design of the optically-transparent microstrip antenna that featured in Chapter 6.

Further work on this topic could include:

- exploration of analytical methods to incorporate the effect of the glass into the quasi-static analysis of the microstrip line.

- Fabrication of resonance-based devices at additional frequency ranges, e.g., 28 GHz.

- Developing a microstrip device that allows a LC layer thickness of ≈ 100 μm to be used, such as a coplanar waveguide feed, so that the surface alignment is maintained through the LC layer.

In the second half of Chapter 5, LC director profile simulations were employed, using an updated director model to account for thermal fluctuations in the LC bulk, to investigate the effect of the large LC layers commonly seen in RF devices that employ nematic LCs, that is, an LC layer $\geq 100\ \mu$m. The two key findings here were; 1) the surface alignment was not maintained through the large LC layer, and 2) to fully align the LC director with an applied E-field, larger voltages were needed as the LC layer thickness increased.

The aim of these simulations was to demonstrate that thermal effects exist in the LC bulk and that these effects become more pronounced as the LC layer thickness increases. Further work could involve ensuring that the LC director is fully aligned with the applied E-field, through the application of a sufficiently large electric field strength. For each of the simulated LC layer thicknesses presented in this work, it was found that an electric field strength of $E = 1$ MV/m was required. However, to maintain the alignment imposed by the surfaces through the bulk of a thick LC layer is not so easily achieved. Future work in this area could cover:

- employing a series of LC devices of increasing thicknesses; for example, from 10 μm to 500 μm in 50 μm increments, to measure the LC permittivity without an electric field to characterise the effect of increasing LC layer thickness on the alignment.
- Utilising the LC director simulations to quantify effects on LC permittivity in the RF band, rather than describe general behaviour.
- Improve the accuracy of the updated LC director model by using software to simulate and visualise the optical appearance of an LC device on a polarising optical microscope (POM), by exporting data directly from the LC director model, and then comparing these visualisations to experimentally-obtained POM images.

9.4 Reconfigurable Optically-Transparent Antenna

A frequency reconfigurable optically-transparent antenna was demonstrated in Chapter 6. This antenna operated in the expected range for sixth-generation (6G) communication frequencies, specifically, at a frequency of 11 GHz, achieving a frequency shift of 90 MHz and reduction in transmittance of only 14% in the visible portion of the EM spectrum, due to the addition of the nematic LC E7 and alignment layers. Drop-on-demand (DoD) inkjet printing facilitated precise deposition of a contiguous layer of the nematic LC, reducing wastage compared with infiltration.

The aim of this work was to combine two important features of a nematic LC: dielectric anisotropy and transparency at optical wavelengths. The results from the first prototype are encouraging, in particular, the antenna performance and reconfigurability surpassed expectations, particularly when considering the LC mixture was not optimised for RF. However, the degree of frequency shift and transparency could yet be enhanced. The next steps for improving the antenna are:

- **Improve the achievable frequency-shift**

  Utilising LCs that are optimised for RF, for example, the nematic mixture ZOC-A019XX, or exploring alignment materials that will enable the use of a fully homeotropic device, i.e., a material that supports stable LC droplets, which could improve the realisable frequency shift. Alternatively, a fully homogeneous alignment layer combined with LC materials exhibiting a negative dielectric anisotropy could be employed.

- **Improve the optical transmittance**

  Using anti-reflective materials to achieve index matching between the air and glass may help to reduce reflections. Reducing the thickness of the LC layer would also improve transmittance, although may be detrimental to the frequency shift.

- **Examine alternative antenna designs**

  This could include bespoke designs to improve reconfigurability from the LC; exploring alternative transparent conducting films (TCFs), such as graphene; or employing a hybrid TCF/metal mesh system.

Once optimisation of the antenna parameters has been achieved, it is likely that fundamental antenna characteristics, such as the antenna gain, will remain unfavourable for practical adoption of this technology. Hence, this single-element antenna could be used to inform the design of an optically-transparent reconfigurable antenna array: antenna arrays exhibit an improvement in the signal-to-noise-ratio of the communications link related to the number of elements in the array, N. Transparent antenna arrays enable the array to be located in a mobile phone screen, $N \approx 100$, or the window of a building, $N \approx 10,000$, assuming the array is designed to operate at 28 GHz.

Further, alternative LC materials could be incorporated into the array that respond to environmental conditions. Towards this end, UV light or temperature could be used external stimuli, to produce an array with integrated sensing and communications (ISAC), a key metric for 6G systems [113]. One specific example is for the agriculture sector, where very large 'smart' greenhouses are utilised: an optically-transparent reconfigurable antenna array could be designed to monitor the environment inside the greenhouse and communicate this information in an ISAC scenario.

9.5 Liquid Crystal-Based Reconfigurable Intelligent Surfaces for Radio Frequencies

Chapter 7 detailed an investigation into the viability of a nematic LC to affect a continuous phase-shift on reflected RF signals of up to 360° in a RIS unit cell. A set of conditions were outlined to test four LC-based unit cell designs against, with the conditions intended to elicit a unit cell well suited for the fifth-generation (5G) n257 frequency band, and which performed at least as well as the leading alternative, in this case a p-i-n diode-based RIS. A further three benchmarks were used to assess the LC-based unit cell, with each delineating a distinct level of phase-shift performance.

CST Studio Suite periodic boundary simulations suggested that two of these designs, a circular and a rectangular patch, met each of the conditions, but only attained a continuous phase shift of up to 290° and 260°, respectively. Nonetheless, the periodic boundary simulations suggested that these two LC-based unit cells outperformed the leading alternative and were fabricated and measured in the BAC. These measurements indicated that the circular and rectangular unit cells each met the stipulated conditions, in agreement with the periodic boundary simulations, although the phase-shift attained for each measured unit cell was significantly worse, reaching just 20°. This disparity was attributed to the periodic assumption of the simulated unit cell and the sub-wavelength separation facilitating strong mutual coupling between elements that increased the phase-shift, compared with the single unit cell that was measured. Therefore, to move forward with this LC-based RIS, the difference between the periodic boundary simulations and measurements should be addressed by fabricating a periodic unit cell; for example, a 3×3 grid. Measuring such a device in the BAC would provide a more reasonable comparison between the measurement and periodic boundary simulation results. Assuming this leads to positive results, the next steps would be:

- **Optimise the operating frequency**

  The rectangular or circular patch dimensions can be adjusted to ensure the unit cell operates across the n257 band.

- **Explore LC materials**

  Dual-frequency LCs can improve the switching times of the unit cells but may reduce the bandwidth or achievable phase-shift. The level of precision that can be achieved in terms of the voltage input versus phase-shift output, which is important in determining the maximum number of phase-shift levels that an LC-based RIS could realistically produce, should be investigated.

- **Simulate the full RIS**

  CST Microwave Studio can be used to move from a unit cell simulation to the full RIS, including the phase-distribution at each element, assuming a 1-bit or 2-bit RIS.

- **Construct the full RIS**

  Using the same methods and materials as the unit cell, construct a full LC-RIS, with a 20×20 array of unit cells and test the proposed RIS in the BAC, using the phase distribution calculated from the CST simulations. Performance could then be compared against the leading alternative.

Pre-calculating the phase-distribution of the RIS, which is a function of frequency, location in the array, and distance from the transmitter, determines the phase-shift applied at the RIS, rather than having to do this in real time, thereby simplifying the measurement. Demonstrating a 1-bit RIS also simplifies the initial validation, and allows for a fair comparison to the alternative. Further work can then focus on developing the number of phase levels applied by the LC-based RIS.

9.6 Dual-Mode Reconfigurable Intelligent Surface Unit Cell for Visible Light Communications

In the final research Chapter, the investigation into LC-based RIS unit cells was extended to the visible portion of the EM spectrum, featuring a dual-mode unit cell for visible light communications (VLC). The aim of this Chapter was to experimentally validate a unit cell for a VLC RIS system, which had not previously been achieved, and to propose a novel dual-mode concept; that is, a RIS that can operate either in reflection or transmission mode. The dual-mode capability was achieved by employing a chiral nematic LC (CLC) that could transmit or reflect light signals by applying or removing a voltage across the CLC layer, respectively. A second LC layer, utilising the nematic LC mixture, E7, was employed to impart a phase shift on incident light signals of up to 2π radians.

The dual-mode unit cell was then characterised by evaluating the reflection band of the CLC, ensuring it was centred at the operating wavelength of a laser source (633 nm). Two laser interferometers were then constructed to characterise the unit cell in transmission and reflection modes, switching times of the CLC device, and phase-shift from the nematic LC device. Results demonstrated a transmittance of 82% for the unit cell in transmission mode, and reflectance of 75% in reflection mode. Switching times for the CLC and nematic LC were in the millisecond range and both modes demonstrated an achievable phase-shift of $> 2\pi$ radians, congruent with LC director profile simulations of the nematic device.

The initial work to develop the dual-mode VLC RIS element yielded positive results. To further investigate the dual-mode VLC unit cell, the following steps can be taken:

- **Produce a broad reflection band CLC**
  Combining a nematic LC with a chiral dopant and polymer stabilisation can produce a gradient in the pitch of the helix and will elicit a broadband reflection of incident light, thereby reducing the angular dependence of the unit cell.

- **Optimise the unit cell design**

  For this prototype, the CLC, quarter-wave plates and nematic LC device were separate elements. These could be combined, reducing the number of glass layers, to improve the transmittance of the unit element. Other nematic LCs could also be considered in the chiral and/or achiral nematic LC device.

- **Characterise the angular dependence of the unit cell**

  Ideally once a broad reflection band CLC has been established, additional methods to mitigate the angular dependence could be investigated.

- **Simulate a RIS-assisted VLC Channel**

  A model of an LC-based RIS in the VLC channel was derived in [104], however, it contained many oversimplifications and requires a variable phase-shift to be included in the updated model. The model could then be tested as part of a VLC channel to assess the following: continuous versus discrete phase-shifts, the dual-mode operation, and an LC-based RIS versus a mirror array.

- **Employ the dual-mode unit element in VLC comms link**

  An initial experiment could test the unit cell in reflection mode, with no line of sight between the transmitter and receiver, to assess the link performance achieved by reflecting incident light towards the receiver.

- **Constructing a full VLC RIS and testing it in a VLC link**

  As LCs are widespread in the display industry, this is certainly achievable. The main considerations would be programming the RIS phase-shift, determining the channel state information, the trade-off between applying a 1-bit or continuous phase-shift. However, this would also be a novel piece of work and be of significant research and commercial interest.

9.7 Final Remarks

This investigation into LC-based RF devices has demonstrated that the RA and RIS devices considered in this Thesis exhibited a reasonable degree of utility in employing nematic LCs at this frequency range, i.e., 1 GHz - 40 GHz. Many other works on LC devices in this frequency range, such as those detailed in Chapter 1, have found similar conclusions. However, the performance of LCs in this range is limited by the physical properties of the LC as outlined in Chapter 2. In particular, the frequency dependence of the LC, leading to a reduction in dielectric anisotropy at RF, compared to lower frequencies, and the longer wavelengths at RF reducing its interaction with the LC, compared with the shorter wavelengths in the optical domain.

Although bespoke LC materials have been developed for the RF regime, e.g., ZOC-A019XX, these suffer from significantly increased switching times due to an increase in the rotational viscosity of the LC. When combined with the LC layer thickness of RF devices, this results in LC switching times that could render the technologies described here difficult to implement in high-speed networks, although there are other applications that are not as reliant on switching times, such as satellite communications. Compounding this further is the availability of alternative reconfiguration methods, such as p-i-n diodes or variable capacitors.

The advantages of nematic LCs, in particular, the dielectric anisotropy and optical transparency, can be better exploited in communications networks at higher operating frequencies. For example, at 100 GHz, the LC layer thickness and the signal wavelength are significantly reduced, improving the frequency reconfigurability, switching times, and optical transparency. Furthermore, the alternative to LCs, such as p-i-n diodes, are ineffective at this frequency range, leaving nematic LCs as the most well-suited material to be employed in reconfigurable RAs or RISs operating in this regime. Nonetheless the prototype devices presented in this Thesis add to the erstwhile established body of literature on LCs in RAs and RISs, suggesting that the most benefit can be extracted from targeted applications, such as transparent devices in the upper end of the RF regime. Hence, the additional steps discussed in this Chapter present a route towards realising those specified LC-based RF technologies in a practical system.

Bibliography

[1] R. G. Gallager, *Principles of Digital Communication.* Cambridge University Press, 2008.

[2] E. Björnson, Ö. Özdogan, and E. G. Larsson, "Intelligent reflecting surface versus decode-and-forward: How large surfaces are needed to beat relaying?" *IEEE Wireless Communications Letters*, vol. 9, no. 2, pp. 244–248, 2020.

[3] X. Pei et al., "RIS-aided wireless communications: Prototyping, adaptive beamforming, and indoor/outdoor field trials," *IEEE Transactions on Communications*, vol. 69, no. 12, pp. 8627–8640, 2021.

[4] R. Wang, Y. Yang, B. Makki, and A. Shamim, "A wideband reconfigurable intelligent surface for 5G millimeter-wave applications," *IEEE Transactions on Antennas and Propagation*, vol. 72, no. 3, pp. 2399–2410, 2024.

[5] E. U. T. R. Access, "Further advancements for e-UTRA physical layer aspects (release 9)," *European Telecommunications Standards Institute*, 2010.

[6] "Reconfigurable intelligent surfaces (RIS) hardware market," WiseGuy Reports, Global, Tech. Rep., 2024. [Online]. Available: `https://www.wiseguyreports.com/reports/reconfigurable-intelligent-surfaces-ris-hardware-market`.

[7] "Dual-tuner reconfigurable antenna market size, share trends analysis report, 2024–2033," Growth Market Reports, Pune, India, Tech. Rep., 2024. [Online]. Available: `https://growthmarketreports.com/report/dual-tuner-reconfigurable-antenna-market`.

[8] "Global antenna market outlook: Strategic insights forecasts, 2024–2029," Yahoo Finance / Market Research Future, Global, Tech. Rep., 2024. [Online]. Available: `https://finance.yahoo.com/news/global-antenna-market-outlook-strategic-145500225.html`.

[9] J. Sheen, "Comparisons of microwave dielectric property measurements by transmission/reflection techniques and resonance techniques," *Measurement Science and Technology*, vol. 20, no. 4, p. 042 001, Jan. 2009.

[10] R. Kowerdziej and *et al.*, "Microwave complex permittivity of voltage-tunable nematic liquid crystals measured in high resistivity silicon transducers," *Applied Physics Letters*, vol. 102, no. 10, 2013.

[11] H. Maune, M. Jost, R. Reese, E. Polat, M. Nickel, and R. Jakoby, "Microwave liquid crystal technology," *Crystals*, 2018.

[12] C. Fritzsch and M. Wittek, "Recent developments in liquid crystals for microwave applications," in *2017 IEEE International Symposium on Antennas and Propagation USNC/URSI National Radio Science Meeting*, 2017.

[13] A. Penirschke et al., "Cavity perturbation method for temperature controlled characterization of liquid crystals at 38 ghz," 2006.

[14] P. Deo, L. Seddon, and *et al.*, “Microstrip device for broadband (15–65 ghz) measurement of dielectric properties of nematic liquid crystals,” *IEEE Transactions on Microwave Theory and Techniques*, vol. 63, 2015.

[15] M. Yazdanpanahi, S. Bulja, D. Mirshekar-Syahkal, R. James, S. E. Day, and F. A. Fernandez, “Measurement of dielectric constants of nematic liquid crystals at mm-wave frequencies using patch resonator,” *IEEE Transactions on Instrumentation and Measurement*, vol. 59, no. 12, pp. 3079–3085, 2010.

[16] Manabe, Chien, Broer, Chingrinov, and Yoon, “Emerging liquid crystal technologies VIII,” *SPIE*, 2013.

[17] H.-N. Morales-Lovera, J.-L. Olvera-Cervantes, A. Corona-Chavez, and T. K. Kataria, “Dielectric anisotropy sensor using coupled resonators,” *IEEE Transactions on Microwave Theory and Techniques*, vol. 68, no. 4, pp. 1610–1616, 2020.

[18] H.-N. Morales-Lovera, J.-L. Olvera-Cervantes, A.-E. Perez-Ramos, A. Corona-Chavez, and C. E. Saavedra, “Microstrip sensor and methodology for the determination of complex anisotropic permittivity using perturbation techniques,” *Scientific Reports*, vol. 12, no. 4, 2022.

[19] H. Peng, Y. Zhang, S. Zhu, M. Temiz, and A. El-Makadema, “Determining dielectric properties of nematic liquid crystals at microwave frequencies using inverted microstrip lines,” *Liquid Crystals*, vol. 49, no. 15, pp. 2069–2081, 2022.

[20] H. P. Qiang Wu Yongwei Zhang and M. Temiz, “Characterising nematic liquid crystals using a circular patch resonator,” *Liquid Crystals*, vol. 50, no. 6, pp. 1069–1081, 2023.

[21] J. R. Sánchez et al., “Characterization of nematic liquid crystal at microwave frequencies using split-cylinder resonator method,” *IEEE Transactions on Microwave Theory and Techniques*, vol. 67, no. 7, pp. 2812–2820, 2019.

[22] F. Yang, X.-X. Zhang, X. Ye, and Y. Rahmat-Samii, “Wide-band e-shaped patch antennas for wireless communications,” *IEEE Transactions on Antennas and Propagation*, vol. 49, no. 7, pp. 1094–1100, 2001.

[23] P. Soontornpipit, C. Furse, and Y. C. Chung, “Design of implantable microstrip antenna for communication with medical implants,” *IEEE Transactions on Microwave Theory and Techniques*, vol. 52, no. 8, pp. 1944–1951, 2004.

[24] J. Huang and R. Pogorzelski, “A ka-band microstrip reflectarray with elements having variable rotation angles,” *IEEE Transactions on Antennas and Propagation*, vol. 46, no. 5, pp. 650–656, 1998.

[25] C. Balanis, *Antenna Theory: Analysis and Design*. Wiley, 2015.

[26] Ericsson, “Ericsson mobility report,” 2019.

[27] S.-W. Choi, Y.-B. Jung, and S.-O. Park, “Multi-band and multi-polarised reconfigurable antenna for next generation mobile communication base-station applications,” *IET Microwaves, Antennas & Propagation*, vol. 7, no. 10, pp. 819–824, 2013.

[28] K. Natesan, R. Subramaniam, and C. Sivathanu, “Bandwidth and frequency agile MIMO antenna for cognitive vehicular communications,” *International Journal of Communication Systems*, vol. 36, no. 14, e5551, 2023.

[29] D. C. Nguyen et al., “6G internet of things: A comprehensive survey,” *IEEE Internet of Things Journal*, vol. 9, no. 1, pp. 359–383, 2022.

[30] A. Fathy et al., “Silicon-based reconfigurable antennas-concepts, analysis, implementation, and feasibility,” *IEEE Transactions on Microwave Theory and Techniques*, vol. 51, no. 6, pp. 1650–1661, 2003.

[31] Y. Wu et al., “3D printed active origami dielectrics for frequency tunable antennas through mechanical actuation,” *IEEE Access*, vol. 10, pp. 103 552–103 562, 2022.

[32] P. Rawal and S. Rawat, “A bowtie shaped frequency reconfigurable microstrip patch antenna with wide coverage area,” in *2020 5th IEEE International Conference on Recent Advances and Innovations in Engineering (ICRAIE)*, 2020, pp. 1–4.

[33] P. Upender and A. Kumar, “Implementing reconfigurable circularly polarized two port MIMO DRA for thz applications,” *Opt Quant Electron 55*, 2023.

[34] C. G. Christodoulou, Y. Tawk, S. A. Lane, and S. R. Erwin, “Reconfigurable antennas for wireless and space applications,” *Proceedings of the IEEE*, vol. 100, no. 7, pp. 2250–2261, 2012.

[35] R. Reese et al., “A millimeter-wave beam-steering lens antenna with reconfigurable aperture using liquid crystal,” *IEEE Transactions on Antennas and Propagation*, vol. 67, no. 8, pp. 5313–5324, 2019.

[36] S. Bildik, S. Dieter, C. Fritzsch, W. Menzel, and R. Jakoby, “Reconfigurable folded reflectarray antenna based upon liquid crystal technology,” *IEEE Transactions on Antennas and Propagation*, vol. 63, no. 1, pp. 122–132, 2015.

[37] Z. J. Silva, C. R. Valenta, and G. D. Durgin, “Optically transparent antennas: A survey of transparent microwave conductor performance and applications,” *IEEE Antennas and Propagation Magazine*, vol. 63, no. 1, pp. 27–39, 2021.

[38] A. Porch, D. V. Morgan, R. M. Perks, M. Jones, and P. P. Edwards, “Electromagnetic absorption in transparent conducting films,” *Journal of Applied Physics*, vol. 95, pp. 4734–4737, 2004.

[39] T. Yasin, R. Baktur, and C. Furse, “A study on the efficiency of transparent patch antennas designed from conductive oxide films,” in *2011 IEEE International Symposium on Antennas and Propagation (APSURSI)*, 2011, pp. 3085–3087.

[40] J. R. Saberin and C. Furse, “Challenges with optically transparent patch antennas,” *IEEE Antennas and Propagation Magazine*, vol. 54, no. 3, pp. 10–16, 2012.

[41] S. Hong, S. H. Kang, Y. Kim, and C. W. Jung, “Transparent and flexible antenna for wearable glasses applications,” *IEEE Transactions on Antennas and Propagation*, vol. 64, no. 7, pp. 2797–2804, 2016.

[42] Y. Morimoto, S. Shiu, I. W. Huang, E. Fest, G. Ye, and J. Zhu, “Optically transparent antenna for smart glasses,” *IEEE Open Journal of Antennas and Propagation*, vol. 4, pp. 159–167, 2023.

[43] C. M. Lee, Y. Kim, Y. Kim, I. K. Kim, and C. W. Jung, “A flexible and transparent antenna on a polyamide substrate for laptop computers,” *Microwave and Optical Technology Letters*, vol. 57, no. 5, pp. 1038–1042, 2015.

[44] J. Park, S. Y. Lee, J. Kim, D. Park, W. Choi, and W. Hong, “An optically invisible antenna-on-display concept for millimeter-wave 5G cellular devices,” *IEEE Transactions on Antennas and Propagation*, vol. 67, no. 5, pp. 2942–2952, 2019.

[45] F. Nashad, M. Elsdon, S. Foti, D. Smith, and O. Yurduseven, “Development of transparent patch antenna element integrated with solar cells for ku-band satellite applications,” 2016.

[46] B. Xi, X. Liang, Q. Chen, K. Wang, J. Geng, and R. Jin, “Optical transparent antenna array integrated with solar cell,” *IEEE Antennas and Wireless Propagation Letters*, vol. 19, no. 3, pp. 457–461, 2020.

[47] G. Sun, B. Muneer, and Q. Zhu, “A study of microstrip antenna made of transparent ITO films,” in *2014 IEEE Antennas and Propagation Society International Symposium (APSURSI)*, 2014, pp. 1867–1868.

[48] S. Hong, Y. Kim, and C. Won Jung, “Transparent microstrip patch antennas with multilayer and metal-mesh films,” *IEEE Antennas and Wireless Propagation Letters*, vol. 16, pp. 772–775, 2017.

[49] M. S.-S. Shahin Sheikh and M.-M. Bagheri-Mohagheghi, “Transparent microstrip antenna made of fluorine doped tin oxide: A comprehensive study,” *Journal of Electromagnetic Waves and Applications*, vol. 29, no. 12, pp. 1557–1569, 2015.

[50] M. Wawrzyniak, J. Bras, A. Denneulin, and T. P. Vuong, “Influence of mesh geometries on the design of transparent antennas at 2.45 ghz,” *2019 16th European Radar Conference (EuRAD)*, pp. 425–428, 2019.

[51] J. P. Lombardi et al., “Copper transparent antennas on flexible glass by subtractive and semi-additive fabrication for automotive applications,” in *2018 IEEE 68th Electronic Components and Technology Conference (ECTC)*, 2018, pp. 2107–2115.

[52] S. H. Kang and C. W. Jung, “Transparent patch antenna using metal mesh,” *IEEE Transactions on Antennas and Propagation*, vol. 66, no. 4, pp. 2095–2100, 2018.

[53] P. Aghabeyki, P. de la Rosa, M. Caño-García, X. Quintana, R. Guirado, and S. Zhang, “Optically transparent beam-steering reflectarray antennas based on a liquid crystal for millimeter-wave applications,” *IEEE Transactions on Antennas and Propagation*, vol. 72, no. 1, pp. 614–627, 2024.

[54] W. Hu et al., “Design and measurement of reconfigurable millimeter wave reflectarray cells with nematic liquid crystal,” *IEEE Transactions on Antennas and Propagation*, vol. 56, no. 10, pp. 3112–3117, 2008.

[55] *Ericsson Mobility Report June 2022*.

[56] E. Basar, M. Di Renzo, J. De Rosny, M. Debbah, M.-S. Alouini, and R. Zhang, “Wireless communications through reconfigurable intelligent surfaces,” *IEEE Access*, vol. 7, pp. 116 753–116 773, 2019.

[57] M. Di Renzo et al., “Smart radio environments empowered by reconfigurable intelligent surfaces: How it works, state of research, and the road ahead,” *IEEE Journal on Selected Areas in Communications*, vol. 38, no. 11, pp. 2450–2525, 2020.

[58] W. Tang et al., “Wireless communications with reconfigurable intelligent surface: Path loss modeling and experimental measurement,” *IEEE Transactions on Wireless Communications*, vol. 20, no. 1, pp. 421–439, 2021.

[59] E. Björnson and L. Sanguinetti, “Power scaling laws and near-field behaviors of massive MIMO and intelligent reflecting surfaces,” *IEEE Open Journal of the Communications Society*, vol. 1, pp. 1306–1324, 2020.

[60] K. Zhi, C. Pan, H. Ren, K. K. Chai, and M. Elkashlan, “Active RIS versus passive RIS: Which is superior with the same power budget?” *IEEE Communications Letters*, vol. 26, no. 5, pp. 1150–1154, 2022.

[61] Z. Zhang et al., “Active RIS vs. passive RIS: Which will prevail in 6G?” *IEEE Transactions on Communications*, vol. 71, no. 3, pp. 1707–1725, 2023.

[62] W. Tang and et al., “Wireless communications with programmable metasurface: Transceiver design and experimental results,” *China Communications*, vol. 16, no. 5, pp. 46–61, 2019.

[63] Ö. T. Demir, E. Björnson, and L. Sanguinetti, “Efficient channel estimation with shorter pilots in RIS-aided communications: Using array geometries and interference statistics,” *IEEE Transactions on Wireless Communications*, vol. 24, no. 1, pp. 462–478, 2025.

[64] M. Haghshenas, P. Ramezani, M. Magarini, and E. Björnson, “Parametric channel estimation with short pilots in RIS-assisted near- and far-field communications,” *IEEE Transactions on Wireless Communications*, vol. 23, no. 8, pp. 10 366–10 382, 2024.

[65] H. Feng, Y. Xu, and Y. Zhao, “Deep learning-based joint channel estimation and CSI feedback for RIS-assisted communications,” *IEEE Communications Letters*, vol. 28, no. 8, pp. 1860–1864, 2024.

[66] Y. Youn et al., “Liquid-crystal-driven reconfigurable intelligent surface with cognitive sensors for self-sustainable operation,” *IEEE Transactions on Antennas and Propagation*, vol. 71, no. 12, pp. 9415–9423, 2023.

[67] R. Neuder, Y. Liu, N. Dzieia, D. Wang, and A. Jiménez-Sáez, “Unit cell design for dual-polarized liquid crystal reconfigurable intelligent surface based on defected delay lines,” in *2024 54th European Microwave Conference (EuMC)*, 2024, pp. 228–231.

[68] R. Guirado, G. Perez-Palomino, M. Caño-García, M. A. Geday, and E. Carrasco, “Mm-wave metasurface unit cells achieving millisecond response through polymer network liquid crystals,” *IEEE Access*, vol. 10, pp. 127 928–127 938, 2022.

[69] R. Guirado, G. Perez-Palomino, M. Ferreras, E. Carrasco, and M. Caño-García, “Dynamic modeling of liquid crystal-based metasurfaces and its application to reducing reconfigurability times,” *IEEE Transactions on Antennas and Propagation*, vol. 70, no. 12, pp. 11 847–11 857, 2022.

[70] D. C. Zografopoulos, A. Ferraro, and R. Beccherelli, “Liquid-crystal high-frequency microwave technology: Materials and characterization,” *Advanced Materials Technologies*, vol. 4, no. 2, p. 1 800 447, 2019.

[71] S.-T. Wu and D.-K. Yang, *Fundamentals of Liquid Crystal Devices.* 2006.

[72] P. de Gennes and J. Prost, *The Physics of Liquid Crystals* (International Series of Monographs on Physics). Clarendon Press, 1993, ISBN: 9780198517856.

[73] D. Andrienko, “Introduction to liquid crystals,” *Journal of Molecular Liquids*, vol. 267, pp. 520–541, 2018, Special Issue Dedicated to the Memory of Professor Y. Reznikov, ISSN: 0167-7322.

[74] I. Bahl, M. Bozzi, and R. Garg. 2013.

[75] A. Goldsmith, *Wireless Communications.* Cambridge University Press, 2005.

[76] Q. Wu and R. Zhang, “Towards smart and reconfigurable environment: Intelligent reflecting surface aided wireless network,” *IEEE Communications Magazine*, vol. 58, no. 1, pp. 106–112, 2020.

[77] L. L. Slawomir Koziel, *Surrogate-Based Modeling and Optimization.* Springer New York, 2016.

[78] S. Abeywickrama, R. Zhang, and C. Yuen, “Intelligent reflecting surface: Practical phase shift model and beamforming optimization,” *ICC 2020 - 2020 IEEE International Conference on Communications (ICC)*, pp. 1–6, 2020.

[79] R. Corporation, *RO4000 laminates: Ro4003c and ro4350b - data sheet*, Accessed: 2025-07-01, 2023. [Online]. Available: `https://rogerscorp.com/-/media/project/rogerscorp/documents/advanced-electronics-solutions/english/data-sheets/ro4000-laminates-ro4003c-and-ro4350b---data-sheet.pdf`.

[80] E. Huber, M. Mirzaee, J. Bjorgaard, M. Hoyack, S. Noghanian, and I. Chang, "Dielectric property measurement of PLA," in *2016 IEEE International Conference on Electro Information Technology (EIT)*, 2016, pp. 0788–0792.

[81] Nanosurf AG, *Coreafm: Compact atomic force microscope – technical specifications*, `https://www.nanosurf.com`, Manufacturer brochure. Z-axis noise specified in the tens to hundreds of picometres RMS, 2023.

[82] Emerson and Cuming, *WAVASORB - data sheet*, Accessed: 2025-07-01, 2022. [Online]. Available: `https://www.ecanechoicchambers.com/pdf/WAVASORB%20-%20VHP.pdf`, `https://www.ecanechoicchambers.com/pdf/WAVASORB%20-%20AN.pdf`.

[83] H. Allinson and H. F. Gleeson, "Dielectric permittivity properties of a fulgide dye guest–host liquid crystal," *Liquid Crystals*, vol. 19, no. 4, pp. 421–425, 1995. DOI: `10.1080/02678299508036563`.

[84] B. Garibello and S. Barbin, "A single element compact printed bowtie antenna enlarged bandwidth," in *SBMO/IEEE MTT-S International Conference on Microwave and Optoelectronics, 2005.*, 2005, pp. 354–358.

[85] J. George, M. Deepukumar, C. Aanandan, P. Mohanan, and K. Nair, "New compact microstrip antenna," *Electronics Letters*, vol. 32, pp. 508–509, 6 1996.

[86] R. Reese et al., "A millimeter-wave beam-steering lens antenna with reconfigurable aperture using liquid crystal," *IEEE Transactions on Antennas and Propagation*, vol. 67, no. 8, pp. 5313–5324, 2019.

[87] H. Xu, O. Trushkevych, N. Collings, and W. A. Crossland, "Measurement of dielectric anisotropy of some liquid crystals for microwave applications," *Molecular Crystals and Liquid Crystals*, vol. 502, pp. 235–244, 2009.

[88] Y. Xia et al., "Reconfigurable wearable antenna for 5G applications using nematic liquid crystals," *Nano Select*, vol. 4, no. 8, pp. 513–524, 2023.

[89] B.-J. Che, F.-Y. Meng, Y.-L. Lyu, and Q. Wu, "Reconfigurable dual-band metamaterial antenna based on liquid crystals," *Journal of Physics D: Applied Physics*, vol. 51, no. etc. r5102, 2018.

[90] OFCOM, *Spectrum above 6 ghz for future mobile communications*, Jan. 2015. [Online]. Available: `https://www.ofcom.org.uk/siteassets/resources/documents/consultations/uncategorised/7886-above-6ghz/summary/spectrum_above_6_ghz_cfi.pdf?v=334124`.

[91] *ITO glass substrates (unpatterned)*, Ossilla, 2024. [Online]. Available: `https://www.ossila.com/products/ito-glass-substrates-unpatterned`.

[92] S. Bulja, D. Mirshekar-Syahkal, R. James, S. E. Day, and F. A. Fernández, "Measurement of dielectric properties of nematic liquid crystals at millimeter wavelength," *IEEE Transactions on Microwave Theory and Techniques*, vol. 58, no. 12, pp. 3493–3501, 2010.

[93] R. Guirado, P. de la Rosa, G. Perez-Palomino, M. Caño-García, E. Carrasco, and X. Quintana, "Characterization and application of dual-frequency liquid-crystal mixtures in mm-wave reflectarray cells to improve their temporal response," *IEEE Transactions on Antennas and Propagation*, vol. 71, no. 8, pp. 6535–6545, 2023.

[94] N. Chi, Y. Zhou, Y. Wei, and F. Hu, "Visible light communication in 6G: Advances, challenges, and prospects," *IEEE Vehicular Technology Magazine*, vol. 15, no. 4, pp. 93–102, 2020.

[95] G. A. Mapunda, R. Ramogomana, L. Marata, B. Basutli, A. S. Khan, and J. M. Chuma, "Indoor visible light communication: A tutorial and survey," *Wireless Communications and Mobile Computing*, vol. 2020, no. 1, p. 8 881 305, 2020.

[96] L. Mucchi et al., “Physical-layer security in 6G networks,” *IEEE Open Journal of the Communications Society*, vol. 2, pp. 1901–1914, 2021.

[97] S. Sun, T. Wang, F. Yang, J. Song, and Z. Han, “Intelligent reflecting surface-aided visible light communications: Potentials and challenges,” *IEEE Vehicular Technology Magazine*, vol. 17, no. 1, pp. 47–56, 2022.

[98] A. M. Abdelhady, A. K. S. Salem, O. Amin, B. Shihada, and M.-S. Alouini, “Visible light communications via intelligent reflecting surfaces: Metasurfaces vs mirror arrays,” *IEEE Open Journal of the Communications Society*, vol. 2, pp. 1–20, 2021.

[99] G. Zhang et al., “Free-space optical communication link with liquid crystal beam-steering,” *IEEE Photonics Technology Letters*, vol. 35, no. 22, pp. 1199–1202, 2023.

[100] S. Aboagye, T. M. N. Ngatched, O. A. Dobre, and A. R. Ndjiongue, “Intelligent reflecting surface-aided indoor visible light communication systems,” *IEEE Communications Letters*, vol. 25, no. 12, pp. 3913–3917, 2021.

[101] S. Sun, F. Yang, W. Mei, J. Song, Z. Han, and R. Zhang, “Channel estimation for optical intelligent reflecting surface-assisted VLC system: A joint space-time sampling approach,” *IEEE Journal on Selected Areas in Communications*, vol. 43, no. 3, pp. 867–882, 2025.

[102] A. M. Abdelhady, O. Amin, A. K. S. Salem, M.-S. Alouini, and B. Shihada, “Channel characterization of IRS-based visible light communication systems,” *IEEE Transactions on Communications*, vol. 70, no. 3, pp. 1913–1926, 2022.

[103] A. R. Ndjiongue, T. M. N. Ngatched, O. A. Dobre, and H. Haas, “Re-configurable intelligent surface-based VLC receivers using tunable liquid-crystals: The concept,” *Journal of Lightwave Technology*, vol. 39, no. 10, pp. 3193–3200, 2021.

[104] S. Aboagye, A. R. Ndjiongue, T. M. N. Ngatched, and O. A. Dobre, “Design and optimization of liquid crystal RIS-based visible light communication receivers,” *IEEE Photonics Journal*, vol. 14, no. 6, pp. 1–7, 2022.

[105] O. Maraqa and T. M. N. Ngatched, “Optimized design of joint mirror array and liquid crystal-based RIS-aided VLC systems,” *IEEE Photonics Journal*, vol. 15, no. 4, pp. 1–11, 2023.

[106] O. Maraqa, S. Aboagye, and T. M. N. Ngatched, “Optical STAR-RIS-aided VLC systems: RSMA versus NOMA,” *IEEE Open Journal of the Communications Society*, vol. 5, pp. 430–441, 2024.

[107] S.-M. Kim, M.-W. Baek, and S. H. Nahm, “Visible light communication using TDMA optical beamforming,” *EURASIP Journal on Wireless Communications and Networking*, vol. 2017, no. 1, p. 56, 2017.

[108] D. Broer, J. Lub, and G. Mol, “Wide-band reflective polarizers from cholesteric polymer networks with a pitch gradient,” *Nature*, vol. 378, no. 6556, pp. 467–469, 1995.

[109] H. Jung and S.-M. Kim, “A full-duplex LED-to-LED visible light communication system,” *Electronics*, vol. 9, no. 10, p. 1713, 2020.

[110] Y.-L. Nian, P.-C. Wu, and W. Lee, “Optimized frequency regime for the electrohydrodynamic induction of a uniformly lying helix structure,” *Photon. Res.*, vol. 4, no. 6, pp. 227–232, Dec. 2016.

[111] P. P. Verbunt, D. K. de Boer, D. J. Broer, and M. G. Debije, “Special dispersion chiral nematic reflectors for luminescent solar concentrators,” in *2015 IEEE 42nd Photovoltaic Specialist Conference (PVSC)*, 2015, pp. 1–6.

[112] H.-Y. Chen, Y.-C. Tsao, C.-H. Chang, and J.-J. Chen, "Stable reflective state induced by a disturbed planar texture in surface-treatment-free chiral nematic liquid crystals," *Optics Express*, vol. 29, no. 19, pp. 30 644–30 654, 2021.

[113] F. Liu et al., "Integrated sensing and communications: Toward dual-functional wireless networks for 6G and beyond," *IEEE Journal on Selected Areas in Communications*, vol. 40, no. 6, pp. 1728–1767, 2022.